

**ELECTROANALYTICAL APPLICATIONS OF REDUCED-
GRAPHENE OXIDE FOR SENSING OF BIOANALYTES**

NORAZRIENA BINTI YUSOFF

**FACULTY OF SCIENCE
UNIVERSITY OF MALAYA
KUALA LUMPUR**

2017

**ELECTROANALYTICAL APPLICATIONS OF
REDUCED-GRAPHENE OXIDE FOR SENSING OF
BIOANALYTES**

NORAZRIENA BINTI YUSOFF

**THESIS SUBMITTED IN FULFILLMENT OF THE
REQUIREMENTS FOR THE DEGREE OF DOCTOR OF
PHILOSOPHY**

**DEPARTMENT OF PHYSICS
FACULTY OF SCIENCE
UNIVERSITY OF MALAYA
KUALA LUMPUR**

2017

UNIVERSITY OF MALAYA
ORIGINAL LITERARY WORK DECLARATION

Name of Candidate: **Norazriena Binti Yusoff** (I.C/Passport No:)

Registration/Matric No: **SHC130074**

Name of Degree: **Doctor of Philosophy**

Title of Project Paper/Research Report/Dissertation/Thesis ("this Work"):

Electroanalytical Applications of Reduced-Graphene Oxide for Sensing of Bioanalytes

Field of Study: **Experimental Physics**

I do solemnly and sincerely declare that:

- (1) I am the sole author/writer of this Work;
- (2) This Work is original;
- (3) Any use of any work in which copyright exists was done by way of fair dealing and for permitted purposes and any excerpt or extract from, or reference to or reproduction of any copyright work has been disclosed expressly and sufficiently and the title of the Work and its authorship have been acknowledged in this Work;
- (4) I do not have any actual knowledge nor do I ought reasonably to know that the making of this work constitutes an infringement of any copyright work;
- (5) I hereby assign all and every rights in the copyright to this Work to the University of Malaya ("UM"), who henceforth shall be owner of the copyright in this Work and that any reproduction or use in any form or by any means whatsoever is prohibited without the written consent of UM having been first had and obtained;
- (6) I am fully aware that if in the course of making this Work I have infringed any copyright whether intentionally or otherwise, I may be subject to legal action or any other action as may be determined by UM.

Candidate's Signature

Date:

Subscribed and solemnly declared before,

Witness's Signature

Date:

Name:

Designation:

ABSTRACT

The development of a sensor for the precise and selective measurement of biological analytes (such as dopamine (DA), nitric oxide (NO), hydrogen peroxide (H_2O_2) and L-Cysteine (L-Cys)) at the low levels characteristic of living systems can make a great contribution to disease diagnosis. The discovery of an electrochemical technique for the detection of various biological analytes was induced by the strong demand on developing a sensing technique that able to offer a rapid response, high sensitivity, simplicity and low operating cost. In order to enhance the analytical performance of electrochemical biosensor, several challenges associated with the sensors need to be solved including: (i) sluggish electron-transfer rate properties at the electrode's surface which led to the poor response signal; (ii) limited sensitivity and selectivity capabilities towards target analyte detection due to occurrence of fouling effect; and (iii) overlapping voltammetric response caused by the co-existence of various interfering species. We have sought to address these problems through chemical modification of conventional working electrode surface with an electrochemically active material, which is reduced graphene oxide (rGO)-based material. The thesis reports the preparation of novel reduced graphene oxide-nafion@metal (rGO-Nf@metal) nanohybrid materials which were then used to modify glassy carbon electrode (GCE) for the detection of various biological analytes. The strategy of using these nanohybrid materials is driven by the excellent individual properties owned by rGO and metal nanoparticles which essential in boosting the sensing performance. There are four important studies that have been presented in this thesis; (i) reduced graphene oxide-nafion (rGO-Nf) nanohybrid modified electrode for electrochemical detection of DA and NO; (ii) reduced graphene oxide-nafion@silver (rGO-Nf@Ag) nanohybrid modified electrode for electrochemical detection of H_2O_2 ; (iii) reduced graphene oxide-

nafion@gold (rGO-Nf@Au) nanohybrid modified electrode for electrochemical detection of NO; (iv) reduced graphene oxide-nafion@palladium (rGO-Nf@Pd) nanohybrid modified electrode for electrochemical detection of L-Cys. To sum up, we have successfully developed a simple, highly sensitive, and selective electrochemical sensor using rGO-Nf@metal-based nanohybrids for the detection of various biological analytes. The novelty of presented work lies in the used of simple, rapid, and facile method for synthesis that is hydrothermal method, and the used of small amount of metal which could reduce the cost of production. Moreover, the combination of three individual materials (rGO, Nf, and metal nanoparticles) to form a ternary nanohybrid material proven to be suitable material for boosting the electrochemical sensor performance, thus open up a new path to develop new catalyst for electrochemical sensor.

ABSTRAK

Pembangunan alat pengesanan analit biologi (seperti dopamine (DA), nitrik oksida (NO), hidrogen peroksida (H_2O_2), dan L-Cysteine (L-Cys)) bagi pengukuran yang tepat dan terpilih pada kepekatan yang rendah dalam sistem hidup boleh memberi sumbangan besar kepada bidang diagnosis penyakit. Permintaan yang tinggi untuk mewujudkan satu teknik penderiaan yang menyediakan tindak balas yang cepat dan sensitif, kemudahan penggunaan dan kos rendah, membawa kepada penemuan teknik elektrokimia untuk mengesan pelbagai analit biologi. Dalam usaha untuk meningkatkan prestasi biopenderia elektrokimia, beberapa isu yang perlu diselesaikan termasuklah: (i) Kadar pemindahan-elektron yang lembap pada permukaan elektrod membawa kepada isyarat tindak balas yang lemah; (ii) kepekaan dan kemampuan untuk memilih analit sasaran yang terhad kerana berlakunya kesan penempilan; dan (iii) tindak balas voltametri yang bertindih disebabkan oleh kewujudan bersama pelbagai spesies yang mengganggu. Kami telah berusaha untuk menangani masalah ini melalui pengubahsuaian kimia terhadap permukaan elektrod kerja yang konvensional dengan bahan aktif iaitu bahan berasaskan grafen. Tesis ini melaporkan penyediaan bahan nanohybrid bagi grafen teroksida-nafion@logam (rGO-Nf@logam) yang kemudiannya digunakan untuk mengubah suai elektrod karbon berkaca (GCE) untuk mengesan pelbagai analit biologi. Strategi untuk menggunakan bahan-bahan nanohybrid didorong oleh sifat-sifat cemerlang individu yang dimiliki oleh rGO dan nanopartikel logam yang mana penting dalam meningkatkan prestasi penderiaan. Terdapat empat kajian penting yang telah dibentangkan di dalam tesis ini; (i) Elektrod diubahsuai oleh grafen teroksida-nafion (rGO-Nf) nanohybrid digunakan untuk mengesan DA dan NO; (ii) Elektrod diubahsuai oleh grafen teroksida-nafion@argentum (rGO-Nf@Ag) nanohybrid digunakan untuk mengesan H_2O_2 ; (iii) Elektrod diubahsuai oleh grafen teroksida-nafion@emas (rGO-Nf@Au) nanohybrid digunakan untuk mengesan NO; (iv) Elektrod

diubahsuai oleh grafen teroksida-nafion@palladium (rGO-Nf@Pd) nanohybrid digunakan untuk mengesan L-Cys. Kesimpulannya, kami telah berjaya membangunkan pengesan elektrokimia yang mudah, sangat sensitif, dan selektif menggunakan bahan berasaskan rGO-Nf@logam nanohybrid untuk mengesan pelbagai analit biologi. Sesuatu yang baru tentang kerja yang dibentangkan adalah terletak pada penggunaan kaedah sintesis yang mudah iaitu kaedah hidroterma, dan penggunaan sejumlah kecil logam yang boleh mengurangkan kos pengeluaran. Selain itu, gabungan tiga bahan individu (rGO, Nf dan partikel logam bersaiz nano) untuk membentuk bahan nanohybrid pertigaan terbukti berkesan untuk meningkatkan prestasi pengesan elektrokimia, sekali gus membuka laluan baru untuk membangunkan pemangkin baru untuk pengesan elektrokimia.

ACKNOWLEDGEMENTS

In the name of Allah, the Most Gracious and the Most Merciful.

Alhamdulillah, all praises to Allah for the strengths and His blessing I managed to complete my PhD studies within two and a half years. Without His blessed and guidance, I would never have been able to finish my dissertation for partial fulfillment of the requirements for getting my PhD. Throughout these years I have learned many things since day one until the end of my studies which makes me more mature and wiser in addressing problems that comes up in life. There are number of peoples without whom I will not be successfully completed this journey and this thesis might not have been written, and to whom I am greatly indebted.

First and foremost I would like to wish a special note of thanks to my supervisor, Dr. Huang Nay Ming for his continuous advices, valuable ideas and precious time. His technical and editorial advice really helps me in completing this thesis. He also has been a constant source of encouragement and enthusiasm since the two years of my Master study until now. His wisdom, knowledge and patience toward research work never fail to inspire and motivate me to work harder and smarter.

I would like to express my deepest gratitude to Dr. Alagarsamy Pandikumar, Dr. Perumal Rameshkumar, and Mr. Shahid Mehmood for their expertise experimental guidance and discussion of some results presented in this thesis. Sincere thanks to my lab mates: Ms. Fadilah, Mrs. Nurul Izrini, Mrs. Marlinda, Mr. Mohd. An'amt, Dr. Lim Su Pei, Dr. John Gan, Ms. Peik See, and Mr. Gregory for always inspiring me when I felt hopeless and also the precious friendship. I would like to extend my thanks to all

Low Dimensional Materials Research Center's (LDMRC) members for their kindness and moral support during my study.

Special acknowledgement goes to my parents (Yusoff Bin Zakaria and Che Salia Binti Yaacob) and also my siblings, who have been supportive in every way. Thank you for taught me for not easily giving up on my dreams and always work harder to change my dreams into a reality. To my lovely husband; Mohd. Asraf Bin Aris and my little son; Hazim Husaini Bin Mohd. Asraf, thank you for your endless love, prayers and encouragement. Your patient and understanding meant the world to me and I could not imagine having to go through this challenging journey without both of you. I am truly thankful for having all of you in my life.

NORAZRIENA BINTI YUSOFF

TABLE OF CONTENTS

| | |
|--|-----------|
| ABSTRACT..... | iii |
| ABSTRAK..... | v |
| ACKNOWLEDGEMENTS..... | vii |
| TABLE OF CONTENTS..... | ix |
| LIST OF FIGURES..... | xv |
| LIST OF TABLE..... | xxiv |
| LIST OF SYMBOLS AND ABBREVIATIONS..... | xxvi |
| | |
| CHAPTER 1: INTRODUCTION..... | 1 |
| 1.1 Research Background..... | 1 |
| 1.2 Problem Statement..... | 4 |
| 1.3 Research Aim and Objectives..... | 4 |
| 1.4 Outline of Thesis..... | 6 |
| | |
| CHAPTER 2: LITERATURE REVIEW..... | 10 |
| 2.1 Biomolecules..... | 10 |
| 2.1.1 Dopamine (DA)..... | 10 |
| 2.1.2 Nitric Oxide (NO)..... | 11 |
| 2.1.3 Hydrogen Peroxide (H ₂ O ₂)..... | 13 |
| 2.1.4 L-Cysteine (L-Cys)..... | 14 |
| 2.2 Analytical Techniques for the Detection of Biomolecules..... | 15 |
| 2.3 Materials for Electrode Modification..... | 21 |
| 2.3.1 Graphene-based Materials..... | 22 |
| 2.3.2 Nafion (Nf)..... | 24 |
| 2.3.3 Metal Nanoparticles..... | 26 |

| | |
|--|-----------|
| CHAPTER 3: RESEARCH METHODOLOGY | 29 |
| 3.1 Materials | 29 |
| 3.2 Sample Preparation | 30 |
| 3.2.1 Preparation of Graphene Oxide (GO)..... | 30 |
| 3.2.3 Synthesis of rGO-Nf@Ag Nanohybrid | 32 |
| 3.2.4 Synthesis of rGO-Nf@Au Nanohybrid | 33 |
| 3.2.5 Synthesis of rGO-Nf@Pd Nanohybrid | 34 |
| 3.3 Electrochemical Cell Set-up..... | 35 |
| 3.4 Fabrication of Chemically Modified Electrode (CME) | 36 |
| 3.5 Electrochemical Sensing Techniques..... | 36 |
| 3.5.1 Linear Sweep Voltammetry (LSV)..... | 37 |
| 3.5.2 Cyclic Voltammetry (CV) | 37 |
| 3.5.3 Differential Pulse Voltammetry (DPV) | 38 |
| 3.5.4 Square Wave Voltammetry (SWV) | 38 |
| 3.5.5 Amperometry | 39 |
| 3.6 Optical Characterization Technique..... | 39 |
| 3.6.1 UV-visible Absorption Spectroscopy | 39 |
| 3.7 Crystalline and Structural Characterization Techniques..... | 40 |
| 3.7.1 X-ray Diffraction (XRD) | 40 |
| 3.7.2 Raman Spectroscopy | 41 |
| 3.7.3 X-ray Photoelectron Spectroscopy (XPS) | 42 |
| 3.8 Morphological Characterization Techniques | 43 |
| 3.8.1 Field Emission Scanning Electron Microscopy (FESEM) | 43 |
| 3.8.2 High Resolution Transmission Electron Microscopy (HRTEM) | 44 |
| 3.9 Electrochemical Characterization | 45 |
| 3.9.1 Electrochemical Impedance Spectroscopy (EIS)..... | 45 |

| | |
|--|-----------|
| 3.9.2 Voltammetry Technique | 46 |
| CHAPTER 4: REDUCED GRAPHENE OXIDE-NAFION NANOHYBRID MODIFIED ELECTRODE FOR ELECTROCHEMICAL DETECTION OF DOPAMINE AND NITRIC OXIDE | 48 |
| 4.1 Introduction | 48 |
| 4.2 Results and Discussion..... | 51 |
| 4.2.1 Optical Characterization of rGO-Nf Nanohybrids | 51 |
| 4.2.2 Structural Characterization of rGO-Nf Nanohybrids | 54 |
| 4.2.3 Morphological Characterization of rGO-Nf Nanohybrids | 57 |
| 4.2.4 Electrochemical Characterization of GC/rGO-Nf Modified Electrode | 60 |
| 4.2.5 Electrochemical Determination of Dopamine | 63 |
| 4.2.5.1 Electrocatalytic Oxidation of Dopamine | 63 |
| 4.2.5.2 Optimization Studies | 65 |
| 4.2.5.3 Linear Sweep Voltammetry (LSV) Response of Dopamine | 70 |
| 4.2.5.4 Simultaneous Determination of Dopamine and Ascorbic Acid .. | 71 |
| 4.2.5.5 Interference Study | 73 |
| 4.2.5.6 Reproducibility, Repeatability, and Stability Studies..... | 74 |
| 4.2.5.7 Real Sample Analysis..... | 76 |
| 4.2.6 Electrochemical Determination of Nitric Oxide..... | 76 |
| 4.2.6.1 Electrocatalytic Oxidation of Nitric Oxide..... | 76 |
| 4.2.6.2 Optimization Studies | 79 |
| 4.2.6.3 Square Wave Voltammetry (SWV) Response of Nitric Oxide ... | 81 |
| 4.2.6.4 Interference Study | 83 |
| 4.2.6.5 Reproducibility and Repeatability Studies | 84 |
| 4.3 Summary | 85 |

| | |
|---|------------|
| CHAPTER 5: REDUCED GRAPHENE OXIDE-NAFION@SILVER | |
| NANOHYBRID MODIFIED ELECTRODE FOR ELECTROCHEMICAL | |
| DETECTION OF HYDROGEN PEROXIDE | 87 |
| 5.1 Introduction | 87 |
| 5.2 Results and Discussion..... | 90 |
| 5.2.1 Optical Characterization of rGO-Nf@Ag Nanohybrids | 90 |
| 5.2.2 Crystalline and Structural Characterization of rGO-Nf@Ag Nanohybrids.. | 91 |
| 5.2.3 Morphological Characterization of rGO-Nf@Ag Nanohybrids | 95 |
| 5.2.4 Electrochemical Characterization of GC/rGO-Nf@Ag Modified Electrode | 100 |
| 5.2.5 Electrochemical Determination of Hydrogen Peroxide..... | 104 |
| 5.2.5.1 Electrocatalytic Reduction of Hydrogen Peroxide | 104 |
| 5.2.5.2 Optimization Studies | 107 |
| 5.2.5.3 Amperometric Response of Hydrogen Peroxide | 110 |
| 5.2.5.4 Interference Study | 113 |
| 5.2.5.5 Reproducibility, Repeatability, and Stability Studies..... | 115 |
| 5.2.5.6 Real Sample Analysis..... | 116 |
| 5.3 Summary | 117 |
| CHAPTER 6: REDUCED GRAPHENE OXIDE-NAFION@GOLD | |
| NANOHYBRID MODIFIED ELECTRODE FOR ELECTROCHEMICAL | |
| DETECTION OF NITRIC OXIDE..... | 119 |
| 6.1 Introduction..... | 119 |
| 6.2 Results and Discussion..... | 121 |
| 6.2.1 Optical Characterization of rGO-Nf@Au Nanohybrids | 121 |
| 6.2.2 Crystalline and Structural Characterization of rGO-Nf@Au Nanohybrids | 123 |
| 6.2.3 Morphological Characterization of rGO-Nf@Au Nanohybrids | 127 |

| | |
|--|----------------|
| 6.2.4 Electrochemical Characterization of GC/rGO-Nf@Au Modified Electrode ... | 131 |
| 6.2.5 Electrochemical Determination of Nitric Oxide..... | 134 |
| 6.2.5.1 Electrocatalytic Oxidation of Nitric Oxide..... | 134 |
| 6.2.5.2 Optimization Studies | 136 |
| 6.2.5.3 Amperometric Response of Nitric Oxide | 139 |
| 6.2.5.4 Interference Study | 143 |
| 6.2.5.5 Reproducibility, Repeatability, and Stability Studies..... | 144 |
| 6.2.5.6 Real Sample Analysis..... | 145 |
| 6.3 Summary | 146 |
| CHAPTER 7: REDUCED GRAPHENE OXIDE/NAFION@PALLADIUM NANOHYBRID MODIFIED ELECTRODE FOR ELECTROCHEMICAL DETECTION OF L-CYSTEINE..... | 148 |
| 7.1 Introduction..... | 148 |
| 7.2 Results and Discussion..... | 151 |
| 7.2.1 Crystalline and Structural Characterization of rGO-Nf@Pd Nanohybrids | 151 |
| 7.2.2 Morphological Characterization of rGO-Nf@Pd Nanohybrids..... | 154 |
| 7.2.3 Electrochemical Characterization of GC/rGO-Nf@Pd Modified Electrode | 158 |
| 7.2.4 Electrochemical Determination of L-Cysteine | 160 |
| 7.2.4.1 Electrocatalytic Oxidation of L-Cysteine..... | 160 |
| 7.2.4.2 Optimization Studies | 163 |
| 7.2.4.3 Amperometric Response of L-Cysteine | 166 |
| 7.2.4.4 Interference Study | 169 |
| 7.2.4.5 Reproducibility, Repeatability, and Stability Studies..... | 170 |
| 7.2.4.6 Real Sample Analysis..... | 172 |

| | |
|--|------------|
| 7.3 Summary | 173 |
| CHAPTER 8: CONCLUSIONS | 175 |
| 8.1 Conclusion | 175 |
| 8.2 Recommendations for Future Works | 180 |
| REFERENCES | 182 |
| LIST OF PUBLICATIONS AND PAPERS PRESENTED | 205 |

LIST OF FIGURES

| | | |
|----------------------|--|----|
| Figure 1.1 : | Flowchart of the research studies..... | 9 |
| Figure 2.1 : | Summary information about four types of biomolecules..... | 15 |
| Figure 3.1 : | Schematic representation for synthesis of GO using Simplified Hummers' method..... | 30 |
| Figure 3.2 : | Illustration of preparation of rGO/Nf nanohybrid via hydrothermal method..... | 31 |
| Figure 3.3 : | Schematic illustration for formation of rGO-Nf@Ag nanohybrid via hydrothermal method..... | 32 |
| Figure 3.4 : | Schematic illustration for synthesis of rGO-Nf@Au nanohybrid... | 33 |
| Figure 3.5 : | Schematic diagram for the synthesis of PdNPs decorated rGO-Nf film using hydrothermal method..... | 34 |
| Figure 3.6 : | Schematic representation of the electrochemical cell setup..... | 35 |
| Figure 3.7 : | Thermo Scientific Evolution 300 ultraviolet-visible (UV-Vis) absorption spectrophotometer..... | 40 |
| Figure 3.8 : | X-ray diffraction (XRD) from PANalytical Empyrean..... | 41 |
| Figure 3.9 : | Renishaw inVia Raman microscope..... | 42 |
| Figure 3.10 : | FEI Nova NanoSEM 400 operated at 10.0 kV..... | 43 |
| Figure 3.11 : | FEI Tecnai G2 F20 X-TWIN TEM..... | 44 |
| Figure 3.12 : | PAR-VersaSTAT 3 electrochemical work station..... | 46 |
| Figure 4.1 : | UV–vis absorption spectra of prepared (i) GO, (ii) Nf, (iii) GO-Nf, (iv) rGO-Nf (8 h), (v) rGO-Nf (16 h) and (vi) rGO-Nf (24 h) nanohybrids..... | 52 |
| Figure 4.2 : | PL spectra of (A) GO and (B) three different rGO-Nf nanohybrids..... | 53 |
| Figure 4.3 : | Raman spectra that obtained for the (i) GO, (ii) rGO-Nf (8 h), (iii) rGO-Nf (16 h) and (iv) rGO-Nf (24 h) nanohybrids..... | 55 |
| Figure 4.4 : | C1s XPS spectra for the (A) rGO, (B) Nf and (C) three different nanohybrids; (i) rGO-Nf (8 h), (ii) rGO-Nf (16 h) and (iii) rGO- | |

| | |
|--|----|
| Nf (24 h) nanohybrids..... | 56 |
| Figure 4.5 : FESEM images of (A) GO, (B) rGO-Nf (8 h) nanohybrid, (C) rGO-Nf (16 h) nanohybrid and (D) rGO-Nf (24 h) nanohybrid..... | 58 |
| Figure 4.6 : HRTEM images of (A) GO, (B) rGO-Nf (8 h) nanohybrid, (C) rGO-Nf (16 h) nanohybrid and (D) rGO-Nf (24 h) nanohybrid..... | 59 |
| Figure 4.7 : AFM phases and 3D topographic images of rGO-Nf nanohybrids obtained after hydrothermal treatment periods of (A) 8 h, (B) 16 h and (C) 24 h..... | 60 |
| Figure 4.8 : (A) CV and (B) Nyquist plots of electrochemical impedance spectroscopy (EIS) for bare GCE and GC/rGO-Nf nanohybrids with different hydrothermal processing times obtained in presence of 0.1 M KCl with 5 mM $K_3[Fe(CN)_6]$, (Inset shows the electrical equivalent circuit that fit the Nyquist plot of GC/rGO-Nf (16 h)) and (C and D) bode plots obtained for different modified electrodes..... | 62 |
| Figure 4.9 : CV curves obtained for bare GCE, GC/GO, GC/Nf, GC/GO-Nf, and three different GC/rGO-Nf modified electrodes in presence of 0.1 M PBS (pH 6.5) solution containing 100 μ M DA at a scan rate of 100 mV/s..... | 64 |
| Figure 4.10 : Schematic representation of detection of DA at GC/rGO-Nf modified electrode..... | 64 |
| Figure 4.11 : (A) CV curves obtained for the GC/rGO-Nf (16 h) modified electrode in the presence of 0.1 M PBS (pH 6.5) and different concentration of DA (10 to 350 μ M) at a scan rate of 50 mV/s and (B) linear relationship between I_{pa} and the concentration of DA..... | 66 |
| Figure 4.12 : (A) CV plot obtained for GC/rGO-Nf (16 h) modified electrode in 0.1 M PBS (pH 6.5) with presence of 100 μ M DA at a scan rates of 10–500 mV/s, (B) the corresponding plot of anodic and cathodic peak currents versus scan rate, (C) relationships of anodic and cathodic peak potentials against natural logarithm of scan rate (10–3000 mV/s) and (D) relationships of the anodic and cathodic peak potentials against natural logarithm of scan rate at a scan rate of 300–900 mV/s..... | 67 |
| Figure 4.13 : (A) CV curves obtained for GC/rGO-Nf (16 h) modified electrode with different amount of sample loading and (B) plot of anodic peak current response versus rGO-Nf (16 h) loading | |

| | |
|--|----|
| obtained for the 50 μM DA in 0.1 M PBS (pH 6.5) at a scan rate of 50 mV/s..... | 68 |
| Figure 4.14 : (A) CV curves obtained for GC/G-Nf (16 h) modified electrode in presence of 50 μM DA in 0.1 M PBS at different pH values ranging from pH 3 to 10 at a scan rate of 100 mV/s and (B) the corresponding plot of peak potential versus pH values..... | 70 |
| Figure 4.15 : (A) LSV obtained for GC/rGO-Nf (16 h) modified electrode in the presence of DA at concentrations of 100 nM to 200 μM in 0.1 M pH 6.5 PBS with a scan rate of 100 mV/s and (B) the corresponding plot of anodic peak current (<i>I</i>) against concentration of DA in the range of 100 nM to 1 μM DA..... | 71 |
| Figure 4.16 : (A) SWV curves and their corresponding, (B) calibration plots obtained for GC/rGO-Nf (16 h) modified electrode in presence of 300 μM DA and different concentrations of AA (4 to 10 mM) in PBS (pH 6.5), (C) SWV curves and their corresponding and (D) calibration plots obtained for GC/rGO-Nf (16 h) modified electrode in the presence of 5 mM AA and different concentrations of DA (300 nM to 0.7 μM)..... | 72 |
| Figure 4.17 : LSV obtained for GC/rGO-Nf (16 h) modified electrode in presence of (i) 5 mM AA, (ii) 50 μM DA, (iii) mixture of 5 mM AA and 50 μM DA, and (iv) mixture of 5 mM AA, 50 μM DA, and 5 μM UA in 0.1 M PBS (pH 6.5)..... | 73 |
| Figure 4.18 : (A) CV curves of five different GC/rGO-Nf (16 h) modified electrodes, (B) CV curves of five successive measurement of single GC/rGO-Nf (16 h) modified electrode with 50 μM DA in 0.1 M PBS (pH 6.5) at a scan rate of 100 mV/s and (C) CV curves of GC/rGO-Nf (16 h) modified electrode up to 100 continuous cycles..... | 75 |
| Figure 4.19 : (A) CV curves obtained for the bare GCE, GC/GO, GC/Nf, GC/GO-Nf and GC/rGO-Nf (16 h) modified electrodes in the presence of 0.1 M PBS (pH 2.5) containing 1 mM NO at a scan rate of 50 mV/s and (B) CV obtained for the GC/GO-Nf, GC/rGO-Nf (8 h), GC/rGO-Nf (16 h) and GC/rGO-Nf (24 h) modified electrodes in the presence of 0.1 M PBS (pH 2.5) containing 1 mM NO at a scan rate of 50 mV/s..... | 77 |
| Figure 4.20 : Schematic diagram for the electrocatalytic oxidation of NO at the GC/rGO-Nf modified electrode..... | 78 |
| Figure 4.21 : (A) CV curves obtained for the GC/rGO-Nf (16 h) modified | |

| | |
|---|----|
| electrode in the presence of 0.1 M PBS (pH 2.5) and different concentration of NO (1 to 10 mM) at a scan rate of 50 mV/s and (B) linear relationship between I_{pa} and the concentration of NO..... | 79 |
| Figure 4.22 : (A) CV curves obtained for the GC/rGO-Nf (16 h) modified electrode in the presence of 0.1 M PBS (pH 2.5) containing 1 mM NO at different scan rates and (B) plot of anodic peak current versus square root of the scan rate obtained for the GC/rGO-Nf (16 h) modified electrode..... | 80 |
| Figure 4.23 : (A) CV curves obtained for GC/rGO-Nf (16 h) modified electrode with different amount of sample loading and (B) plot of rGO-Nf (16 h) loading versus anodic peak current response obtained for the 1 mM NO in 0.1 M PBS (pH 2.5) at a scan rate of 50 mV/s..... | 81 |
| Figure 4.24 : (A) SWV obtained for GC/rGO-Nf (16 h) modified electrode in 0.1 M PBS pH 2.5 containing different concentration of NO (50 μ M to 10 mM) at a scan rate of 50 mV/s and (B) correlation between the concentrations of NO and peak current quantified from the SWV (Inset shows the enlarged view of plot obtained for the peak current versus concentration of NO at lower concentration level)..... | 82 |
| Figure 4.25 : LSV obtained for the GC/rGO-Nf (16 h) modified electrode in 0.1 M PBS (pH 2.5) with the mixture of 5 mM AA, 50 μ M DA and 5 mM NO..... | 83 |
| Figure 4.26 : (A) CV curves of five different GC/rGO-Nf (16 h) modified electrodes and (B) CV curves of five successive measurements of single GC/rGO-Nf (16 h) modified electrode with 1 mM NO in 0.1 M PBS (pH 2.5) at a scan rate of 100 mV/s..... | 84 |
| Figure 5.1 : UV-vis absorption spectra of (A) GO, rGO, Nf, rGO-Nf and (B) rGO-Nf@Ag nanohybrids with three different Ag contents..... | 91 |
| Figure 5.2 : XRD patterns of (i) rGO-Nf@Ag4, (ii) rGO-Nf@Ag6 and (iii) rGO-Nf@Ag8 nanohybrids..... | 92 |
| Figure 5.3 : Raman spectra of (A) GO, rGO, rGO-Nf and (B) rGO-Nf@Ag nanohybrids with three different Ag contents in the range of 1100 to 1800 cm^{-1} | 93 |
| Figure 5.4 : XPS spectra of GO, rGO, rGO-Nf and rGO-Nf@Ag nanohybrids with three different Ag contents and their corresponding (A-C) | |

| | |
|---|-----|
| C1s and (D) Ag3d core-level spectra..... | 95 |
| Figure 5.5 : FESEM images of (A) GO, (B) rGO, (C) rGO-Nf, (D) rGO-Nf@Ag4 nanohybrid, (E) rGO-Nf@Ag6 nanohybrid and (F) rGO-Nf@Ag8 nanohybrid..... | 96 |
| Figure 5.6 : (A) Mapping of rGO-Nf@Ag8 nanohybrid at the selected area and (B) its EDX spectrum captured for the selected region..... | 97 |
| Figure 5.7 : (A-C) HRTEM images of rGO-Nf@Ag4 nanohybrid, rGO-Nf@Ag6 nanohybrid and rGO-Nf@Ag8 nanohybrids with their corresponding histogram of AgNPs sizes (D-F) (Inset shows the individual AgNPs on rGO-Nf sheet)..... | 99 |
| Figure 5.8 : (A&B) Nyquist plots obtained for bare GCE, GC/GO, GC/Nf and three different GC/rGO-Nf@Ag modified electrodes obtained in presence of 0.1 M KCl with 5 mM $K_3[Fe(CN)_6]$ (Inset shows the equivalent circuit that fits the impedance spectrum of GC/rGO-Nf@Ag6) and (C&D) bode plots obtained for above said different modified electrodes..... | 101 |
| Figure 5.9 : CV curves for control modified electrode as well as three different nanohybrids modified electrodes obtained in the presence of 0.1 M KCl with 5 mM $K_3[Fe(CN)_6]$ (Inset shows the enlargement of CV curves obtained from GC/Nf and GC/GO)..... | 104 |
| Figure 5.10 : (A&B) CV curves obtained for bare GCE, GC/GO, GC/Nf, GC/rGO, GC/rGO-Nf and three different GC/rGO-Nf@Ag modified electrodes in the presence of 0.2 M PBS (pH 7.2) containing 10 mM H_2O_2 at a scan rate of 50 mV/s..... | 105 |
| Figure 5.11 : Schematic representation for the fabrication of rGO-Nf@Ag nanohybrid modified GCE and the mechanism of electrocatalytic reduction of H_2O_2 | 106 |
| Figure 5.12 : (A) CV curves obtained for the GC/rGO-Nf@Ag6 modified electrode in the presence of 0.2 M PBS (pH 7.2) and different concentrations of H_2O_2 (1 to 30 mM) at a scan rate of 50 mV/s and (B) the corresponding plot of cathodic peak currents versus different H_2O_2 concentrations..... | 107 |
| Figure 5.13 : (A) CV plots obtained for GC/rGO-Nf@Ag6 modified electrode in 0.2 M PBS (pH 7.2) with presence of 10 mM H_2O_2 at a scan rates of 10–300 mV/s and (B) the corresponding plot of cathodic peak currents versus square root of scan rate..... | 108 |

| | | |
|----------------------|---|-----|
| Figure 5.14 : | (A) CV curves obtained for GC/rGO-Nf@Ag6 modified electrode with different amount of sample loading and (B) plot of rGO-Nf@Ag6 loading versus cathodic peak current response obtained for the 5 mM H ₂ O ₂ in 0.2 M PBS (pH 7.2) at a scan rate of 50 mV/s..... | 109 |
| Figure 5.15 : | (A) Amperometric (I-t) curve of the GC/rGO-Nf@Ag6 modified electrode on successive additions of H ₂ O ₂ stirred into 0.2 M PBS (pH 7.2) at an applied potential of -0.6 V and (B) the corresponding calibration plot of current against concentration of H ₂ O ₂ | 111 |
| Figure 5.16 : | Amperometric (I-t) curve responses obtained at GC/rGO-Nf@Ag6 modified electrode for the successive addition of (a) 1 mM H ₂ O ₂ and each 5 mM of (b) NaCl, (c) urea, (d) glucose, (e) DA, (f) UA and (g) AA in 0.2 M PBS (pH 7.2) at a regular time interval of 60 sec at an applied potential of -0.6 V versus SCE..... | 114 |
| Figure 5.17 : | (A) CV curves of five different GC/rGO-Nf@Ag6 modified electrodes, (B) CV curves of five successive measurements of single GC/rGO-Nf@Ag6 modified electrode with 20 mM H ₂ O ₂ in 0.2 M PBS (pH 7.2) at a scan rate of 50 mV/s and (C) CV curves of GC/rGO-Nf@Ag6 modified electrode after placed in air for five days..... | 116 |
| Figure 6.1 : | UV-vis spectra of three different rGO-Nf@Au nanohybrids (Inset shows the UV-vis spectra for GO, rGO and rGO-Nf nanohybrid).. | 122 |
| Figure 6.2 : | XRD patterns of (A) GO and rGO. (B) XRD pattern of (i) rGO-Nf@Au4, (ii) rGO-Nf@Au8 and (iii) rGO-Nf@Au12 nanohybrids..... | 123 |
| Figure 6.3 : | Raman spectra of (i) rGO, (ii) rGO-Nf@Au4, (iii) rGO-Nf@Au8 and (iv) rGO-Nf@Au12 nanohybrids (Inset shows the Raman spectrum for GO..... | 126 |
| Figure 6.4 : | XPS spectra of the (A) C1s and (B) Au4f core level region for (i) rGO-Nf@Au4, (ii) rGO-Nf@Au8 and (iii) rGO-Nf@Au12 nanohybrids..... | 127 |
| Figure 6.5 : | FESEM images and particle size distribution histograms of (A, D) rGO-Nf@Au4 nanohybrid, (B,E) rGO-Nf@Au8 nanohybrid and (C,F) rGO-Nf@Au12 nanohybrid..... | 128 |
| Figure 6.6 : | (A) Elemental mapping images and (B) EDX of rGO-Nf@Au8 | |

| | |
|--|-----|
| nanohybrid..... | 129 |
| Figure 6.7 : HRTEM images of (A) rGO-Nf@Au4 nanohybrid, (B) rGO-Nf@Au8 nanohybrid, (C) rGO-Nf@Au12 nanohybrid and (D) lattice resolved TEM image of individual AuNPs on the rGO-Nf sheet..... | 130 |
| Figure 6.8 : (A) CV, (B) Nyquist and (C) Bode plots obtained for several modified electrodes in a solution containing 0.1 M KCl and 5 mM K ₃ [Fe(CN) ₆] (the scan rate of CV is 50 mV/s and the frequency range of EIS is from 0.01 Hz to 100 kHz) and (D) equivalent circuit for the impedance spectroscopy obtained using GC/rGO-Nf@Au8 modified electrode..... | 133 |
| Figure 6.9 : (A and B) CV curves recorded at different modified electrodes for 1 mM of NO in 0.1 M PBS (pH 2.5) at a scan rate of 50 mV/s..... | 135 |
| Figure 6.10 : (A) CV responses of GC/rGO-Nf@Au8 modified electrode with change in NO concentrations from 1 to 10 mM at a scan rate of 50 mV/s and (B) the corresponding plot of anodic peak current versus concentration of NO..... | 136 |
| Figure 6.11 : (A) CV curves of GC/rGO-Nf@Au8 modified electrode collected at different scan rates ranging from 10 to 500 mV/s in 0.1 M PBS (pH 2.5) containing 1 mM NO and (B) the corresponding plot of anodic peak current versus square root of scan rate..... | 137 |
| Figure 6.12 : (A) CV curves obtained for GC/rGO-Nf@Au8 modified electrode with different amount of sample loading and (B) plot of rGO-Nf@Au8 loading versus anodic peak current response obtained for the 1 mM NO in 0.1 M PBS (pH 2.5) at a scan rate of 50 mV/s..... | 138 |
| Figure 6.13 : (A) Amperometric (I-t) response of different modified electrodes to subsequent additions of 50 µM NO in 0.1 M PBS (pH 2.5) at an applied potential of +0.8 V and (B) the corresponding calibration curve of current versus concentration of NO for different modified electrode..... | 139 |
| Figure 6.14 : (A) Amperometric (I-t) response of GC/rGO-Nf@Au8 modified electrode in 0.1 M PBS (pH 2.5) at an applied potential of +0.8 V upon successive additions of different concentration of NO in a step of 1, 5, and 10 µM (Inset shows the I-t response from 200 to 850 sec) and (B) the corresponding calibration curve of current versus concentration of NO (Inset shows the enlargement | |

| | |
|---|-----|
| of the calibration curve from 1 to 10 μM of NO concentration)..... | 141 |
| Figure 6.15 : Amperometric (I-t) response of (a) 1 μM NO at GC/rGO-Nf@Au8 modified electrode in 0.1 M PBS (pH 2.5) with successive additions of different interfering species such as (b) DA, (c) AA, (d) UA, (e) NaCl, (f) glucose and (g) urea; each with 10 μM concentration..... | 143 |
| Figure 6.16 : (A) CV curves of ten different GC/rGO-Nf@Au8 modified electrodes, (B) CV curves of ten successive measurements of GC/rGO-Nf@Au8 modified electrode with 1 mM NO in 0.1 M PBS (pH 2.5) at a scan rate of 50 mV/s and (C) CV curves of GC/rGO-Nf@Au8 modified electrode after placed in air for five days..... | 145 |
| Figure 7.1 : XRD patterns of (i) rGO-Nf@Pd3, (ii) rGO-Nf@Pd6 and (iii) rGO-Nf@Pd9 nanohybrids (Inset shows the XRD patterns for GO and rGO)..... | 152 |
| Figure 7.2 : Raman spectra of (i) rGO-Nf@Pd3, (ii) rGO-Nf@Pd6 and (iii) rGO-Nf@Pd9 nanohybrids (Inset shows the Raman spectrum for GO)..... | 153 |
| Figure 7.3 : FESEM images of (A) rGO-Nf, (B) rGO-Nf@Pd3, (C) rGO-Nf@Pd6 and (D) rGO-Nf@Pd9 nanohybrids..... | 154 |
| Figure 7.4 : (A) Qualitative elemental mapping and (B) EDX analysis of rGO-Nf@Pd6 nanohybrid..... | 155 |
| Figure 7.5 : (A-C) HRTEM images of rGO-Nf@Pd3, rGO-Nf@Pd6 and rGO-Nf@Pd9 nanohybrids with their corresponding histogram of PdNPs sizes (D-F) (Inset shows the individual PdNPs on rGO-Nf sheet)..... | 157 |
| Figure 7.6 : (A & B) CV curves obtained at various modified electrode in a 0.1 M KCl with 5 mM $\text{K}_3[\text{Fe}(\text{CN})_6]$ (scan rate: 50 mV/s)..... | 159 |
| Figure 7.7 : (A) Nyquist plots for bare GCE, GC/rGO-Nf@Pd3, GC/rGO-Nf@Pd6, and GC/rGO-Nf@Pd9 in a solution of 0.1 M KCl with 5 mM $\text{K}_3[\text{Fe}(\text{CN})_6]$ (frequency range: 10 mHz to 10 kHz) and (B) the equivalent circuit for modelling of EIS experimental data of GC/rGO-Nf@Pd6..... | 160 |
| Figure 7.8 : (A & B) CV curves of different modified electrodes in 0.1 M PBS (pH 7) containing 5 mM L-Cys at a scan rate of 50 mV/s..... | 161 |

| | | |
|----------------------|--|-----|
| Figure 7.9 : | Schematic diagram of the electrocatalytic oxidation of L-Cys at the GCE/rGO-Nf@Pd modified electrode..... | 162 |
| Figure 7.10 : | (A) CV curves of GC/rGO-Nf@Pd6 modified electrode in a 0.1 M PBS (pH 7) containing different concentrations of L-Cys scanning at a scan rate of 50 mV/s and (B) the corresponding plot of peak current versus concentration of L-Cys..... | 163 |
| Figure 7.11 : | (A) CV curves of GC/rGO-Nf@Pd6 modified electrode in 0.1 M PBS (pH 7) containing 1 mM L-Cys scanning at different scan rates and (B) plotting of peak current as a function of scan rate ranging from 50 to 500 mV/s..... | 164 |
| Figure 7.12 : | (A) CV curves of GCE modified by rGO-Nf@Pd6 nanohybrid with different loading amounts in 0.1 M PBS (pH 7) with the presence of 1 mM L-Cys at a scan rate of 50 mV/s and (B) the corresponding plot of anodic peak current as a function of different loading amount of rGO-Nf@Pd6 nanohybrid..... | 165 |
| Figure 7.13 : | (A) CV curves of GC/rGO-Nf@Pd6 in 1 mM L-Cys at different pH (0.1 M PBS) at a scan rate of 50 mV/s and (B) plot of anodic peak potential versus pH values..... | 166 |
| Figure 7.14 : | (A) Amperometric current response of GC/rGO-Nf@Pd6 for successive addition of L-Cys range from 0.5 μ M to 65 μ M in 0.1 M PBS (pH 7) at an applied potential of +0.6 V (Inset shows the enlarge image of the amperometric current response from 0 to 1240 sec) and (B) the corresponding calibration plot of current response versus L-Cys concentration (Inset shows the enlarge image of calibration plot for the low L-Cys concentration of 0.5 to 10 μ M)..... | 167 |
| Figure 7.15 : | Amperometric (I-t) response of GC/rGO-Nf@Pd6 modified electrode at +0.6 V versus SCE in 0.1 M PBS (pH 7) with the successive addition of 5 μ M L-Cys, and each 100 μ M of AA, UA, DA, H ₂ O ₂ , urea and glucose..... | 170 |
| Figure 7.16 : | (A) CV curves of five different GC/rGO-Nf@Pd6 modified electrodes, (B) CV curves of five successive measurements of GC/rGO-Nf@Pd6 modified electrode with 1 mM L-Cys in 0.1 M PBS (pH 7) at a scan rate of 50 mV/s and (C) CV curves of GC/rGO-Nf@Pd6 modified electrode after placed in air at room temperature for five days..... | 171 |

LIST OF TABLES

| | | |
|--------------------|--|-----|
| Table 2.1 : | The comparison of various modified electrode towards the detection of biomolecules by using electroanalytical method..... | 20 |
| Table 2.2 : | Comparison of various graphene-based modified electrodes for the detection of different bioanalytes using electrochemical technique..... | 24 |
| Table 2.3 : | Comparison of various conducting polymer-based modified electrodes for the detection of different bioanalytes using electrochemical technique..... | 26 |
| Table 2.4 : | Comparison of various metals nanoparticles-based modified electrodes for the detection of different bioanalytes by using electrochemical technique..... | 28 |
| Table 3.1 : | List of chemicals and materials used in this work..... | 29 |
| Table 4.1 : | Comparison of analytical parameters of several modified electrode based on graphene-polymer composite for DA determination..... | 72 |
| Table 4.2 : | Results of DA determination in urine samples (n = 3) using GC/rGO-Nf (16 h) modified electrode..... | 76 |
| Table 4.3 : | Comparison of analytical parameters of several modified electrode for NO determination..... | 83 |
| Table 5.1 : | Comparison of the analytical performance of various electrodes in electrochemical detection of H ₂ O ₂ | 112 |
| Table 5.2 : | Detection and recovery of H ₂ O ₂ in apple juice by using the novel GC/rGO-Nf@Ag ₆ modified electrode..... | 117 |
| Table 6.1 : | Comparison in the sensing performance of GC/rGO-Nf@Au ₈ modified electrode with other reported sensor electrodes for the determination of NO..... | 142 |

| | | |
|--------------------|--|-----|
| Table 6.2 : | Detection and recovery of NO in real water samples by using the novel GC/rGO-Nf@Au8 modified electrode..... | 146 |
| Table 7.1 : | Comparison of the sensing performance of the proposed GC/rGO-Nf@Pd6 modified electrode with previously reported sensor electrodes for L-Cys detection..... | 168 |
| Table 7.2 : | Detection and recovery of L-Cys in human urine samples by using the novel GC/rGO-Nf@Pd6 modified electrode..... | 172 |

LIST OF SYMBOLS AND ABBREVIATIONS

| | | |
|-----------------------------------|---|--|
| AA | : | Ascorbic acid |
| AFM | : | Atomic force microscopy |
| AgNPs | : | Silver nanoparticles |
| AuNPs | : | Gold nanoparticles |
| CV | : | Cyclic voltammetry |
| DA | : | Dopamine |
| DPV | : | Differential pulse voltammetry |
| EIS | : | Electrochemical impedance spectroscopy |
| FESEM | : | Field emission scanning electron microscopy |
| GCE | : | Glassy carbon electrode |
| GO | : | Graphene oxide |
| HCl | : | Hydrochloric acid |
| HRTEM | : | High resolution transmission electron microscopy |
| H ₂ O ₂ | : | Hydrogen peroxide |
| H ₂ SO ₄ | : | Sulphuric acid |
| H ₃ PO ₄ | : | Phosphoric acid |
| KMnO ₄ | : | Potassium permanganate |
| L-Cys | : | L-Cysteine |
| Nf | : | Nafion |
| NH ₃ .H ₂ O | : | Ammonia solution |
| NO | : | Nitric oxide |
| PdNPs | : | Palladium nanoparticles |
| PL | : | Photoluminescence |
| rGO | : | Reduce graphene oxide |

| | | |
|--------|---|----------------------------------|
| SWV | : | Square wave voltammetry |
| UA | : | Uric acid |
| UV-vis | : | UV-visible |
| WE | : | Working electrode |
| XPS | : | X-ray photoelectron spectroscopy |
| XRD | : | X-ray diffraction |

CHAPTER 1

INTRODUCTION

1.1 Research Background

In general, sensor can be defined as a device that detect a physical stimulus such as heat, light, sound, temperature, pressure and magnetism, and then give responses in the way of transmitting the resulting impulse to a measuring or control instrument. In medical and biotechnology terms, sensor can be described as a tool used to detect specific biological, chemical, or physical processes and then translate it into a measurable signal. Meanwhile, an analytical device that combines a biological recognition element with a physicochemical detector to detect a biological analyte was known as biosensor (Turner, 2013). Sensor plays a vital role especially in medical technology as it aid in accurate monitoring, diagnosis and treatment. Up to date, there are plenty of sensors with various function have been commercialized that is convenient for self-care at home such as home pregnancy test which was used to detect the presence of a hormone named human chorionic gonadotrophin (hCG) in the urine of women as an indication of pregnancy.

The history of sensor was started in 1956 when the concept of electrochemical oxygen sensor was proposed which consist of several components including platinum (Pt) cathode and silver anode which acts as an electron receiver and electron donor, respectively, potassium chloride (KCl) as an electrolyte solution, thin oxygen-permeable membrane as a separator for electrodes and the electrolyte solution from the analyzed solution and a voltage source (Clark *et al.*, 1953). This invention has remained as the guiding principle for measuring dissolved oxygen in biomedical, environmental and industrial applications. In 1962, Clark and Lyons from the Children's Hospital of

Cincinnati have invented the first sensor to detect glucose levels in blood by combining the Clark oxygen sensor with glucose oxidase (GOx) (Clark *et al.*, 1962). The idea was to monitor the oxygen consumed by the enzyme-catalyzed reaction when the GOx was entrapped at the oxygen electrode using dialysis membrane. The Yellow Springs Instrument Company analyzer (Model 23A YSI analyzer) has become the first glucose sensor uses Clark's technology launched in 1975.

Since then, various techniques for detecting biological compounds have been developed as a result of the rapid development of nanotechnology and each technique has their own advantages and disadvantages. Among the techniques includes capillary electrophoresis mass spectrometry (Phan *et al.*, 2013), chromatography (Kipping *et al.*, 1963), fluorimetry (Ito *et al.*, 2013), rapid liquid chromatography/tandem mass spectrometry (LC-MS/MS) (Yang *et al.*, 2006), chemiluminescence (Yang *et al.*, 2015), electrochemiluminescence (ECL) (Lu *et al.*, 2014), Surface enhanced Raman scattering (SERS) (Kuang *et al.*, 2016) and colorimetric (Wu *et al.*, 2016) techniques. Although these methods provide high sensitivity in the detection of biological analytes, they have several drawbacks like requiring a complex system, long time consumption, high cost and take a substantial large amount of workspace. Hence, the detection of biological analytes by electrochemical method is a more suitable approach in evaluating the low concentration of analytes under physiological conditions.

An electrochemical sensor is defined as a device used to quantify the concentration of biomolecule by transforming the electrochemical information which generated by biochemical mechanism into an analytically useful signal. By comparing the electrochemical sensor with other existing sensor technique, it leading by a series of advantages including high sensitivity and selectivity towards electro active analytes,

rapid and accurate response, and most importantly it is portable and cost effective. Moreover, it also offers a wide linear response range and good stability and reproducibility. By principle, a working or sensing electrode consists of two basic components in the electrochemical sensor which works together that known as a chemical recognition system and physicochemical transducer. The reference and counter electrodes are also required in this sensor besides this working electrode. All three electrodes where next inserted in the sensor housing in contact with a liquid electrolyte and target analytes.

The sensitivity of the electrochemical sensor will be affected based on; (i) the surface modification techniques, (ii) electrochemical transduction mechanisms and (iii) the choice of the recognition receptor molecules. The most common strategy used by most of the researchers to enhance the sensor performance is by chemically modifying the surface of working electrode. The surface architectures which link the sensing element with the biological samples play an important role in determining the performance of electrochemical sensor. Metal (Fawcett *et al.*, 1994), metal oxide (Aydoğdu *et al.*, 2013), carbon nanotubes (Claussen *et al.*, 2010) and polymer (Narayana *et al.*, 2014) are some examples of active materials that frequently been used among the researcher to modify the sensor electrode. In the past few years, researchers have found that graphene-based material can further benefit electrochemical sensors because it possesses high electrical conductivity, large surface area, fast mass transfer and excellent stability which could enhance the electrochemical activity of important bioanalytes. Until now, an extensive research is still undergoing in finding the suitable modifier materials based on graphene with the intention to boost the performance of electrochemical sensor in terms of its sensitivity and selectivity.

1.2 Problem Statement

In spite of good progress in developing an electrochemical sensor for the determination of various biological analytes, it holds several challenges in the fabrication of efficient electrochemical sensor including:

- The slow heterogeneous electron transfer at the surface of electrode which led to the low sensitivity together with high detection limit.
- The use of biological enzyme and DNAs has increased the cost of production as enzymes are expensive. Its positive response toward temperature, pH, toxic chemicals and humidity prompted the instability of the electrode besides making the immobilization process more challenging.
- The occurrence of fouling effect which causes the simultaneous determination of several biological analytes is very difficult.
- The slow response times has lowered the sensitivity of the electrode and further limit its application in the real time monitoring of biological processes.

Therefore, the fundamental research in finding the suitable material for modifying the electrode needs to be conducted by taking into account the low cost of production, simple preparation method, high conductivity and large active surface area.

1.3 Research Aim and Objectives

The primary focus of the proposed research activity is to explore the potential of new materials that are the rGO-Nf and rGO-Nf@metal-based nanohybrids which could be use next in the development of a highly sensitive and selective electrochemical sensor

for determination of various biological compounds. In order to achieve this goal, a list of specific objectives has been made including:

- To synthesize rGO-Nf and rGO-Nf@metal nanohybrid using hydrothermal method.
- To characterize these materials using analytical techniques such as UV-visible (UV-vis), X-ray diffraction (XRD), Raman, field emission scanning electron microscopy (FESEM) and etc.
- To study the electrochemical properties of these nanohybrid materials-modified electrode.
- To investigate the electrochemical detection of biologically important analytes such as DA, NO, H₂O₂ and L-Cys using the nanohybrid modified electrode.
- To employ the as-fabricated electrochemical sensors in real sample analysis.

The drawback of enzymatic electrochemical sensor such as expensive cost of production and difficult immobilization process motivated us to develop a non-enzymatic electrochemical sensor for detection of various biological compounds. Meanwhile, the selection of metal nanoparticles to be combined together with graphene is driven by its excellent physical and chemical properties, which is capable to enhance the electroactive surface area and improving the electrocatalytic features of the electrode. The incorporation of Nf in the nanohybrid helps to improve the dispersibility of the nanohybrid and at the same time increase the stability of the sensor electrode. In addition, the antifouling capacity and high permeability to cations properties owned by Nf helps in improving the sensitivity and selectivity of the sensor electrode. Several factors have been taken into account in realizing these objectives including the use of

simple technique to synthesize the nanohybrid materials, minimum use of raw material, effective sensing technique and validation of the proposed sensor electrode in term of its capability of the detection in real sample, reproducibility and stability.

1.4 Outline of Thesis

The brief introduction about this research has been elaborated in Chapters 1, covering several sub-topics including the problem statement, the aims and objectives of the proposed research, and significances of this research. The flow of the thesis has also been outlined in this chapter.

Chapter 2 begins with a brief overview of the background and development of electrochemical sensor with particular emphasis on detecting DA, NO, H₂O₂ and L-Cys. Most of the topic discussed in this chapter has been published in RSC Advances and Microchimica Acta as a review paper.

Chapter 3 outlines the procedure manuals for synthesizing the nanohybrids and materials used throughout the research studies. The general procedure for the fabrication chemically modified electrode has been discussed and the brief introduction about characterization techniques involved in this research has also been explained in this section.

Chapter 4 reports a selective and sensitive electrochemical sensing platform based on hydrothermally prepared rGO-Nf modified electrodes toward the detection of DA and NO. The influences of experimental parameters such as the hydrothermal reaction time on electrocatalytic performance were also investigated. The ability of the sensor electrode to resist the interference from AA and UA will also been investigated in this

section. The proposed modified electrode also has been tested as a sensor electrode for DA detection in real sample analysis by using urine sample. A modified version of this chapter has been published in Science of Advanced Materials and Analytical Methods.

Chapter 5 presents the findings of our study on the development of a sensitive and selective enzymeless electrochemical sensor for H_2O_2 based on the novel rGO-Nf@Ag nanohybrid material modified electrode. The nanohybrid was facilely synthesized using one-pot hydrothermal method with the aid of micromolar concentration of Ag. The influence of the AgNPs content in the nanohybrid on the electrocatalytic reduction of H_2O_2 was investigated and optimized to achieve a high sensor performance. The proposed sensor was successfully applied for the validation of known concentration of H_2O_2 in the apple juice sample. A version of this chapter has been published in Biosensors and Bioelectronics.

Chapter 6 focuses on the development of a highly sensitive and selective electrochemical NO sensor by using self-designed electrode that was chemically modified using a nanohybrid of rGO-Nf and AuNPs. Graphene oxide (GO) and gold(III) chloride trihydrate ($\text{HAuCl}_4 \cdot 3\text{H}_2\text{O}$) were used as the precursor for rGO and AuNPs, respectively. Three different concentration of $\text{HAuCl}_4 \cdot \text{H}_2\text{O}$ were used in order to study the effect of AuNPs content on the electrochemical sensing performance. Some possible coexisting electroactive components such as DA, AA, UA, glucose, NaCl and urea were examined in order to evaluate the anti-interference of the constructed modified sensor electrode. The study presented in this chapter has been compiled as a full research paper and has been published in Microchimica Acta.

Chapter 7 demonstrates the preparation of a novel rGO-Nf@Pd nanohybrid using hydrothermal method that was then employed as a sensing electrode material in an electrochemical sensor to study its sensitivity and selectivity toward L-Cys. Detection linearity, repeatability, reproducibility and long-term stability for the proposed sensor electrode were also been studied. Further, the analytical applicability of the sensor electrode was evaluated for the quantification of L-Cys in urine sample and the results were presented in the end of this section. The study presented in this chapter has been compiled as a full research paper and submitted for publication.

The summary of our research works has been included in Chapter 8 by covering the important findings from each study. The suggestion of possible future work arising from this research works were proposed at the end of this chapter. The flowchart of the research work was illustrated in Figure 1.1 in order to give a basic idea of how the whole doctoral work was conducted.

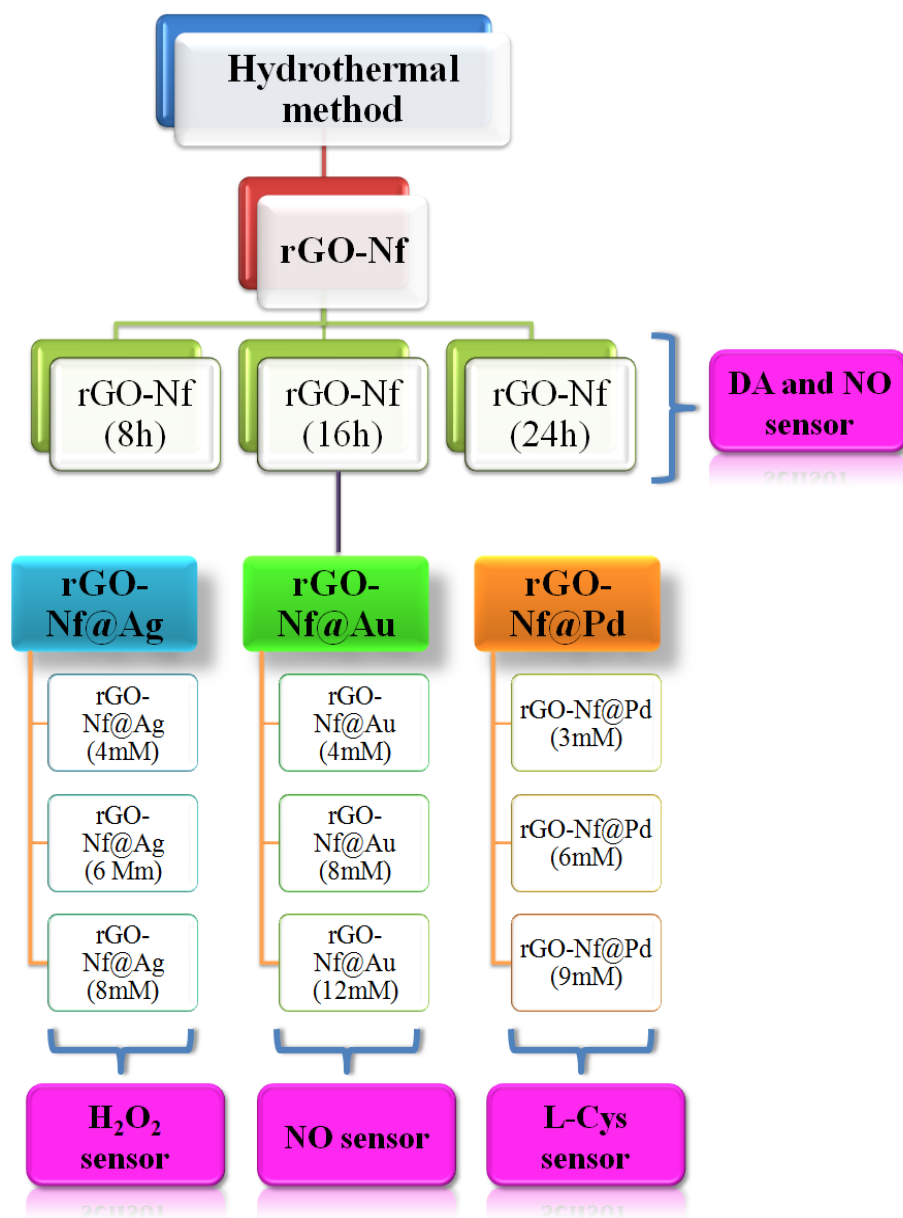


Figure 1.1: Flowchart of the research studies.

CHAPTER 2

LITERATURE REVIEW

2.1 Biomolecules

Biomolecules can be defined as an organic compound composed of two or more atoms that are bonded together and occurred naturally in living organisms. Most of the biomolecules are made up from basic element of atom such as oxygen, hydrogen, carbon, sulphur and nitrogen that acts as chemical building blocks of living organisms. These fundamental elements can be combined in many ways which determines the type of organic compound formed. Each of biomolecules have its own roles in the living system especially in human body in order to make sure all part of our body system can functioning well. Some example for important biomolecules in human body are dopamine (DA), nitric oxide (NO), hydrogen peroxide (H_2O_2) and l-cysteine (L-Cys), which has been discussed about its importance and functions in the next subtopic.

2.1.1 Dopamine (DA)

In the human body, all the neurologic information and signal from the brain is delivered to other cells, organs, muscles or tissues through an endogenous chemical messenger known as neurotransmitters. Neurotransmitters are synthesized by a number of amino acids that act as a building block. Various vitamins and minerals also play as cofactors which necessary for neurotransmitter production. Neurotransmitters are important for a large array of functions in both the central and the peripheral nervous systems as it delivers the message in the form of a nerve impulse from the brain. One example of important neurotransmitter is known as dopamine (DA). DA can be produced only in a few, very specific region of the brain such as at the substantia nigra

and the ventral tegmental area. Other than assist in regulating the movement and emotional responses, it also controls the brain's reward and pleasure centres. For example, the feelings of enjoyment to do certain activities and motivation to get things done are results of the excitation of DA in our body.

In addition, DA has a significant role in the operation of the cardiovascular, renal, central nervous as well as hormonal systems which associated with memory, behaviour and cognition, learning, attention and inhibition of prolactin production. An abnormal DA level in the brain causes several disease conditions, such as pleasurable, rewarding feelings and sometimes even euphoria. Depression, stress, mental exhaustion, fatigue, low sex drive and low motivation are some of the symptoms of low DA level in human body. A deficiency of DA in motor area of the brain may lead to muscle rigidity that commonly known as Parkinson's disease which involves uncontrollable muscle tremor. The neurological disorders such as schizophrenia and social anxiety or social phobia associated with the presence of excessive amounts of DA in human body (Pandikumar *et al.*, 2014). Besides that, the disorder of DA in the prefrontal cortex and frontal lobes of the brain contribute to attention deficit disorder and decline in neurocognitive functions, especially memory, attention and problem solving, respectively.

2.1.2 Nitric Oxide (NO)

Other biomolecule that is important in living organism is nitric oxide (NO) or also known as nitrogen monoxide as it consists of one nitrogen and one oxygen atom. NO is a hydrophobic, highly labile free radical that is naturally produced within the body. In 1992, NO has been announced as the 'molecule of the year' by Science Journal due to its importance in neuroscience, physiology and immunology (Cech *et al.*, 1992). Since then, the research on this molecule has expanded rapidly and in 1998, Ignacio and his

team were awarded the Nobel Prize in Medicine for the finding of the function of NO as a cardiovascular signaling molecule (Ignarro, 2002). After this discovery, NO was not only known as a potent environmental pollutant but now has become an important biomolecule that plays a vital role in a wide range of biological and cellular functions. NO is used for communication between cells by transmitting signals throughout the entire body and is involved in the regulation of blood pressure, the immune response, platelet aggregation and clotting, neurotransmission and possibly respiration (Bredt *et al.*, 1992; Burnett, 1997). It has been reported that the largest amount of NO was produced by the interior surface of arteries named endothelium.

The capacity to produce NO will decreased upon the growth of plaque in the arteries which made up from fat, cholesterol, platelets and other substances, thus led to the atherosclerosis disease. As 70 to 90 % of NO will be washed away by blood, the remaining will diffuses to the wall of arteries and veins, next triggers a cascade of events which cause the smooth muscle relaxation and dilating the blood vessel (Malinski, 2000). When the level of NO release from endothelium was low due to the decrease in the blood flow, the vascular muscles do not relax to the appropriate degree, thus induce the vasoconstriction which responsible for hypertension. Other diseases caused by deficiency in NO production are diabetes (both type I and II), ischemia (stroke, heart Alzheimer's disease), fibrosis and cancer (Napoli *et al.*, 2001; Petros *et al.*, 1991). Meanwhile, septic shock, hypotension, meningitis and rheumatoid arthritis are some example of disease associated with the overproduction of NO (Petros *et al.*, 1994).

2.1.3 Hydrogen Peroxide (H₂O₂)

Hydrogen peroxide (H₂O₂) is another example of biomolecules that is beneficial to human body. This biomolecule is by-product in a variety of enzymatic reactions and it could directly produce by oxidase enzymes such as glycolate, glucose, cholesterol and monoamine oxidases (Edmondson, 2014). Research has found that H₂O₂ is also involved in several biological events and intracellular pathways including the peroxisomal pathway for β -oxidation of fatty acids (de Groot *et al.*, 1989). Therefore, the concentration of H₂O₂ can be used as an indicator of the progress of the reaction. In respiratory system, the existence of H₂O₂ could be detected in the exhaled air of humans from phagocytes or other lung cells. The increase in the level of exhaled H₂O₂ is the sign of inflammatory lung diseases (Halliwell *et al.*, 2000).

Recent studies have proved that H₂O₂ can also be utilized as a signaling molecule to regulate diverse biological processes (Stone *et al.*, 2006). H₂O₂ which produced by a sub-class of white blood cells called neutrophils acts as a first line of defense against toxins, parasites, bacteria, viruses and yeast. Besides that, it also play a role in the regulation of renal function and as an antibacterial agent in the urine (Halliwell *et al.*, 2000). It was observed that increased H₂O₂ concentration in human body will induced the oxidative stress due to the production of hydroxyl radicals, which causes the damage on DNA and cell death. Parkinson, Alzheimer, diabetes, high blood pressure as well as increased rate in the aging process are some of the diseases related to the oxidative damage (Oikawa, 2005). Moreover, the excessive production of H₂O₂ generated in blood plasma could give a negative effect on human health and it also constitutes a pathogenic factor in vascular organ damage attendant upon systemic hypertension (Lacy *et al.*, 1998).

2.1.4 L-Cysteine (L-Cys)

L-Cysteine (L-Cys) is a type of biomolecule which belongs to the family of proteinogenic amino acid that is crucially important in human body. Under the normal physiological conditions, the L-Cys can be produced in human liver from essential amino acid known as methionine. An adequate amount of methionine is needed to produce L-Cys, however, methionine cannot be synthesized in the human body. Therefore, methionine has been supplied to our body by other sources such as meat, fish, eggs, dairy, quinoa, buckwheat, sesame seeds and Brazil nuts. Other than natural source, L-Cys can also be synthesized commercially using enzymatic and fermentative processes (Wada *et al.*, 2006). L-Cys is a vital amino acid that plays significant roles in numerous biological functions that helps functioning our body properly. For example, L-Cys act as an antioxidant that can prevent the harmful effects of tobacco and alcohol including liver and skin damages.

Besides that, it could also act as the antitoxin due to the presence of high sulfur content in L-Cys which helps in the conversion of toxic heavy metal compounds into stable complexes before disposal it from the body. L-Cys is also one of the building blocks for glutathione; one of the biomolecules that involve in inhibits inflammatory reactions and leads to an increased production of immune cells. The level of L-Cys in our body controls the rate of production of glutathione, thus, L-Cys could help in boosting the immune system of our body by stimulating natural killer cell production.

Additionally, L-Cys involved in the formation of many structural proteins of the connective tissues, hence promotes the development of healthy skin, hair and nails. Others important functions of L-Cys are acting as the radiation protector and cancer indicator and also able to prevent debilitating diseases like Alzheimer's and Parkinson's

(Özkan *et al.*, 2007). The L-Cys level in human body need to monitor because of it deficiency causes the liver damage, heart diseases, skin lesions, slow growth and depigmentation of hair (Prasad *et al.*, 2015). Meanwhile the high level of L-Cys causes many diseases including L-cystinuria and Parkinson's diseases while low level of L-Cys may associate to acquired immune deficiency syndrome (AIDS) (Dröge, 1993).

2.2 Analytical Techniques for the Detection of Biomolecules

The biological activity summary about these above said biomolecules including DA, NO, H₂O₂ and L-Cys was presented in Figure 2.1.

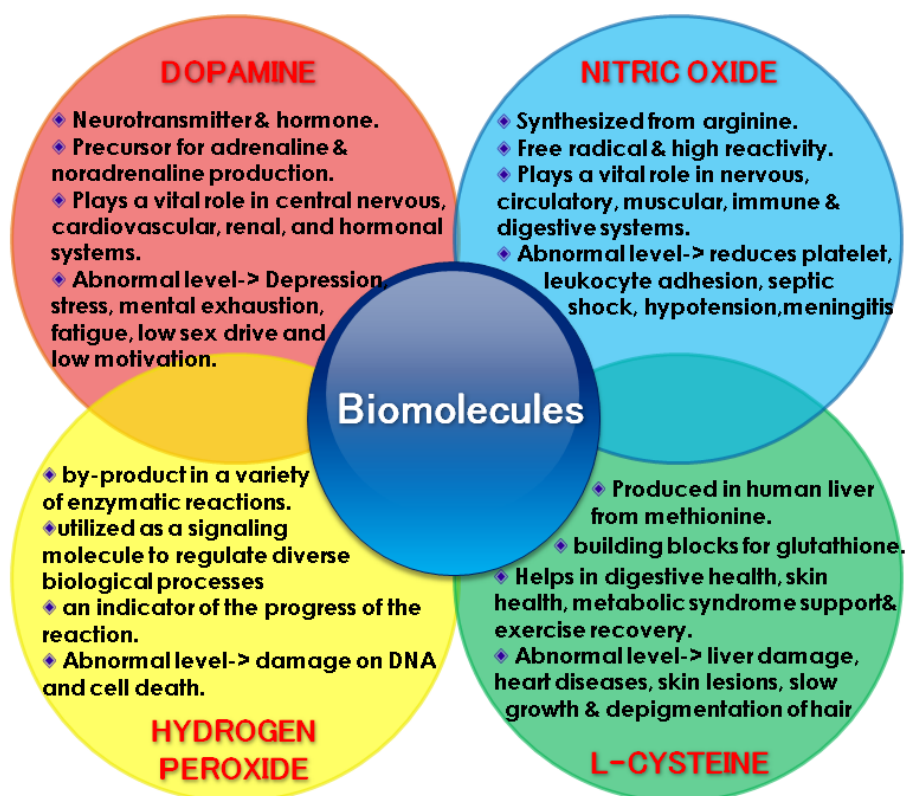


Figure 2.1: Summary information about four types of biomolecules.

Over the past decade, several analytical techniques for biomolecule detection have been developed as a result of the rapid development of nanotechnology. However, each technique associated with their own merits and limitations. Some of these techniques

have been discussed in this subtopic including colorimetric, high performance liquid chromatography (HPLC), electrochemiluminescence (ECL), surface enhanced Raman Spectroscopy (SERS) and electroanalytical techniques. Colorimetric sensing involves the measurement of the change in light absorption/emission which could be determined spectroscopically or directly observed by naked eyes. In the colorimetric sensing, an indicator that could change its color upon interaction with analytes is required to produce optical signals where the observed optical signal is correlated with the concentration of target compounds. Despite the simplicity showed by colorimetric technique, there are few drawbacks that restrict their application in real sample analysis. One of the obstacles is the time dependent color change of the suspension resulted from the non-directive aggregation of nanoparticles (NPs) that formed an unstable solution with larger particle size and reduced surface repelling force. This would lead to the imprecise determination of the target, hence the results is unreliable. Second obstacle is the large aggregate NPs which reduce the detection sensitivity and stability.

The high performance liquid chromatography (HPLC) is one of the advanced forms of liquid chromatography which has the ability to separate the complex mixture of substances in the mobile phase (liquid or gas) to their basic individual compound. Upon the separation, the identification and quantification of this individual compound will be made. This HPLC technique is suitable for separation of non-volatile chemical and biological compounds such as pharmaceuticals, organic chemicals like polymers, thermally unstable compounds like enzyme and heavy hydrocarbons like asphalt. Despite its advantages, this sensing technique suffer from bad reproductivity and background interference, besides require complicated system setup and large quantities of expensive organics. Moreover, HPLC also have low sensitivity for certain compounds, and there are certain compounds that cannot be detected using this technique.

The electrogenerated chemiluminescence or electrochemiluminescence (ECL) is a type of light emission that is produced directly or indirectly upon high-energy electron transfer reaction occurring between the electrogenerated species at the electrode which forms an excited state. By combining the ECL with the electroanalytical chemistry, an ECL sensor can be developed based on the principle that particular labels will generate an optical signal triggered by an electrochemical reaction that stimulated by the electrode potential. In the ECL analysis, high sensitivity and low detection limit were achieved by using a photodetector such as photomultiplier tube (PMT), photodiode or charge-coupled device camera (CCD) to detect the electro-triggered eye-invisible weak light. However, it needs a high cost to produce due to the consumption of the expensive reagent and extra pump to deliver the reagent to the electrochemical cell continuously. The one time use of probe, inherent toxicity, lower ECL signals and requirement of high negative potential limits its application in sensors.

Surface-enhanced Raman scattering (SERS) technique offered several advantages over other techniques such as faster and simple as it requires minimum sample preparation, high sensitivity as it allowing for single molecule detection and can be used to detect various analytes such as metal ion (Shaban *et al.*, 2016), organic molecules (Ignat *et al.*, 2009) and biomolecules (Fazio *et al.*, 2016). The SERS technique uses the idea that the molecules illuminated by fixed-frequency light to trigger inelastic scattering closely related to the vibrational and rotational modes excited in the molecules. These molecules when irradiated with different frequencies light generate a specific frequency pattern where this spectrum information is used as a fingerprint for detecting and identifying specific substances. The plasmon phenomenon will be generated on the metal surface induced by laser light and this phenomenon allowing us to collect rare information that could not be obtained from Raman signal. Therefore, this

technique has the potential as a sensor for the detection of various chemicals and biological molecules.

However, the scattering properties of most substances are normally weak, therefore these substances need to be directly combined with metal surface such as gold (Au) and silver (Ag) to enhance the Raman signal that arise from the effect of electromagnetic field and chemical enhancement. In order to acts as a sensor, this frequency signal must be amplified; therefore a metallic surface is used to amplify the frequency signal generated by the target molecules. The intensity of Raman will increase when a high concentration of target analyte is used or located close to a metallic surface. In spite of all the advantages of SERS sensing technique, it has several limitations such as high cost of production and difficult in miniaturization as it requires expensive and sophisticated equipment.

Even though there are many analytical techniques used for biomolecules detection, however all these reported analytical methods required a high cost with larger in size instrumentation facility and complicated multiple operations of the fabricated sensors, which is not convenient to handle. Besides that, it also has a low sensitivity towards specific biomolecules. Strong demand to create a sensing technique which provides a rapid response and sensitivity, ease of use and low cost led to the discovery of an electrochemical technique for the detection of biomolecules. An electrochemical is a technique that has been used to measure the concentration of biomolecules due to the direct transforms of electrochemical information produced by biochemical mechanism into an analytically useful signal. Electrochemical biosensor has a series of advantages such as high sensitivity and selectivity towards electroactive species, rapid and accurate

response and most importantly it is portable and inexpensive compared to other existing biosensor.

Besides that, it also offers advantages of wide linear response range and good stability and reproducibility. There are two basic components of an electrochemical sensor which works together as a working or sensing electrode that are a chemical recognition system and physicochemical transducer. Other than working electrode (WE), reference and counter electrodes are also required in this sensor where next enclosed in the sensor housing in contact with a liquid electrolyte and biomolecules. In order to acts as biosensor, the recognition layers will interaction with the target biomolecules and the physicochemical transducer will translates the bio-recognition event into a useful electrical signal which can be detected by electrochemical workstation. Amperometry, cyclic voltammetry (CV) and potentiometry are some of the examples of electrical signal resulted from the transduction of biological signal.

One of the most important components in electrochemical sensing technique is the WE because it is the place where all the electrochemical oxidation and reduction process occurs. There are various types of WE that have been commercialized such as platinum (Pt), gold (Au), mercury (Hg) and carbon electrode. Even though Pt electrode demonstrating good electrochemical inertness, however, it required high cost for production and it is easily be interrupted by the presence of small amounts of water or acid in the electrolyte. It will reduced hydrogen ion to form hydrogen gas (hydrogen evolution) at low negative potential, hence obscures any useful analytical signal.

Another metal electrode that behaves almost similar like Pt electrode is the Au electrode. Au electrode provide good electron transfer kinetics and a wide anodic potential range, however it have exhibit weakness in the positive potential range due to the oxidation of its surface. Mercury electrode is another example of WE that has been used in electrochemical sensing technique due to its high hydrogen over voltage which can extend the cathodic potential window. Besides that it also possesses highly reproducible, renewable and smooth surface, which is very beneficial in electrochemical analysis. The most common form of mercury electrode is dropping mercury electrode, hanging mercury drop electrode and mercury film electrode. Nevertheless, the toxicity and limited anodic range of mercury has lead to a limited use these days. Among the different types of electrode, carbon electrode such as carbon paste electrode (CPE) and glassy carbon electrode (GCE) has been commonly used as WE as it allow scans to more negative potentials than other electrode as well as good anodic potential windows. Moreover, carbon electrodes also have a low background current, rich surface chemistry as well as comparative chemical inertness. Therefore, researchers commonly used the carbon electrode as the WE in electrochemical sensing. Table 2.1 shows the example of modified electrode used for detecting biomolecules *via* electrochemical technique.

Table 2.1: The comparison of various modified electrode towards the detection of biomolecules by using electroanalytical method.

| Modified electrode | Target bioanalyte | Detection method | Detection limit | Reference |
|----------------------|-------------------|------------------|--------------------------|---------------------------------|
| rGO-poly(Cu-AMT)/GCE | DA | DPSV | 3.48 nM | (Yaru <i>et al.</i> , 2017) |
| FeS/rGO/GCE | DA | Amperometry | 98 nM | (Liu <i>et al.</i> , 2017) |
| MIP/NPAMR | DA | CV | 7.63×10^{-14} M | (Yingchun <i>et al.</i> , 2016) |
| G-Au/GCE | NO | LSV | 0.04 μ M | (Geetha <i>et al.</i> , 2017) |
| AuPt-rGO/GCE | NO | Amperometry | 2.88 nM | (Liu <i>et al.</i> , 2016) |

Table 2.1, continued

| Modified electrode | Target bioanalyte | Detection method | Detection limit | Reference |
|--------------------------------------|-------------------------------|------------------|-----------------|---------------------------------|
| Pt-GO-Fe ₂ O ₃ | NO | LSV | 13.04 mM | (Adekunle <i>et al.</i> , 2015) |
| ERGO/GCE | H ₂ O ₂ | Amperometry | 0.7 µM | (Mutyala <i>et al.</i> , 2016) |
| Sm ₂ O ₃ /GCE | H ₂ O ₂ | Amperometry | 1 µM | (Yan <i>et al.</i> , 2016) |
| PAA/Au-SPE | H ₂ O ₂ | Amperometry | 2 µM | (Zamfir <i>et al.</i> , 2016) |
| GO/CCNTs/AuNPs@MnO ₂ /GCE | L-Cys | DPV | 3.4 nM | (Wang <i>et al.</i> , 2015) |
| SnO ₂ -MWCNTs/GCE | L-Cys | Amperometry | 0.03 µM | (Dong <i>et al.</i> , 2014) |
| Au-SH-SiO ₂ @Cu-MOF/GCE | L-Cys | DPV | 0.008 µM | (Hosseini <i>et al.</i> , 2013) |

rGO=reduced graphene oxide; poly(Cu-AMT)=copper-2-amino-5-mercapto-1,3,4-thiadiazole; GCE=glassy carbon electrode; DPSV=differential pulse stripping voltammetry; FeS=Iron(II) sulphide; MIP=molecularly imprinted polymer; NPAMR=nanoporous Au-Ag alloy microrod; G=graphene; LSV=linear sweep voltammetry; AuPt=gold platinum; GO=graphene oxide; Fe₂O₃=iron(III) oxide; ERGO=electrochemically reduced graphene oxide; Sm₂O₃=samarium oxide; PAA=polyamic acid; SPE=screen printed electrode; CCNTs=carboxylated multiwalled carbon nanotube; MnO₂=manganese dioxide; SnO₂=tin dioxide; MWCNTs=multiwall carbon nanotubes; SiO₂=silicon dioxide; Cu=copper; MOF=metal organic framework.

2.3 Materials for Electrode Modification

The sensitivity of the electrochemical sensor will be affected based on the surface modification techniques, electrochemical transduction mechanisms and the choice of the recognition receptor molecules. Therefore, the surface architectures which link the sensing element with the biological samples play an important role in determining the performance of electrochemical sensor. The reason why electrode surface need to be modified is that electrode surface tends to absorb water molecules when dipped into a solution, hence blocking the access for the target molecules to reach the electrode surface. Thus, the current response obtained from electrochemical process will be smaller and lowering the sensitivity of the sensor. The discussion about several potential materials for modifying the electrode including graphene-based, Nafion (Nf) and metal nanoparticles were presented in this subtopic.

2.3.1 Graphene-based Materials

In recent years, carbon-based materials have received considerable attention due to its unique properties such as high surface to volume ratio, high electrical conductivity, chemical stability, biocompatibility and robust mechanical strength (Avouris *et al.*, 2007). Besides that, it is also easy to prepared, reproducible, stable and has low ohmic resistance. Up to date, various types of carbon-based materials has been discovered to have valuable potential as electrode sensor including graphene (Zhang *et al.*, 2016), carbon nanotube (CNT) (Musameh *et al.*, 2002), multi walled carbon nanotube (MWCNT) (Jain *et al.*, 2012) and single-walled carbon nanotube (SWCNT) (Weber *et al.*, 2011). Among these materials, graphene have been extensively studied because of their fascinating properties such as high electrical conductivity, excellent mechanical flexibility and good chemical stability, which make it potentially useful for the fabrication of various electrochemical sensors (Atta *et al.*, 2015).

Graphene is a 2D sheet of sp^2 bonded carbon atoms, densely packed in a honeycomb crystal lattice structure in which each of these layers is held together by weak van der Waals forces (Choi *et al.*, 2010). The most important property of graphene is its excellent electrical conductivity which could enhance the mobility of charge carriers, thus improved the sensing performance. The sp^2 hybridization, unique electronic configuration, its extraordinary electron transport property, so called ballistic conductivity, and the number and position of the oxygen functionalities of graphene helps to promote and accelerate the electron transfer process during electrochemical detection (Pandikumar *et al.*, 2014).

Moreover, the ability of rapid electron transfer kinetics at the basal planes of graphene sheets that act as nanoconnectors and thus electrically facilitates the heterogeneous electron transfer between the biomolecules and electrode substrate, resulting in excellent sensing performance. The various forms of graphene-based materials include thermally reduced graphene oxide (TRGO), chemically reduced graphene oxide (CRGO) and electrochemically reduced graphene oxide (ERGO), contains oxygen-containing functional groups and certain amounts of defects.

The rapid electron transfer takes place at the surface of edge planes and defects when compared to the basal planes for the electrochemical sensors fabricated with graphene-based materials. The presence of these structural defects in the chemically modified graphene can be exploited for electrochemical sensors. The presence of oxygen-containing functional groups in the graphene-based materials play a vital role in the electrochemical sensors, which makes the adsorption and preconcentration of the redox species (which is of our analytical interest) and effectively catalyst the redox reactions. In addition, the presence of these functional groups makes an effective functionalization with various biomolecules (Chen *et al.*, 2011). The functionalization of these graphene-based materials with specific functional groups enable the use of these excellent materials for electrochemical sensor applications with specific analytes. The functionalized graphene materials also make rapid electron transfer by pre-concentrating the target analytes at the electrode surface. The graphene-based materials are commonly used for electrochemical sensing of various biomolecules and some of previous reports have been listed in Table 2.2.

Table 2.2: Comparison of various graphene-based modified electrodes for the detection of different bioanalytes using electrochemical technique.

| Electrode | Target analyte | Analytical method | Linear range | Detection limit | Reference |
|-----------|-------------------------------|-------------------|----------------------|-----------------|--------------------------------------|
| ERGO/GCE | H ₂ O ₂ | Amperometry | 1–16 μ M | 0.7 μ M | (Mutyala <i>et al.</i> , 2016) |
| PG/GCE | DA | Amperometry | 5.00 – 710 μ M | 2.0 μ M | (Qi <i>et al.</i> , 2015) |
| GO/GCE | DA | DPV | 1 – 15 μ M | 0.27 μ M | (Gao <i>et al.</i> , 2013) |
| ERGO/GCE | DA | DPV | 0.5 – 60 μ M | 0.5 μ M | (Yang <i>et al.</i> , 2014) |
| MWCNT/Ta | H ₂ O ₂ | CV | 5 μ M – 0.025 mM | 0.09 μ M | (Vijayalakshmi <i>et al.</i> , 2016) |

PG=pristine graphene; DPV=differential pulse voltammetry; Ta=tantalum.

2.3.2 Nafion (Nf)

Conducting polymers which also known as intrinsically conducting polymers (ICPs) are a new class of polymers that possesses a high electron affinity and high electronic conductivity by several orders of magnitude of doping (while maintaining mechanical flexibility and high thermal stability). These can be associated to the π -electron backbone owned by ICPs. ICPs have been long synthesized and used for the various applications including electrochemical biosensor. One of the advantages possess by ICPs is that it is easy to synthesize through chemical or electrochemical process which produces a stable and reproducible dispersion. This has encourages researchers to employ ICPs material in the fabrication of sensors especially for detecting biomolecules. Other remarkable advantages of using ICPs is that it provides an excellent signal transduction for molecular detection due to its high sensitivity in their conductivity and electrochemical activity towards molecular interaction, thus renders possibilities for sensor application (Janata *et al.*, 2003). Moreover, ICPs can act as an electron promoter that are compatible with biological molecules in neutral aqueous solutions (Mulchandani *et al.*, 1996). Besides that, the ICPs itself can be modified to

bind biomolecules to a sensor, thus able to increase the sensitivity of the sensor (Rahman *et al.*, 2008).

Some of the ICPs groups that are frequently used in sensors application are polyacetylene (Zeng *et al.*, 2009), polythiophene (Védrine *et al.*, 2003), poly(p-phenylenevinylene) (Srinivas *et al.*, 2012), poly(3,4-ethylenedioxythiophene) (Nien *et al.*, 2006), polypyrrole (Uang *et al.*, 2003) and polyaniline (Langer *et al.*, 2004). Among them, Nf is one of the most extensively used ICPs in the design of bioanalytical sensors. Nf is a sulfonated tetrafluoroethylene based fluoropolymer-copolymer with a conductive properties. Due to the presence of perfluoroalkyl backbones in Nf, it has high hydrophobicity properties hence making it an effective matrix to disperse graphene in an aqueous solution as graphene tend to agglomerate or even restack to form graphite through strong π - π stacking and van der Waal's interaction (Yin *et al.*, 2010). In sensor application, Nf was used as an electrode modifier for sensor electrode fabrication due to its antifouling capacity, chemical inertness and high permeability to cations (Zarei *et al.*, 2015).

Besides that, Nf also helps to enhance the stability of graphene modified electrodes due to its excellent film forming ability. As a cation exchange polymer, Nf helps to blocks the anionic species from reaching the electrode surfaces and allows the cation conduction to pass through, thus leads to good selectivity (Chou *et al.*, 2009). Interestingly, the hydrophilic negatively charged sulfonate group in Nf film enables selective pre-concentration of positively charged biomolecules through electrostatic interaction, whereas, the hydrophobic fluorocarbon network of the polymer gives a selectivity for the hydrophobic part of the molecule (Nigović *et al.*, 2014a). These advantages making Nf an ideal choice for the fabrication of electrochemical sensors.

The comparison of various conducting polymer-based modified electrodes for the detection of different bioanalytes by using electrochemical technique has been listed in Table 2.3.

Table 2.3: Comparison of various conducting polymer-based modified electrodes for the detection of different bioanalytes using electrochemical technique.

| Electrode | Target analyte | Analytical method | Linear range | Detection limit | Reference |
|----------------------|----------------|-------------------|---------------------|-----------------|--|
| CPPDAN | NE | DPV | 9.90 - 90.9 μ M | 1.82 μ M | (Guedes da Silva <i>et al.</i> , 2011) |
| PAH/SPE | NADH | Amperometry | 0.01 - 5 mM | 0.22 μ M | (Rotariu <i>et al.</i> , 2014) |
| nanoporous PEDOT/GCE | NADH | Amperometry | 5 - 45 μ M | 3.8 μ M | (Rajaram <i>et al.</i> , 2015) |
| Nf/p(FcAni)-CNTsPE | DA | DPV | 1- 150 μ M | 0.21 μ M | (Sroysee <i>et al.</i>) |
| Pty/GCE | DA | LSSV | 1-7 μ M | 161 nM | (Khudaish <i>et al.</i> , 2012) |

CPPDAN=Cathodically Pretreated Poly(1,5-diaminonaphthalene); NE=norepinephrine; NADH=nicotinamide adenine dinucleotide; PAH=Poly(allylamine hydrochloride); SPE=screen-printed carbon electrode; PEDOT=poly(3,4)ethylenedioxythiophene; p(FcAni)=poly(*m*-ferrocenylaniline; CNTsPE=carbon nanotubes-paste electrode; Pty=polytyramine; LSSV=linear square stripping voltammetry.

2.3.3 Metal Nanoparticles

Metal nanoparticles such as gold (Au), silver (Ag), platinum (Pt), palladium (Pd), copper (Cu), zinc (Zn) and etc, have attracted much attention because of their extraordinary properties in different fields of optics (Augustine *et al.*, 2014), optoelectronics (Borsella *et al.*, 1999; Conoci *et al.*, 2006), catalysts (Lesiak *et al.*, 2014; Li *et al.*, 2014), solar cell (Hai *et al.*, 2013; Kang *et al.*, 2010) and sensors (Li *et al.*, 2014). The unique chemical and physical properties of metal nanoparticles make it potentially useful for designing new and improved sensing devices, especially for electrochemical sensors. Their excellent electrocatalytic properties and high load capacity for biomolecules have given advantages for metal nanoparticles to be

employed as electrochemical signal enhancer in sensor application. With regard to this, silver nanoparticles (AgNPs) have been extensively investigated as an effective electrocatalyst for electrochemical sensor applications. AgNPs keep on being of enormous current research attention because it required low production cost, environmentally friendly, low toxicity and biocompatibility. Moreover, AgNPs possessed the advantages of excellent catalytic activity, high conductivity and high surface energy, which makes them a promising catalyst material. Furthermore, their high surface to volume ratio allows large fraction of metal atoms to get exposed to reactant molecules and it is very much desirable for sensor application (Rastogi *et al.*, 2014). Besides that, it is also the best conductor among all of the noble metals (Jiang *et al.*, 2013). Due to these properties, AgNPs may facilitate more efficient electron transfer than the other noble metal nanoparticles.

Besides AgNPs, gold nanoparticles (AuNPs) also have recently drawing an increasing attention of many researchers in the field of sensors. AuNPs have attracted more attention from researcher due to its novel chemical, optical and physical properties such as high effective surface to volume ratio, excellent electrical and heat conductivity, and strong absorption in the visible and near infrared wavelength region (380 to 750 nm). Important physical properties of AuNPs include surface plasmon resonance (SPR) and the ability to quench fluorescence (Yeh *et al.*, 2012). Besides that, it is also have an excellent biocompatibility and low toxicity which make is suitable to be applied in biotechnology (Khlebtsov *et al.*, 2011). AuNPs also exhibit high chemical stability and inertness under physiological conditions as well as possesses excellent electrocatalysis properties. All these properties make AuNPs an attractive material for electrochemical and biological devices. More interestingly, the properties of Au can be controlled by tuning the shape and size (Jain *et al.*, 2006). Because of its small size, Au

could provide high active surface area, thus, improve the electron transfer. This will lead to the enhancement in sensitivity and signal to noise ratio, therefore improve the analytical performance.

Another noble metal that has the potential as a catalyst for the electrochemical sensor is palladium nanoparticles (PdNPs). PdNPs have attracted extensive attention because of their good chemical and physical properties, including its wear and corrosion resistance as well as good stability. Its high specific surface areas would increase the mass transport and enhance the electron transfer kinetics, thus, improves the electrocatalytic activity. Besides that, PdNPs is also an important material in applications involving hydrogen storage and gas sensing due to its ability to absorb hydrogen at high capacity (Tobiška *et al.*, 2001). Table 2.4 compiles the analytical parameters for electrochemical sensing of biomolecules by using various metals nanoparticles as the sensor electrode that have been reported in literature.

Table 2.4: Comparison of various metals nanoparticles-based modified electrodes for the detection of different bioanalytes by using electrochemical technique.

| Electrode | Target analyte | Analytical method | Linear range | Detection limit | Reference |
|------------|-------------------------------|-------------------|---|---------------------|--|
| AgNPs/MCPE | DA | DPV | 1 – 5 μM | 0.085 μM | (Vidya <i>et al.</i> , 2016) |
| ITO/AuNPs | DA | DPV | 1×10^{-7} - 9×10^{-4} M | 34.5 μM | (Aldana-González <i>et al.</i> , 2013) |
| Ag-Pd/GCE | L-Cys | CV | - | 2.8 μM | (Murugavelu <i>et al.</i> , 2014) |
| Fe@Pt/C | H ₂ O ₂ | Amperometry | 2.5 μM -41.605 mM | 750 nM | (Mei <i>et al.</i> , 2016) |
| Au/ITO | 5-HT | SWV | 1.0×10^{-8} – 2.5×10^{-4} M | 3 nM | (Goyal <i>et al.</i> , 2007) |

AgNPs=silver nanoparticles; MCPE=modified carbon paste electrode; ITO=indium tin oxide; Pd=palladium; CV=cyclic voltammetry; Fe=ferum; Pt=platinum; C=carbon; 5-HT=serotonin; SWV=square wave voltammetry.

CHAPTER 3

RESEARCH METHODOLOGY

3.1 Materials

All chemicals and solvents were used as-received without any further purification unless other-wise stated. Aqueous solutions were all made in deionized water (DI water) throughout the work. The materials and chemicals used in this work are summarized in Table 3.1.

Table 3.1: List of chemicals and materials used in this work.

| Chemicals | Formula | Purity (%) | Brand |
|---------------------------------|--|------------|-----------------------|
| Graphite flakes | - | - | Asbury Graphite Mills |
| Nafion | - | - | Ion Power Inc. |
| Sulfuric acid | H ₂ SO ₄ | 95~97 | Merck |
| Phosphoric acid | H ₃ PO ₄ | 85 | Merck |
| Hydrochloric acid | HCl | 37 | Merck |
| Ammonia solution | NH ₄ OH | 25 | Merck |
| Hydrogen peroxide | H ₂ O ₂ | 35 | System |
| Potassium permanganate | KMnO ₄ | - | R&M Chemicals |
| Silver nitrate | AgNO ₃ | 99.9 | Merck |
| Gold(III) chloride trihydrate | HAuCl ₄ .3H ₂ O | 99.9 | Abcr.Gmbh & Co. KG |
| Sodium tetrachloropalladate(II) | Na ₂ PdCl ₄ | 98 | Sigma-Aldrich |
| Sodium phosphate monobasic | NaH ₂ PO ₄ | 99 | Sigma-Aldrich |
| Disodium phosphate dihydrate | Na ₂ HPO ₄ .2H ₂ O | 99 | Sigma-Aldrich |
| 3-hydroxytyraminium chloride | 3,4-(OH) ₂ C ₆ H ₃ CH ₂ CH ₂ NH ₂ .HCl | - | Merck Schuchardt OHG |
| Sodium nitrite | NaNO ₂ | 98 | Sigma-Aldrich |
| L(+)-Ascorbic acid | C ₆ H ₈ O ₆ | 99 | Sigma-Aldrich |
| Sodium chloride | NaCl | 99.5 | Sigma-Aldrich |
| L-Cysteine | C ₃ H ₇ NO ₂ S | 97 | Sigma-Aldrich |
| Uric acid | C ₅ H ₄ N ₄ O ₃ | 99 | Sigma-Aldrich |
| D-(+)Glucose | C ₆ H ₁₂ O ₆ | 99.5 | Sigma-Aldrich |
| Urea | CO(NH ₂) ₂ | 98 | Merck |

3.2 Sample Preparation

3.2.1 Preparation of Graphene Oxide (GO)

In this work, GO was synthesized according to Simplified Hummers' method which use graphite flakes as the precursor. The schematic diagram of the Simplified Hummers' method for synthesizing GO is shown in Figure 3.1. Initially, 400 mL mixture that contained with concentrated H_2SO_4 and concentrated H_3PO_4 was prepared using a ratio of 9:1. Next, 3.0 g of graphite flakes was added into the mixture while stirring. Then, 18.0 g of KMnO_4 was added slowly and the solution was left to oxidize for 3 days with continuous stirring. After 3 days, 400 mL ice with 20 mL of 35 % H_2O_2 were poured into the solution in order to stop the oxidation process. The solution was left for few minutes to remove excessive KMnO_4 . Finally, the solution was washed with 1.0 M HCl for 3 times and continued with DI water for 6 times. The solution was centrifuged at 12000 rpm for 10 min and finally, the GO was obtained.

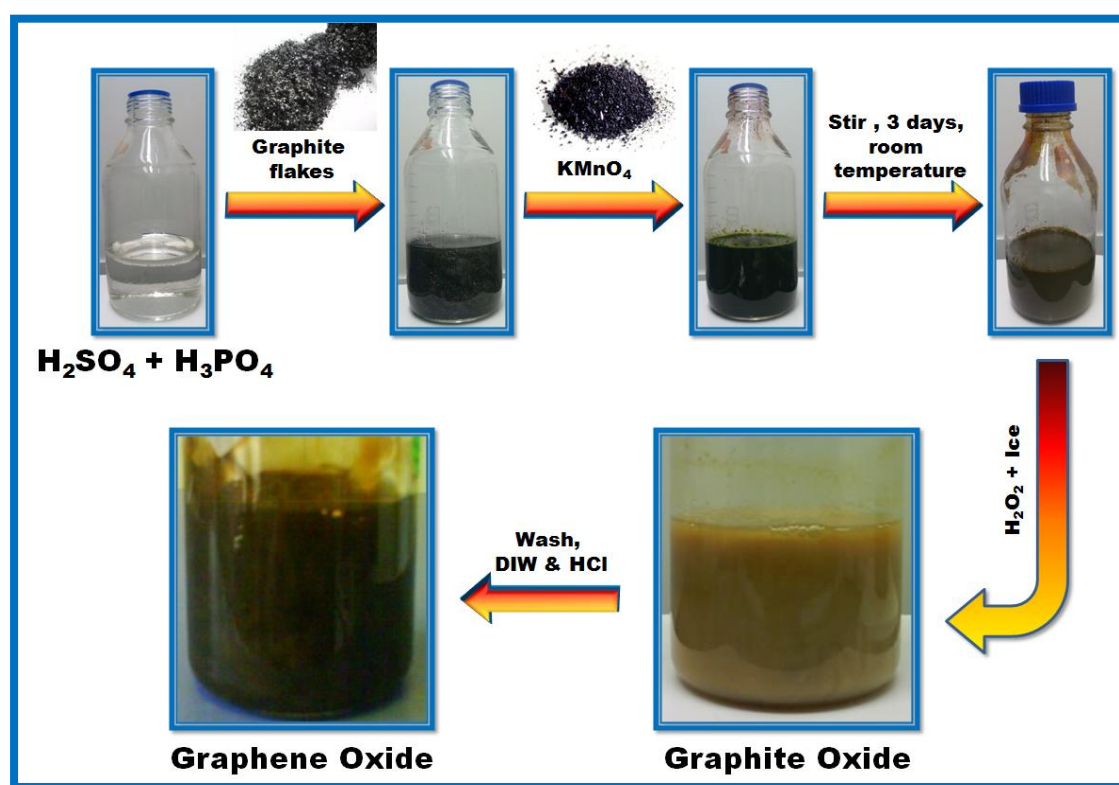


Figure 3.1: Schematic representation for synthesis of GO using Simplified Hummers' method.

3.2.2 Synthesis of rGO-Nf Nanohybrid

The rGO-Nf nanohybrid was prepared as follows. Briefly, 50 mL of a GO solution with a concentration of 0.5 mg/mL was sonicated for 30 min. Meanwhile, a Nf solution with concentration of 0.5 mg/mL was prepared by dissolving Nf powder in an ethanol-DI water mixture solution with a ratio of 1:1. Then, 10 mL of the Nf solution was added to 10 mL of the GO solution, and this mixture was subjected to sonication for 30 min. Finally, the reaction mixture (GO-Nf) was transferred to a Teflon-lined stainless-steel autoclave and heated at 180 °C. Three samples were prepared with different hydrothermal treatment durations (8, 16 and 24 h) and labeled as rGO-Nf (8 h), rGO-Nf (16 h) and rGO-Nf (24 h). The whole process was schematically depicted in Figure 3.2.

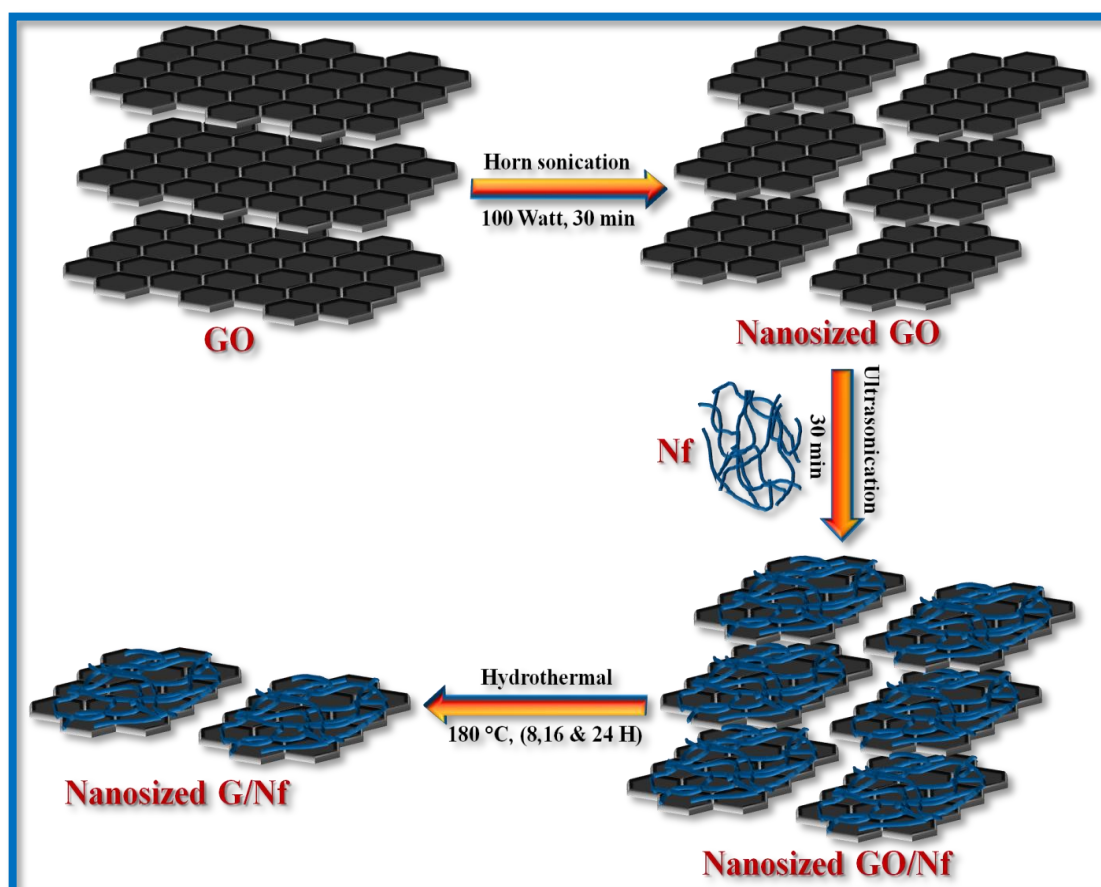


Figure 3.2: Illustration of preparation of rGO/Nf nanohybrid *via* hydrothermal method.

3.2.3 Synthesis of rGO-Nf@Ag Nanohybrid

Initially, 10 mL of GO (0.5 mg/mL) solution were sonicated for 30 min. Meanwhile, 10 mL of Nf solution were prepared by dissolving Nf powder in an ethanol:DI water (1:1 v/v) mixture. The prepared GO and Nf solutions were mixed together and sonicated continuously for 30 min. 2 mL of AgNO_3 were added drop by dropwise into the GO-Nf solution and stirred for 15 min. Later, 13 mL of NH_4OH were added drop by drop to the mixture and stirred at room temperature for another 15 min. The reaction mixture was transferred into a Teflon-lined stainless autoclave before subsequently being put into an oven maintained at 180°C for 16 h. After cool to room temperature, the black precipitates were collected and washed with DI water and ethanol several times and then dried naturally. Three different concentrations of AgNO_3 (4, 6 and 8 mM) were used to prepare three different nanohybrids. The final products were labeled as rGO-Nf@Ag4, rGO-Nf@Ag6 and rGO-Nf@Ag8 nanohybrids. The above mentioned synthetic protocol is schematically illustrated in Figure 3.3.

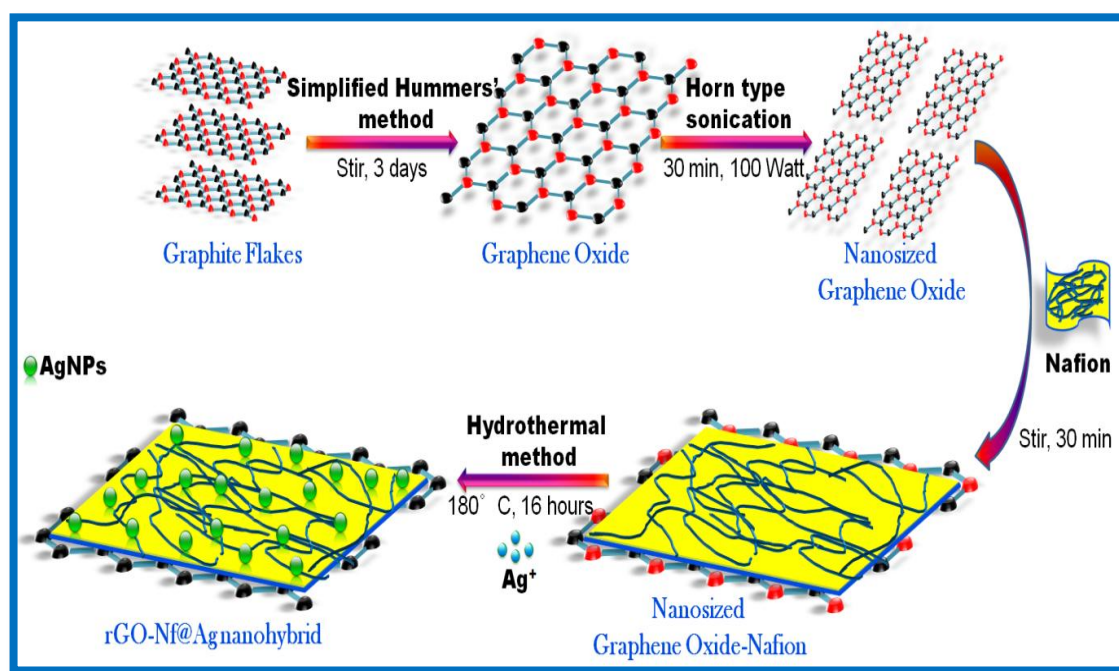


Figure 3.3: Schematic illustration for formation of rGO-Nf@Ag nanohybrid *via* hydrothermal method.

3.2.4 Synthesis of rGO-Nf@Au Nanohybrid

In the first step, GO-Nf solution was prepared by using ultrasonication method according to the procedure given in section 3.2.2. Next, 20 mL of GO-Nf solution was mixed with 2 mL of $\text{HAuCl}_4 \cdot 3\text{H}_2\text{O}$ solution. Above mixture was then stirred for 15 min under room temperature. For a control experiment, three different concentrations of $\text{HAuCl}_4 \cdot 3\text{H}_2\text{O}$ (4, 8 and 12 mM) were used. Then, 13 mL of NH_4OH were slowly added into the solution while stirring to avoid sudden agglomeration. Prior to transferring to a Teflon-lined autoclave, the solution mixture was homogeneously stirred for 15 min. The hydrothermal synthesis was carried out at temperature of 180 °C for 16 h and subsequently cooled down to room temperature naturally after the reaction. Afterwards, the black precipitate was collected by centrifugation and washed with DI water and ethanol for several times, and dried at 60 °C in the oven for 24 h. The obtained powder was labeled as rGO-Nf@Au4, rGO-Nf@Au8 and rGO-Nf@Au12. The schematic illustration for synthesizing rGO-Nf@Au nanohybrid was shown in Figure 3.4.

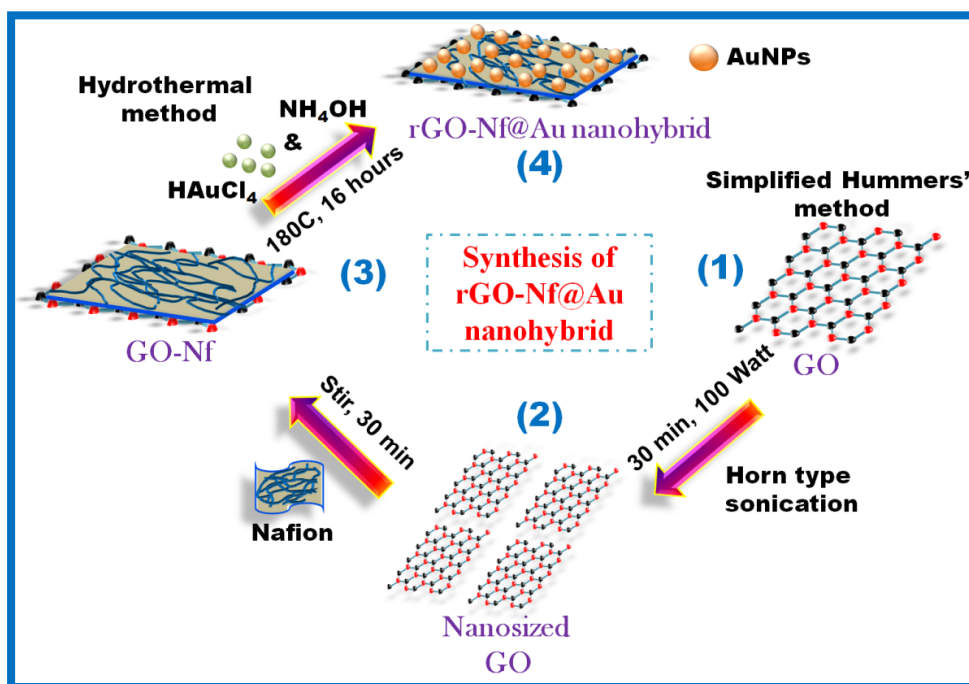


Figure 3.4: Schematic illustration for synthesis of rGO-Nf@Au nanohybrid.

3.2.5 Synthesis of rGO-Nf@Pd Nanohybrid

Briefly, 10 mL Nf solution was added in 10 mL GO solution and the mixture was subjected to horn type sonication for 30 min. The Nf solution was prepared by placing Nf powder in a glass beaker containing a mixture of ethanol and DI water (1:1 v/v). Next, 2 mL Na_2PdCl_4 solution was added in the mixture and stirred for 15 min at room temperature. For a control experiment, three different concentration of Na_2PdCl_4 (3, 6, and 9 mM) were used. Then, 13 mL NH_4OH was added dropwise into the mixture. The mixture was stirred continuously for another 15 min to make sure the entire compounds used are well blended before transferred into an autoclave and subjected to the hydrothermal reduction at 180 °C for 16 h. Afterward, the black solution were washed several times with DI water and ethanol and then dried in oven for 24 h to get powder form samples. The final products were named as rGO-Nf@Pd3, rGO-Nf@Pd6 and rGO-Nf@Pd9. The schematic illustration for preparing these nanohybrids was shown in Figure 3.5.

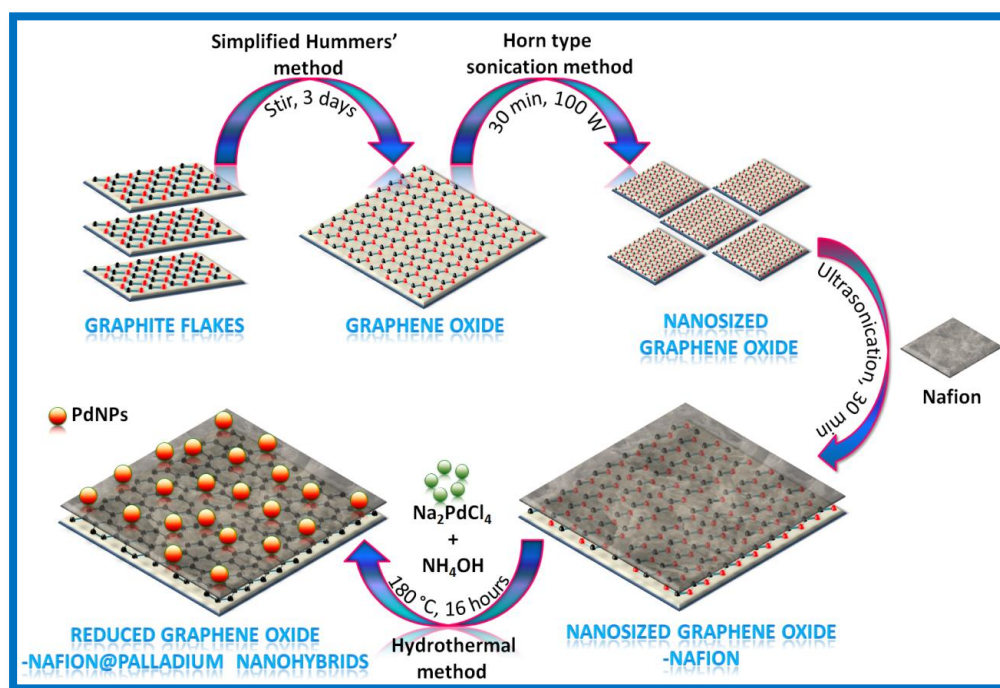


Figure 3.5: Schematic diagram for the synthesis of PdNPs decorated rGO-Nf film using hydrothermal method.

3.3 Electrochemical Cell Set-up

The electrochemical measurements were carried out at room temperature by using a VersaSTAT 3 workstation supplied by Princeton Applied Research and controlled by Nova software. A conventional three electrode electrochemical cell was used, consisting of modified electrode (GCE, dia. 3 mm) as the WE, a saturated calomel electrode (SCE) and silver/silver chloride (Ag/AgCl) as the reference electrode (depends on the bioanalyte measured) and platinum wire as the counter electrode. Unless otherwise stated, the WE potentials stated in this paper are with reference to the SCE and all electrochemical studies were carried out by flowing N_2 gas atmosphere. As the supporting electrolyte, phosphate buffer solution (PBS) was prepared by mixing the NaH_2PO_4 and $Na_2HPO_4 \cdot 2H_2O$ solutions which were prior dissolved in DI water. For the purpose of adjusting the pH, 1.0 M NaOH or H_3PO_4 were used when necessary. A schematic diagram showing the electrochemical cell setup was presented in Figure 3.6.

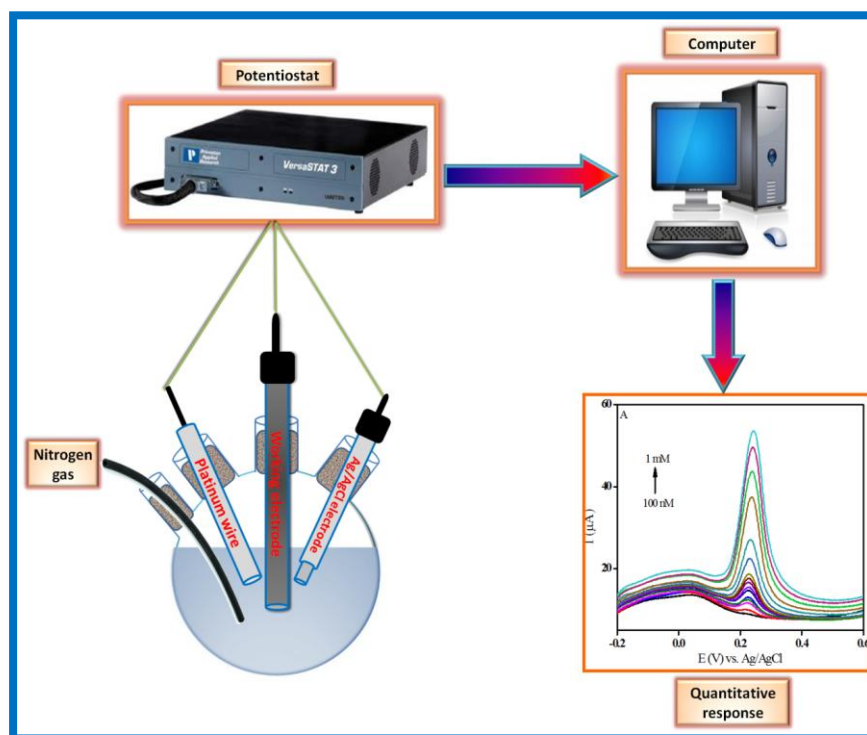


Figure 3.6: Schematic representation of the electrochemical cell setup.

From the calibration plot of current response versus concentration of analyte, the values for limit of detection (LoD) and limit of quantitation (LoQ) were calculated based on Equations (1) and (2), as follows:

$$\text{Limit of detection (LoD)} = \frac{3\sigma}{m} \quad (1)$$

$$\text{Limit of quantitation (LoQ)} = \frac{10\sigma}{m} \quad (2)$$

where σ is the residual standard deviation of the linear regression and m is the slope of the regression line (Shrivastava *et al.*, 2011).

3.4 Fabrication of Chemically Modified Electrode (CME)

The modified electrode was prepared by a simple drop-casting method. In a typical procedure, the GCE was polished with 0.05 μm alumina slurry on a polishing cloth for a few times before rinsed with DI water. Then, the electrode was undergone pretreatment by running 20 cycles of CV at potential between +1 and -1 V in 0.1 M H_2SO_4 solution. After the cleaning process, 5 μL of the as-prepared nanohybrids solution (1 mg/mL) were drop casted onto the pre-treated GCE surface and air dried at room temperature for about 30 min.

3.5 Electrochemical Sensing Techniques

In electrochemical sensor, there are a number of sensing techniques can be used to determine the interested analytes at low concentration level. In this work, we have used two different voltammetric techniques (linear sweep voltammetry (LSV), and cyclic voltammetry (CV)), three different pulse-voltammetric techniques (differential pulse voltammetry (DPV) and square wave voltammetry (SWV) and amperometric technique (chronoamperometry (CA)). It was chosen based on which sensing technique shows more sensitivity toward the detection of analytes at the modified electrode.

3.5.1 Linear Sweep Voltammetry (LSV)

Linear sweep voltammetry (LSV) technique is one of the voltammetric methods that used to identify the existence of analytes in solution. The basic principle of LSV involves in monitoring the electroanalytical current signals generated upon applying a voltage to the WE that was immersed in an electrolyte solution containing target analytes. The electrode potential was varied linearly between two limits and the scan rate was kept constant throughout the process. The result obtained from LSV was presented as a plot of oxidation or reduction current response against the applied voltage that is the potential for working electrode. The current is measured between the WE and the counter electrode. The oxidation or reduction of analyte was represented by a peak or trough in the current signal at the potential at which the species begins to be oxidized or reduced.

3.5.2 Cyclic Voltammetry (CV)

Cyclic voltammetry (CV) is one of the sensing techniques that are frequently used to detect the presence of bioanalyte in the solution due to its simple procedure. In CV, the applied potential was ramped in the opposite direction to return to the initial potential after it reached the set potential and these cycles of ramps in potential can be repeated. Basically, CV is the extension of LSV where two linear sweeps run back to back, however, CV has a few advantages over LSV. For example, CV can give more information about the chemical reactions existing at the electrode surface by observing the peaks that appeared in CV. The reversibility of a redox couple can be evaluated by determines the potential difference between the anodic and cathodic peak potential of corresponding redox couple. Moreover, CV allowing the conversion of a species back to its original form and in the same time prevents the accumulation of unwanted species due to the reverse scanning in CV.

3.5.3 Differential Pulse Voltammetry (DPV)

Differential pulse voltammetry (DPV) is one of the pulse voltammetry techniques that is highly sensitive to trace the levels of the analytes. Theoretically, the potential wave form in DPV composed of small pulses with constant amplitude normally in the range of 10 to 100 mV. These small pulses were superimposed on a slowly changing base potential. The current was sampled twice in each pulse period that is at the beginning and ending of the same pulse to permit the decay of the nonfaradaic (charging) current. The final result was displayed in a plot of the current difference between these two points for each single pulse versus base potential. The height of DPV is directly proportional to the concentration of analyte. In DPV, the species of target analytes can be identified by observing the peak potential, therefore it give advantage especially for simultaneous detection of analytes. As compared to CV, the background current in DPV is smaller because the charging current contribution is negligible. In order to increase its sensitivity and achieve lowest limit of detection, several parameters need to be optimized including the modulation amplitude, step potential, and step width.

3.5.4 Square Wave Voltammetry (SWV)

The most advanced technique in the group of pulse voltammtery technique is the square wave voltammetry (SWV). The potential wave form in SWV was made up from a superimposed of symmetrical square wave pulses with constant amplitude on a staircase wave form of step height. In this case, the forward pulse of the square wave coincides with the staircase step. The current in this technique was determined at two points, intially at the end of the forward potential pulse and then at the end of the reverse potential pulse. The current measured at these two points are known as oxidation and reduction current and the difference between these two currents was calculated to obtain the net current in SWV. This net current is directly proportional to

the concentration of the analyte which often give a lowest detection limit in the range of nanomolar, thus make it more sensitive compared to DPV. The advantage of SWV over other techniques is the speed as it allows the experiments to be performed repeatedly and increase the signal to noise ratio. Moreover, the fast technique offered by SWV enable us to study the kinetics of fast electron transfer reactions and the kinetics of rapid chemical reactions coupled to the target analytes.

3.5.5 Amperometry

The amperometry is one of the sensing techniques belongs to the family of controlled potential technique. The relatively simple technique owned by amperometry making it the most frequently used for direct determination of the analyte concentration. In amperometry, a steady state current was measured as a function of time upon applying a constant square-wave potential to the working electrode. The constant potential value was selected based on the existing well-established essential point of reference provided by CV. In this work, the point of reference will be the oxidation or reduction potential for our target analytes. The mass transfer throughout this process is solely governed by diffusion. The final data collected from amperometry will be translated in the plot of current-time (I-t) dependence. The value of peak current measured over a linear potential range is directly proportional to the bulk concentration of the analyte.

3.6 Optical Characterization Technique

3.6.1 UV-visible Absorption Spectroscopy

The UV-visible absorption spectra for the prepared samples were recorded on a Thermo Scientific Evolution 300 ultraviolet-visible (UV-Vis) absorption spectrophotometer (Figure 3.7). The sample in solution form was poured in quartz cuvettes to run the measurement which works in the range between 200 to 800 nm at

room temperature. UV-vis characterization was used to validate the chemical changes in GO after hydrothermal process to form rGO, by examining the shifting in wavelength position and its intensity. Besides that, the identification of as-prepared materials were also been made by using UV-vis characterization through comparison of the absorption spectra obtained from our samples with spectra of standard raw material. The appearance of absorption peak for rGO and metal nanoparticles in the same spectrum could be used as evidence of successful formation of nanohybrids.



Figure 3.7: Thermo Scientific Evolution 300 ultraviolet-visible (UV-Vis) absorption spectrophotometer.

3.7 Crystalline and Structural Characterization Techniques

3.7.1 X-ray Diffraction (XRD)

The crystalline structures of the powder samples were collected by X-ray diffraction (XRD; PANalytical Empyrean) with the used of copper $K\alpha$ radiation ($\lambda = 1.5418 \text{ \AA}$) at a scan rate of 0.02 sec^{-1} (Figure 3.8). The XRD pattern was formed based on the plotting of the intensity of X-rays scattered at different angles produced by a sample. It is notable that each phase of material produced unique XRD pattern, thus XRD characterization was commonly used for phase identification of a crystalline material.

The XRD data was analysed using the PANalytical X'pert Highscore software including compare the diffraction peak obtained with the standard diffraction pattern from Joint Committee on Powder Diffraction Standard (JCPDS) database in order to examine type of materials that has been produced. In this work, XRD measurements were employed mainly to confirm the existence of metal nanoparticles on the surface of the rGO sheets. The XRD pattern obtained from a composite material should contain all of the diffraction patterns produced by each material in the composite.



Figure 3.8: X-ray diffraction (XRD) from PANalytical Empyrean.

3.7.2 Raman Spectroscopy

Raman spectroscopy is a powerful technique for the characterization of carbon-based materials. The dispersion of electromagnetic radiation by molecules or atoms upon the illumination by the laser provides us information including rotational, vibrational, and other low frequency modes of molecules. Besides that, Raman characterization can also be used to identify unknown materials by matching their unique Raman spectral fingerprints with the one listed in databases of known spectra. Further study on the characterization of sp^2 and sp^3 hybridized carbon atoms to determine ordered and

disordered crystal structures of graphene were made by using Raman spectroscopy. In this work, Raman spectra of the nanohybrid were carried out by using a Renishaw inVia Raman microscope linked to the 514 nm line of an argon ion laser as the excitation source and performed at room temperature (Figure 3.9). The samples with concentration 1 mg/mL was drop casted on a cleaned glass slide and dried in oven for overnight before Raman characterization.



Figure 3.9: Renishaw inVia Raman microscope.

3.7.3 X-ray Photoelectron Spectroscopy (XPS)

In XPS, the surface of a sample was illuminated with mono-energetic x-rays which trigger the emission of photoelectron from the surface of the sample. The energy of the emitted photoelectrons was measured by using an electron energy analyzer which was recorded as a plot of intensity of a photoelectron peak versus binding energy. The elemental identity, chemical state, and quantity of a detected element can be determined using XPS. In this work, XPS was performed to obtain evidence that the metal nanoparticles were formed on rGO-Nf surfaces and also to analyze the quantity of elements and the surface electronic state of the obtained products. XPS was measured at

the beam-line, BL3.2 (a), of the Synchrotron Light Research Institute in Thailand. All samples were prepared by depositing the nanohybrid material on washed silicon substrate using the drop-casting technique.

3.8 Morphological Characterization Techniques

3.8.1 Field Emission Scanning Electron Microscopy (FESEM)

The surface morphology of the as-prepared samples were analyzed by using the field emission scanning electron microscopy (FESEM). In FESEM, a strong electric field was used to emit the electrons from the surface of a conductor and the acceleration voltages ranging from 0.5 to 30 kV was used. Compared to SEM, the image quality obtained from FESEM is better caused by the production of electron beam that is about 1000 times smaller than in a standard microscope with a thermal electron gun. Therefore, FESEM has become one of the important tools in the fields of material science for high resolution surface imaging.



Figure 3.10: FEI Nova NanoSEM 400 operated at 10.0 kV.

FESEM images were obtained by a JEOL JSM-7600F operated at 10.0 kV and the energy dispersive x-ray spectroscopy (EDX) analysis was also done along with FESEM to confirm the composition of the materials (Figure 3.10). The nanohybrid materials were drop-casted on a silicon wafer, which was used as the substrates for FESEM characterization and dried in oven for overnight.

3.8.2 High Resolution Transmission Electron Microscopy (HRTEM)

The morphology and structural features of the nanohybrids were elucidated by using the high resolution transmission electron microscopy (HRTEM). HRTEM is a powerful technique used in material science for analyzing the quality, surface structure, shape, and size of a material. Since HRTEM provides high resolution images at atomic scale level, the crystal structure and features in the structure such as dislocations and grain boundaries can also be observed. This is allowed to analyze the lattice imperfections in materials on an atomic resolution scale such as point defects and stacking faults.



Figure 3.11: FEI Tecnai G2 F20 X-TWIN TEM.

HRTEM images were obtained by FEI Tecnai G2 F20 X-TWIN Transmission Electron Microscope (TEM) operated at 200 kV (Figure 3.11). The nanohybrid materials were drop casted on a lacey carbon copper grid which was used as the substrates for HRTEM. I-solution software was used to measure the size of metal nanoparticles and its lattice spacing.

3.9 Electrochemical Characterization

3.9.1 Electrochemical Impedance Spectroscopy (EIS)

The electrochemical impedance spectroscopy (EIS) was used for the characterization of each modified electrode surface in order to clarify the differences among the electrochemical behaviour. Any intrinsic material property or specific processes that could influence the conductivity, resistivity or capacitance of an electrochemical system and it can be studied by EIS technique (Grieshaber *et al.*, 2008). In general, electrochemical impedance is the response of an electrochemical system to an applied potential which usually displayed in Nyquist plot and also can be presented as a Bode plot. The frequency dependence of this impedance can reveal underlying chemical processes that happen at the electrode/electrolyte interface. There are several parameters relevant to impedance could be obtained such as electrolyte resistance, double layer capacitance, charge transfer resistance and diffusion (Sekar *et al.*, 2013). The EIS experiment was performed at a PAR-VersaSTAT 3 electrochemical work station using a conventional three electrodes system. It was carried out in a solution containing 5 mM $K_3[Fe(CN)_6]$ and 0.1 M KCl within the frequency range from 0.01 Hz to 100 KHz. From the Bode plot obtained, the electron recombination lifetime was calculated based on the Equation (3):

$$\tau_n = 1/2\pi f_{max} \quad (3)$$

where τ_n is the electron recombination lifetime and f_{max} is the frequency peak.



Figure 3.12: PAR-VersaSTAT 3 electrochemical work station.

3.9.2 Voltammetry Technique

Another useful electrochemical technique used to characterize electrode material is cyclic voltammetry (CV). CV is a common electrochemical technique conducted in order to study the electrochemical reaction mechanisms that generate the electroanalytical current signals. These involve the mechanism of redox system (oxidation or reduction process) and transport properties of an electroactive species in solution. Moreover, several important informations can be gained by varying the concentration of analytes and scan rate including the number of electrons transferred in the redox process (n); the diffusion coefficient (D), the electroactive surface area, and electrochemical reversibility. The electrochemical experiments were performed with a VersaSTAT 3 by Princeton Applied Research using a conventional three electrodes system. The modified GCE was used as the WE, a platinum wire served as a counter electrode and Ag/AgCl and saturated calomel electrode (SCE) was used as a reference electrode. A solution containing 5 mM $K_3[Fe(CN)_6]$ and 0.1 M KCl was used as the

electrochemically reversible redox system. Based on the CV that obtained for different scan rate, the heterogeneous electron transfer rate constant (k_s) was further estimated from the following Equation (4):

$$\log k_s = \alpha \log(1 - \alpha) + (1 - \alpha) \log \alpha - \log\left(\frac{RT}{nFv}\right) - \alpha(1 - \alpha) \frac{nF\Delta E_p}{2.3RT} \quad (4)$$

where α is the charge transfer coefficient; n is the number of electron transfers; R is the ideal gas constant; T is the temperature in Kelvin; F is the Faraday constant; and ΔE_p is the peak-to-peak potential separation.

For diffusion controlled electrochemical process, the diffusion coefficient (D) can be calculated by using the Randles Sevcik Equation (5):

$$I_p = 0.4463 nFAC \sqrt{\frac{nFD}{RT}} \sqrt{v} \quad (5)$$

Therefore, the slope of graph peak currents versus square root of scan rate

$$= 0.4463 nFAC \sqrt{\frac{nFD}{RT}} \quad (6)$$

where, I_p is the peak current, n is the number of electrons, F is the Faraday constant (9.65×10^4 C/mol), T is the temperature in Kelvin, R is the gas constant ($8.314 \text{ JK}^{-1} \text{ mol}^{-1}$), A is the surface area of the electrode (cm^2), D is the diffusion coefficient ($\text{cm}^2 \text{ s}^{-1}$), and C is the concentration of the analytes (mol/cm^3).

CHAPTER 4

REDUCED GRAPHENE OXIDE-NAFION NANOHYBRID MODIFIED ELECTRODE FOR ELECTROCHEMICAL DETECTION OF DOPAMINE AND NITRIC OXIDE

4.1 Introduction

Dopamine (DA) is an important biomolecule. It is formed by the decarboxylation of DOPA and is a precursor of two other neurotransmitters; adrenaline and noradrenalin. DA is a well-known catecholamine neurotransmitter of the human central nervous system and brain. It controls the brain's reward and pleasure centers as well as helps to regulate movement and emotional responses. In addition, DA plays a vital role in the functioning of the central nervous, cardiovascular, renal and hormonal systems (Lévesque *et al.*, 2007). An abnormal DA level in the brain causes several disease conditions, such as pleasurable, rewarding feelings and sometimes even euphoria. Meanwhile, a deficiency of DA in the brain may lead to neurological disorders, such as schizophrenia and Parkinson's disease (Cederfjäll *et al.*, 2013). Selvaraju *et al.* (Selvaraju *et al.*, 2003a, 2003b; Selvaraju *et al.*, 2005; Selvaraju *et al.*, 2014) and Abraham John and his coworkers (Kalimuthu *et al.*, 2009; Raj *et al.*, 2013; Revin *et al.*, 2012) extensively investigated the electrochemical detection of DA in the presence of many interference such as ascorbic acid (AA), uric acid (UA), tyrosine (Tyr), methionine (Met) and serotonin (5-HT).

Where else, nitric oxide (NO) is a hydrophobic, highly labile free radical that is naturally produced within the human body and plays a vital role in a wide range of biological and cellular functions. NO is used for communication in between cells and

involve in the regulation of blood pressure, the immune response, platelet aggregation and clotting, neurotransmission and possibly respiration (Bredt *et al.*, 1992; Burnett, 1997). Abnormal NO production and bioavailability may cause several diseases such as obesity, diabetes (both type I and II), atherosclerosis, hypertension and heart failure (Napoli *et al.*, 2001; Petros *et al.*, 1991). Thus, the development of sensor for the precise and selective measurement of NO that appears to be in low level within living systems can make a great contribution to disease diagnosis.

Several methods have been reported to detect DA and NO, including chemiluminescence (Beckman *et al.*, 1995), paramagnetic resonance spectrometry (Wennmalm *et al.*, 1990), paramagnetic resonance imaging spectrophotometry (Kuppusamy *et al.*, 1996) and bioassay (Wallace *et al.*, 1995). Among these methods, the electrochemical detection of DA and NO is the only available technique sensitive enough to detect relevant concentrations of DA and NO in real time and *in vivo*. Electrochemical biosensor has a series of advantages such as high sensitivity towards electroactive species, rapid and accurate response and most importantly it is portable and inexpensive compared to other existing biosensor. Moreover, this technique is also highly selective toward DA and NO in the presence of interfering species such as nitrite, nitrate, AA, UA and L-arginine.

A variety of materials have been reported to have potential as electrochemical sensors, including organic conjugated polymer (Mulchandani *et al.*, 1995; Mulchandani *et al.*, 1996), metal and semiconductor nanoparticles (Yin *et al.*, 2011) and carbon nanomaterials (Shah *et al.*, 2013). Among the carbon nanomaterials, graphene has been widely explored in the fabrication of electrochemical sensors, and especially biosensor, because of its fascinating two dimensional conjugated structures and unique properties

such as a high conductivity (Li *et al.*, 2009), high electrocatalytic activity (Wang *et al.*, 2010) and large surface area (Reina *et al.*, 2008). These properties give graphene an advantage as a sensor. For example, Zhou *et al.* has successfully fabricated the chemically reduced graphene oxide-modified GCE (CR-GO/GC) for the detection of inorganic and organic electroactive compounds (H_2O_2 , NADH, DA, AA, UA, glucose) (Zhou *et al.*, 2009). Their research has proved that CR-GO demonstrated favourable electrochemical activity which extremely attractive for a wide range of electrochemical sensing and biosensing applications. Moreover, the potential sensor application of graphene cooperated with metal such as platinum (Pt) were also been studied by some researchers. In 2011, Sun *et al.* have studied the simultaneous electrochemical detection of AA, DA and UA at the glassy carbon electrode modified by graphene-Pt nanocomposite (Sun *et al.*, 2011). The observed results show that this new nanocomposite posses a great potential as electrochemical biosensors.

Up to date, the hybridization of graphene with a polymer has attracted wide attention because this graphene-based polymer composite has remarkable electrocatalytic, mechanical, electrical and thermal properties. Many polymers have been used to synthesize graphene/polymer composites. For example, Liu and co-workers (Liu *et al.*, 2014) developing a poly(o-phenylenediamine) (PoPD)/graphene hybrid composite using electropolymerization technique which performed on the graphene/GCE for the detection of DA in human urine samples. This modified electrode has a detection limit of 7.5 mM. Meanwhile, Han and his co-workers (Han *et al.*, 2010) has synthesize chitosan-graphene composite by a together-blending and in situ chemical reduction method to modify a GCE for DA sensor. The simultaneous detection of DA in the presence of AA and UA shows a detection limit of 1 μM . Thus, this study focused on the synthesis of a reduced graphene oxide-based polymer composite with Nf. Nf is a

conductive polymer, which is important in enhancing the properties of the hybrid material. It also acts as a dispersant for graphene because of its perfluoroalkyl backbone, which has a higher hydrophobicity and leads to a stronger interaction with graphene. In addition, Nf has advantages as an electrode modifier because it possesses an excellent antifouling capacity, high permeability to cations and strong adsorption ability (Nigović *et al.*, 2014b).

Herein, we report a selective and sensitive electrochemical sensing platform based on hydrothermally prepared rGO-Nf nanohybrid modified electrode toward the detection of DA in the presence of AA and UA. The influences of experimental parameters such as hydrothermal process time, scan rate and pH of the electrolyte on electrocatalytic performance were also investigated. To the extent of our knowledge, there is little research focused on the rGO-Nf nanohybrid materials for the electrochemical detection of NO with a lowest detection limit. In this present work, the novel rGO-Nf nanohybrid was also employed as a sensing electrode material in an electrochemical sensor to study its sensitivity and selectivity toward NO. The electrochemical signal obtained from the NO sensor could be optimized by controlling the loading volume of the material on the electrode surface. The interference of AA and DA during the determination of NO was also studied. The high sensitivity and selectivity of the rGO-Nf nanohybrid modified electrode could make them a suitable candidate for detection of a wide range of biomolecules in biosensor.

4.2 Results and Discussion

4.2.1 Optical Characterization of rGO-Nf Nanohybrids

The absorption spectra of the as-prepared samples were measured and their results were shown in Figure 4.1. As can be seen from Figure 4.1(i), the GO exhibits a strong

absorption peak at 230 nm and a shoulder at around 300 nm due to the $\pi \rightarrow \pi^*$ transitions of aromatic C-C bonds and the $n \rightarrow \pi^*$ transition of the C=O bonds (carbonyl groups), respectively. Meanwhile, the Nf shows an absorption peak at 190 nm (Figure 4.1(ii)) that could be assigned to the C=C bonds that are produced during the polymerization or modification reactions of Nf with water during ultrasonication (De Almeida *et al.*, 1997). After the hydrothermal treatment of the rGO-Nf for different duration of time, the absorption peaks occurred at ~190 and ~261 nm, due to the Nf and rGO, respectively (Figure 4.1(iv-vi)). Upon the hydrothermal treatment, the GO peak red-shifted to 261 nm, which suggests the effective restoration of the sp^2 carbon networks (C=C bonds) within the sheets. Moreover, this bathochromic shift further confirmed that the GO had been reduced to rGO during hydrothermal treatment.

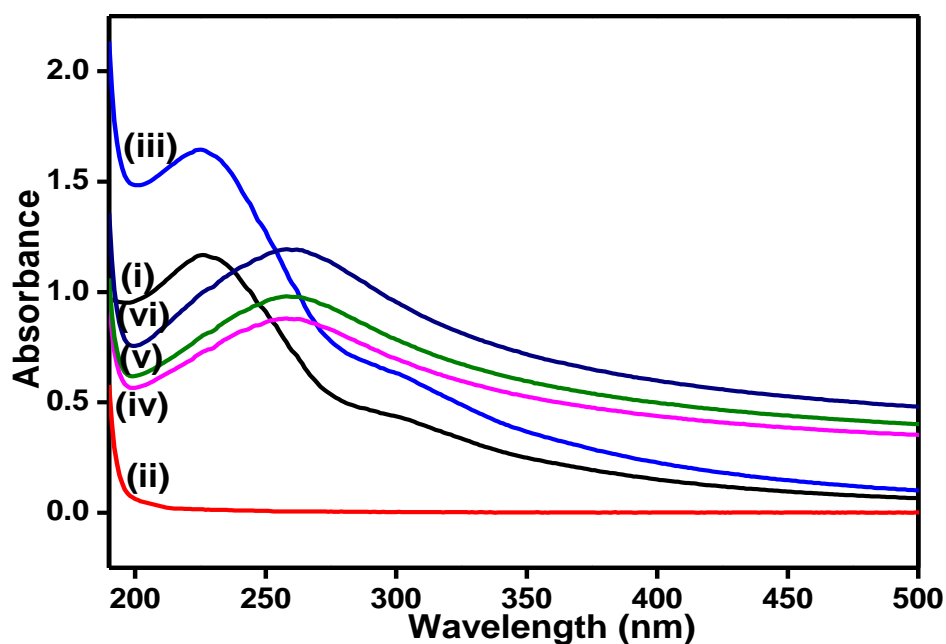


Figure 4.1: UV-vis absorption spectra of prepared (i) GO, (ii) Nf, (iii) GO-Nf, (iv) rGO-Nf (8 h), (v) rGO-Nf (16 h) and (vi) rGO-Nf (24 h) nanohybrids.

As shown in Figure 4.2(A), the photoluminescence (PL) spectra for an aqueous solution of GO possess a broad emission peak at around 590 nm on excitation wavelength of 325 nm. The emission peak at longer wavelength is a result of significant

number of disorder-induced defect state within $\pi \rightarrow \pi^*$ transition possess by GO (Chuang *et al.*, 2014). After hydrothermal process, the PL spectra of all three rGO-Nf nanohybrids were blue shifted to 416 nm as shown in Figure 4.2(B). This result demonstrated that the number of sp^2 domains in reducing GO has increased, hence proving the successful of reduction process. Moreover, the position of the emission peak was similar as previously reported by Liu *et al.* which indicate the formation of graphene quantum dots (Liu *et al.*, 2014).

The increases in degree of reduction of GO result in more shifted toward shorter wavelength due to the increase number of sp^2 domain (Chuang *et al.*, 2014). Therefore, rGO-Nf (16 h) nanohybrid has the highest degree of reduction as its peak shifting to the shortest wavelength. Besides that, one can find that the intensity of PL spectra decrease in order of: rGO-Nf (24 h) > rGO-Nf (8 h) > rGO-Nf (16 h). The PL emission is the result of the recombination of excited electrons and holes. Thus, the recombination rate of electrons and holes will affect the PL intensity. In general, a lower recombination rate for photogenerated electron and hole pairs will result in a lower PL intensity and thus possess higher photocatalytic activity (Hu *et al.*, 2010; Kim *et al.*, 2012). Therefore, the rGO-Nf (16 h) nanohybrid is believed to show great sensing performance due to high photocatalytic activity.

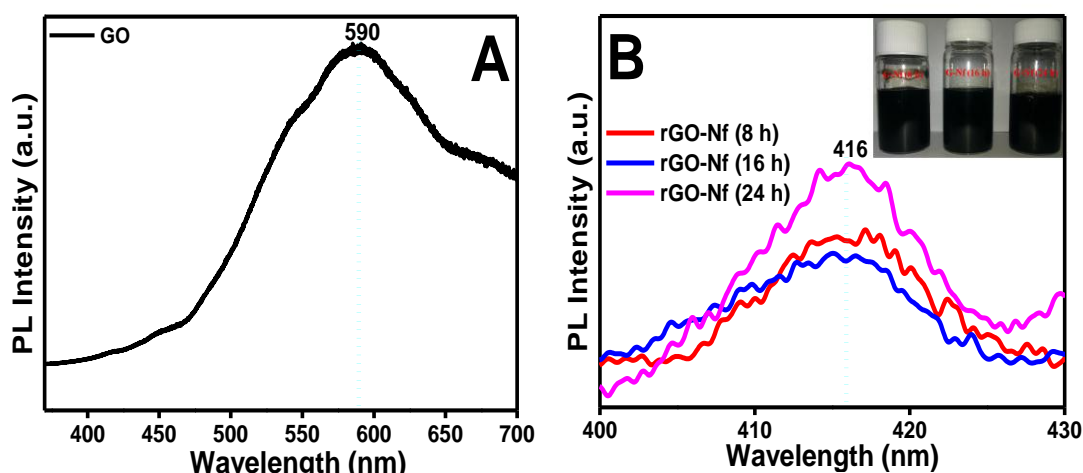


Figure 4.2: PL spectra of (A) GO and (B) three different rGO-Nf nanohybrids.

4.2.2 Structural Characterization of rGO-Nf Nanohybrids

The Raman spectra of GO and three different rGO-Nf nanohybrids were shown in Figure 4.3. Generally, the two of the most representative features of graphene could be detected from its Raman spectrum, namely the D and G bands. It has been reported that the D peak corresponds to the defects and disorder activated Raman mode arising from the vibrations of sp^3 carbon atoms, while the G peak arises from sp^2 hybridized carbon atoms in a graphitic 2D hexagonal lattice (Ferrari *et al.*, 2006). It can be seen in the Raman spectra for GO and the others that there were two prominent peaks at 1355 and 1595 cm^{-1} , which correspond to the D and G bands, respectively. The G band has slightly shifted to 1600 cm^{-1} for the rGO-Nf nanohybrids, which indicates the existence of a charge transfer between the graphene and Nf (Liu *et al.*, 2009), thus confirming the formation of rGO-Nf nanohybrids. It has been reported that the intensity ratio of the D and G bands will give information on the establishment of sp^2 hybridization and deoxygenation (Nyoni *et al.*, 2014).

From the Raman spectra, the I_D/I_G ratio for GO was 0.87, which markedly increased to 0.99 for rGO-Nf upon 8 h of hydrothermal treatment. This increase indicates the formation of the graphene lattice, which contained structural defects due to the decreases in the average size of the sp^2 domains as a result of the hydrothermal treatment (Mehrali *et al.*, 2014). Moreover, it reflects an increase in disorder after being hybridized with the Nf, and the I_D/I_G ratio further decreased to 0.97 after 16 h of hydrothermal treatment. This result was attributed to the further reduction of rGO and the lower concentration of defects due to the restoration of the majority of the conjugate structure in the rGO-Nf (16 h) nanohybrid as a result of the longer hydrothermal treatment. However, the I_D/I_G ratio for rGO-Nf (24 h) slightly increased to 1.03. This might indicate that a longer thermal exfoliation would form stacks of rGO, which would

increase the defects and disordered structure. These results also confirmed that the degrees of reduction and defectiveness of the rGO were varied by employing different times for the hydrothermal treatment during their fabrication (Liu *et al.*, 2013).

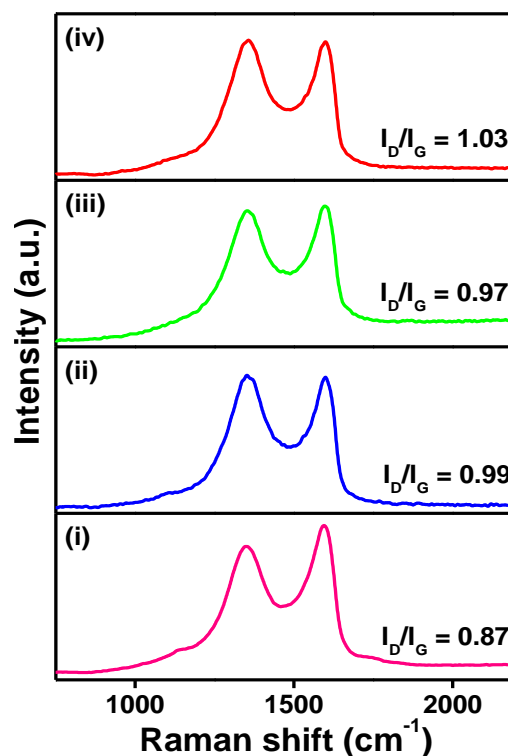


Figure 4.3: Raman spectra that obtained for the (i) GO, (ii) rGO-Nf (8 h), (iii) rGO-Nf (16 h) and (iv) rGO-Nf (24 h) nanohybrids.

X-ray photoelectron spectroscopy (XPS) was employed to confirm the formation of nanohybrid in between rGO and Nf. The XPS C1s spectra of rGO, Nf, and three different rGO-Nf nanohybrids were shown in Figure 4.4. Curve fitting of the C1s spectra for rGO and Nf were performed using a Gaussian peak shape after performing a polynomial background correction. A main peak at binding energy of 284.8 eV can be observed in the C1s XPS spectra of rGO that can be fitted by four Gaussian components at 284.8, 286.6, 288.3 and 289.3 eV and thus assigned to C-C, C-O, C=O and O=C-O species, respectively (Figure 4.4(A)) (Choi *et al.*, 2012). Meanwhile, the peak at 291.4 eV which corresponded to the C-F group of Nf appeared in the C1s XPS spectra of Nf (Figure 4.4(B)) (Zhang *et al.*, 2008). This peak can be fitted to three components that

centered at 289.2, 291.4, and 293.8 eV correspond to OCFSO₂, CF₂ and CF₃ in Nf, respectively.

As can be seen in Figure 4.4(C), the C1s XPS spectrum of all three nanohybrids contained two prominent peaks at binding energy of 284.8 and 291.4 eV which were assigned to the C-C and C-F groups, respectively. The sp^2 carbon network of rGO was retained in all three nanohybrids, as indicated by the presence of C-C peak. This indicates that Nf and rGO presence in the nanohybrids, thus confirmed the successful formation of rGO-Nf nanohybrids via hydrothermal reaction. One can notice that the graphitic C-C species were dominant after reduction except for rGO-Nf (8 h) nanohybrid, as can be seen in **Figure 4.4(C(i))**. The appearance of C-C peak in rGO-Nf (8 h) nanohybrid that is broader than other nanohybrids may result from a quite high contribution of the oxygenated carbons as compared to other nanohybrids, indicating that deoxygenation has partially occurred at the carbon surface.

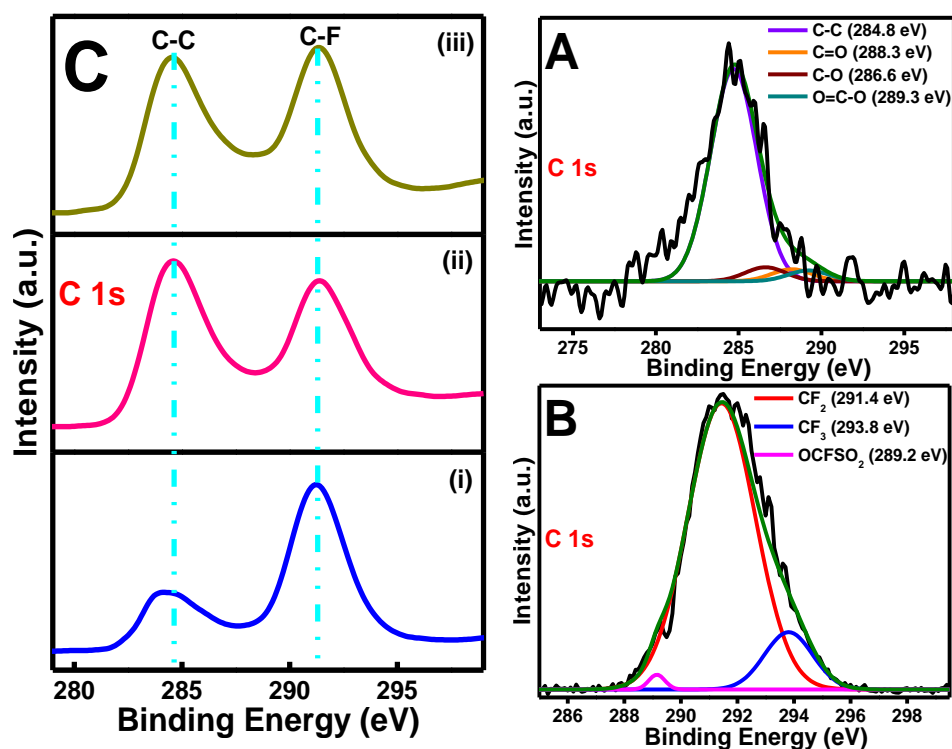


Figure 4.4: C1s XPS spectra for the (A) rGO, (B) Nf and (C) three different nanohybrids; (i) rGO-Nf (8 h), (ii) rGO-Nf (16 h) and (iii) rGO-Nf (24 h) nanohybrids.

4.2.3 Morphological Characterization of rGO-Nf Nanohybrids

The morphology and structural features of the rGO-Nf nanohybrids were elucidated by using FESEM. Figure 4.5 reveals the typical FESEM images of GO and three different nanohybrids. A sheet-like structure with wavy wrinkles on the surfaces can be observed from FESEM images of GO as shown in Figure 4.5(A). This corrugation of the GO sheets was attributed to the disruption of the planar sp^2 carbon sheets by the introduction of sp^3 -hybridized carbon upon oxidation (Wang *et al.*, 2009). Meanwhile, the FESEM images that obtained from three different rGO-Nf nanohybrids were shown in Figure 4.5(B) to (D) and we can notice that the images show more crumple and rougher surfaces. This result indicates that Nf was successfully inserted into rGO sheets, hence forming the nanohybrids. However, there is no obvious difference between all three samples; therefore, to get clearer picture on the morphology of rGO-Nf nanohybrids, HRTEM has been conducted.

Figure 4.6 shows the HRTEM images of the GO and rGO-Nf nanohybrids, where we can clearly see the flake-like shapes. The GO flakes possess an average lateral dimension of more than 1.5 μm , with wavy wrinkles on their surfaces. They possess more sp^3 carbon atoms and have defects, as shown in Figure 4.6(A). According to Figure 4.6(B-D), it can be observed that the rGO with the Nf layer coating has a rough surface, with an average diameter of approximately 18 nm. The lack of unchanged in the average diameter of rGO may be due to the use of the same sonication time before hydrothermal treatment. The thickening and roughening of the rGO-Nf nanohybrids suggest that Nf chains were successfully grafted on the rGO. However, the distribution of rGO was different upon a different period of hydrothermal treatment. The rGO tended to stack together to form agglomerations after 24 h of hydrothermal treatment as compared to 8 and 16 h, after which it looked more well distributed. This result

confirmed the higher defects detected in the Raman spectra for the rGO-Nf (24 h) nanohybrid, as indicated by the lower I_D/I_G ratio.

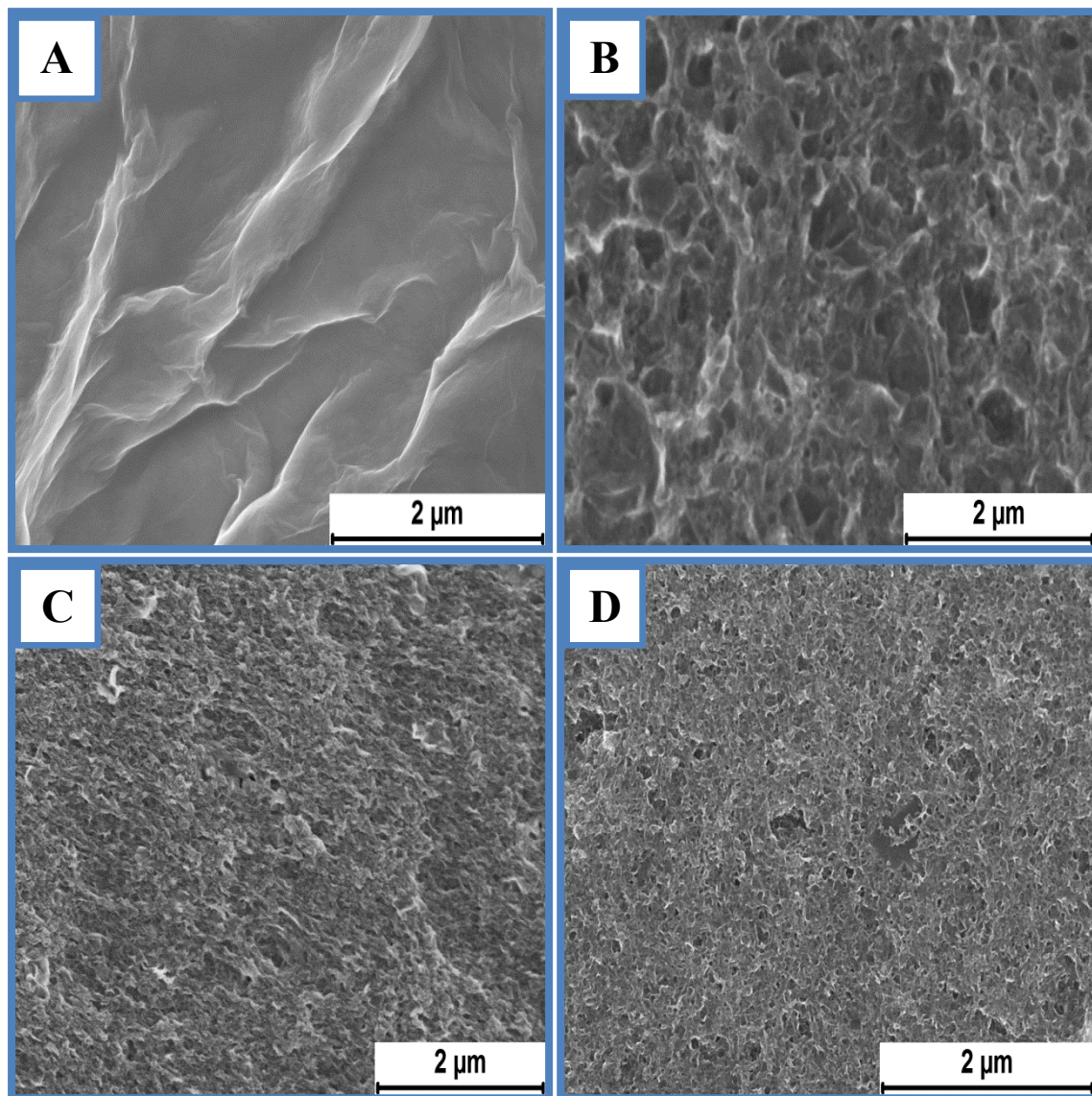


Figure 4.5: FESEM images of (A) GO, (B) rGO-Nf (8 h) nanohybrid, (C) rGO-Nf (16 h) nanohybrid and (D) rGO-Nf (24 h) nanohybrid.

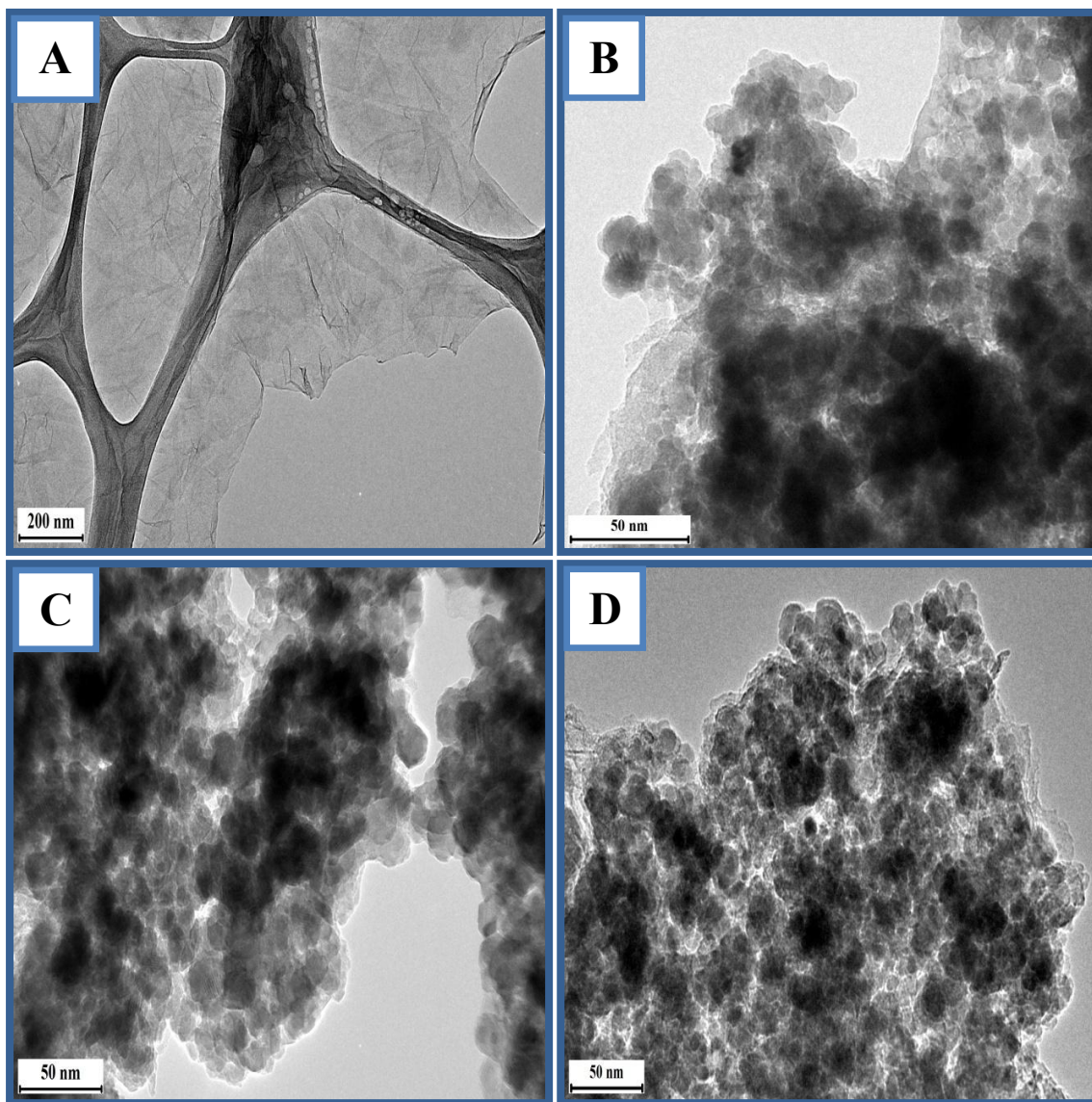


Figure 4.6: HRTEM images of (A) GO, (B) rGO-Nf (8 h) nanohybrid, (C) rGO-Nf (16 h) nanohybrid and (D) rGO-Nf (24 h) nanohybrid.

Figure 4.7 presents AFM phase contrast images of the rGO-Nf nanohybrids (top row), along with three-dimensional views of the same surfaces (bottom row). The heights of the samples are represented by different color codes from dark to bright, which show the rough surfaces of the as-obtained rGO-Nf nanohybrids. The rGO-Nf (8 h) appeared to be built up from a few larger flakes of graphene that stacked together to form thicker flakes, as visualized by Figure 4.7(A). The stacking of a few layers of graphene sheets might cause an increase in the thickness of the sample. As the

hydrothermal processing time increases to 16 h, the rGO-Nf nanohybrid appears to be highly uniform with a smaller size and height compared to the rGO-Nf (8 h) hybrid (Figure 4.7(B)). In addition, the 3D view reveals a good smoothness on the surface, which demonstrates a uniform distribution. However, after 24 h of hydrothermal treatment, the nanosized graphene tended to combine together and form agglomerations which then led to an increase in thickness of the surface roughness, as shown in Figure 4.7(C).

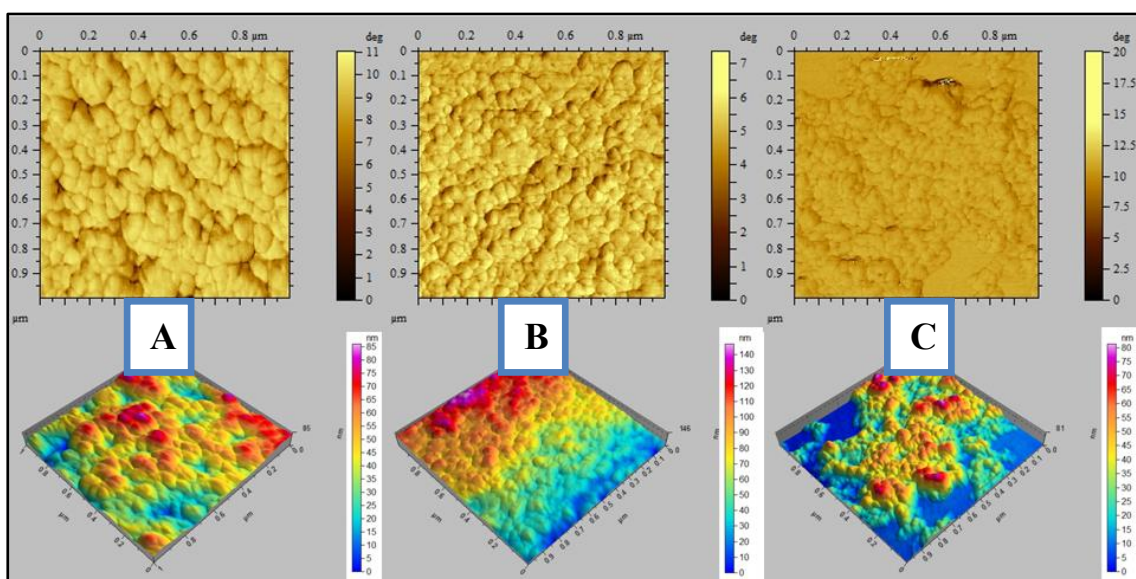


Figure 4.7: AFM phases and 3D topographic images of rGO-Nf nanohybrids obtained after hydrothermal treatment periods of (A) 8 h, (B) 16 h and (C) 24 h.

4.2.4 Electrochemical Characterization of GC/rGO-Nf Modified Electrode

The electrochemical properties of the GC/rGO-Nf modified electrodes were characterized by using CV and electrochemical impedance spectroscopy (EIS). Figure 4.8(A) depicts a series of CV plots that obtained for rGO-Nf nanohybrids with different hydrothermal processing times in 0.1 M KCl containing 5 mM $K_3[Fe(CN)_6]$. The CV plots for the rGO-Nf (8 h), rGO-Nf (16 h) and rGO-Nf (24 h) nanohybrids show a quasi-reversible redox reaction with peak-to-peak separations of approximately 150 mV, 99 mV and 170 mV, respectively. The redox peak current increased in the

following order: rGO-Nf (24 h) < rGO-Nf (8 h) < rGO-Nf (16 h). It can be noticed that the redox peak current of the GC/rGO-Nf (16 h) modified electrode was higher than other modified electrodes. The high peak current and small peak-to-peak separation indicated that the electron transfer rate of the GC/rGO-Nf (16 h) modified electrode was promoted (Lee *et al.*, 2013) and the effective surface area was increased.

Figure 4.8(B) presents the Nyquist plot recorded for GCE and three other GC/rGO-Nf modified electrodes. The Nyquist plot for the bare GCE shows the existence of one semicircle in the high frequency range with an inclined line in the low frequency range. In general, the diameter of the semicircle represents the charge transfer resistance (R_{ct}), whereas the inclined straight line can be considered to be the impedance attributed to the diffusion of ions through the graphene sheets (Jiang *et al.*, 2014). The Nyquist plot for GC/rGO-Nf (24 h) also consists of one semicircle with an inclined straight line. However, the diameter of the semicircle for GC/rGO-Nf (24 h) was smaller than that of the bare GCE, which demonstrated that the R_{ct} value decreased when the rGO-Nf (24 h) was coated on the bare GCE surface. The R_{ct} values for GC/rGO-Nf (8 h) and GC/rGO-Nf (16 h) were close to zero, which suggest that rGO-Nf possessed the ability to accelerate the electron transfer between the electrochemical probe $[\text{Fe}(\text{CN})_6]^{3-/4-}$ and the electrode surface with a higher rate (Xi *et al.*, 2012). The uniform distributions of rGO-Nf (8 h) and rGO-Nf (16 h) nanohybrids on the GCE surface may produce a better electrical contact, and thus enhance the electrical conductivity compared to rGO-Nf (24 h), which tended to agglomerate (based on the HRTEM results). The equivalent electrical circuit used for fitting the impedance spectra was shown in the inset of Figure 4.8(C). This circuit consists of an active electrolyte resistance (R_s) that is in series with the parallel combination of R_{ct} and a constant phase element (CPE).

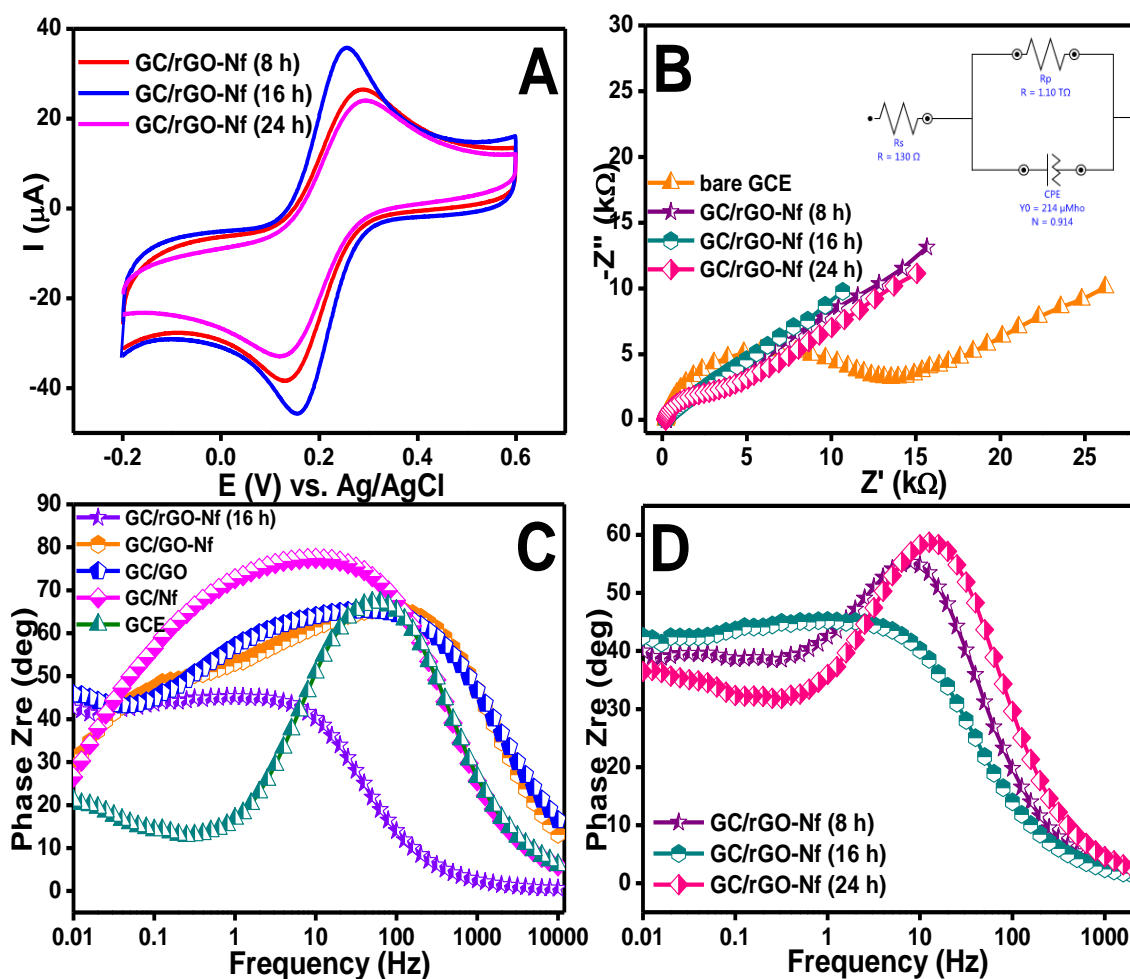


Figure 4.8: (A) CV and (B) Nyquist plots of electrochemical impedance spectroscopy (EIS) for bare GCE and GC/rGO-Nf nanohybrids with different hydrothermal processing times obtained in presence of 0.1 M KCl with 5 mM $K_3[Fe(CN)_6]$, (Inset shows the electrical equivalent circuit that fit the Nyquist plot of GC/rGO-Nf (16 h)) and (C and D) bode plots obtained for different modified electrodes.

Figure 4.8(C) shows the Bode plots of the phase angle versus frequency for the bare GCE, GC/Nf, GC/GO, GC/GO-Nf and GC/rGO-Nf (16 h). Bare GCE shows a sharp peak at higher frequency, which gives an indication of a higher R_{ct} value. This peak started to broaden when we coated the GCE surface with Nf, GO, GO-Nf and rGO-Nf (16 h). This showed a lower resistance when the charges were transferred, which improve the electrical conductivity. Figure 4.8(D) displays the Bode plots obtained from GC/rGO-Nf (8 h), GC/rGO-Nf (16 h) and GC/rGO-Nf (24 h). It is noticed that the peak

at a higher frequency started to shift to a lower frequency following the order of GC/rGO-Nf (24 h) < GC/rGO-Nf (8 h) < GC/rGO-Nf (16 h). The values of the corresponding electron recombination lifetime; τ_n of GC/rGO-Nf (24 h), GC/rGO-Nf (8 h) and GC/rGO-Nf (16 h) could be calculated to be 9.05, 20.04 and 31.76 ms, respectively. These results demonstrate that rGO-Nf (16 h) has the longest electron recombination lifetime, which shows its application potential for electrocatalysis, photoelectrochemical cells, and solar cells (Yeh *et al.*, 2012).

4.2.5 Electrochemical Determination of Dopamine

4.2.5.1 Electrocatalytic Oxidation of Dopamine

CV curves were recorded for the different modified electrodes in the presence of DA to determine the best sensor electrode for the electrochemical detection of DA. The CV characteristics of bare GCE, GC/GO, GC/Nf, GC/GO-Nf and three different GC/rGO-Nf modified electrodes were recorded in a 0.1 M PBS (pH 6.5) solution containing 100 μ M DA at a scan rate of 100 mV/s, and the results were shown in Figure 4.9. We can see that a pair of redox peaks appears for all the samples. Among these, the GC/rGO-Nf (16 h) modified electrode showed an excellent electrochemical response towards the oxidation of DA with a higher current as compared to the other electrodes. The response for the GC/rGO-Nf modified electrode toward DA was about five to six times greater than that of GC/GO-Nf. This enhanced electrocatalytic activity due to the rapid electron transfer process was confirmed by the lower peak to peak potential separation (ΔE_p), which was calculated to be 36.80 mV. Hence, the rGO-Nf (16 h) nanohybrid will be chosen as the sensor electrode for further study of DA sensing.

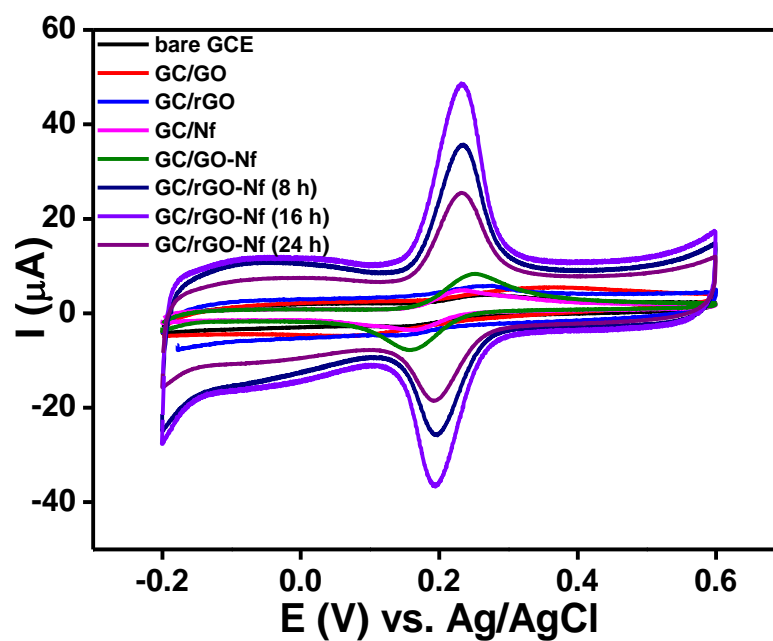


Figure 4.9: CV curves obtained for bare GCE, GC/GO, GC/Nf, GC/GO-Nf and three different GC/rGO-Nf modified electrodes in presence of 0.1 M PBS (pH 6.5) solution containing 100 μ M DA at a scan rate of 100 mV/s.

An electrocatalytic mechanism is proposed in Figure 4.10 to understand the reaction process that occurs at the GC/rGO-Nf modified electrode.

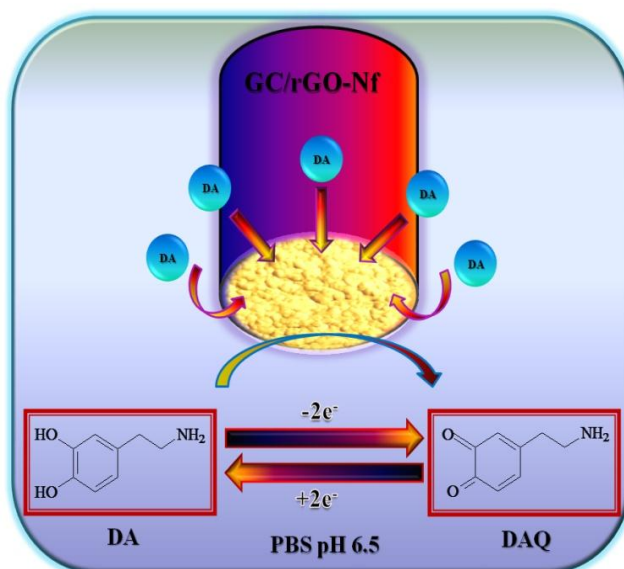


Figure 4.10: Schematic representation of detection of DA at GC/rGO-Nf modified electrode.

It is well known that DA can easily be oxidized electrocatalytically to produce dopamine-quinone (DAQ) at a conventional electrode. Under the optimized condition, DA was easily oxidized to form DAQ after the exchange of equal amounts of electrons and protons upon the application of a potential to the GC/rGO-Nf modified electrode. Later, a faradaic current was produced as a result of the donation of these electrons to the modified electrode (Huang *et al.*, 2012). The higher current response occurs due to the possible electrostatic attraction between the DA cation and the negative surface of the rGO-Nf nanohybrid materials that deposited on the modified electrode.

The GC/rGO-Nf (16 h) modified electrode showed the highest current response toward the oxidation of DA compared to the other modified electrodes because of the good synergistic effects between the rGO and Nf, which resulted in the a electronic conductivity and DA accessibility. The electron density in the plane of graphene was changed by the electron withdrawing groups of Nf ($-\text{CF}_2$ and $-\text{SO}_3^-$) using p-type doping, which moved the Fermi level towards the valence band (Aragaw *et al.*, 2013). The conductivity of the rGO in the hybrid material increased due to the movement of the Fermi level, which facilitated the electron transfer rate between the DA and the surface of the electrode, showing an excellent electrochemical performance.

4.2.5.2 Optimization Studies

(a) *Effect of Different Concentration of Dopamine*

The redox behavior of DA at different concentration was investigated by using CV in 0.1 M PBS (pH 6.5) at a scan rate of 50 mV/s with the intention of to study the electrochemical performance of the GC/rGO-Nf (16 h) modified electrode. It is evidenced from Figure 4.11(A) that the peak currents of DA increased linearly with the increase of concentrations over the range of 10 to 350 μM . As shown in Figure 4.11(B),

the calibration equation of DA was obtained in the range of 10 to 350 μM : $I_p(\mu\text{A}) = 0.0768 [\text{DA}](\mu\text{M}) + 8.168 \mu$ with correlation coefficient of $R^2 = 0.9907$. This result indicates that the GC/rGO-Nf (16 h) modified electrode exhibits a good linear behavior for DA in the examined concentration range.

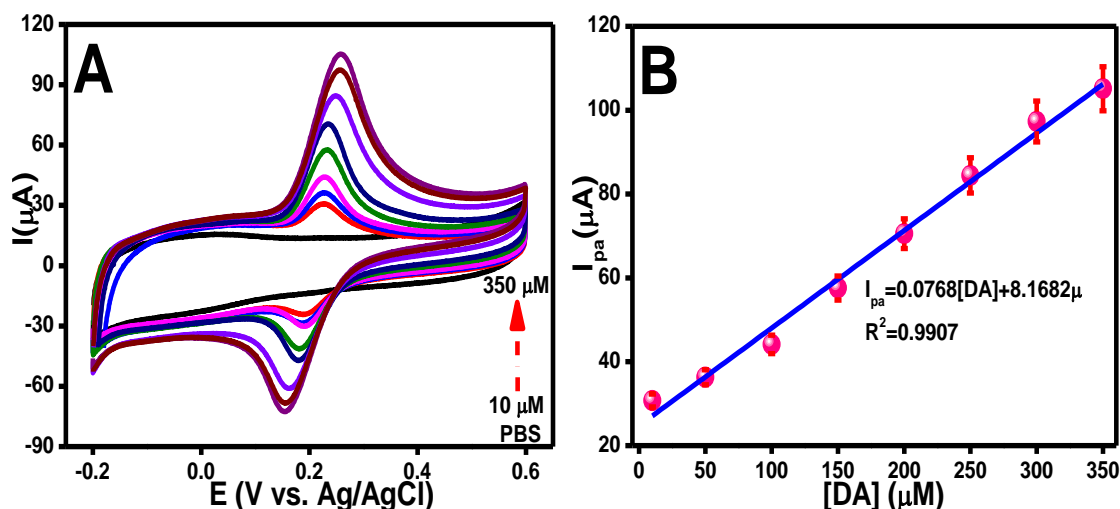


Figure 4.11: (A) CV curves obtained for the GC/rGO-Nf (16 h) modified electrode in the presence of 0.1 M PBS (pH 6.5) and different concentration of DA (10 to 350 μM) at a scan rate of 50 mV/s and (B) linear relationship between I_{pa} and the concentration of DA.

(b) Effect of Scan Rate

The influence of the scan rate on the electrochemical performance of the GC/rGO-Nf (16 h) modified electrode toward DA was investigated, and the results are depicted in Figure 4.12(A). The anodic peak was positively shifted with an increase in the scan rate, and it showed good linearity between the peak current and scan rate in the range of 10 to 500 mV/s (Figure 4.12(B)). The anodic and cathodic peak currents followed the linear equations of $I_{pa} = 0.317v + 8.604$ and $I_{pc} = -0.312v - 2.721$ with regression coefficient (R^2) values of 0.994 and 0.996, respectively. These results confirmed that the direct electron transfer between the rGO-Nf and DA was mainly controlled by an adsorption process (Dessie *et al.*, 2014). The kinetic parameters

α_c (cathodic transfer coefficient) and α_a (anodic transfer coefficient) were obtained by plotting the peak potentials of the redox peaks against the logarithmic scan rate (Figure 4.12(C)).

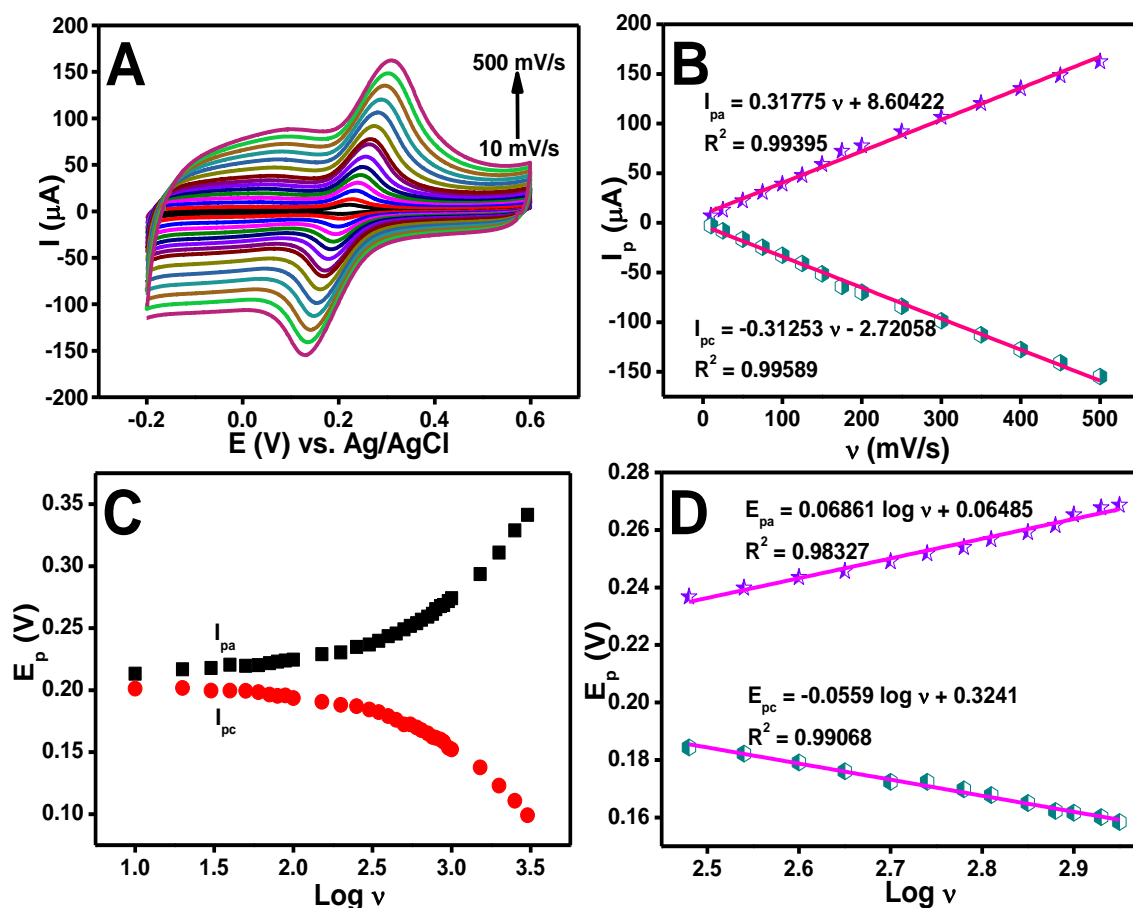


Figure 4.12: (A) CV plot obtained for GC/rGO-Nf (16 h) modified electrode in 0.1 M PBS (pH 6.5) with presence of 100 μM DA at a scan rates of 10–500 mV/s, (B) the corresponding plot of anodic and cathodic peak currents versus scan rate, (C) relationships of anodic and cathodic peak potentials against natural logarithm of scan rate (10–3000 mV/s) and (D) relationships of the anodic and cathodic peak potentials against natural logarithm of scan rate at a scan rate of 300–900 mV/s.

The relationships between the anodic and cathodic peak potentials and the natural logarithm of the scan rate were linear up to the scan rate of 300 to 900 mV/s (Figure 4.12(D)). The calculated slopes of the linear segments are equal to $\frac{2.303RT}{(1-\alpha)nF}$ and $\frac{-2.303RT}{\alpha nF}$ for the anodic and cathodic peaks, respectively, based on the Laviron equation

(Mazloun *et al.*, 2010). The estimated value for the anodic transfer coefficient (α_a) was 0.565, which is consistent with the typical value of 0.5 as-observed for electrochemical reactions (Skúlason *et al.*, 2007). The standard electron transfer rate constant; k_s was calculated to be 6.26 s^{-1} by taking the scan rate of 300 mV/s. The calculated k_s value was quite high for the GC/rGO-Nf (16 h) modified electrode, and it exhibited a rapid electron transfer rate toward the electrocatalytic oxidation of DA.

(c) Effect of rGO-Nf (16 h) Loading

The loading content of rGO-Nf (16 h) nanohybrid was optimized in order to get the best performance of the sensor. The CVs responses of GC/rGO-Nf (16 h) modified electrode in Figure 4.13(A) clearly show that the current response is mainly influenced by the rGO-Nf (16 h) loading content.

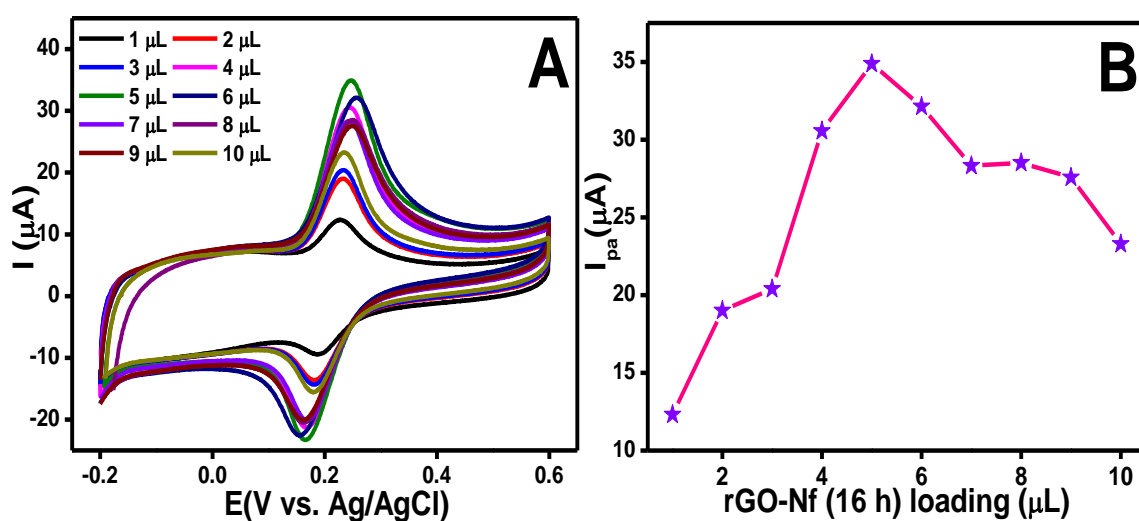


Figure 4.13: (A) CV curves obtained for GC/rGO-Nf (16 h) modified electrode with different amount of sample loading and (B) plot of anodic peak current response versus rGO-Nf (16 h) loading obtained for the 50 μM DA in 0.1 M PBS (pH 6.5) at a scan rate of 50 mV/s.

As can be seen in Figure 4.13(B), the DA redox current increased as we increase the loading content from 1 to 4 μL and it reached the maximum current at 5 μL of rGO-Nf (16 h) nanohybrid. This is due to increment of number of effective surface area for DA oxidation. However, when we gradually increased the aliquots from 6 to 10 μL , the current response started to decrease. This happen because of the formation of thick layers on the surface of electrode which blocks the electron from reaches the electrode and thus lowering its sensitivity. Hence, 5 μL of rGO-Nf (16 h) nanohybrid was used throughout the study.

(d) Effect of pH

The influence of the pH on the electrocatalytic oxidation of DA with the GC/rGO-Nf (16 h) modified electrode was studied, and the results are shown in Figure 4.14(A). The oxidation peak potential toward DA oxidation was shifted from a higher to lower potential value with increasing of pH values ranging from 3 to 10, which clearly suggests that protons participate in the electrode reaction processes (Huang *et al.*, 2008). Moreover, the plot of the peak potential versus pH value shows a well linear relationship between oxidation peak potential and pH, with the equation $E_{pa} = -0.0587 \text{ pH} + 0.625$ and a correlation coefficient of 0.994 (Figure 4.14(B)).

The observed slope value of -58.7 mV/pH was very close to the theoretical value (-59 mV/pH), which indicates that equal numbers of electrons and protons were involved in the electrochemical reaction (Ghorbani *et al.*, 2010). Besides that, this is a consequence of a deprotonation step involved in all oxidation processes that is facilitated at higher pH values. The result also showed that the peak currents are the largest in near neutral pH of 6.5, thus, the subsequent determination experiment was performed in 0.1 M PBS with the pH of 6.5 under the consideration of peak current.

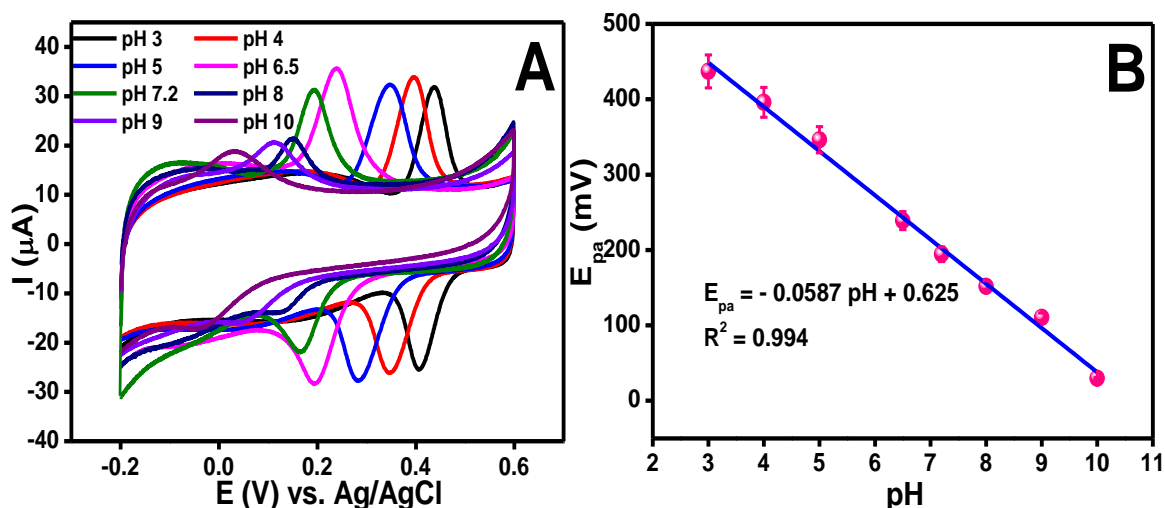


Figure 4.14: (A) CV curves obtained for GC/G-Nf (16 h) modified electrode in presence of 50 μM DA in 0.1 M PBS at different pH values ranging from pH 3 to 10 at a scan rate of 100 mV/s and (B) the corresponding plot of peak potential versus pH values.

4.2.5.3 Linear Sweep Voltammetry (LSV) Response of Dopamine

In order to study the electrochemical detection of DA on the GC/rGO-Nf (16 h) modified electrode, a series of linear sweep voltammetry (LSV) plots were recorded as can be seen in Figure 4.15. From Figure 4.15(A), we can see that the oxidation peak current at a position around +0.23 V increases with successive additions of 100 nM DA into the buffer solution. Besides that, the peak potential shifts in the positive direction with the increase in the concentration and the peak current also increases with the increase in the DA concentration. The calibration plot of as plotted in Figure 4.15(B) shows the linear relation between the anodic peak current and the DA concentration in the range of 100 nM to 1 μM . The calibration plot has a correlation coefficient (R^2) of 0.984 with a regression equation: I (μA) = 7.695(μM) – 0.142 μ . The limit of detection was calculated to be 102 nM (signal-to-noise ratio (S/N) = 3) by substituting the blank standard deviation ($\sigma = 0.262\mu$) and sensitivity ($m = 7.695 \mu\text{A}/\mu\text{M}$) in the $\frac{3\sigma}{m}$ criterion.

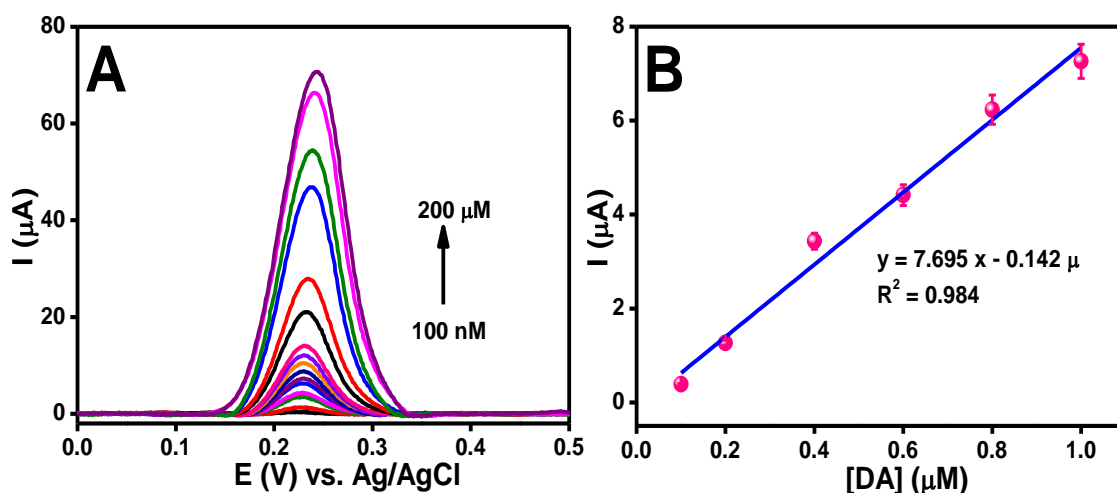


Figure 4.15: (A) LSV obtained for GC/rGO-Nf (16 h) modified electrode in the presence of DA at concentrations of 100 nM to 200 μM in 0.1 M pH 6.5 PBS with a scan rate of 100 mV/s and (B) the corresponding plot of anodic peak current (I) against concentration of DA in the range of 100 nM to 1 μM DA.

4.2.5.4 Simultaneous Determination of Dopamine and Ascorbic Acid

In order to investigate the selectivity and sensitivity of the GC/rGO-Nf (16 h) modified electrode toward the detection of DA in the presence of AA, a series of square wave voltammetry (SWV) plots were recorded and are shown in Figure 4.16, which demonstrate the well-resolved peaks of DA and AA. Figure 4.16(A) reveals that the oxidation peak current of AA increase proportionally with an increasing concentration of AA, whereas the peak current of DA remain constant (300 μM), indicating that the GC/rGO-Nf (16 h) modified electrode was only sensitive to AA. The detection limit for AA was calculated to be about 0.748 mM ($S/N = 3$), based on the calibration plot shown in Figure 4.16(B). When the DA concentration was increased, the peak current increased linearly in the presence of a fixed concentration of AA (5 mM) (Figure 4.16(C)), and it showed a linear relationship between the peak current and the DA concentration when the AA concentration was fixed at a constant 5 mM (Figure 4.16(D)). The detection limit for DA was 166 nM. Table 4.1 shows the comparison of analytical parameters of several modified electrodes for DA determination.

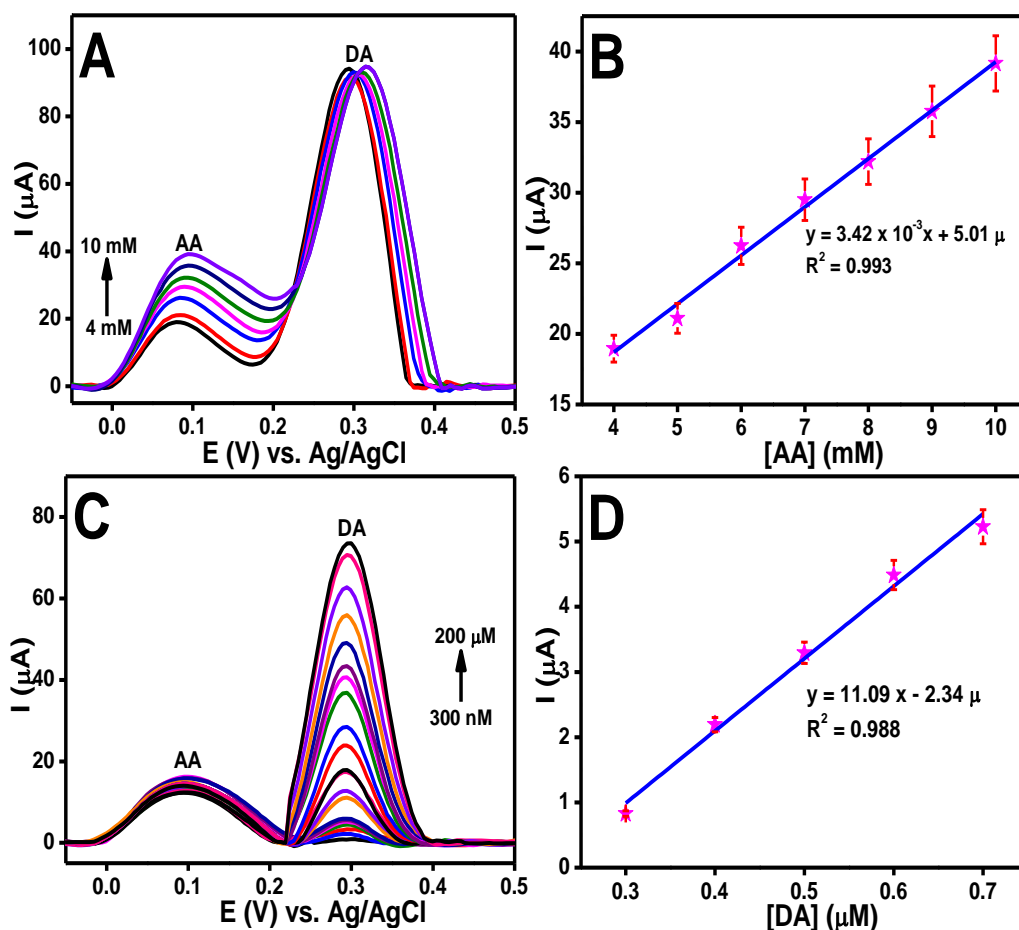


Figure 4.16: (A) SWV curves and their corresponding, (B) calibration plots obtained for GC/rGO-Nf (16 h) modified electrode in presence of 300 μM DA and different concentrations of AA (4 to 10 mM) in PBS (pH 6.5), (C) SWV curves and their corresponding and (D) calibration plots obtained for GC/rGO-Nf (16 h) modified electrode in the presence of 5 mM AA and different concentrations of DA (300 nM to 0.7 μM).

Table 4.1: Comparison of analytical parameters of several modified electrode based on graphene-polymer composite for DA determination.

| Electrode | Detection Method | Limit of Detection | Interferent | Reference |
|-----------------|------------------|--------------------|-------------|----------------------------------|
| GC/rGO/PpPD | Amperometry | 0.36 μM | AA, UA | (Liu <i>et al.</i> , 2013) |
| GC/GNs/PEI/AuNP | DPV | 0.2 μM | AA | (Ponnusamy <i>et al.</i> , 2014) |
| GC/G/Chitosan | DPV | 1 μM | AA, UA | (Han <i>et al.</i> , 2010) |
| GC/rGO-Nf | SWV | 166 nM | AA | This work |

PpPD= poly(p-phenylenediamine); GNs= Graphene nanosheets; PEI= Polyethyleneimine; G=graphene;

4.2.5.5 Interference Study

The GC/rGO-Nf (16 h) modified electrode was further used to simultaneously detect the three analytes; DA, AA and UA. Figure 4.17 shows the LSV curves recorded at the GC/rGO-Nf (16 h) modified electrode in a mixture of DA, AA and UA with concentrations of 50 μ M, 5 mM and 5 μ M, respectively.

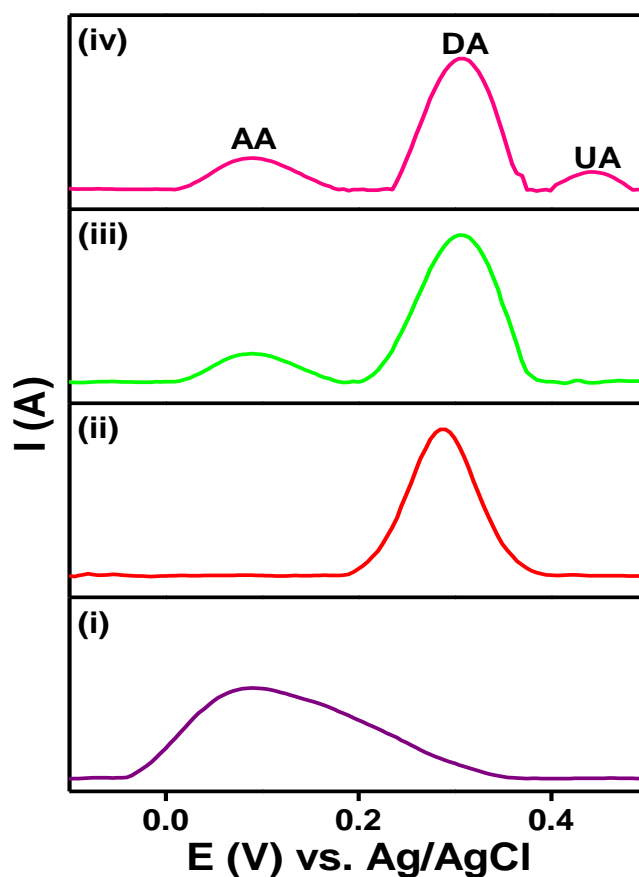


Figure 4.17: LSV obtained for GC/rGO-Nf (16 h) modified electrode in presence of (i) 5 mM AA, (ii) 50 μ M DA, (iii) mixture of 5 mM AA and 50 μ M DA, and (iv) mixture of 5 mM AA, 50 μ M DA and 5 μ M UA in 0.1 M PBS (pH 6.5).

Based on these results, it can be observed that the simultaneous determinations of DA, AA and UA could be possible because the anodic current peaks of these analytes are well separated. This selectivity and well resolved oxidation peaks for DA, AA and UA are arises due the following reasons. The Nf in the hybrid film swelled in water, which resulted in the expansion of the interconnected sulfonate ($-\text{SO}_3^-$) ionic cluster

regions and the pinholes in the Nf (Bennett, 2005). At pH 6.5, the cationic DA molecules were preconcentrated at the swelled rGO-Nf film and the DA oxidation current increased at the GC/rGO-Nf modified electrode. In the case of electrochemical response of AA and UA, both the biomolecules interacted with rGO that was exposed upon the swelling of Nf in the rGO-Nf film and underwent electrochemical oxidation. The oxidation potentials of DA, AA and UA were influenced by the type of interaction with the rGO-Nf material, which brought about the shift in the oxidation potentials of these molecules, paving the way for the simultaneous detection of all three biomolecules. This clearly suggests that the fabricated GC/rGO-Nf (16 h) modified electrode shows excellent selectivity toward the DA in the presence of interference from AA and UA.

4.2.5.6 Reproducibility, Repeatability, and Stability Studies

The reproducibility of the GC/rGO-Nf (16 h) modified electrode for the detection of 50 μ M DA in the PBS (pH 6.5) solution was evaluated by recording the CV curves at a series of freshly prepared five electrodes (Figure 4.18(A)). The result revealed that this modified electrode showed good reproducibility with a relative standard deviation (RSD) of 4.19 %. The repeatability of GC/rGO-Nf (16 h) modified electrode was investigated by recording the CV curves for five repetitive measurements of 50 μ M DA on a single sensor electrode (Figure 4.18(B)). DI water was used to rinse the electrode surface after each measurement. The results indicated that the modified electrode possessed an excellent repeatability with a RSD of 5.71 % for five successive measurements.

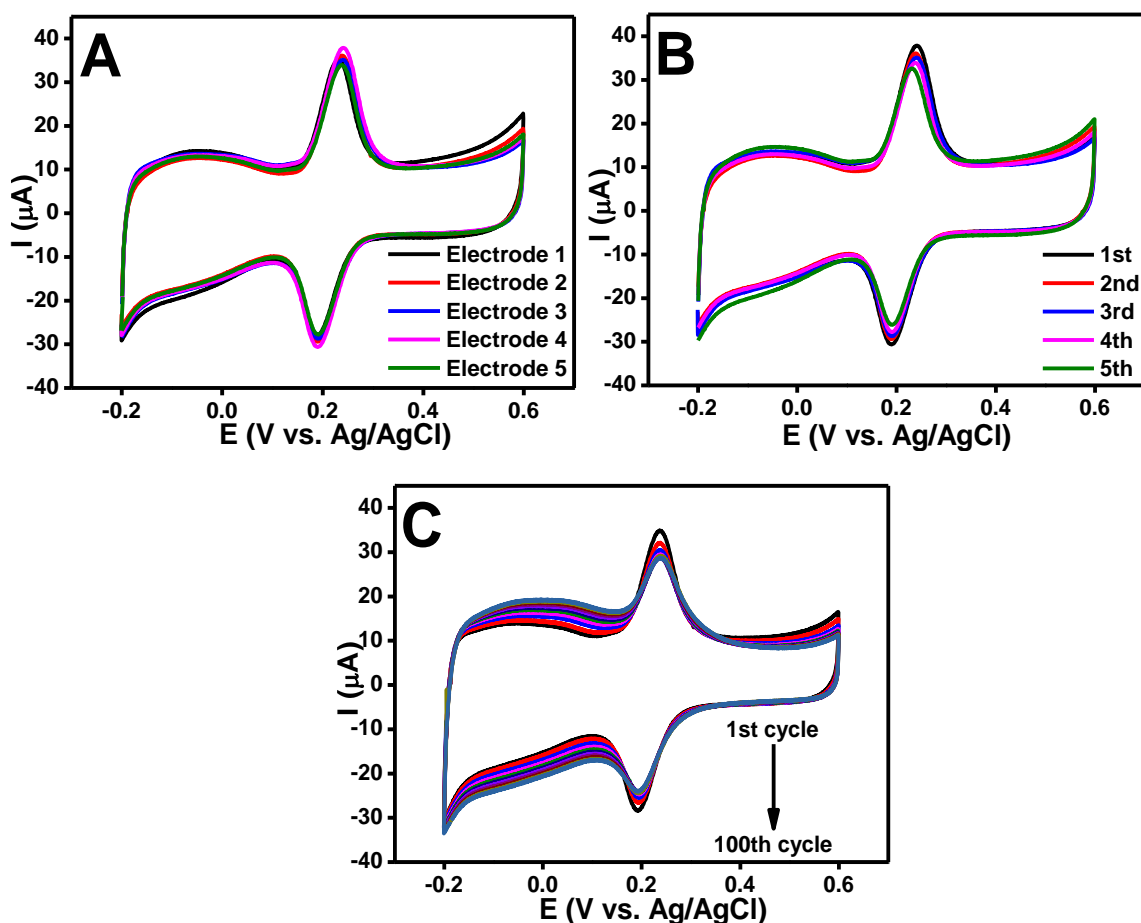


Figure 4.18: (A) CV curves of five different GC/rGO-Nf (16 h) modified electrodes, (B) CV curves of five successive measurement of single GC/rGO-Nf (16 h) modified electrode with 50 μM DA in 0.1 M PBS (pH 6.5) at a scan rate of 100 mV/s and (C) CV curves of GC/rGO-Nf (16 h) modified electrode up to 100 continuous cycles.

The operational stability of the GC/rGO-Nf (16 h) modified electrode was also investigated by measuring the electrode response with 50 μM DA for 100 cycles and the result was plotted in Figure 4.18(C). After 100 cycles, it continued to show stable behavior where the response of this modified electrode to DA lost about 9.35 % of its original response indicating that the GC/rGO-Nf (16 h) modified electrode did not undergo surface fouling by the oxidized products. The results obtained from the reproducibility, repeatability, stability, and interference tests indicated that GC/rGO-Nf (16 h) modified electrode are suitable for testing in real samples.

4.2.5.7 Real Sample Analysis

The GC/rGO-Nf (16 h) modified electrode was used for the determination of DA in urine samples in order to evaluate the practical applicability of the as prepared sensor. The urine samples did not show any DA signal. Hence, the determination of DA was performed by the standard addition method and the results were listed in Table 4.2. Three different urine samples were used to detect the DA concentration and the DA contents of the same samples were measured three times. The obtained results showed good agreement with the actual addition with the recoveries of the developed method varying from 96.58 to 103.0 %. The RSD were calculated to be 1.5 to 5.8 % for three measurements, indicating good electrode reproducibility. Based on these results, it is clear that the fabricated GC/rGO-Nf (16 h) modified electrode demonstrated a high ability to detect DA in real samples and the interferences in urine samples can be neglected.

Table 4.2: Results of DA determination in urine samples (n = 3) using GC/rGO-Nf (16 h) modified electrode.

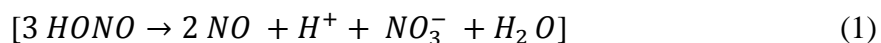
| Sample | DA added (μM) | DA detected ^a (μM) | RSD (%) | Recovery (%) |
|---------|-------------------------------|---|------------|-----------------|
| Urine 1 | 6 | 6.18 | 3.1 | 103.00 |
| Urine 2 | 20 | 19.48 | 5.8 | 97.40 |
| Urine 3 | 50 | 48.29 | 1.5 | 96.58 |

^a Average of three determinations.

4.2.6 Electrochemical Determination of Nitric Oxide

4.2.6.1 Electrocatalytic Oxidation of Nitric Oxide

It is well known that sodium nitrite (NaNO_2) serves as a source of NO by undergoing a disproportionation reaction (1) in an acidic solution ($\text{pH} < 4$) (Tripatara *et al.*, 2007). Hence, NaNO_2 was used as a precursor to produce NO in solution during the electrochemical study. The concentration of NO was determined by controlling the concentration of the injected NaNO_2 (Pandikumar *et al.*, 2011; Sivanesan *et al.*, 2010).



CV curves were recorded by using a 1 mM NO solution in 0.1 M PBS (pH 2.5) at a scan rate of 50 mV/s, and are shown in Figure 4.19. The modified electrode did not show any voltammetric response in the blank PBS, as can be seen in Figure 4.19(A). Upon the addition of the 1 mM NO in the PBS, an anodic peak potential at +0.85 V which can be related to the direct oxidation of NO can only be observed on the GC/rGO-Nf modified electrode. Upon hydrothermal treatment the GO is reduced to form rGO in the rGO-Nf nanohybrid. It is known from the literature, the rGO have better conductivity and electrocatalytic activity than the GO. Hence the hydrothermally prepared rGO-Nf nanohybrid showed better electrocatalytic activity thereby increases the current response towards NO oxidation than the other electrode.

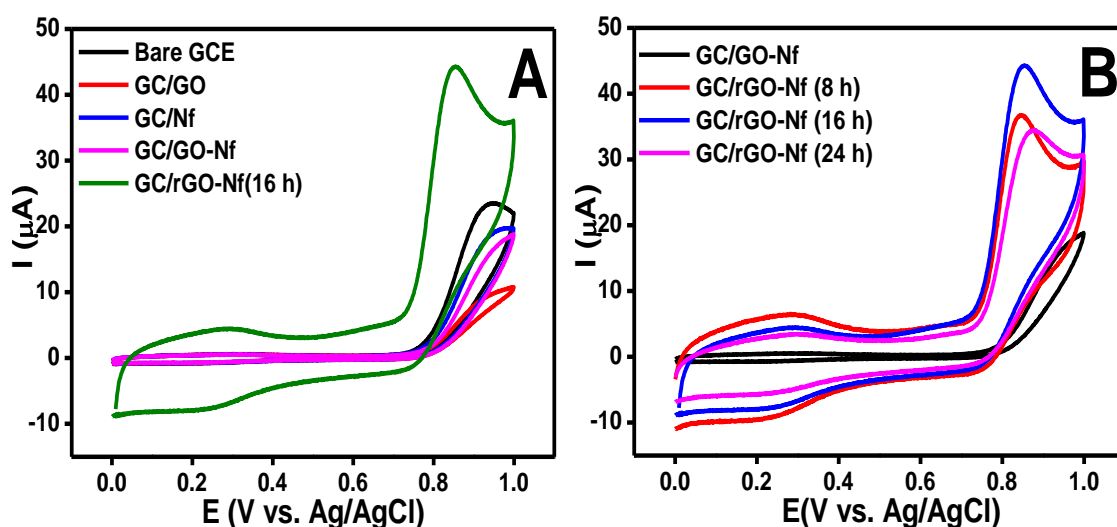


Figure 4.19: (A) CV curves obtained for the bare GCE, GC/GO, GC/Nf, GC/GO-Nf and GC/rGO-Nf (16 h) modified electrodes in the presence of 0.1 M PBS (pH 2.5) containing 1 mM NO at a scan rate of 50 mV/s and (B) CV obtained for the GC/GO-Nf, GC/rGO-Nf (8 h), GC/rGO-Nf (16 h) and GC/rGO-Nf (24 h) modified electrodes in the presence of 0.1 M PBS (pH 2.5) containing 1 mM NO at a scan rate of 50 mV/s.

Moreover, the synergic effect results from the hybridization of nanosized rGO and Nf facilitates the electron-transfer processes between the electrolyte and the GCE, thus increases the current respond. It was found that the current response toward the NO oxidation was higher for the GC/rGO-Nf (16 h) modified electrode compared to the bare GCE and other modified electrodes (Figure 4.19(B)). This result indicates a high electrocatalytic activity of GC/rGO-Nf (16 h) modified electrode toward the oxidation of NO. Moreover, this result also revealed that the high degree of reduction and low defectiveness of the rGO-Nf (16 h) nanohybrid may lead to a high current response for NO oxidation. Hence, this GC/rGO-Nf (16 h) modified electrode was chosen as a sensor electrode for the sensitive and selective detection of NO.

The schematic view of the process of the detection of NO is given in Figure 4.20 and the possible reaction involved is shown in Equation (2) (Li *et al.*, 2006).

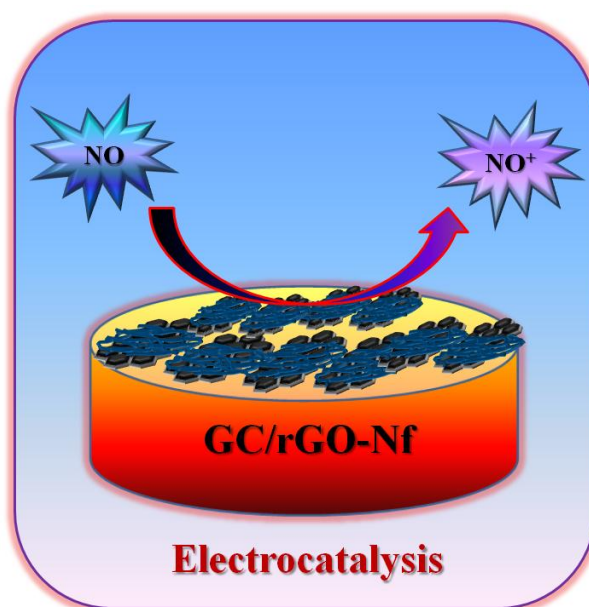


Figure 4.20: Schematic diagram for the electrocatalytic oxidation of NO at the GC/rGO-Nf modified electrode.

It is suggested that the rGO-Nf acted as an electrocatalyst for the oxidation of NO to form nitrosonium ion (NO^+) during the electrocatalytic process (Wang *et al.*, 2011). The GC/rGO-Nf modified electrode exhibited high electrocatalytic activity towards NO oxidation, which enhances the electron transfer kinetics and improved the performance for detecting NO.

4.2.6.2 Optimization Studies

(a) Effect of Different Concentration of Nitric Oxide

The effect of different concentrations of NO on the current response of the GC/rGO-Nf (16 h) modified electrode was evaluated by CV, as shown in Figure 4.21. It is obvious that the anodic peak current increase with the increment in the NO concentration. The relationship between peak current and concentration can be described with the linear regression equations of $I_{pa} = 0.033[\text{NO}] + 0.278 \mu$ ($R^2 = 0.993$), for the concentration of NO ranging between 1 to 10 mM.

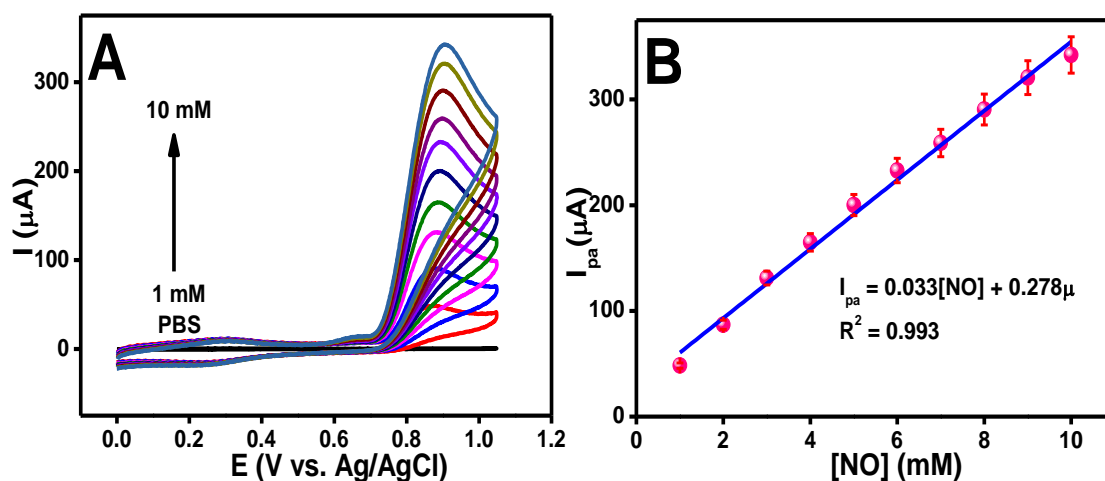


Figure 4.21: (A) CV curves obtained for the GC/rGO-Nf (16 h) modified electrode in the presence of 0.1 M PBS (pH 2.5) and different concentration of NO (1 to 10 mM) at a scan rate of 50 mV/s and (B) linear relationship between I_{pa} and the concentration of NO.

(b) Effect of Scan Rate

The influence of the scan rate on the oxidation peak potential (E_{pa}) and peak current for NO at the GC/rGO-Nf (16 h) modified electrode in 0.1 M PBS (pH 2.5) were studied by using CV, as shown in Figure 4.22. The current responses were found to increase with the increment in the scan rate from 10 to 500 mV/s (Figure 4.22(A)). The linear relation between the anodic peak currents and the square root of the scan rate was shown in **Figure 4.22(B)**. As can be seen, the anodic peak current (I_{pa}) for the 1 mM NO varied linearly with the square root of the scan rate ($v^{1/2}$), with a linear regression equation of $I_p(\mu A) = 2.221 v^{1/2} + 8.045$ and a correlation coefficient $R^2 = 0.986$. This result indicates that the electron transfer of the GC/rGO-Nf (16 h) modified electrode was mainly controlled by a diffusion-controlled electrochemical process (Wang *et al.*, 2011). The diffusion coefficient was calculated and gives a value of $8.51 \times 10^{-7} \text{ cm}^2 \text{ s}^{-1}$.

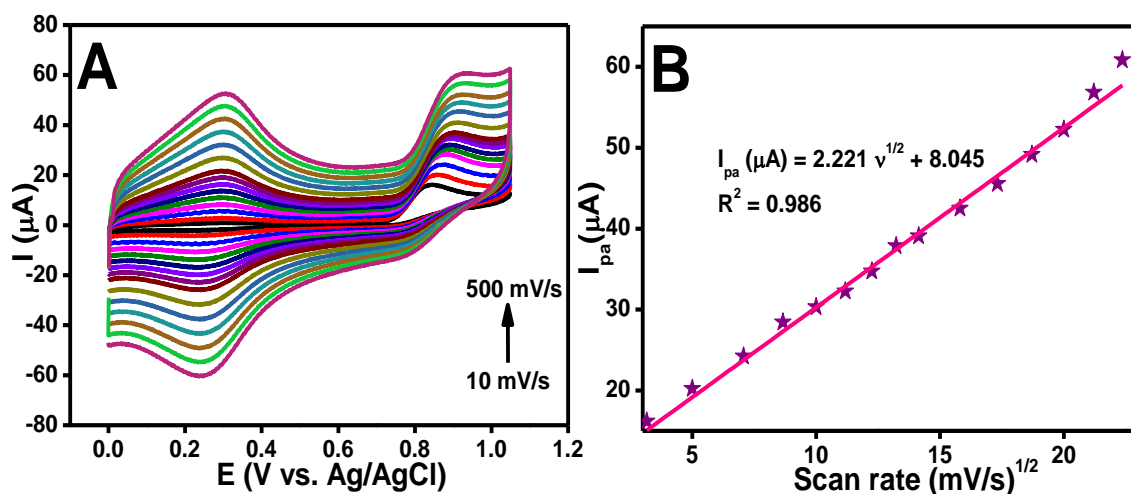


Figure 4.22: (A) CV curves obtained for the GC/rGO-Nf (16 h) modified electrode in the presence of 0.1 M PBS (pH 2.5) containing 1 mM NO at different scan rates and (B) plot of anodic peak current versus square root of the scan rate obtained for the GC/rGO-Nf (16 h) modified electrode.

(c) Effect of rGO-Nf Loading

The influence of the rGO-Nf loading amount on the electrocatalytic oxidation performance was investigated and shown in Figure 4.23(A). Figure 4.23(B) displays the

relation between the current response after the injection of 1 mM NO and the loading amount of the rGO-Nf (16 h) nanohybrid. It can be seen that the current response increases when the volume of rGO-Nf (16 h) increases from 1 to 5 μL . The current response started to decrease after more than 5 μL was used to modify the GCE. This may have been due to the limited mass transport of the NO inside a thicker layer of rGO-Nf (16 h) formed on the surface of the GCE. Hence, 5 μL of rGO-Nf (16 h) was chosen to modify the GCE.

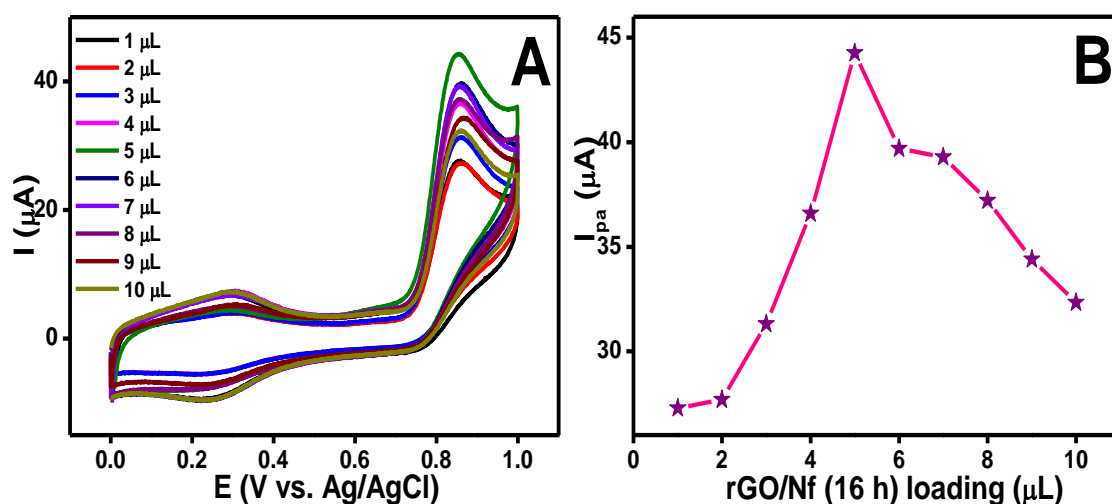


Figure 4.23: (A) CV curves obtained for GC/rGO-Nf (16 h) modified electrode with different amount of sample loading and (B) plot of rGO-Nf (16 h) loading versus anodic peak current response obtained for the 1 mM NO in 0.1 M PBS (pH 2.5) at a scan rate of 50 mV/s.

4.2.6.3 Square Wave Voltammetry (SWV) Response of Nitric Oxide

The sensitivity and selectivity of the sensor under the optimized detection conditions were tested, and a series of SWV curves were recorded with different NO concentrations at the GC/rGO-Nf (16 h) modified electrode, as shown in Figure 4.24(A). It could be observed that the anodic peak current increased linearly with an increase in the concentration of NO in the range of 0.05 to 0.45 mM, with a linear regression equation of $I_{pa} = 0.062 [\text{NO}] + 11.71 \mu$ ($R^2 = 0.998$) (Figure 4.24(B)).

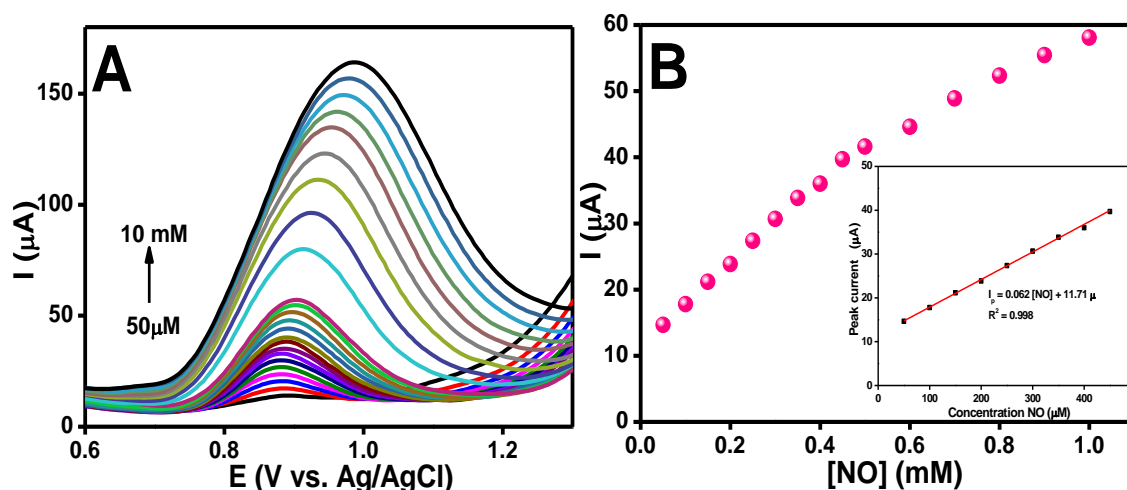


Figure 4.24: (A) SWV obtained for GC/rGO-Nf (16 h) modified electrode in 0.1 M PBS pH 2.5 containing different concentration of NO (50 μM to 10 mM) at a scan rate of 50 mV/s and (B) correlation between the concentrations of NO and peak current quantified from the SWV (Inset shows the enlarged view of plot obtained for the peak current versus concentration of NO at lower concentration level).

The limit of detection and sensitivity were calculated at a signal-to-noise ratio (S/N) of 3 and gave values of 11 μM and 62 $\mu\text{A mM}^{-1}$, respectively. The sensitivity was determined from slope of the calibration figure. The very low detection limit observed can be ascribed to the tightly binding and well distributed rGO-Nf (16 h) nanohybrid on the surface of the GCE, which provided a larger surface area with better contact on the electrode surface. This resulted in an increase in the electron transfer reaction rate at the electrode–solution interface. In addition, the high degree of reduction and low defectiveness of the rGO-Nf (16 h) nanohybrid helps to increase the electrocatalytic activity, thus improve the sensing performance. The comparison of analytical parameters of several modified electrode for NO determination were showed in Table 4.3.

Table 4.3: Comparison of analytical parameters of several modified electrode for NO determination.

| Electrode | Fabrication method | Detection Method | Linear range (M) | Detection limit (M) | Reference |
|---|------------------------------|------------------|---|------------------------|-------------------------------|
| Nano-TiO ₂ /Nafion film/GC | - | DPV | $3.6 \times 10^{-7} - 5.4 \times 10^{-5}$ | 5.4×10^{-8} | (Yazhen <i>et al.</i> , 2006) |
| PEI/[(PSS/PAH) ₂ /PSS/AuNP] ³ | Infiltration, layer by layer | CV | $0.05 \times 10^{-3} - 0.5 \times 10^{-3}$ | 0.010×10^{-3} | (Yu <i>et al.</i> , 2003) |
| Hemoglobin-DNA/PG | Deposition | DPV | $0.1 \times 10^{-3} - 1 \times 10^{-3}$ | 1.8×10^{-5} | (Fan <i>et al.</i> , 2000) |
| GC/rGO-Nf | Hydrothermal | SWV | $0.05 \times 10^{-3} - 0.45 \times 10^{-3}$ | 11×10^{-6} | This work |

PEI/[(PSS/PAH)₂/PSS/AuNP]³=poly-(ethylenimine)/[(poly(sodium 4 styrenesulfonate)/poly(allylamine hydrochloride))₂/ poly(sodium 4-styrenesulfonate)/gold nanoparticles]³, PG=pyrolytic graphite.

4.2.6.4 Interference Study

In order to verify the selectivity of the GC/rGO-Nf (16 h) modified electrode toward NO, the current response toward a ternary mixture containing 5 mM AA, 50 μ M DA and 5 mM NO was investigated by using LSV and the result shows in Figure 2.45.

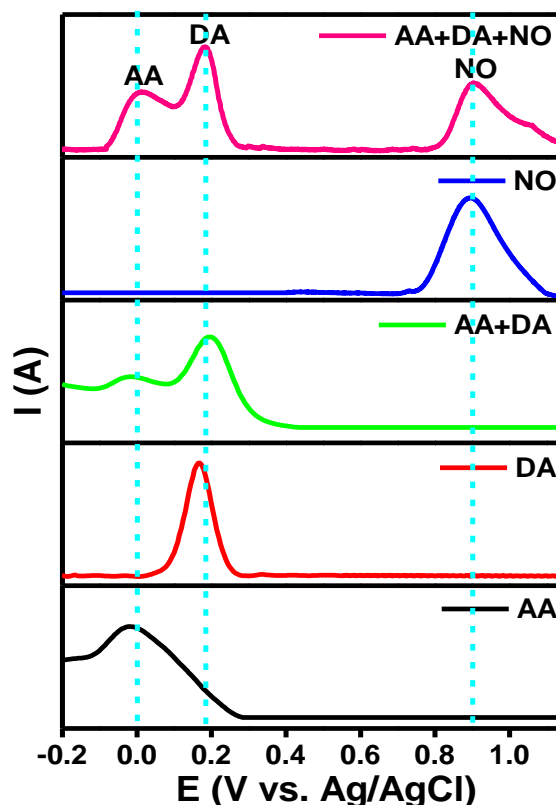


Figure 4.25: LSV obtained for the GC/rGO-Nf (16 h) modified electrode in 0.1 M PBS (pH 2.5) with the mixture of 5 mM AA, 50 μ M DA and 5 mM NO.

As shown in Figure 4.25, the anodic peaks of all three analytes were well resolved at the GC/rGO-Nf (16 h) modified electrode, with peak potentials at -0.02, +2.0 and +0.85 V, respectively, for AA, DA and NO. These observations suggest that the GC/rGO-Nf (16 h) modified electrode had a good selectivity toward NO and the simultaneous determinations of AA, DA and NO could be possible in a real sample because the anodic peaks of these analytes were well separated.

4.2.6.5 Reproducibility and Repeatability Studies

In order to evaluate the fabrication reproducibility of our proposed NO sensor, four GC/rGO-Nf (16 h) modified electrodes were prepared by the same procedure and the modified electrodes were used to detect 1 mM NO by CV in 0.1 M PBS (pH 2.5).

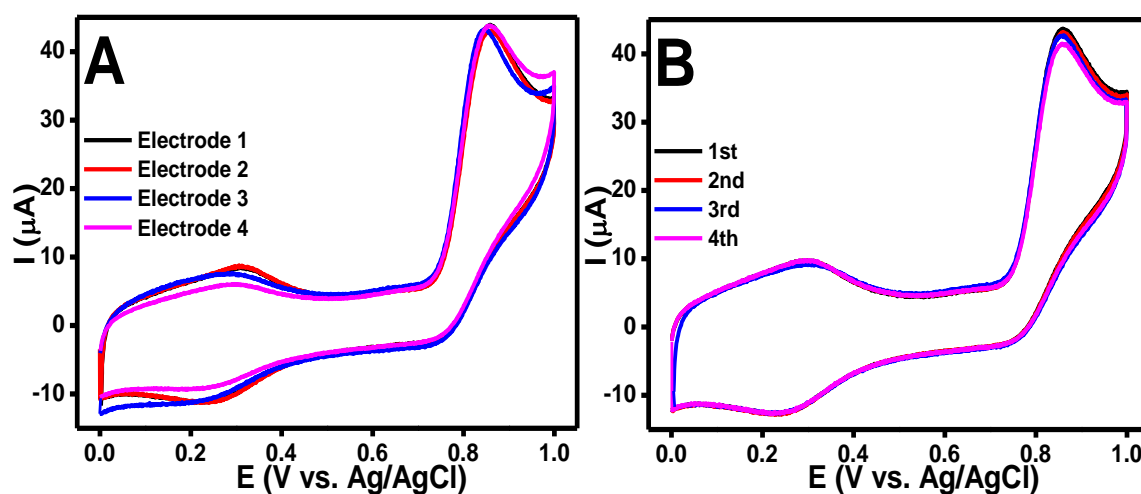


Figure 4.26: (A) CV curves of five different GC/rGO-Nf (16 h) modified electrodes and (B) CV curves of five successive measurements of single GC/rGO-Nf (16 h) modified electrode with 1 mM NO in 0.1 M PBS (pH 2.5) at a scan rate of 100 mV/s.

As can be seen in Figure 4.26(A), there was no obvious peak current changes could be observed for all four modified electrode. A RSD of 0.71 % was obtained which demonstrated the good reproducibility of the proposed NO sensor. The repeatability of the GC/rGO-Nf (16 h) modified electrode was also investigated by recording the CV

curves for 1 mM NO in 0.1 M PBS (pH 2.5) on a single electrode for four repetitive measurements. DI water was used to rinse the electrode before each measurement. The results obtained for four successive detections were presented in Figure 4.26(B) and the RSD value was calculated to be 2.24 %. The low RSD values obtained suggest that the GC/rGO-Nf (16 h) modified electrode exhibited excellent reproducibility and repeatability.

4.3 Summary

As a conclusion, stable rGO-Nf nanohybrid was formed in a nanosized rGO solution with the aid of Nf as a dispersant using a hydrothermal process. HRTEM study revealed that the nanosized rGO had an average size of ~18 nm after hydrothermal treatment. Further, well dispersed nanosized rGO were successfully synthesized in an Nf matrix under a hydrothermal process at 180 °C. The influence of the hydrothermal treatment time on the formation of the rGO-Nf nanohybrid was studied, and it was found that the rGO-Nf nanohybrid formed after 16 h of hydrothermal treatment had a more uniform distribution compared to rGO-Nf nanohybrids obtained after 8 h and 24 h of hydrothermal treatment, which tended to agglomerate. These optimized hydrothermal conditions led to the excellent electrochemical detection of DA with a lower detection limit of about 166 nM which is comparable with other existing modified electrodes. The results of this study demonstrate that this sample also exhibited an extraordinarily high sensitivity and selectivity to DA in the presence of interference from AA and UA.

Besides that, we also demonstrated the benefits of using rGO-Nf as the active material for NO sensing. The developed NO sensor showed a lower detection limit of 11 μM and a higher sensitivity of 62 $\mu\text{A mM}^{-1}$. The lower detection limit for DA and NO at the GC/rGO-Nf (16 h) modified electrode seemed to result from the high degree

of reduction and low defectiveness of rGO-Nf (16 h), which helped to increase the electrocatalytic activity and thus improved the sensing performance. This modified electrode also allowed the simultaneous selective detections of NO, AA and DA. The results indicate that the proposed modified electrode has great potential to be applied as a sensor for DA and NO detection in real sample analysis. Moreover, the modified electrode also showed a good reproducibility and high stability. Hence, this GC/rGO-Nf modified electrode has great potential for biosensor applications.

CHAPTER 5

REDUCED GRAPHENE OXIDE-NAFION@SILVER NANOHYBRID MODIFIED ELECTRODE FOR ELECTROCHEMICAL DETECTION OF HYDROGEN PEROXIDE

5.1 Introduction

Hydrogen peroxide (H_2O_2) is a compound that not only beneficial to the human body, it is also a well known by-product in a variety of enzymatic reactions, but it also plays a crucial role in diverse fields of practice, such as the cosmetic, food, diagnostic, pharmaceutical, clinical and environmental protection industries (Chen *et al.*, 2012; Clifford *et al.*, 1982; Pryor *et al.*, 1991). In the human body, H_2O_2 which is produced by a subclass of white blood cells called neutrophils acts as the first line of defence against toxins, parasites, bacteria, viruses and yeast (Clifford *et al.*, 1982). H_2O_2 also play a vital role in regulating of renal function and as an antibacterial agent in urine (Halliwell *et al.*, 2000).

Additionally, it signals the immune system to send more white blood cells to the site of an injury. High concentrations of H_2O_2 generated in blood plasma can adversely affect on human health, including irritating the eyes, skin, mouth, stomach and intestines and it can constitute a pathogenic factor in vascular organ damage attendant upon systemic hypertension (Lacy *et al.*, 1998). In industrial applications, H_2O_2 is one of the components as tooth whitening paste, laundry detergent and other products for cleaning, hygiene, and healing purposes and it also used for the bleaching of textiles and paper. In the food industry, H_2O_2 is used as a chemical agent for sterilization due to its powerful oxidizing properties that allow it to react with bacteria, viruses, spores and

yeasts, making it an excellent disinfectant. Because of the importance of H_2O_2 in all of the above applications, the creation of an instrument that can detect concentrations of H_2O_2 is of practical significance, especially for industrial and medical purposes.

The electrochemical techniques are advantageous in the detection of biologically relevant analytes because of their easy operation, high sensitivity, fast response and low cost fabrication (Chen *et al.*, 2006). Basically there are two categories of electrochemical H_2O_2 sensors that are enzymatic and non-enzymatic sensors. Among these two developed sensor techniques, the enzyme-based electrochemical H_2O_2 sensors has been rapidly used by the researcher as it possesses high selectivity of the biological recognition elements and excellent sensitivity of electrochemical transduction process. However, the enzymatic sensors suffer from limitations such as high costs as it used expensive materials, restricted activity and storage time, elaborate immobilization procedure and insufficient reproducibility. By considering these drawbacks, the developments of non-enzymatic H_2O_2 electrochemical sensors without standing properties have received extensive attention in recent years. In comparison with the enzymatic sensor, the non-enzymatic technique has a series of advantages including low operational cost, high stability, good reproducibility, simple operational procedure as well as high selectivity and sensitivity. In order to improve the sensing performance of enzymeless H_2O_2 sensor, the modification of the sensor electrode using graphene-based nanocomposites has been developed.

Graphene has offered great potential in electrochemical sensor applications ever since its discovery in 2004 due to its remarkable physicochemical properties. It is a single layer of carbon atoms organized in a closely packed honeycomb two dimensional lattice, has attracted great attention because of its unique nanostructure and

extraordinary properties, such as high surface area, excellent conductivity, high mechanical strength and ease of functionalization and mass production (Chabot *et al.*, 2014; Pandikumar *et al.*, 2014). The high surface area of electrically conductive graphene sheets can give rise to high densities of attached analyte molecules. This in turn can facilitate high selectivity, sensitivity and device miniaturization in electrochemical sensors.

Variety of graphene-based materials, such as graphene-metal composite (Cui *et al.*, 2014; Palanisamy *et al.*, 2015), graphene-metal oxide composite (Li *et al.*, 2014; Palanisamy *et al.*, 2012) and graphene-polymer composite (Nguyen *et al.*, 2014), have proven to be very effective as electrochemical sensors for the detection of H₂O₂. Jiang *et al.* have reported an H₂O₂ sensor made of a cuprous oxide/nitrogen-doped graphene/Nafion (Cu₂O/N-graphene/Nafion) nanocomposite modified GCE (Jiang *et al.*, 2014). This Cu₂O/N-graphene/Nafion-modified electrode exhibited excellent sensing behavior toward H₂O₂, with a low detection limit (LoD) of 0.8 μM and high sensitivity of 26.67 $\mu\text{A mM}^{-1}$. It is believed that the enhancement of electrocatalytic reduction of H₂O₂ was caused by the direct incorporation of Cu₂O on rGO matrix which provides good electrical contact between Cu₂O and rGO and affords an efficient pathway for charge transfer.

Meanwhile, due to the excellent properties of silver nanoparticles (AgNPs) such as good biocompatibility and conductivity, and a large surface area with sufficient binding points for biomolecule immobilization, Li and co-workers have constructed a non-enzymatic biosensor for H₂O₂ based on AgNPs/rGO nanocomposites (Li *et al.*, 2012). The amperometric response of the AgNPs/rGO/GC modified electrode exhibits an increment upon addition of H₂O₂ and a LoD of 3.6 μM (S/N=3), with a linear detection

range of 0.1 to 100 mM. However, most of the reported sensors for H₂O₂ exhibit some limitations including intrinsic simplicity of preparing the sensor electrode, low sensitivity and selectivity, poor repeatability and reproducibility. Therefore, we have sought to address those issues through fabricating a sensor electrode based on the novel nanohybrid material, which allows for the reliable, accurate, sensitive, selective, rapid and low cost determination of H₂O₂.

5.2 Results and Discussion

5.2.1 Optical Characterization of rGO-Nf@Ag Nanohybrids

The successful preparation of rGO-Nf@Ag nanohybrids was confirmed by the ultraviolet–visible (UV-vis) absorption spectroscopic method. Figure 5.1 shows the UV-vis absorption spectra of aqueous dispersion of the nanohybrids, scanned from the wavelength of 190 to 800 nm. It can be clearly seen that the GO exhibits a strong absorption peak at 228 nm and a shoulder at around 300 nm due to the $\pi \rightarrow \pi^*$ transitions of aromatic C–C bonds and the $n \rightarrow \pi^*$ transitions of C=O bonds (carbonyl groups), respectively (Yusoff *et al.*, 2015) (Figure 5.1(A)).

Upon hydrothermal treatment, the GO peak shifted from 228 to 261 nm and the shoulder at 300 nm disappeared as a result of effective restoration of the sp^2 carbon networks (C–C bonds) within the sheets. The successful decoration of AgNPs on the rGO-Nf surface was confirmed by the appearance of a broad peak at around 448 nm due to the characteristic feature of surface plasmon resonance (SPR band), as can be seen in Figure 5.1(B) (Zainy *et al.*, 2012). The increase in SPR band intensity with increasing AgNO₃ concentration (from 4 to 8 mM) in the ternary nanohybrid indicates the existence of greater amounts of AgNPs in the nanohybrids. Moreover, the absorption edge of rGO-Nf@Ag nanohybrids also displays a slight red-shift to higher wavelengths

with increasing AgNPs loading, which is ascribed to the chemical interaction between AgNPs and rGO-Nf.

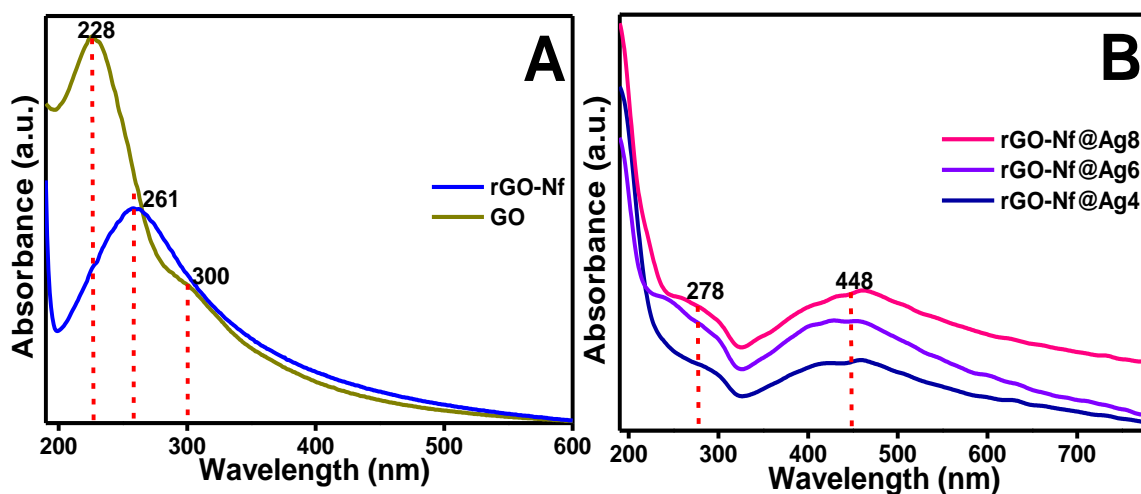


Figure 5.1: UV-vis absorption spectra of (A) GO, rGO, Nf, rGO-Nf and (B) rGO-Nf@Ag nanohybrids with three different Ag contents.

5.2.2 Crystalline and Structural Characterization of rGO-Nf@Ag Nanohybrids

The X-ray diffraction (XRD) analysis was conducted in order to verify the formation of the rGO-Nf@Ag nanohybrids. Figure 5.2 shows the XRD patterns of three different rGO-Nf@Ag nanohybrids. A broad rGO characteristic peak at 26° which corresponding to the (0 0 2) crystalline plane can be observed in the XRD pattern of all three nanohybrids, demonstrate the existence of rGO in the nanohybrids (Khan *et al.*, 2015). It can be seen in the XRD pattern of rGO-Nf@Ag8 nanohybrid (Figure 5.2(iii)), that four peaks appeared at 2θ of 38.2° , 44.5° , 64.6° and 77.4° , which assigned to the (1 1 1), (2 0 0), (2 2 0), and (3 1 1) planes of Ag (JCPDS No. 65–2871). This result reveals the presence of AgNPs in the nanohybrids. However, only a certain peaks of Ag could be seen in the XRD patterns of rGO-Nf@Ag4 and rGO-Nf@Ag6 nanohybrids as depicted in Figure 5.2(i) and 5.2(ii), respectively. This may due to the low content of AgNPs in the nanohybrids. The intensity of the diffraction peaks also varies with increasing concentration of the Ag precursors.

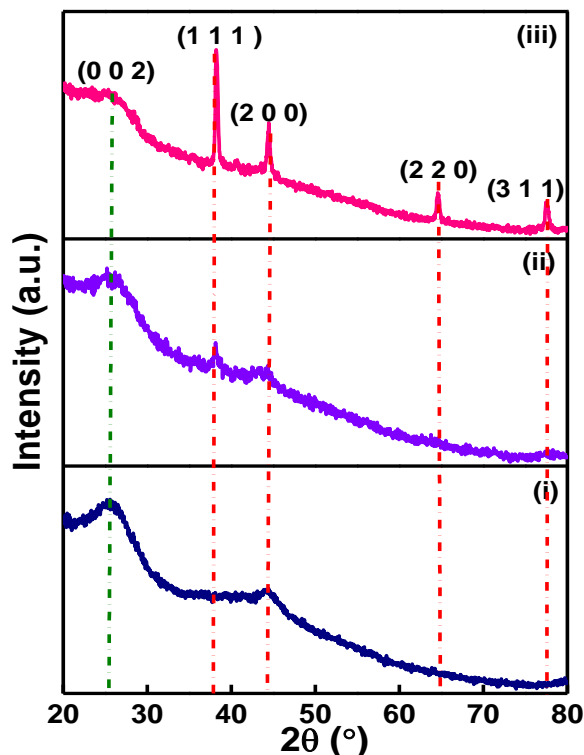


Figure 5.2: XRD patterns of (i) rGO-Nf@Ag4, (ii) rGO-Nf@Ag6 and (iii) rGO-Nf@Ag8 nanohybrids.

Further study on the characterization of sp^2 and sp^3 hybridized carbon atoms to determine ordered and disordered crystal structures of graphene were made by using Raman spectroscopy. Figure 5.3 shows the Raman spectra for the as-prepared materials scanned from 1100 to 1800 cm^{-1} . The broad D (1350 cm^{-1}) and G bands (1597 cm^{-1}) observed in Raman spectra for GO, rGO, rGO-Nf and three different ternary nanohybrids were associated with the signature peaks of carbon (the building block for graphene). According to previously reported work, the D peak corresponds to the defects and disorder in activated Raman mode arising from the vibrations of sp^3 carbon atoms, while the G peak arises from sp^2 hybridized carbon atoms in a graphitic 2D hexagonal lattice (Ferrari *et al.*, 2006). Meanwhile, the intensity ratio between D and G peaks provides information about the establishment of sp^2 hybridization and deoxygenation (Nyoni *et al.*, 2014). The as-obtained result shows that the I_D/I_G ratio for

rGO increased from 0.92 to 1.07 after the hydrothermal treatment, as indicated in Figure 5.3(A). This increment is attributed to the defect cause by the removal of oxygen groups as well as the introduction of large amounts of sp^2 domain with small average sizes after the hydrothermal treatment (Wong *et al.*, 2015).

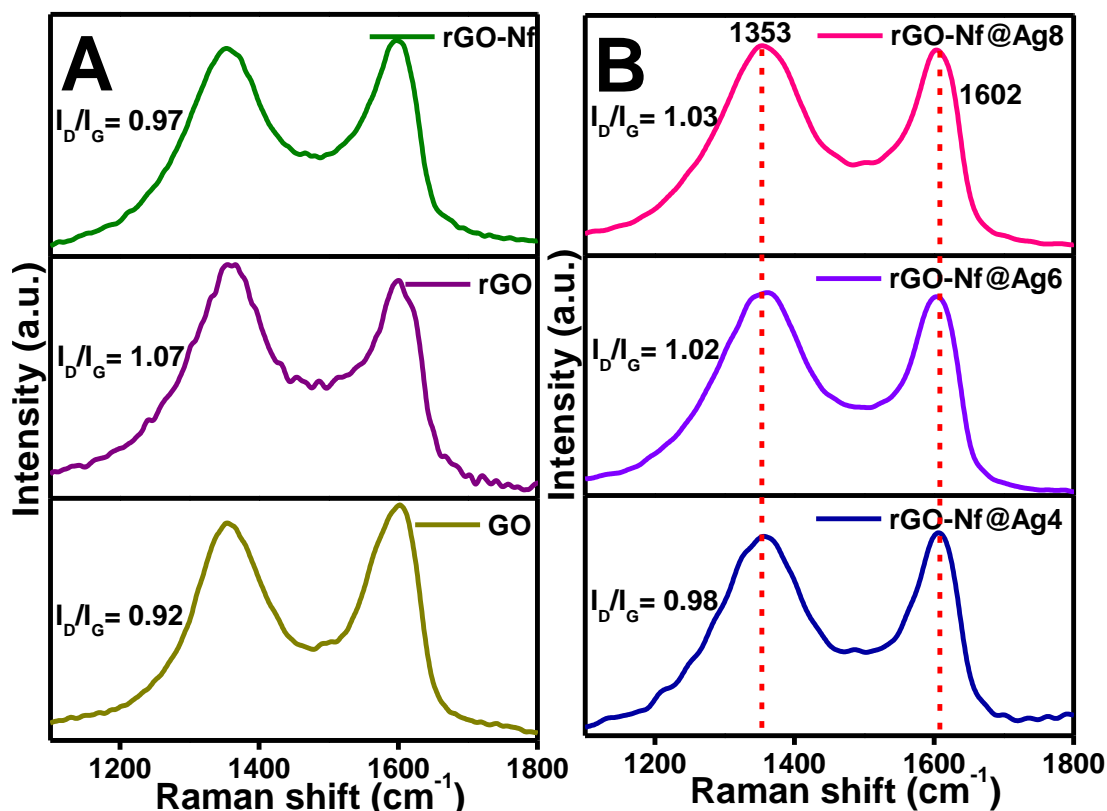


Figure 5.3: Raman spectra of (A) GO, rGO, rGO-Nf and (B) rGO-Nf@Ag nanohybrids with three different Ag contents in the range of 1100 to 1800 cm^{-1} .

Representative Raman spectra measured for three different rGO-Nf@Ag nanohybrids were plotted in Figure 5.3(B). As can be seen, the signals measured at all three nanohybrids maintained the fine features of a graphene peak, where as the intensity was increased, and D and G peak positions were slightly shifted to 1353 and 1602 cm^{-1} , respectively. The enhancement in intensity and shifting in peak position toward higher wavenumbers after coupling with AgNPs mainly arose from the electromagnetic mechanism effect, based on the charge transfer between graphene and AgNPs (Lee *et al.*, 2010), thus efficiently attesting to the existence of AgNPs in the

nanohybrids. It is worth noting that the I_D/I_G ratio of the ternary nanohybrids was significantly enhanced by deposition of AgNPs. This is because the insertion of AgNPs within the rGO-Nf layers leads to an increase in the defects on the nanohybrid materials. One can also notice significant increment in the I_D/I_G ratio, from 0.98 to 1.03, as the AgNO_3 concentration increased from 4 to 8 mM, which was associated with the higher defectiveness induced by the increment of AgNPs content in the nanohybrids.

XPS was performed to obtain evidence that the AgNPs were formed on rGO-Nf surfaces. The C1s core-level spectra of GO in Figure 5.4(A) shows a broadened peak that can be fitted by four Gaussian components at 283.3, 284.8, 286.1 and 287.3 eV and assigned to the C-C (aromatic rings), C-O (hydroxyl and epoxy), C=O (carbonyl) and O=C-O (carboxyl) functional groups, respectively (Ganguly *et al.*, 2011). It is notable that the intensity of all oxide functional groups had reduced after the hydrothermal treatment indicating the successful deoxygenation of GO to form rGO (Figure 5.4(B)). As to the C1s core-level spectra of rGO-Nf and three different nanohybrids (Figure 5.4(C)), the binding energy at 284.9 eV can be assigned to the C-C group from rGO, while the appearance of binding energy at 291.2 eV can be ascribed to the C-F (CF_2 , FCO, CF_3 , OCFSO_2) group from Nf (Aragaw *et al.*, 2013). Figure 5.4(D) shows the Ag3d core-level spectra of all three nanohybrids, which exhibit well defined double peak formations located at binding energies of 368.3 and 374.4 eV, corresponding to the $\text{Ag3d}_{5/2}$ and $\text{Ag3d}_{3/2}$, respectively. The difference of about 6.1 eV between these two binding energies verifies the formation of metallic AgNPs (Lim *et al.*, 2015). Overall results obtained from the XPS core-level spectra suggest the successful coupling between AgNPs, rGO and Nf to form ternary nanohybrid materials.

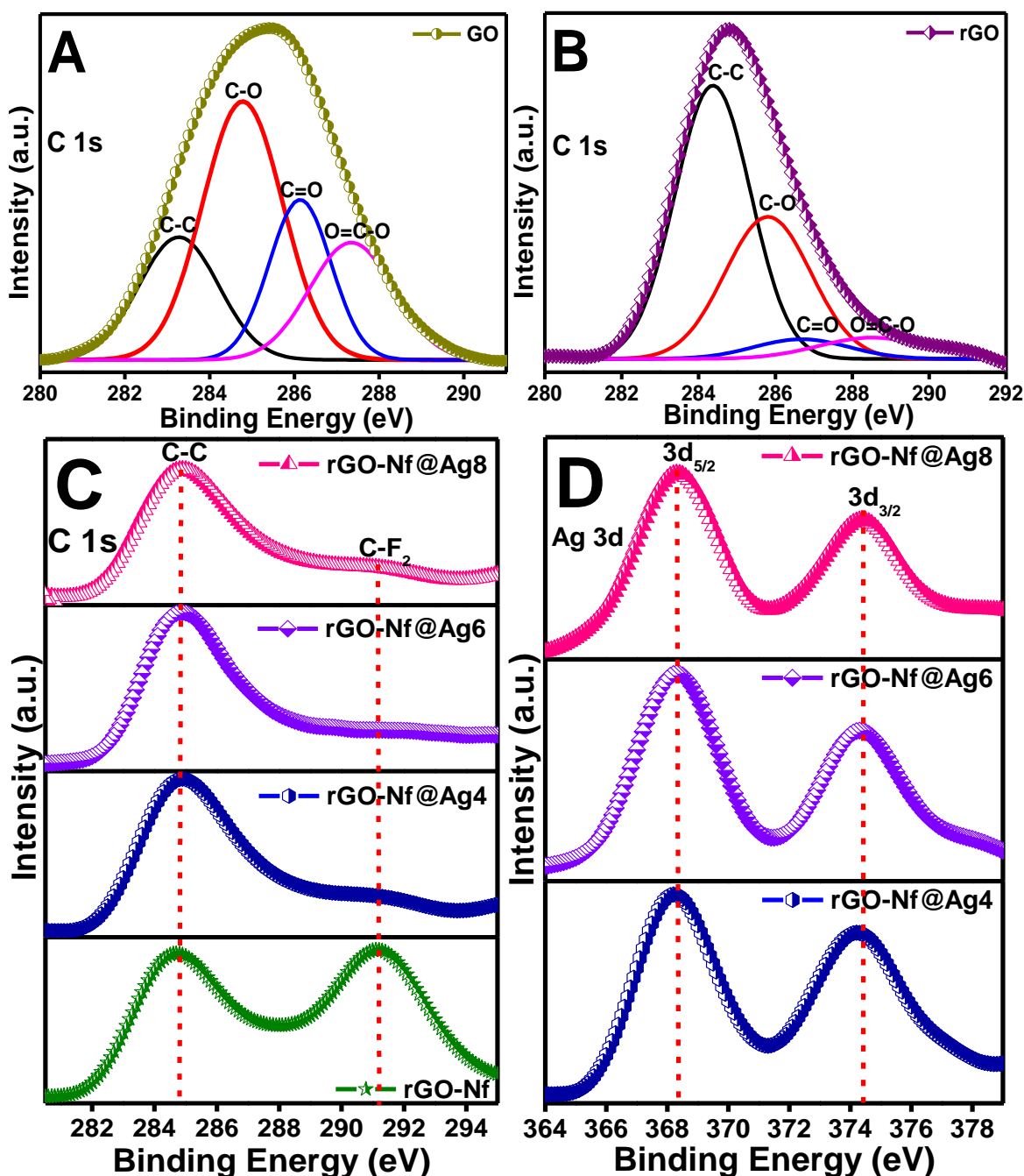


Figure 5.4: XPS spectra of GO, rGO, rGO-Nf and rGO-Nf@Ag nanohybrids with three different Ag contents and their corresponding (A-C) C1s and (D) Ag3d core-level spectra.

5.2.3 Morphological Characterization of rGO-Nf@Ag Nanohybrids

Figure 5.5(A) presents the representative FESEM image of free standing GO nanosheets. The GO flakes possess an average lateral dimension of more than 3 μm that appears to be built up from a few larger flakes of graphene that stack together to form

thicker GO flakes with wavy wrinkles on their surfaces. This corrugation of the GO sheets was attributed to the disruption of the planar sp^2 carbon sheets by the introduction of sp^3 hybridized carbon upon oxidation (Wang *et al.*, 2009).

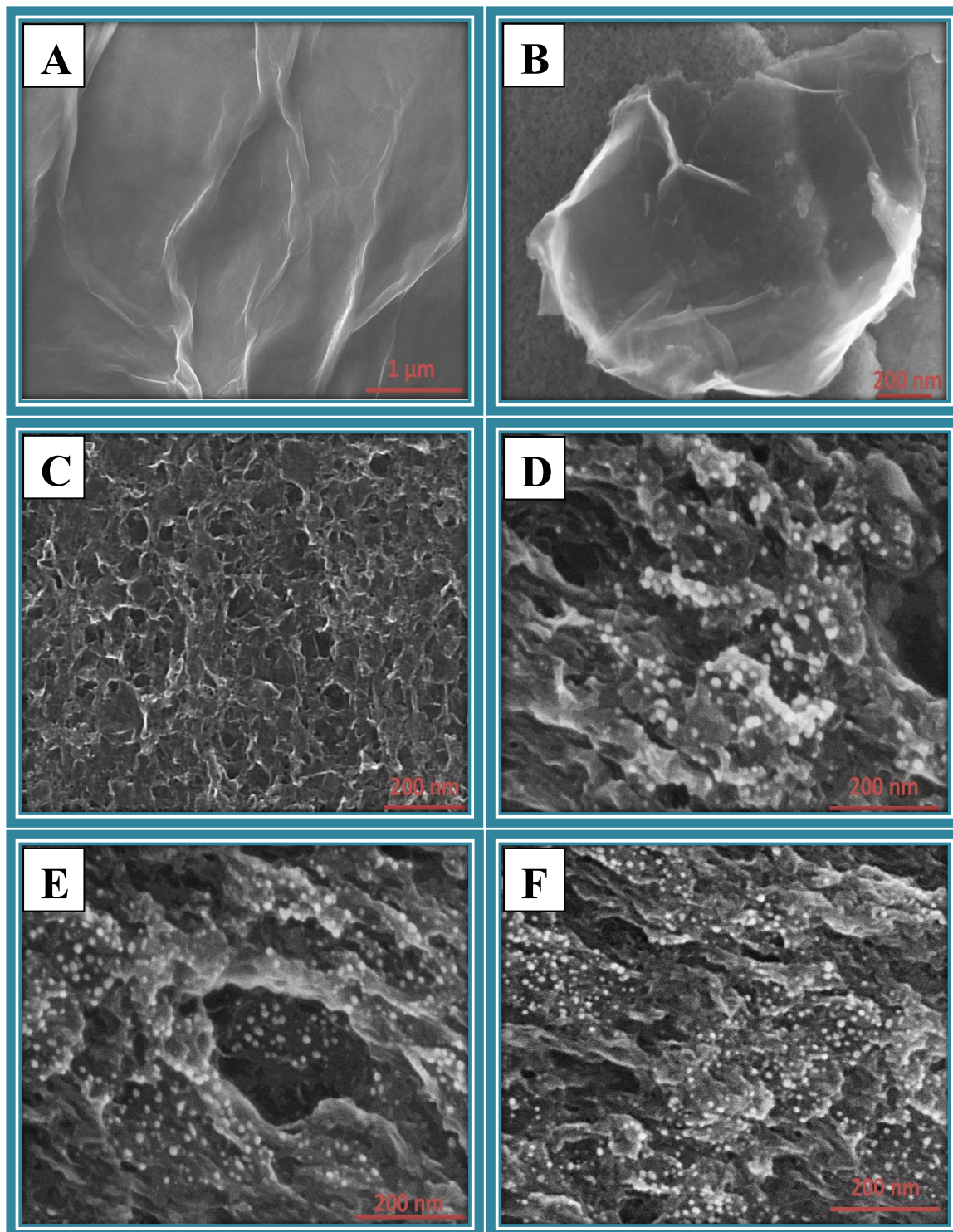


Figure 5.5: FESEM images of (A) GO, (B) rGO, (C) rGO-Nf, (D) rGO-Nf@Ag4 nanohybrid, (E) rGO-Nf@Ag6 nanohybrid and (F) rGO-Nf@Ag8 nanohybrid.

Most of the wrinkle on the surface disappeared after the hydrothermal reduction process, as shown in Figure 5.5(B), due to the removal of oxygen-containing functional groups in GO. The rGO-Nf nanohybrid exhibits a rough wrinkle and crumpled surface due to the incorporation of the Nf layer into the nanohybrid, thus confirming the formation of rGO-Nf nanohybrid (Figure 5.5(C)). The morphologies of rGO-Nf@Ag nanohybrids with different AgNPs loading were shown in Figure 5.5(D-F). The well formed AgNPs covering the surface of rGO-Nf with high dispersion can be clearly observed in all three nanohybrids.

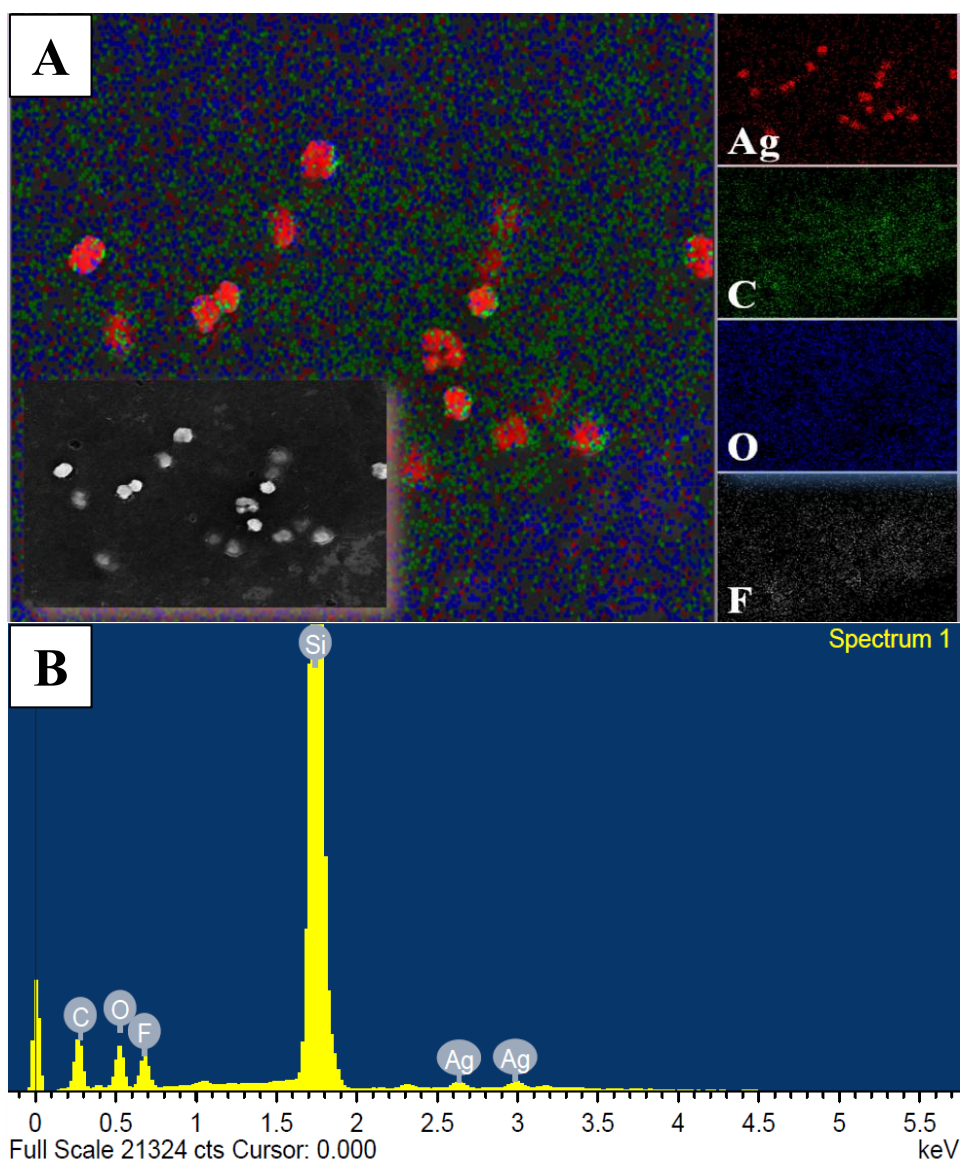


Figure 5.6: (A) Mapping of rGO-Nf@Ag8 nanohybrid at the selected area and (B) its EDX spectrum captured for the selected region.

The composite energy dispersive X-ray spectroscopic (EDX) characterization and elemental mapping were carried out to verify the composition of the rGO-Nf@Ag8 nanohybrid and the results were shown in Figure 5.6. The presence of AgNPs, Nf and rGO in the nanohybrid was confirmed by element mapping, as shown in Figure 5.6(A). Four main elements can be observed in which carbon (C) and oxygen (O) elements corresponding to rGO while fluorine (F) and Ag elements are correlates to Nf and AgNPs, respectively. The element mapping images also shows homogeneous Ag distributions with major concentration located on the rGO-Nf sheets. EDX analysis was conducted and the result further confirmed that the nanohybrid comprised of C, O, F and Ag elements, as shown in Figure 5.6(B). The silicon (Si) element is originate from the Si substrate that been used.

The surface morphology of the rGO-Nf@Ag nanohybrids were analyzed by using HRTEM. Figure 5.7 shows the HRTEM images of the three different rGO-Nf@Ag nanohybrids. It can be seen that the AgNPs are almost uniformly decorated on the wrinkled surfaces of rGO-Nf sheets with spherical shapes (Figure 5.7(A-C)). The HRTEM results reveal that the AgNPs morphology remains the same despite the increase in the AgNO₃ loading, although the coverage of AgNPs on the rGO-Nf sheets increases significantly with the increment of the AgNO₃ concentrations from 4 to 8 mM. The histogram of the AgNPs size collected from all three nanohybrids was illustrated in Figure 5.7(D-F). The diameters of AgNPs were ranging from 2 to 12 nm with average diameter of 3, 4 and 5 nm for rGO-Nf@Ag4, rGO-Nf@Ag6 and rGO-Nf@Ag8, respectively. The particle size in rGO-Nf@Ag4 was slightly smaller than the size in rGO-Nf@Ag6 and rGO-Nf@Ag8.

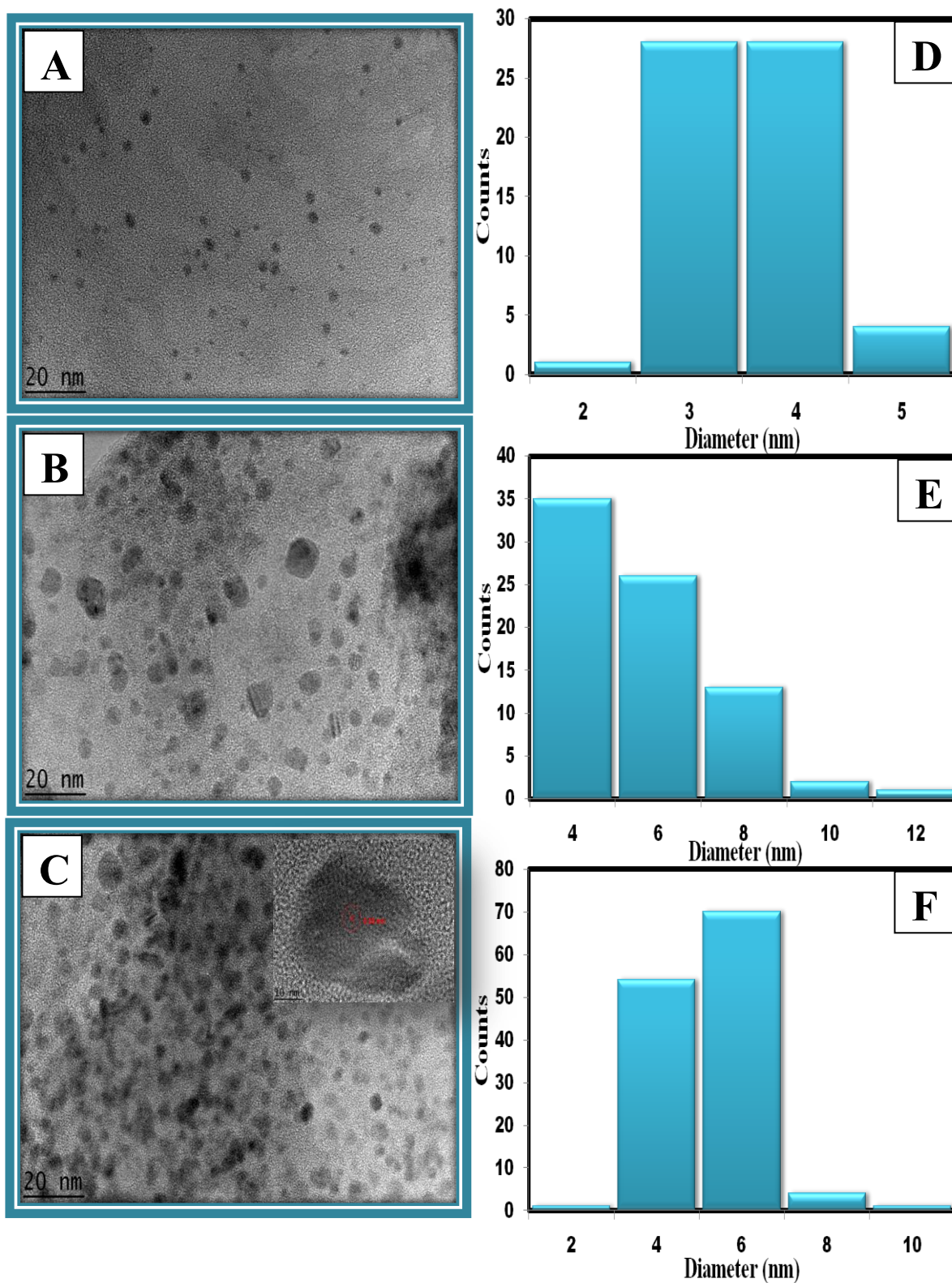


Figure 5.7: (A-C) HRTEM images of rGO-Nf@Ag4 nanohybrid, rGO-Nf@Ag6 nanohybrid and rGO-Nf@Ag8 nanohybrids with their corresponding histogram of AgNPs sizes (D-F) (Inset shows the individual AgNPs on rGO-Nf sheet).

This is because even though the concentration of AgNO_3 increased, the concentration of rGO-Nf remained the same. Thus, the limited nucleation sites on the rGO-Nf sheets led to the formation of a larger particle size as compared with the ones with lower AgNO_3 concentrations. The morphology corresponding to the individual AgNPs on the rGO-Nf sheets is illustrated in inset of Figure 5.7(C). The clear lattice fringes can be easily observed with the d spacing value of 0.28 nm, which can be attributed to the (1 2 2) planes of the face-centered cubic (FCC) phase of AgNPs (according to JCPDS: File No. 4-783) (Roy *et al.*, 2014). The FESEM and HRTEM results further reveal that the AgNPs are firmly anchored on the surface of rGO-Nf@Ag nanohybrids.

5.2.4 Electrochemical Characterization of GC/rGO-Nf@Ag Modified Electrode

All of the modified electrodes were characterized and compared using electrochemical impedance spectroscopy (EIS), which was carried out in a solution containing 5 mM $\text{K}_3[\text{Fe}(\text{CN})_6]$ and 0.1 M KCl within the frequency range from 0.01 Hz to 100 KHz. The Nyquist plot for modified electrodes is shown in Figure 5.8. As seen in Figure 5.8(A), a semicircle followed by a 45° straight line can be observed in all Nyquist plots for bare GC, Nf, GO and rGO modified GCE. The semicircular portion obtained at the lower frequency region corresponds to a charge transfer-limited process, while the linear portion in the higher frequency region can be ascribed to the diffusion-limited electron transfer process (Devadas *et al.*, 2014). The diameter of this semicircle provides a measure of the charge-transfer resistance (R_{ct}) of the as-prepared electrode where higher R_{ct} values insulate the conductive support and the interfacial electron transfer process between the electrode and electrolyte interfaces.

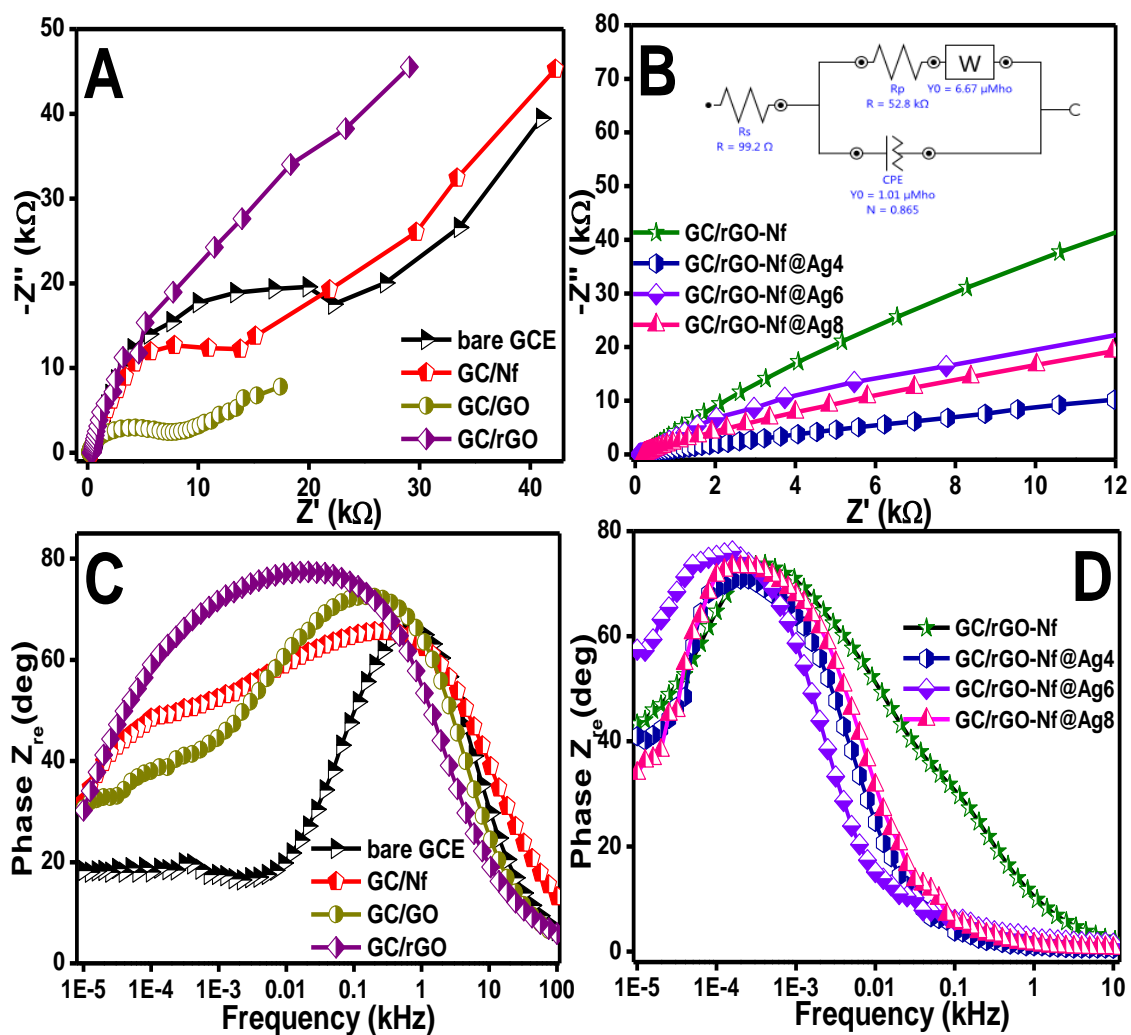


Figure 5.8: (A&B) Nyquist plots obtained for bare GCE, GC/GO, GC/Nf, and three different GC/rGO-Nf@Ag modified electrodes obtained in presence of 0.1 M KCl with 5 mM $K_3[Fe(CN)_6]$ (Inset shows the equivalent circuit that fits the impedance spectrum of GC/rGO-Nf@Ag6) and (C&D) bode plots obtained for above said different modified electrodes.

The Nyquist plots for all of the nanohybrids exhibit only a straight oblique line at lower frequencies, with an almost diminished semicircle (Figure 5.8(B)), thus demonstrating the successful modification of the electrode with the prepared nanohybrids. This indicates that these modified electrodes possess a rapid electron-transfer rate and higher electrocatalytic activity due to the reduced R_{ct} value compared with bare GCE. It has been reported that the intersection at the real axis in Nyquist plots corresponds to the ohmic resistance of the electrolyte and the internal resistance of the

electrode (R_s) (Norazriena *et al.*, 2016). The R_s values rGO-Nf@Ag4, rGO-Nf@Ag6 and rGO-Nf@Ag8 are 204.4, 99.2 and 235.98 Ω , respectively. It was observed that the rGO-Nf@Ag6 nanohybrids exhibit efficient charge transfer across the electrode-electrolyte interface due to the good electrical communication and conduction path between the electrode and electrolyte with lower R_s values compared with other modified electrodes. The impedance data obtained from rGO-Nf@Ag6 nanohybrid was fitted using an equivalent circuit model with NOVA 1.11 software (Metrohm) (inserted in Figure 5.8(B)).

The equivalent circuit was composed of several parameters including R_s , which is in series with the complex component consisting of the constant phase element (CPE) that was in parallel with R_{ct} and the Warburg constant (W). The Warburg impedance (Z_w) resulted from diffusion of the redox probe, whereas the interfacial properties of the electrode, which were highly sensitive to surface modification, were represented by R_{ct} and CPE (Olowu *et al.*, 2010). The frequency dependence of the phase angle of the modified electrode and bare GCE is depicted in Figure 5.8(C) and 5.8(D). A phase angle of greater than or equal to 90° is expected for a pure capacitive behavior. However, it can be clearly seen that none of these modified electrodes behave like an ideal capacitor as the phase angle is less than 90° . At low frequencies, the shifting in the characteristic frequency peak toward lower frequencies could be observed, following the order of: bare GC < GC/Nf < GC/GO < GC/rGO < GC/rGO-Nf < GC/rGO-Nf@Ag8 < GC/rGO-Nf@Ag4 < GC/rGO-Nf@Ag6.

The τ_n value for GC/rGO-Nf, GC/rGO-Nf@Ag4, GC/rGO-Nf@Ag6 and GC/rGO-Nf@Ag8 was calculated to be 62, 100.5, 110.5 and 89.3 ms, respectively. Obviously, the combination of AgNPs with rGO-Nf leads to a longer lifetime and faster diffusion

rate. The overall results interpreted from EIS data can attributed to the ternary nanohybrid materials, especially the rGO-Nf@Ag6 nanohybrid, having good electrical conductivity that was beneficial for the electron transfer process during electrocatalytic reactions, thus leading to the highest electrocatalytic performance with fastest diffusion rate.

The comparative CV profile demonstrating the $[\text{Fe}(\text{CN})_6]^{3-/4-}$ redox process by bare GCE and various modified electrodes were shown in Figure 5.9. Apparently, there was no recognizable redox peak on the CV profile obtained from GC/Nf, probably due to the insulating and blocking of the $[\text{Fe}(\text{CN})_6]^{3-/4-}$ ions to reach the electrode surface caused by the electrostatic repulsion between negatively charged Nf and $[\text{Fe}(\text{CN})_6]^{3-/4-}$ (inserted in Figure 5.9). After modifying the GCE with GO, several redox peaks were observed with lower faradic current of the $[\text{Fe}(\text{CN})_6]^{3-/4-}$ ions, which could be attributed to the non-conductive properties of GO that reduced the interfacial electron transfer rate, thus giving rise to the low current response.

The CV plots of bare GCE and three different GC/rGO-Nf@Ag modified electrodes shows well defined redox peaks, corresponding to the reversible redox reaction of $[\text{Fe}(\text{CN})_6]^{3-/4-}$ ions. Peak-to-peak potential separation (ΔE_p) values of 92.8, 84.3 and 100.9 mV were observed for GC/rGO-Nf@Ag4, GC/rGO-Nf@Ag6 and GC/rGO-Nf@Ag8, respectively. The incorporation between AgNPs and rGO-Nf provides more electroactive surfaces that give rise to the higher electron transfer rate at the electrode/electrolyte interface, thus improving the electrochemical behavior of the modified electrode. Note that the higher redox current with smaller ΔE_p between cathodic and anodic peaks of GC/rGO-Nf@Ag6 demonstrates the fast response

resulting from the excellent electrical conductivity of the newly prepared ternary nanohybrid material.

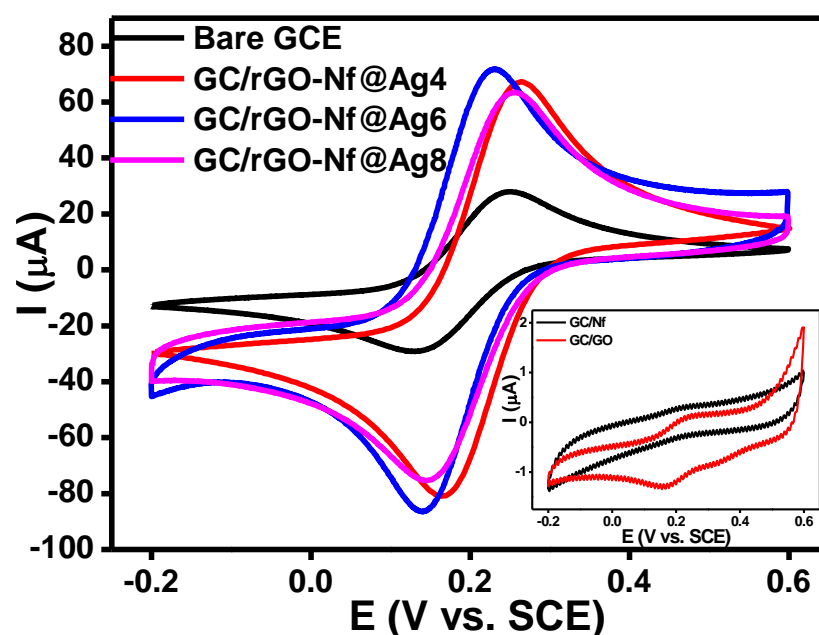


Figure 5.9: CV curves for control modified electrode as well as three different nanohybrids modified electrodes obtained in the presence of 0.1 M KCl with 5 mM $K_3[Fe(CN)_6]$ (Inset shows the enlargement of CV curves obtained from GC/Nf and GC/GO).

5.2.5 Electrochemical Determination of Hydrogen Peroxide

5.2.5.1 Electrocatalytic Reduction of Hydrogen Peroxide

The applicability of the rGO-Nf@Ag nanohybrid modified GCE was explored for the electrocatalytic reduction and detection of H_2O_2 . Figure 5.10 shows the representative CV curves of 10 mM H_2O_2 concentrations in 0.2 M PBS (pH 7.2) using different modified electrodes at a scan rate of 50 mV/s. In the absence of H_2O_2 , no redox peak was observed for the bare GCE (Figure 5.10(A)). Upon the addition of 1 mM H_2O_2 into the PBS, the reduction peak of H_2O_2 still could not be observed by using the bare GCE and several modified electrodes, including GC/Nf, GC/GO, and GC/rGO.

In contrast, the existence of a cathodic peak due to the electrocatalytic reduction of H_2O_2 was observed at a potential of around -0.47 V obtained from the GC/rGO-Nf modified electrode. As can be seen from Figure 5.10(B), no peak could be observed on GC/rGO-Nf@Ag6 without the presence of H_2O_2 . The reduction peak of H_2O_2 appeared on GC/rGO-Nf, GC/rGO-Nf@Ag4, GC/rGO-Nf@Ag6 and GC/rGO-Nf@Ag8 with a peak current of 114.96 , 142.26 , 190.04 and $139.47\text{ }\mu\text{A}$, respectively. It was found that GC/rGO-Nf@Ag6 displays the highest catalytic current response and demonstrates excellent electrocatalytic activity toward the reduction of H_2O_2 in comparison with other modified electrodes. The high surface area provided by AgNPs and excellent conductivity of rGO-Nf greatly contributed to enhancing the electrocatalytic activity for reducing H_2O_2 .

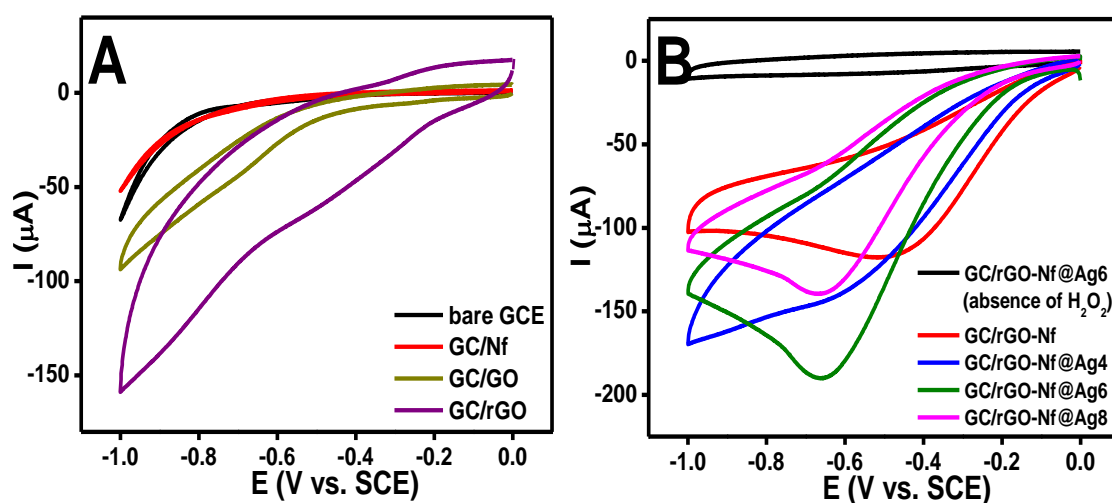


Figure 5.10: (A&B) CV curves obtained for bare GCE, GC/GO, GC/Nf, GC/rGO, GC/rGO-Nf and three different GC/rGO-Nf@Ag modified electrodes in the presence of 0.2 M PBS ($\text{pH } 7.2$) containing 10 mM H_2O_2 at a scan rate of 50 mV/s .

Although the enhancement of sensor performance was related to the concentration of electrocatalytic active sites on the electrode surface provided by AgNPs, excessive AgNPs content forms the aggregation deteriorates the quality of the sensor electrode. The degradation of electrocatalytic ability to reduce H_2O_2 was the consequences of the

increased diffusion layer thickness, which hinders the electron transfer between electrode/electrolyte surfaces, as occurred with the GC/rGO-Nf@Ag8 modified electrode. A possible mechanism of H₂O₂ reduction at the modified electrode is proposed below (Figure 5.11):

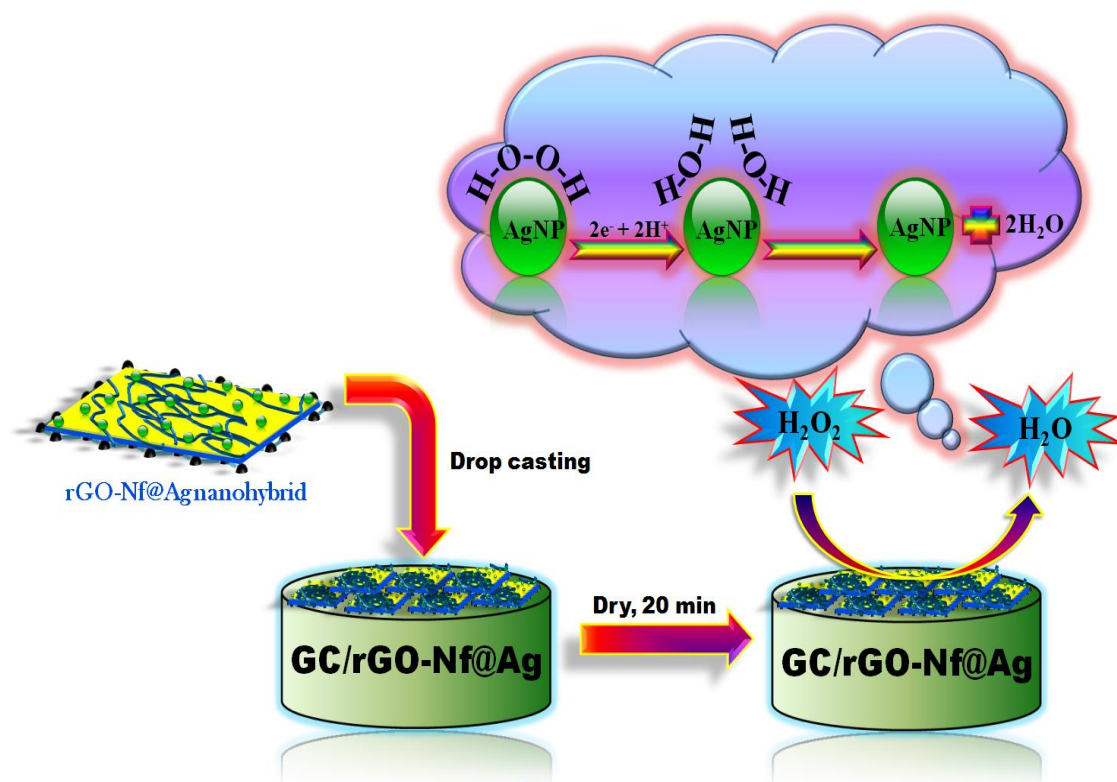
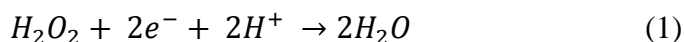


Figure 5.11: Schematic representation for the fabrication of rGO-Nf@Ag nanohybrid modified GCE and the mechanism of electrocatalytic reduction of H₂O₂.

In the case of neutral solution (PBS pH 7.2), the cathodic reduction occurs for H₂O₂ upon an applied constant potential of about -0.65 V, producing a final product of H₂O. The electron transfer was mainly controlled by the diffusion process. The lower R_s value and thinner diffusion layer thickness facilitates the electron transfer rate. The increased amount of AgNPs with smaller size deposited on rGO-Nf layers provides larger active surface areas, thereby enhancing the electrocatalytic activity and boost the

analytical performance. The GC/rGO-Nf@Ag6 modified electrode was chosen as the sensor electrode for further investigation of H_2O_2 sensing due to the outstanding electrochemical behavior and good electrocatalytic reduction performance demonstrated by this modified electrode towards H_2O_2 detection.

5.2.5.2 Optimization Studies

(a) Effect of Different Concentration of Hydrogen Peroxide

The effect of H_2O_2 concentrations on the cathodic peak current due to the electrocatalytic reduction of H_2O_2 was investigated by CV method. A series of CV curves for the GC/rGO-Nf@Ag6 modified electrode in 0.2 M PBS (pH 7.2) with the successive injection of H_2O_2 were recorded and the current response against the time was plotted as shown in Figure 5.12(A). The characteristic shape of CV curve in this potential region indicates that the cathodic peak at a potential around -0.65 V was responsible for the electrocatalytic reduction of H_2O_2 .

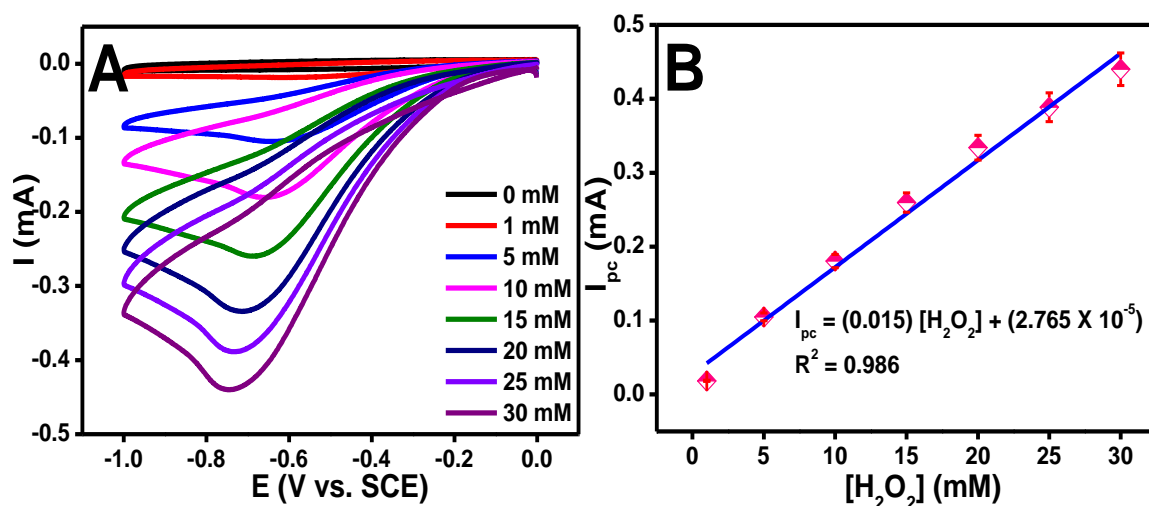


Figure 5.12: (A) CV curves obtained for the GC/rGO-Nf@Ag6 modified electrode in the presence of 0.2 M PBS (pH 7.2) and different concentrations of H_2O_2 (1 to 30 mM) at a scan rate of 50 mV/s and (B) the corresponding plot of cathodic peak currents versus different H_2O_2 concentrations.

The efficient electrocatalytic performance of the modified electrode was proven by the linear relationship between cathodic peak current and H_2O_2 concentrations, as can be seen in Figure 5.12(B). A linear relationship was observed within the range from 1 to 30 mM and can be described by the linear regression equation of $I_{pc} = 0.015[\text{H}_2\text{O}_2] + (2.765 \times 10^{-5})$, with a correlation coefficient, $R^2 = 0.986$.

(b) Effect of Scan Rate

In order to elucidate the variation in the scan rate on the voltammetric behaviors of H_2O_2 at the modified electrode, a control experiment was performed by changing the scan rate from 10 to 300 mV/s. As can be seen in Figure 5.13(A), the cathodic peak current observed at -0.65 V was enhanced markedly as the scan rates increased, whereas the cathodic peak potentials shifted toward more positive potential with increasing scan rate. The shift of the cathodic peak potential clearly suggests that the reduction of H_2O_2 was an irreversible electrochemical reaction and a kinetic limitation in the reaction between the active sites of GC/rGO-Nf@Ag6 and analyte, H_2O_2 .

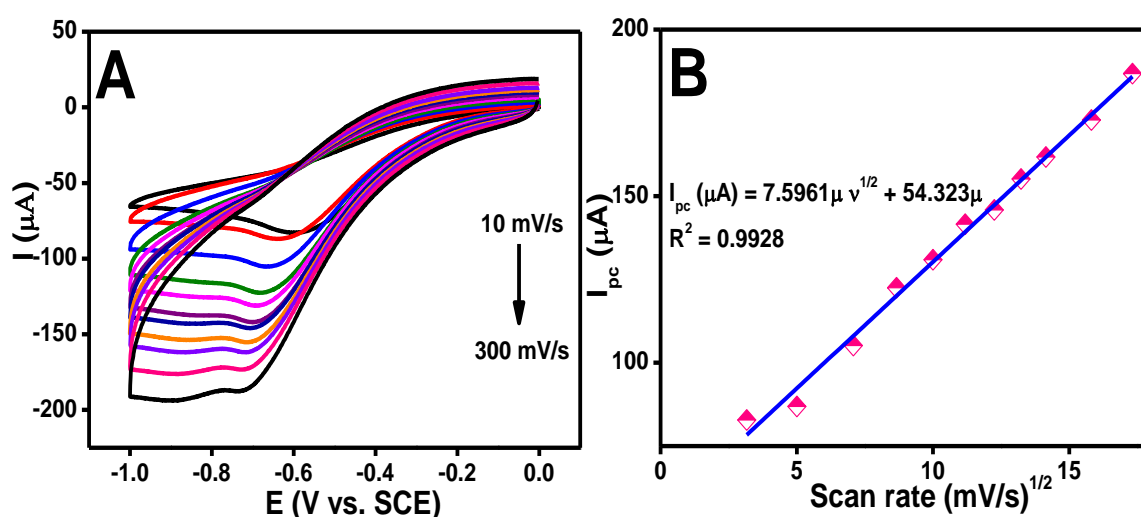


Figure 5.13: (A) CV plots obtained for GC/rGO-Nf@Ag6 modified electrode in 0.2 M PBS (pH 7.2) with presence of 10 mM H_2O_2 at a scan rates of 10–300 mV/s and (B) the corresponding plot of cathodic peak currents versus square root of scan rate.

As indicated from the resulting calibration plots of cathodic peak currents *versus* square root of scan rate (Figure 5.13(B)), a linear relationship was observed for the electrocatalytic reduction of H_2O_2 , with a correlation coefficient of 0.9928. On the basis of the obtained results, it can be stated that the reduction of H_2O_2 at the GC/rGO-Nf@Ag6-modified electrode was diffusion controlled process. The D value was calculated to be about $1.584 \times 10^{-9} \text{ cm}^2 \text{ s}^{-1}$.

(c) Effect of rGO-Nf@Ag6 Loading

In order to evaluate the effect of rGO-Nf@Ag6 loading on the electrocatalytic activity of the modified electrode, the CV curves were measured using the GC/rGO-Nf@Ag6 modified electrode with 5 mM H_2O_2 in 0.2 M PBS as shown in Figure 5.14(A).

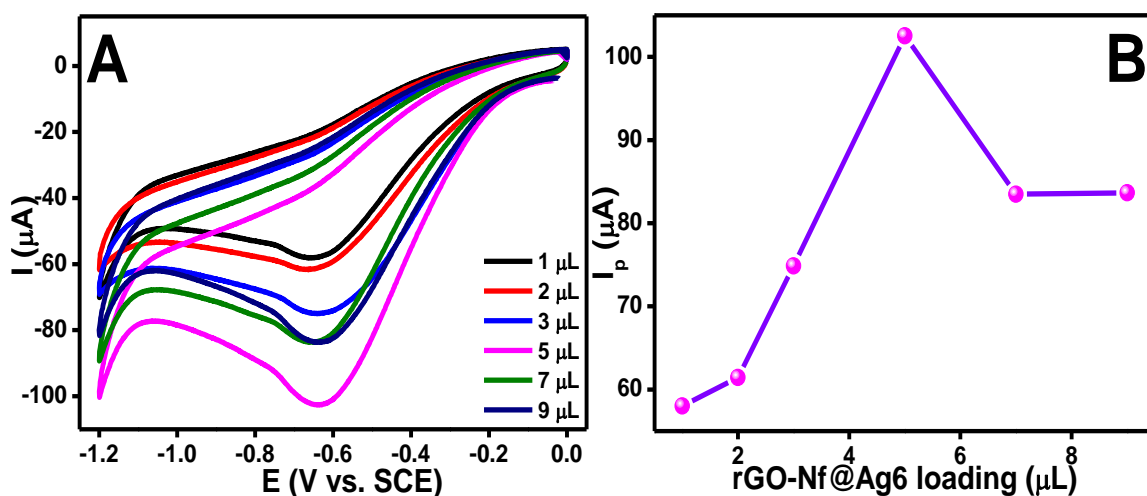


Figure 5.14: (A) CV curves obtained for GC/rGO-Nf@Ag6 modified electrode with different amount of sample loading and (B) plot of rGO-Nf@Ag6 loading versus cathodic peak current response obtained for the 5 mM H_2O_2 in 0.2 M PBS (pH 7.2) at a scan rate of 50 mV/s.

As can be seen in Figure 5.14(B), the reduction peak current increased when the amount of rGO-Nf@Ag6 coating on the electrode surface increased from 1 to 5 μL . This might due to the increased in the amount of effective surface area for H_2O_2 reduction, thus allowed rapid electron transfers which then increase the current response. However, the reduction peak current started to decrease when the volume of rGO-Nf@Ag6 solution was increased from 6 to 9 μL . The thick rGO-Nf@Ag6 films formed on the surface of electrode have increased the diffusion distance of H_2O_2 hence hindering the target analytes from reaching the electrode surface where the reaction occurs. As a result, the current response will decrease. This result demonstrates that the amount of rGO-Nf@Ag6 loaded on the electrode surface affecting the electrocatalytic performance toward the reduction of H_2O_2 .

5.2.5.3 Amperometric Response of Hydrogen Peroxide

The GC/rGO-Nf@Ag6 modified electrode was chosen as a sensor electrode for further investigation of H_2O_2 sensing due to the outstanding electrochemical behavior and good electrocatalytic reduction performance demonstrated by this modified electrode towards H_2O_2 detection. The reduction current with respect to time was recorded for successive additions of H_2O_2 in 0.2 M PBS (pH 7.2) using the fabricated electrode sensor at the applied potential of -0.6 V (Figure 5.15). Figure 5.15(A) shows the typical amperometric curve for the GC/rGO-Nf@Ag6 modified electrode with the successive addition of H_2O_2 concentration.

The enhancement in current response was obvious for the successive injection of different concentrations of H_2O_2 and a linear relationship was observed between the current response and H_2O_2 concentration. Based on the results plotted in Figure 5.15(B), three different linear curves could be observed. The first one corresponds to the

concentration range from 1 to 10 μM with a linear regression equation of $I(\mu\text{A}) = 0.454 [H_2O_2] + 0.048$ ($R^2 = 0.995$). The second and third linear curves correspond to the concentration ranges from 15–80 μM and 90–300 μM with linear regression equations of $I(\mu\text{A}) = 0.116 [H_2O_2] + 0.151$ ($R^2 = 0.985$) and $I(\mu\text{A}) = 0.013 [H_2O_2] + 0.108$ ($R^2 = 0.965$), respectively. The limit of detection (LoD) and limit of quantification (LoQ) were calculated to be 5×10^{-7} M and 1 μM , respectively, with the S/N of 3 and correlation coefficients of 0.993. The sensitivity calculated from the slope of the calibration curve, was found to be $0.4508 \mu\text{A } \mu\text{M}^{-1}$.

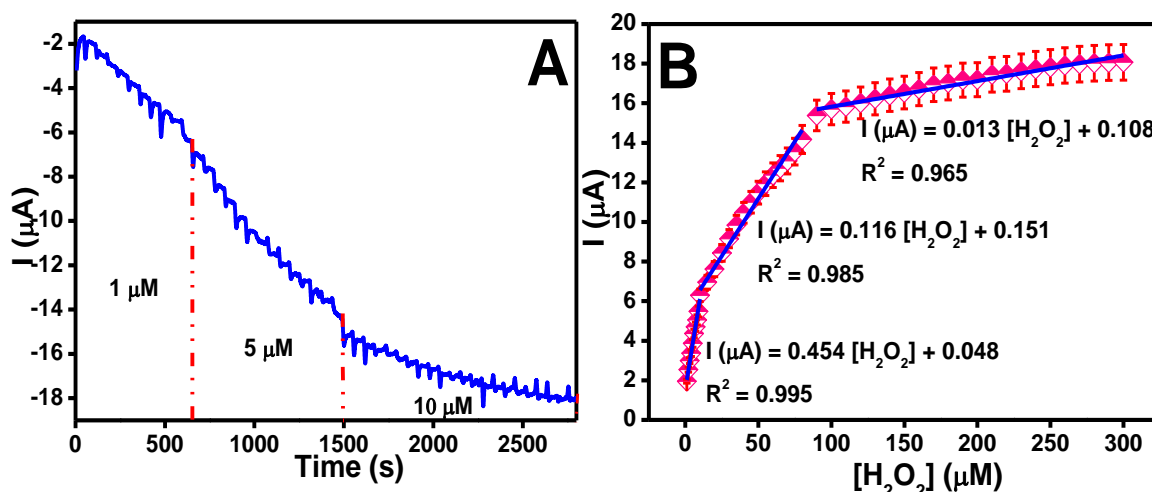


Figure 5.15: (A) Amperometric (I-t) curve of the GC/rGO-Nf@Ag6 modified electrode on successive additions of H_2O_2 stirred into 0.2 M PBS (pH 7.2) at an applied potential of -0.6 V and (B) the corresponding calibration plot of current against concentration of H_2O_2 .

The obtained results confirmed that the existence of AgNPs in rGO-Nf film plays an important role in boosting the sensing performance toward H_2O_2 detection by providing more active surface area for the reaction to occur. Moreover, the strong synergetic effect between each element in these ternary nanohybrids further facilitates the electron transfer kinetics during the electrocatalytic reduction of H_2O_2 , thereby enhancing the sensitivity of the sensor electrode. The rough surfaces and layered structure of the rGO-Nf@Ag nanohybrids could provide an advantage in facilitating the diffusion of analytes

into the rGO-Nf@Ag sheets during the electrocatalytic activity reaction, thereby increasing the effectiveness of the electrode surface.

Table 5.1 compiles the analytical parameters for electrochemical H₂O₂ sensing using various materials for modifying the GCE that have been reported in literature. It can be seen that the LoD for our sensor electrode is competitive with other modified electrodes, such that one can conclude that the GC/rGO-Nf@Ag6 modified electrode can be a good H₂O₂ amperometric sensor.

Table 5.1: Comparison of the analytical performance of various electrodes in electrochemical detection of H₂O₂.

| Electrode | Analytical method | Analysis times (sec) | Limit of detection (μM) | Sensitivity | Interferences | Reference |
|--|-------------------|----------------------|--------------------------------------|---|---|----------------------------------|
| GC/Co-MOF | Amperometry | 2 | 3.76 | $83.10 \mu\text{A mM}^{-1} \text{cm}^2$ | Saccharin sodium, Glycerol, Ethanol, Glucose, Lactic acid | (Yang <i>et al.</i> , 2015) |
| GC/PDDA-rGO/AgNPs | Amperometry | 5 | 35 | $9.17 \text{ m} \mu\text{A} \mu\text{M}^{-1}$ | UA, AA | (Liu <i>et al.</i> , 2013) |
| FTO/ α -Fe ₂ O ₃ NR/FePO ₄ | Amperometry | 15 | 1.3 | $181 \mu\text{A mM}^{-1} \text{cm}^{-2}$ | UA, AA, DA | (Lin <i>et al.</i> , 2015) |
| GC/Ag/C | Amperometry | - | 1.3 | - | UA, AA, Glucose | (Jiang <i>et al.</i> , 2014) |
| GC/Ag@Pt-graphene | Amperometry | - | 0.9 | - | AA, DA, Glucose | (Liu <i>et al.</i> , 2016) |
| GC/Graphene-AgNPLs | Amperometry | 2 | 3 | $183.5 \mu\text{A mM}^{-1} \text{cm}^{-2}$ | - | (Zhong <i>et al.</i> , 2013) |
| GC/AgNP-MWCNT-rGO | Amperometry | 3 | 0.9 | - | AA, Ethanol, Glucose, Glycin | (Lorestani <i>et al.</i> , 2015) |
| AgNPs-rGO-2/ITO | Amperometry | 2 | 5 | - | - | (Golsheikh <i>et al.</i> , 2013) |
| GC/CNT-PDDA@Ag | Amperometry | 2 | 1.6 | - | - | (Shi <i>et al.</i> , 2011) |
| GC/GO-Ag | Amperometry | - | 28.3 | $0.1218 \mu\text{A mM}^{-1}$ | DA, UA, AA, Glucose | (Noor <i>et al.</i> , 2015) |

Table 5.1, continued

| Electrode | Analytical method | Analysis times (sec) | Limit of detection (μM) | Sensitivity | Interferences | Reference |
|-----------------------------------|-------------------|----------------------|--------------------------------------|--|---------------------------------|----------------------------|
| AgPs-SWCNT | Amperometry | 2 | 2.76 | $10.92 \mu\text{A mM}^{-1} \text{mm}^{-2}$ | AA | (Bui <i>et al.</i> , 2010) |
| GC/AgNP/rGO | Amperometry | - | 3.6 | - | - | (Li <i>et al.</i> , 2012) |
| GC/AgNP-TiO₂ NW | Amperometry | 2 | 1.7 | - | UA, AA, DA, Glucose | (Qin <i>et al.</i> , 2012) |
| GC/ERG O-Nafion/AuNPs | Amperometry | 1 | 2.0 | $574.8 \mu\text{A mM}^{-1} \text{cm}^{-2}$ | AA, Methanol, Ethanol, Glucose | (Lv <i>et al.</i> , 2016) |
| GC/rGO-Nf@Ag6 | Amperometry | 1 | 0.535 | $0.4508 \mu\text{A} \mu\text{M}^{-1}$ | DA, UA, AA, Glucose, Urea, NaCl | This work |

Co-MOF=cobalt-metal organic frameworks; PDDA=poly(diallyldimethylammonium chloride); FTO/ α -Fe₂O₃NR/FePO₄=Flourine-doped tin oxide coated glass/iron oxide nanorod arrays/ iron phosphate; C=amorphous carbon; Pt=platinum; AgNPLs=silver nanoplates; MWCNT=multi-walled carbon nanotube; ITO=indium-tin-oxide; CNT-PDDA=carbon nanotubes functionalized by poly(diallyldimethylammonium chloride); SWCNT=single-walled carbon nanotube film; TiO₂ NW=titanium dioxide nanowires.

5.2.5.4 Interference Study

Since there are few species such as NaCl, urea, glucose, DA, UA, and AA were naturally coexist with H₂O₂ in the extracellular fluid of the central nervous system/body fluids, thus, they tend to intervene in detecting the presence of H₂O₂ and determining the concentration of H₂O₂ (Zhu *et al.*, 2016). Moreover, they are also highly active at enzyme-free electrode systems; therefore, it is crucial to study the influence of mentioned species as potential interfering compounds on the H₂O₂ determination. In order to demonstrate the capability of the GC/rGO-Nf@Ag6 modified electrode to distinguish the interfering species from the analyte in the non-enzymatic electrochemical H₂O₂ sensors, the amperometric responses were carried out at an applied potential of -0.65 V in a continuously stirred 0.2 M PBS (pH 7.2) with gradually injected H₂O₂, NaCl, urea, glucose, DA, UA and AA.

Figure 5.16 depicts the typical amperometric response curves obtained for the GC/rGO-Nf@Ag6 modified electrode in the presence of 1 mM H₂O₂ and a few conventional substances that potentially interfere with the detection of H₂O₂.

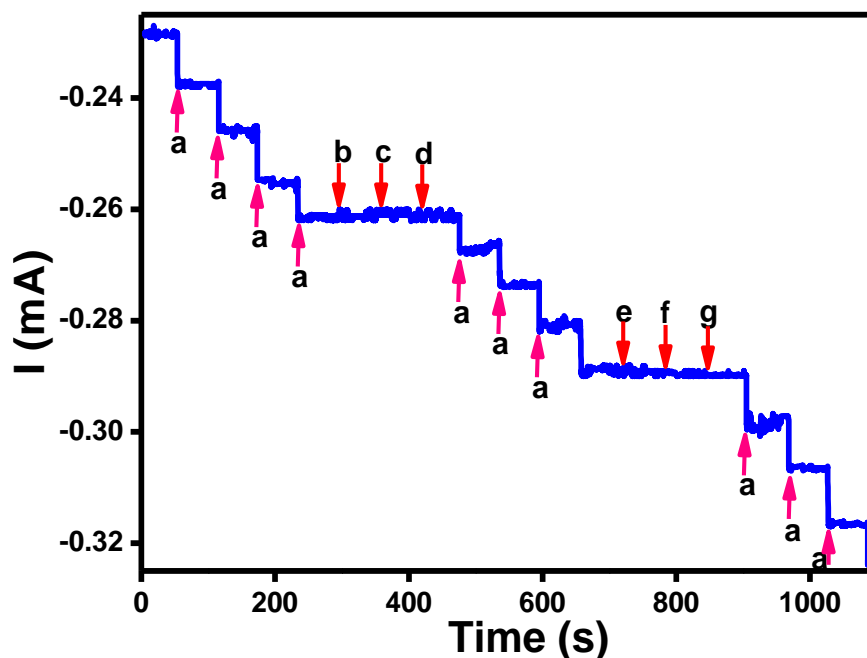


Figure 5.16: Amperometric (I-t) curve responses obtained at GC/rGO-Nf@Ag6 modified electrode for the successive addition of (a) 1 mM H₂O₂ and each 5 mM of (b) NaCl, (c) urea, (d) glucose, (e) DA, (f) UA and (g) AA in 0.2 M PBS (pH 7.2) at a regular time interval of 60 sec at an applied potential of -0.6 V versus SCE.

It is observed that the current signal of H₂O₂ was not significantly affected by the presence of potential interfering species. The results obtained from selectivity experiment suggested that the GC/rGO-Nf@Ag6 modified electrode can detect H₂O₂ even with a five-fold excess concentration of NaCl, urea, glucose, DA, UA, and AA compared with the concentration of H₂O₂. Consequently, the results prove that the GC/rGO-Nf@Ag6 modified electrode can be used as an ideal sensor electrode to achieve the selective detection of H₂O₂ despite the presence of high concentrations of interfering analytes. Thus, the sensitivity and selectivity of the sensor electrode for determining H₂O₂ increased significantly. Recently, Lv *et al.* (2016) developed an amperometric sensor using an electrochemically rGO-Nf/AuNPs modified GCE for the

successful detection of H_2O_2 . However, the present sensor stands out for its facile hydrothermal synthesis, easy fabrication, usage of low-cost metal, LoD and high sensitivity towards H_2O_2 in the presence of interferents.

5.2.5.5 Reproducibility, Repeatability, and Stability Studies

The reproducibility of the GC/rGO-Nf@Ag6 modified electrode was analyzed by recording the CV response to the reduction of 1 mM H_2O_2 carried out at 5 different GC/rGO-Nf@Ag6 modified electrodes that had been prepared separately under the same conditions (Figure 5.17(A)). No obvious cathodic current decay was observed. The as-obtained results imply at high reproducibility for the sensor electrode, where the RSD was calculated to be 0.6 %. The repeatability of the GC/rGO-Nf@Ag6 modified electrode was investigated by repetitive measurements of its response to 1 mM H_2O_2 carried out by using a single modified electrode (Figure 5.17(B)). It was found that the H_2O_2 reduction peak currents maintained about 94.8 % of their initial peak current values after five successive CV measurements, with a RSD of about 2.0 %, for the GC/rGO-Nf@Ag6 modified electrode.

In order to evaluate the stability of the sensor electrode, the GC/rGO-Nf@Ag6 modified electrode was stored in air at ambient temperature for a period of time, and the CV curves were recorded every 24 hours (Figure 5.17(C)). This confirmed that the sensor electrode has good stability, as it was able to retain 96.2 % of its initial current response after a total storage period of 5 days. Overall, the sensor electrode displayed high repeatability, reproducibility, and stability for determining H_2O_2 , which are essential characteristics features for a sensor in practical application.

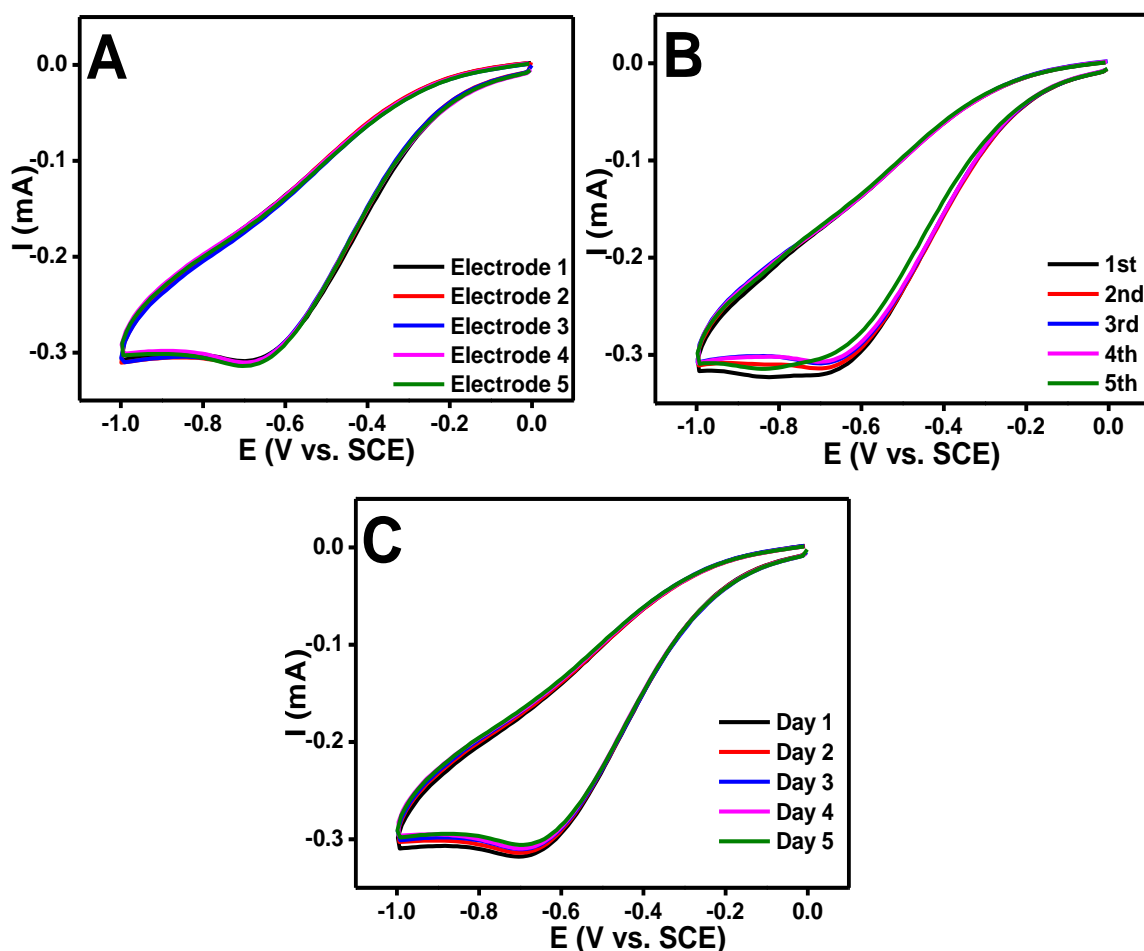


Figure 5.17: (A) CV curves of five different GC/rGO-Nf@Ag6 modified electrodes, (B) CV curves of five successive measurements of single GC/rGO-Nf@Ag6 modified electrode with 20 mM H₂O₂ in 0.2 M PBS (pH 7.2) at a scan rate of 50 mV/s and (C) CV curves of GC/rGO-Nf@Ag6 modified electrode after placed in air for five days.

5.2.5.6 Real Sample Analysis

In food industries, H₂O₂ has been used as the antimicrobial agent for *E. coli* O157:H7 and *Salmonella* spp. in the processed fruit juice and also used as a chemical agent for sterilization (Ansari *et al.*, 2003; Schurman, 2001). Thus, determination of H₂O₂ residues in processed fruit juice is crucial as the remaining of H₂O₂ in high concentration may cause several human health problems such as skin irritants. In order to demonstrate the feasibility of the GC/rGO-Nf@Ag6 nanohybrid modified electrode in the analysis of real sample, the quantification of H₂O₂ in apple juice was carried out

using the GC/rGO-Nf@Ag6 modified electrode. For the validation studies, the apple juice sample was divided into three fractions, and each fractions was diluted by DI water in a ratio of 1:9 (Apple juice:DI water).

Because none of the apple juice samples contained any H_2O_2 , the standard addition method was used to measure the H_2O_2 concentration for real sample analysis. Recovery of the measurement was calculated by comparing the results obtained before and after the addition of standard H_2O_2 solution. The results reveal that the sensor electrode achieved high recoveries of H_2O_2 between 98.8 % and 100 %, with an RSD of 1.09 to 3.97 %, proving that the GC/rGO-Nf@Ag6 modified electrode has strong potential to facilitate applications in biomedical analyse. A summary of the real sample analysis results was presented in Table 5.2.

Table 5.2: Detection and recovery of H_2O_2 in apple juice by using the novel GC/rGO-Nf@Ag6 modified electrode.

| Samples | H_2O_2 Added (μM) | H_2O_2 Found (μM) ^a | Recovery (%) | RSD (%) |
|-------------|--|---|--------------|---------|
| Apple juice | 1 | 0.99 | 99.0 | 3.97 |
| | 5 | 4.94 | 98.8 | 1.96 |
| | 10 | 10.00 | 100.0 | 1.09 |

^a Average of three determinations.

5.3 Summary

This study demonstrates homogenous incorporation of AgNPs on the rGO-Nf surface *via* a simple hydrothermal method. A study on the influence of Ag content on the electrocatalytic reduction of H_2O_2 was performed, and the results show that rGO-Nf@Ag6 nanohybrid exhibits excellent electrocatalytic reduction toward H_2O_2 , demonstrating the highest cathodic current response than that of other control electrodes. A sensitive and selective electrochemical sensor based on modification of GCE using rGO-Nf@Ag6 nanohybrid has been developed to determine H_2O_2 .

Impressively, sensor electrode presents competitive detection limits for H₂O₂ compared with those reported in the literature with LoD and LoQ of 5×10^{-7} M and 1 μ M, respectively.

Further investigations on the selectivity of the sensor electrode indicated that the GC/rGO-Nf@Ag6 modified electrode could serve as a highly selective electrochemical sensor for H₂O₂ in the presence of NaCl, urea, glucose, DA, UA and AA. Additionally, the GC/rGO-Nf@Ag6 modified electrode was found to be highly stable and consistent in detecting H₂O₂, with good repeatability and reproducibility. Furthermore, the results from aforementioned studies show good accuracy and high precision for detecting H₂O₂ concentration in apple juice. Taking advantage of individual components present in this ternary nanohybrid (*i.e.* the good electron conducting ability of rGO, the additional active surface sites provided by AgNPs and the anti-fouling and anti-interferential ability of Nf), the sensing performance for quantification of H₂O₂ has been successfully enriched, thus, making this a highly attractive candidate for practical applications.

CHAPTER 6

REDUCED GRAPHENE OXIDE-NAFION@GOLD NANOHYBRID MODIFIED ELECTRODE FOR ELECTROCHEMICAL DETECTION OF NITRIC OXIDE

6.1 Introduction

One of the highly labile free radical and hydrophobic molecules that is produced naturally within the human body is the nitric oxide (NO). In 1987, a research led by Ignarro had discovered that NO is responsible for the vascular smooth muscle relaxation elicited by endothelium-derived relaxing factor (EDRF) (Ignarro *et al.*, 1987). Later, more research investigations were successfully proved the involvement of NO in a range of defense stress responses and its ability to alleviate the deleterious effects of regulating reactive oxygen species (ROS) by regulating ROS production and degradation (Palmieri *et al.*, 2008).

Moreover, NO was also used for communication between cells and is involved in the regulation of blood pressure, the immune response, platelet aggregation and clotting, as well as neurotransmission (Bredt *et al.*, 1992). The concentration of NO in exhaled breath was also used as a biomarker for several diseases such as asthma (Smith *et al.*, 2005), ulcerative colitis (UC) and Crohn's disease (CD) (Avdagić *et al.*, 2013). The determination of NO level in human body was significant due to the abnormality of its production and bioavailability may led to several diseases such as obesity, diabetes (both type I and II), atherosclerosis, hypertension and heart failure (Özden *et al.*, 2003; Shiekh *et al.*, 2011; Yu *et al.*, 2001). Therefore, the fabrication of an efficient sensor

probe which have a compact design and highly sensitive and selective toward NO is important as it can make a great contribution to disease diagnosis.

One of the effective ways to determine NO is electrochemical detection which has been a primary method for monitoring neurotransmitters *in vivo* due to its simplicity, long term high stability, rapid response, low cost and higher level of sensitivity and selectivity. Since NO is an electroactive molecule which could be detected electrochemically, therefore electrochemical technique is suitable to detect NO level. Several materials has been used for modifying the electrode surface for the determination of NO such as metal (silver (Gan *et al.*, 2004), gold (Kannan *et al.*, 2010)), metal oxide (molybdenum oxides (Kosminsky *et al.*, 2001), titanium dioxide (Wang *et al.*, 2006)), polymer (porphyrins (Lei *et al.*, 2004), poly-*o*-phenylenediamine (Wynne *et al.*, 2014)) and carbon based material (Kan *et al.*, 2009; Xu *et al.*, 2011).

Among these materials, graphene incorporated with metal/metal oxide nanoparticles has attracted much attention because these nanocomposites exhibit unique properties which cannot be found in conventional materials. Hu *et al.* has successfully synthesized reduced graphene oxide-ceria (rGO–CeO₂) composites nanostructures which offered a facile and reliable platform to *in situ* real-time detect bio-signal NO molecules released by living cells (Hu *et al.*, 2015). The improvement in the sensing performance was believed due to the synergic effect from high catalytic activity of the specifically shaped metal oxide nanocrystal and good conductivity and high surface area of rGO.

Meanwhile, Shahid and co-workers had used reduced graphene oxide-cobalt oxide nanocube@platinum (rGO–Co₃O₄@Pt) nanocomposite as active material for the detection of *in situ* generated NO (Shahid *et al.*, 2015). The high catalytic effect of the

rGO–Co₃O₄@Pt nanocomposite was attributed to the synergistic effect of Co₃O₄ nanocubes and Pt nanoparticles present in the rGO matrix, which then contributed to better sensing performance.

Inspired by the large surface area and unique conductivity of rGO, and the excellent electrocatalytic activity of gold nanoparticles (AuNPs), a nanohybrid of rGO-Nf and AuNPs was synthesized for the study of highly sensitive and selective electrochemical detection of NO. The use of ion exchange membranes that is Nf, could enhance the surface area scaffold for the deposition of AuNPs and provide the ion conductive pathway for the electrochemical cell as well as act as a stabilizer.

In this study, one step hydrothermal method was employed to produce rGO-Nf films incorporated with AuNPs. GO and gold(III) chloride trihydrate (HAuCl₄.3H₂O) were used as the precursor for rGO and AuNPs, respectively. The rGO-Nf@Au nanohybrid has been used as the electroactive material for modifying the GCE. This modified electrode was used for the first time in electrochemical detection of NO. Three different concentrations of HAuCl₄.H₂O were used in order to study the effect of AuNPs content on the electrochemical sensing performance. To the best of our knowledge, there has been no report on the use of rGO-Nf@Au nanohybrid modified GCE as an electrochemical sensor for NO.

6.2 Results and Discussion

6.2.1 Optical Characterization of rGO-Nf@Au Nanohybrids

The UV-vis absorption spectra of rGO-Nf@Au nanohybrids were presented in Figure 6.1, while the UV-vis spectra for GO, rGO and rGO-Nf were depicted in the inset of Figure 6.1.

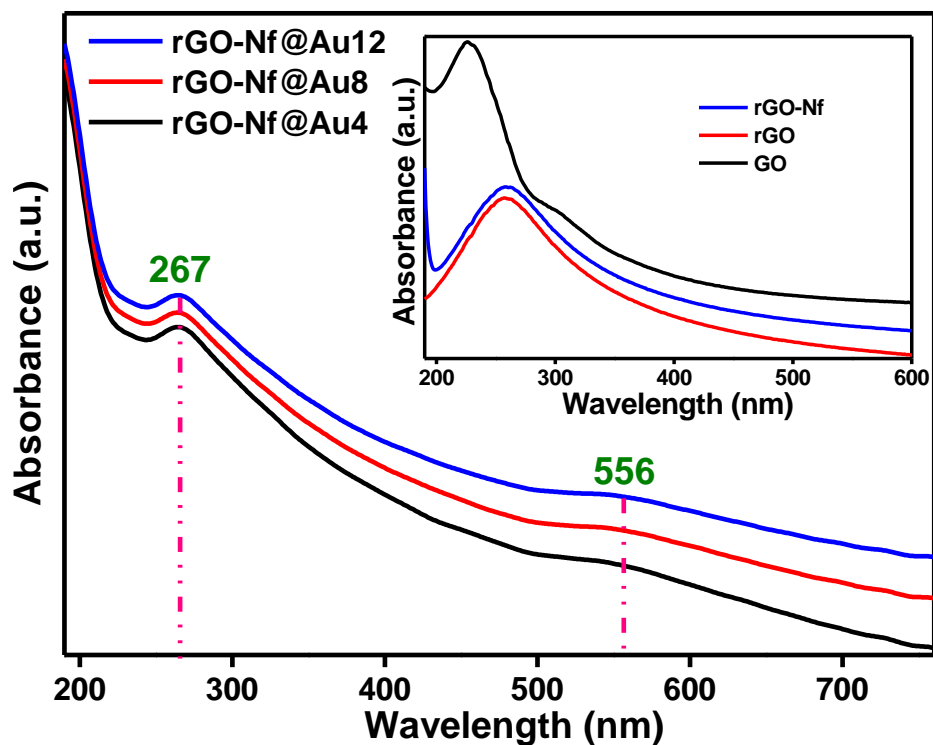


Figure 6.1: UV-vis spectra of three different rGO-Nf@Au nanohybrids (Inset shows the UV-vis spectra for GO, rGO and rGO-Nf nanohybrid).

UV-vis spectra for GO shows a sharp absorption peak at 230 nm corresponds to the $\pi \rightarrow \pi^*$ transitions of aromatic C-C bonds, and a bump at around 300 nm is due to the $n \rightarrow \pi^*$ transition of the C=O bonds (carbonyl groups). Upon the hydrothermal treatment, the absorbance peak of GO was shifted to around 260 nm and the bump disappeared, indicating the successfully removal of oxygen containing functional groups on the surface of GO and restoration of the π -conjugation network after the reduction of GO to form rGO (Johra *et al.*, 2014). According to the UV-vis spectrum of rGO-Nf nanohybrid, Nf present its characteristic absorption peak at 190 nm while the characteristic absorption peaks of rGO remained in this nanohybrid. This indicates that Nf has grafted on the surface of rGO. The UV-vis spectra of AuNPs decorated rGO-Nf sheets gives a characteristic peak at 556 nm which indicates the formation of AuNPs due to its characteristic surface plasmon resonance band and a peak at 267 and 190 nm

arises due to the presence of rGO and Nf, respectively. The results demonstrate the hybridization of AuNPs with the rGO-Nf sheets was succeeding.

6.2.2 Crystalline and Structural Characterization of rGO-Nf@Au Nanohybrids

The crystalline nature of rGO-Nf@Au nanohybrids with different Au content were analyzed by using XRD and the results were shown in Figure 6.2. In general, the XRD pattern for GO shows a characteristic diffraction peak at around 10.5° with an interlayer d -spacing of 8.36 Å (Figure 6.2(A)) (Mhamane *et al.*, 2011). Upon the hydrothermal treatment, this peak disappeared and a new broad peak emerges at round 25° which corresponds to the (0 0 2) plane of hexagonal reduced graphene oxide structure and thus, confirmed the formation of rGO (Khandelwal *et al.*, 2015). The peak at 42.8° which appeared in XRD pattern for rGO corresponded to the turbostratic band of disordered carbon materials (Xu *et al.*, 2010).

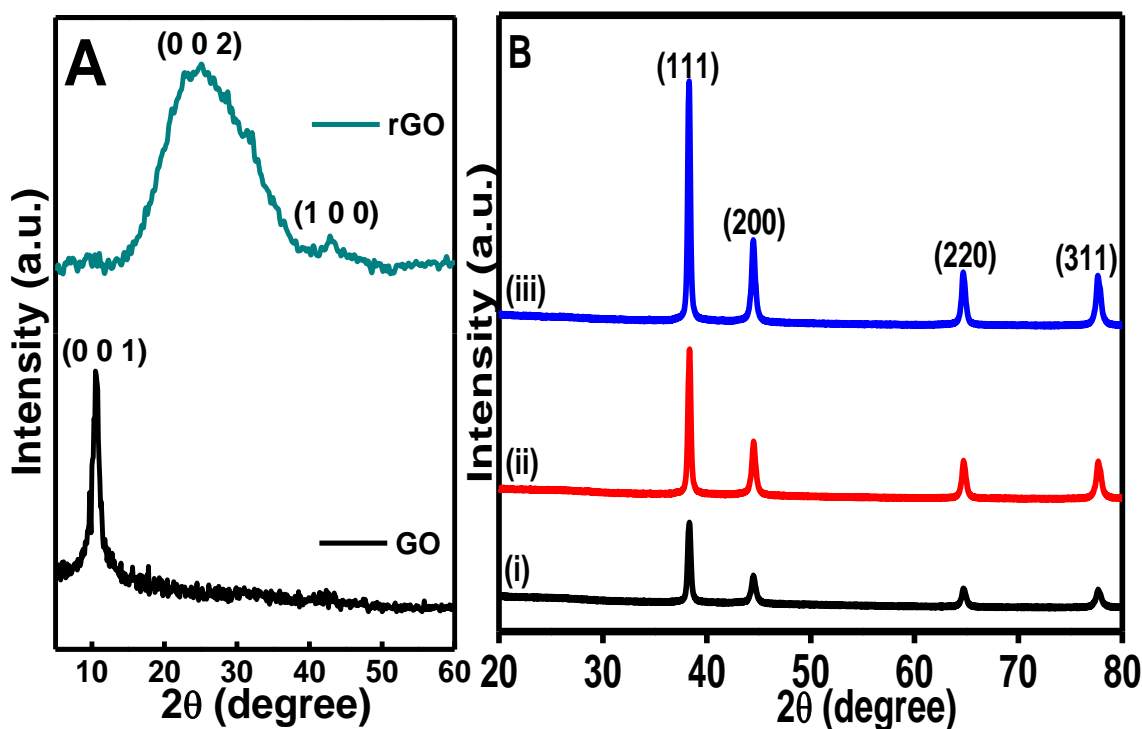


Figure 6.2: XRD patterns of (A) GO and rGO. (B) XRD pattern of (i) rGO-Nf@Au4, (ii) rGO-Nf@Au8 and (iii) rGO-Nf@Au12 nanohybrids.

The decrease in d spacing after hydrothermal reaction due to the removal of the oxide functional groups in GO and also suggested the recovery of graphitic crystal structure after the reduction of GO *via* hydrothermal treatment. The XRD patterns for three different rGO-Nf@Au nanohybrids were demonstrated in Figure 6.2(B). The diffraction peaks observed at 38.29° , 44.48° , 64.68° , and 77.68° were assigned to the (1 1 1), (2 0 0), (2 2 0) and (3 1 1) planes of Au (Shen *et al.*, 2009). All the obtained peaks were well matched and consistent with the standard database (JCPDS card: 65-2870), thus confirmed the existence of AuNPs on the surface of rGO-Nf sheets.

As can be seen, no rGO peak was observed in all XRD patterns of nanohybrids. This was due to the extreme low diffraction intensity of rGO compared to AuNPs suggesting that the surface of the rGO-Nf was covered with AuNPs. All the peaks appeared to be sharp with high intensities and no impurity peak could be observed, indicating the higher crystallinity and purity of the rGO-Nf@Au nanohybrids. The only notable difference between the XRD patterns of all three rGO-Nf@Au nanohybrids was the intensity of their peaks that increased with the increase in AuNPs content from 4 to 12 mM. This result indicated that the existence of AuNPs became dominant in the nanohybrid because more AuNPs were formed on the surface of rGO-Nf sheets when high concentration of AuNPs precursor was used.

A Raman scattering study was performed to confirm the presence of rGO in the nanohybrids. The comparative Raman spectra of rGO and three different rGO-Nf@Au nanohybrids were depicted in Figure 6.3. The Raman spectra obtained from all the nanohybrids exhibited two prominent peaks which can be referred to the characteristic peaks of carbon-based material. As indicated in inset of Figure 6.3, Raman spectra for

GO showed two peak at 1355 and 1602 cm^{-1} which corresponds to the D and G band, respectively.

As is known, the D peak arises from defects in the hexagonal sp^3 carbon network or finite particle size effects, whereas the G peak originates from sp^2 hybridized carbon atoms in a graphitic 2D hexagonal lattice (Yusoff *et al.*, 2014). After the hydrothermal treatment, these peaks were slightly shifted to 1360 and 1600 cm^{-1} (Figure 6.3(i)). The red-shifted trend observed in G band relate to the transformation of sp^3 amorphous GO to sp^2 nanocrystalline graphene, thus attested the success of reduction process to form rGO (Abdolhosseinzadeh *et al.*, 2015). Moreover, the increased ratio of I_D/I_G intensity was interpreted to indicate the defects and disorder in the hexagonal graphitic layers. The I_D/I_G ratio for GO is 0.92 which markedly increased to 1.09 for rGO upon hydrothermal process. The increment attributed to the formation of defects occurs in addition to the removal of oxide functional groups attached to the GO surface, hence give further evidence to the successful reduction of GO (How *et al.*, 2014). It is notable that there was an increment in the Raman spectra intensity upon the incorporation between AuNPs and rGO-Nf sheets (Figure 6.3(ii)-(iv)). These enhancements were occurred due to the surface-enhanced Raman scattering (SERS) properties owned by AuNPs (Wang *et al.*, 2014).

Meanwhile, the I_D/I_G ratios for all nanohybrids were slightly decreased following the order of: rGO-Nf@Au8 (1.03) > rGO-Nf@Au4 (1.02) > rGO-Nf@Au12 (1.01). This may due to the presence of AuNPs that has occupied most of the vacancies in rGO-Nf sheets, thus recovered its defects. Besides that, the G band for all rGO-Nf@Au nanohybrids were further shifted to higher frequency, demonstrated the strong electronic interaction between rGO-Nf sheets and AuNPs. Therefore, it was confirmed

that the successful formation of AuNPs in the rGO-Nf sheets using hydrothermal method.

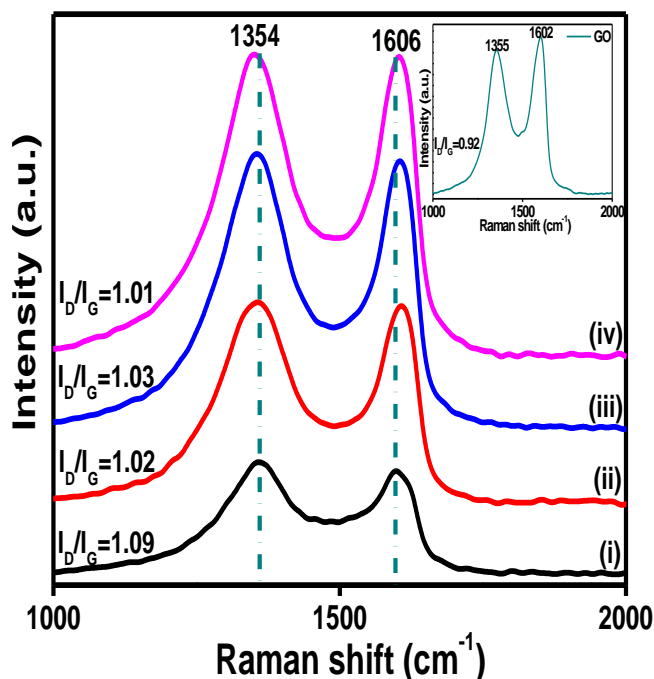


Figure 6.3: Raman spectra of (i) rGO, (ii) rGO-Nf@Au4, (iii) rGO-Nf@Au8 and (iv) rGO-Nf@Au12 nanohybrids (Inset shows the Raman spectrum for GO).

The presence of functional groups on the surfaces of rGO-Nf@Au nanohybrids were evaluated by XPS and the results were shown in Figure 6.4. Figure 6.4(A) shows the XPS peak deconvolution of C1s core levels of the rGO-Nf@Au nanohybrids. It was noted that two characteristic peaks of C-C and C-F were observed at binding energy of 284.5 and 291.1 eV, respectively. It could be attributed to the presence of rGO and Nf in the nanohybrids material. One can also noticed that the intensity of C-C peak for rGO-Nf@Au8 nanohybrid was the highest compared to other nanohybrids.

The results demonstrated that the rGO in this nanohybrid has higher degree of reduction due to effective removal of oxygen functional groups after hydrothermal process. Figure 6.4(B) presents the XPS spectra of Au4f core level in the rGO-Nf@Au nanohybrids. The deconvoluted peaks located at the binding energies of 83.8 and

87.5 eV were assigned to the Au4f_{7/2} and Au4f_{5/2}, respectively (Pocklanova *et al.*, 2016). Therefore, the XPS results further confirmed the formation of AuNPs on the rGO-Nf surface.

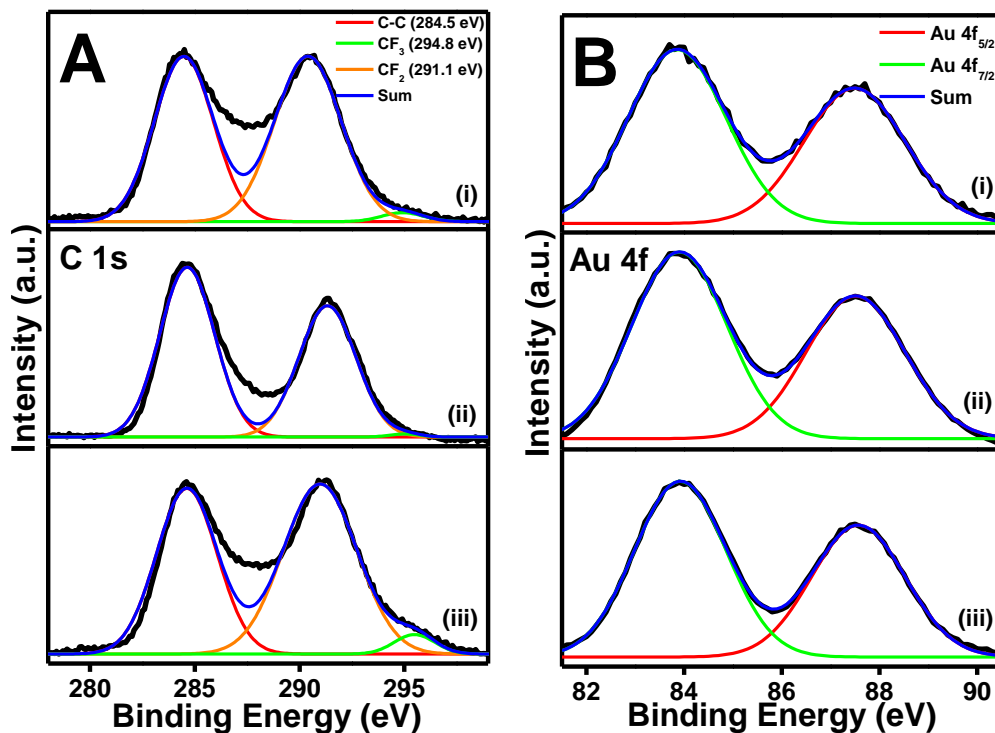


Figure 6.4: XPS spectra of the (A) C1s and (B) Au4f core level region for (i) rGO-Nf@Au4, (ii) rGO-Nf@Au8 and (iii) rGO-Nf@Au12 nanohybrids.

6.2.3 Morphological Characterization of rGO-Nf@Au Nanohybrids

The morphology of the rGO-Nf@Au nanohybrids was characterized using FESEM analysis. Figure 6.5 shows the FESEM images of the rGO-Nf@Au nanohybrids obtained from various AuNPs content and their corresponding histogram represented the particle size distribution. The images indicated that the AuNPs were spherical in shape and it was well wrapped by rGO-Nf matrix but have different size and content for each other. The rough surface of sheets observed in all images reveals the existence of Nf in all nanohybrids.

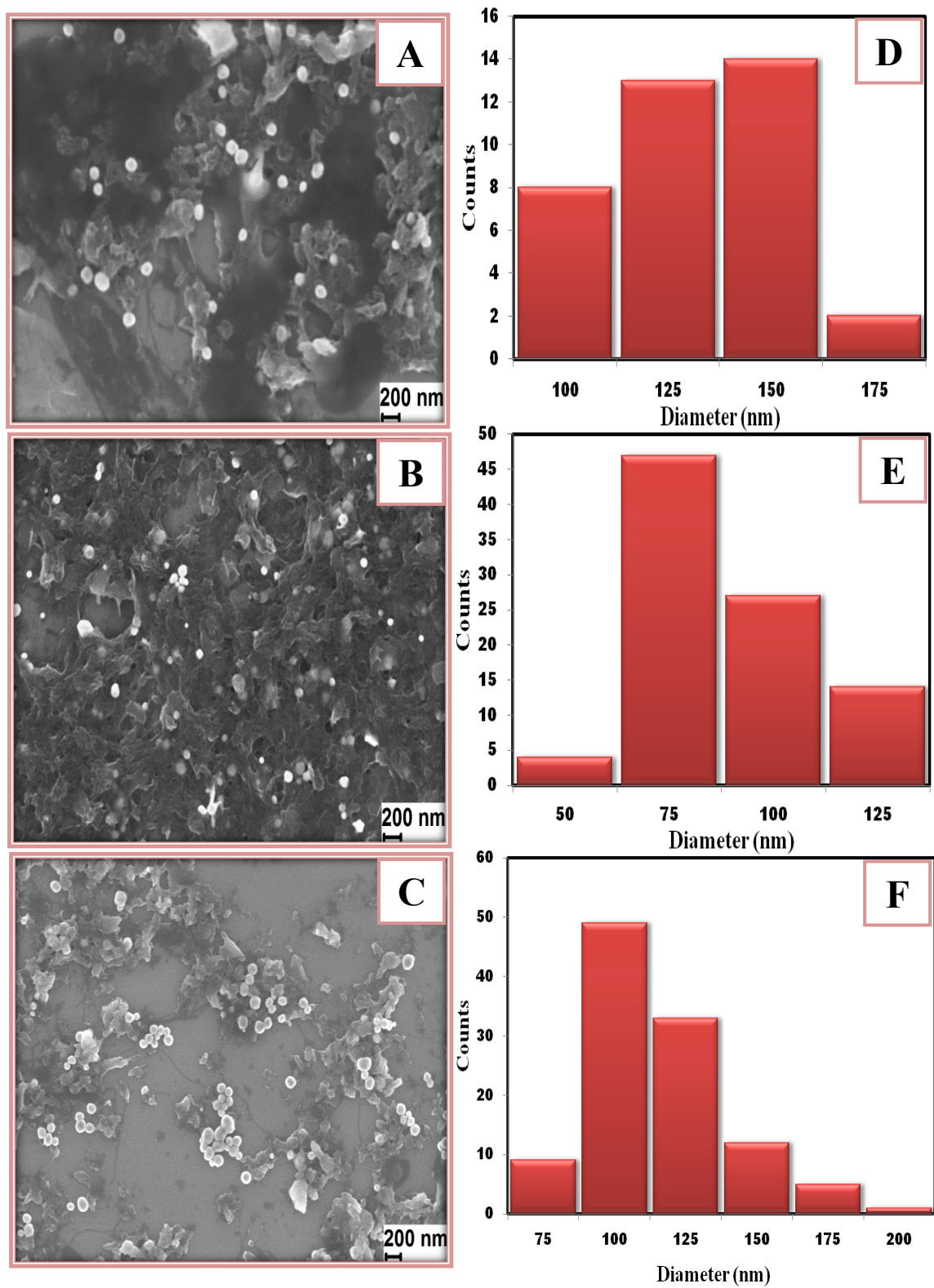


Figure 6.5: FESEM images and particle size distribution histograms of (A, D) rGO-Nf@Au4 nanohybrid, (B,E) rGO-Nf@Au8 nanohybrid and (C,F) rGO-Nf@Au12 nanohybrid.

The FESEM results obtained from rGO-Nf@Au4 nanohybrid disclose a number of spherical AuNPs with diameter ranging from 100 to 175 nm were tightly embedded in the rGO-Nf sheets as depicted in Figure 6.5(A). Furthermore, upon increasing the AuNPs content to 8 mM, more AuNPs were intercalated into the rGO-Nf sheets with diameter of 50 to 125 nm (Figure 6.5(B)). The 75-200 nm diameters of AuNPs with a small portion of particles tend to aggregate could be observed in the FESEM image of rGO-Nf@Au12 nanohybrid as demonstrated in Figure 6.5(C). As we increase the AuNPs content in the nanohybrids, more AuNPs would grow on a limited nucleation sites on the rGO-Nf sheets, resulting in the aggregation of AuNPs.

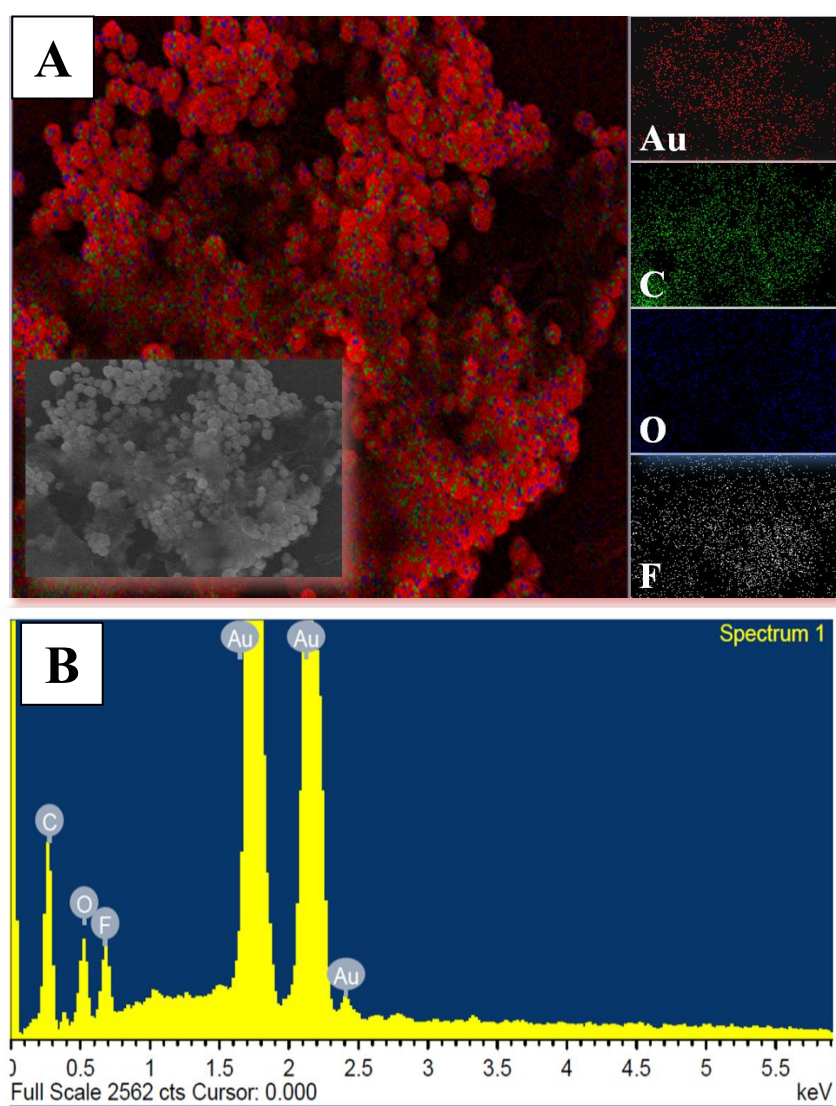


Figure 6.6: (A) Elemental mapping images and (B) EDX of rGO-Nf@Au8 nanohybrid.

The elemental mapping and energy-dispersive X-ray spectrometer (EDX) analysis were employed to determine the composition of rGO-Nf@Au8 nanohybrid and demonstrated in Figure 6.6. The elemental mappings of carbon (C), oxygen (O), fluorine (F) and Au as shown in Figure 6.6(A) reveal that these elements were uniformly distributed in the rGO-Nf@Au8 nanohybrid. Furthermore, the EDX analysis of individual rGO-Nf@Au8 nanohybrid elucidated that there appears a strong signal of C, O, F and Au elements on the rGO-Nf@Au8 nanohybrid (Figure 6.6(B)). The F element was traced from the Nf while C and O elements were originated from the rGO. These results confirmed the attachment of AuNPs to rGO-Nf sheets.

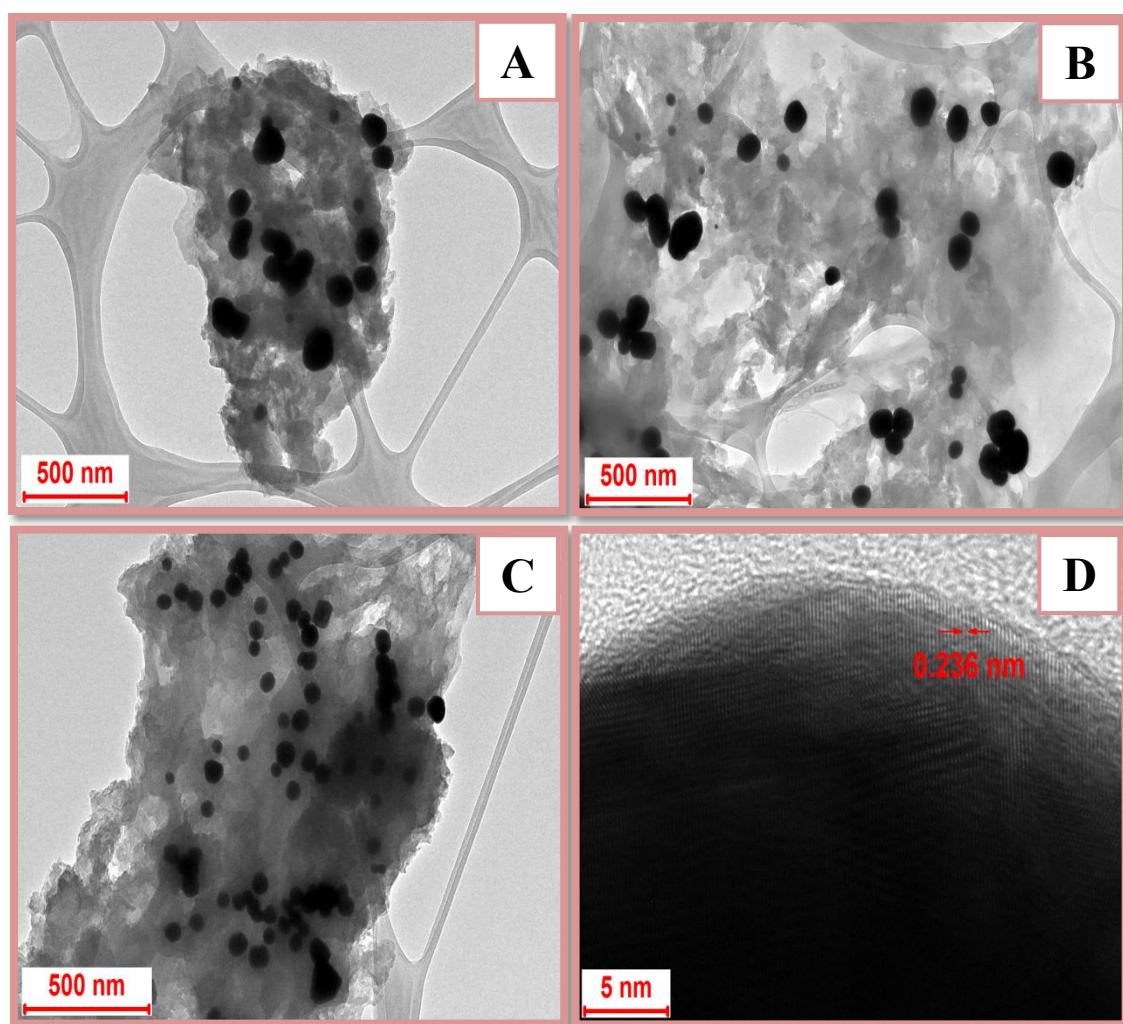


Figure 6.7: HRTEM images of (A) rGO-Nf@Au4 nanohybrid, (B) rGO-Nf@Au8 nanohybrid, (C) rGO-Nf@Au12 nanohybrid and (D) lattice resolved TEM image of individual AuNPs on the rGO-Nf sheet.

The HRTEM was conducted to further analyze the successful loading of AuNPs on rGO-Nf sheets and the results were depicted in Figure 6.7. Figure 6.7(A-C) clearly showed that AuNPs are spherical in shape within nanometer range that embedded on the surface of rGO-Nf sheets. Further, the deposition of distributed Au spherical becomes higher as we increase the Au precursor concentration from 4 to 12 mM. These observations are in good agreement with FESEM results. Meanwhile, in the HRTEM image of the rGO-Nf@Au8 nanohybrid (Figure 6.7(D)), lattice fringes with d spacing values of 0.236 nm was observed, which corresponds to the (1 1 1) plane of the AuNPs. The obtained results demonstrated the formation of AuNPs on rGO-Nf during hydrothermal process.

6.2.4 Electrochemical Characterization of GC/rGO-Nf@Au Modified Electrode

The CV and electrochemical impedance spectroscopy (EIS) were used as the analytical techniques for the characterization of each modified electrode surface in order to clarify the differences among the electrochemical behaviour of each of it. Figure 6.8(A) demonstrated the comparative CV behavior of the bare and modified GCE using three different rGO-Nf@Au nanohybrids, rGO-Nf, GO and Nf, in solution containing 5 mM $K_3[Fe(CN)_6]$ and 0.1 M KCl. A well-defined reversible redox peaks were observed in all the CV curves of modified electrodes and bare GCE. The GC/rGO-Nf@Au8 modified electrode displayed the highest current response which suggested the occurrence of rapid electron transfer at the electrode-solution interface due to the good electrical communication between electrode and electrolyte.

The higher redox current response associated with the low peak-to-peak potential separation (78.5 mV) obtained for GC/rGO-Nf@Au8 modified electrode indicated that the electrochemical reversibility of $[Fe(CN)_6]^{3-/4-}$ ions was greatly improved, as a result of effective surface area provided by rGO-Nf@Au8 nanohybrid. As depicted in inset of

Figure 6.8(A), a redox couple peak with low current signal could be observed at GC/GO, however, no redox peak can be seen in the CV profile for GC/Nf. The electrostatic repulsion between negatively charged Nf and $[\text{Fe}(\text{CN})_6]^{3-/4-}$ hindered the diffusion of $[\text{Fe}(\text{CN})_6]^{3-/4-}$ ions toward the electrode surface (Ye *et al.*, 2015). In order to gain more insight into electrode behavior, the Nyquist plot for all modified electrodes were recorded in 5 mM $\text{K}_3[\text{Fe}(\text{CN})_6]$ and 0.1 M KCl and were depicted in Figure 6.8(B).

A straight oblique line could be observed in the Nyquist plot for GC/rGO-Nf@Au which implies the decrease in the charge transfer resistance of the electrode surface and increase in the charge transfer rate upon employing GC/rGO-Nf@Au modified electrode. However, one semicircle in the high frequency range with an inclined line in the low frequency range were occurred in the Nyquist plot obtained at bare GCE and GC/GO modified electrode as shown in inset of Figure 6.8(B). The diameter of the semicircle represents the charge transfer resistance (R_{ct}), whereas the inclined straight line can be considered to be the impedance attributed to the diffusion of ions through the graphene sheets (Yusoff *et al.*, 2015). The analysis showed that the charge transfer resistance (R_{ct}) at the electrode/electrolyte interface decreased in following the order of: GC/GO (1.01 M Ω) > bare GCE (749 k Ω) > GC/rGO-Nf (578 k Ω) > GC/rGO-Nf@Au4 (262 k Ω) > GC/rGO-Nf@Au12 (77 k Ω) > GC/rGO-Nf@Au8 (10.5 k Ω).

As can be seen, the R_{ct} value was significantly decreased upon decorating rGO-Nf sheets with AuNPs. Among the three nanohybrids, electrode modifying by rGO-Nf@Au8 nanohybrids possess the lowest R_{ct} value. The Bode plots of the phase angle versus frequency for different modified electrode were presented in Figure 6.8(C). A

sharp peak at a higher frequency could be observed in Bode plot obtained at bare GCE and GC/GO which indicates the high R_{ct} value (inserted in Figure 6.8(C)).

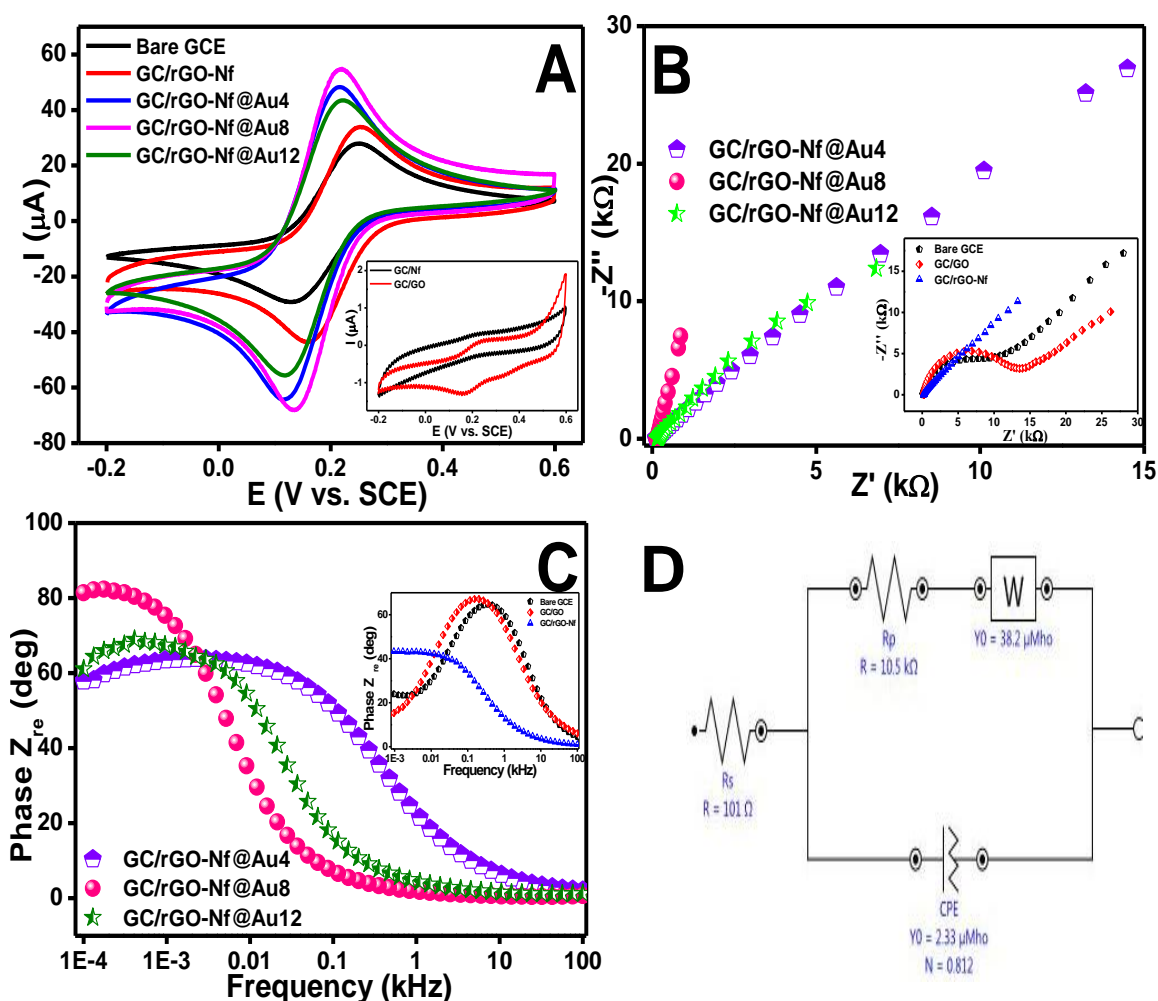


Figure 6.8: (A) CV, (B) Nyquist, and (C) Bode plots obtained for several modified electrodes in a solution containing 0.1 M KCl and 5 mM $K_3[Fe(CN)_6]$ (the scan rate of CV is 50 mV/s and the frequency range of EIS is from 0.01 Hz to 100 kHz) and (D) equivalent circuit for the impedance spectroscopy obtained using GC/rGO-Nf@Au8 modified electrode.

Upon coating the electrode with rGO-Nf and three different rGO-Nf@Au nanohybrids, the existence of a broad peak can be observed with shifted in position toward lower frequency. The characteristic frequency peak shifted to lower frequencies in the following order: GC/rGO-Nf > GC/rGO-Nf@Au4 > GC/rGO-Nf@Au12 > GC/rGO-Nf@Au8. This result attests the ability of rGO-Nf@Au8 as the potential

material for electrocatalysis, photoelectrochemical cells and solar cells applications. The excellent behavior shown by GC/rGO-Nf@Au8 modified electrode emphasizes that this sensor electrode could be a promising candidate for the development of new electrochemical sensing devices. Figure 6.8(D) shows the respective electrochemical equivalent circuit generated for GC/rGO-Nf@Au8 modified electrode that consists of electrolyte resistance (R_s), charge transfer resistance (R_p), Warburg impedance (Z_w) and constant phase element (CPE). The CPE depicts the non-ideal capacitance of the surface layer, while Z_w accounts for the diffusion of ions from the bulk electrolyte to the electrode interface (Yusoff *et al.*, 2016).

6.2.5 Electrochemical Determination of Nitric Oxide

6.2.5.1 Electrocatalytic Oxidation of Nitric Oxide

The electrocatalytic NO oxidation at the rGO-Nf@Au nanohybrid modified electrode was investigated by recording the CV response. In order to produce NO, sodium nitrite (NaNO_2) was used as the precursor where it undergoes disproportionation reaction in acidic solution ($\text{pH} \leq 4$) to generate free NO (Equation (2) and (3)) (Kannan *et al.*, 2010). The concentration of NO was determined by controlling the concentration of the NaNO_2 injected into the bulk electrolyte solution at pH 2.5.

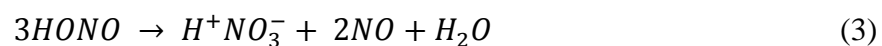
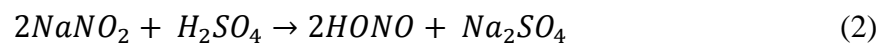


Figure 6.9 compares the electrochemical behavior of all modified electrodes investigated in this work towards the oxidation of 1 mM NO in 0.1 M PBS at pH 2.5 with the scan rate of 50 mV/s. Upon the addition of 1 mM NO in the solution, an anodic peak occurred in CV curves for bare GCE and other modified electrodes due to NO oxidation, but with different amount of current response and peak position were

observed. This anodic peak was assigned to the oxidation of NO at the surface of sensor electrode. As can be seen in Figure 6.7(B), the GC/rGO-Nf@Au8 modified electrode shows higher anodic peak current for the oxidation of NO compared to bare GCE and other modified electrode, suggesting that the incorporation of 8 mM AuNPs with rGO-Nf has significantly improved the performance of the electrode toward NO oxidation.

The current response for each sensor electrode increased follows the order of: GC/GO < GC/Nf < Bare GCE < GC/rGO < GC/rGO-Nf < GC/rGO-Nf@Au4 < GC/rGO-Nf@Au12 < GC/rGO-Nf@Au8. The high current response was the result of enhancement in the electron transfer kinetics at the GC/rGO-Nf@Au8 due to the excellent electrical conductivity of rGO and AuNPs as well as large amount of active surface area on the modified electrode. There was no apparent oxidation peak in the CV curve of rGO-Nf@Au8 could be observed in the absence of NO in the solution as shown in Figure 6.9(B).

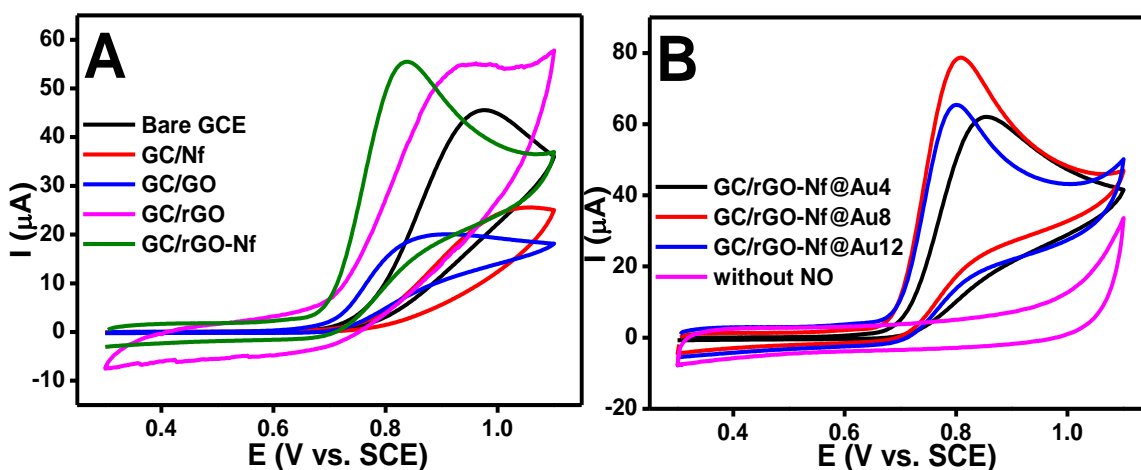


Figure 6.9: (A and B) CV curves recorded at different modified electrodes for 1 mM of NO in 0.1 M PBS (pH 2.5) at a scan rate of 50 mV/s.

6.2.5.2 Optimization Studies

(a) Effect of Different Concentration of Nitric Oxide

Among the various investigated modified electrode, GC/rGO-Nf@Au8 modified electrode showed better electrocatalytic activity towards NO oxidation and hence it was chosen for further optimization studies to achieve better sensing performance. A series of CV curves were recorded at the GC/rGO-Nf@Au8 modified electrode for different concentrations of NO in 0.1 M of PBS (pH 2.5) and plotted in Figure 6.10. When 1 mM of NO was added in the PBS, an anodic peak appeared at potential of +0.8 V which assigned to the oxidation peak of NO (Figure 6.10(A)).

Upon increasing the NO concentration from 1 to 10 mM, the current for this anodic peak was increased linearly with the concentration of NO as can be seen in calibration plot shown in Figure 6.10(B). The linear regression equation for NO was given by $I_{pa} = 0.0492 [NO] + 0.0541$ with a correlation coefficient, R^2 of 0.9923. Therefore, GC/rGO-Nf@Au8 modified electrode demonstrates an effective electrocatalytic oxidation of NO.

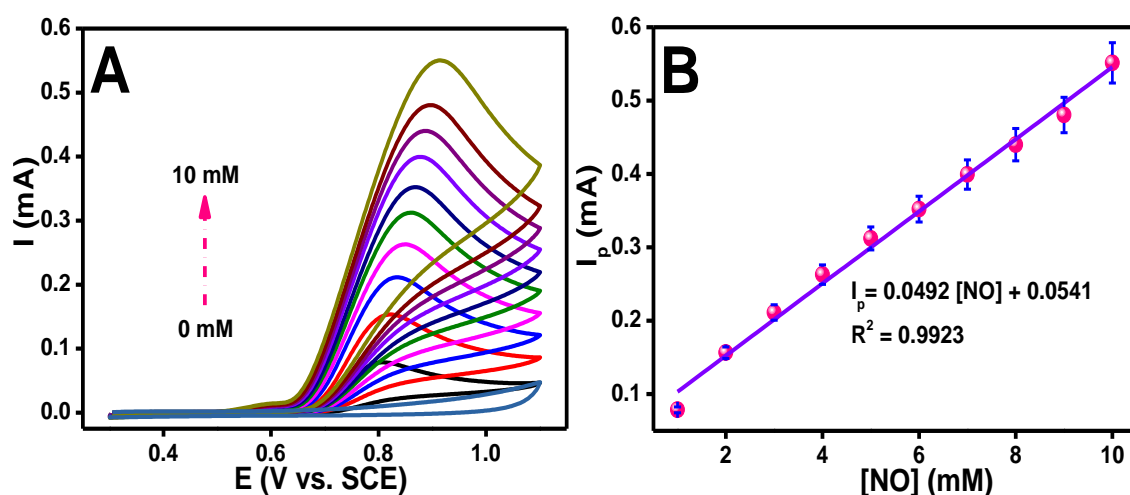


Figure 6.10: (A) CV responses of GC/rGO-Nf@Au8 modified electrode with change in NO concentrations from 1 to 10 mM at a scan rate of 50 mV/s and (B) the corresponding plot of anodic peak current versus concentration of NO.

(b) Effect of Scan Rate

The CV responses of the GC/rGO-Nf@Au8 modified electrode at different scan rates were examined to study the kinetic behavior of the rGO-Nf@Au nanohybrids material in the oxidation of NO (Figure 6.11). The CV curves of 1 mM NO in 0.1 M PBS (pH 2.5) at GC/rGO-Nf@Au8 were recorded at different scan rates in the range of 10 to 500 mV/s as displayed in Figure 6.11(A). Obviously, there was an increment in the anodic peak current with its position shifted toward higher potential as the scan rate increased from 10 to 500 mV/s. The shifting in peak position demonstrates that the electrochemical reaction was irreversible (Raoof *et al.*, 2016).

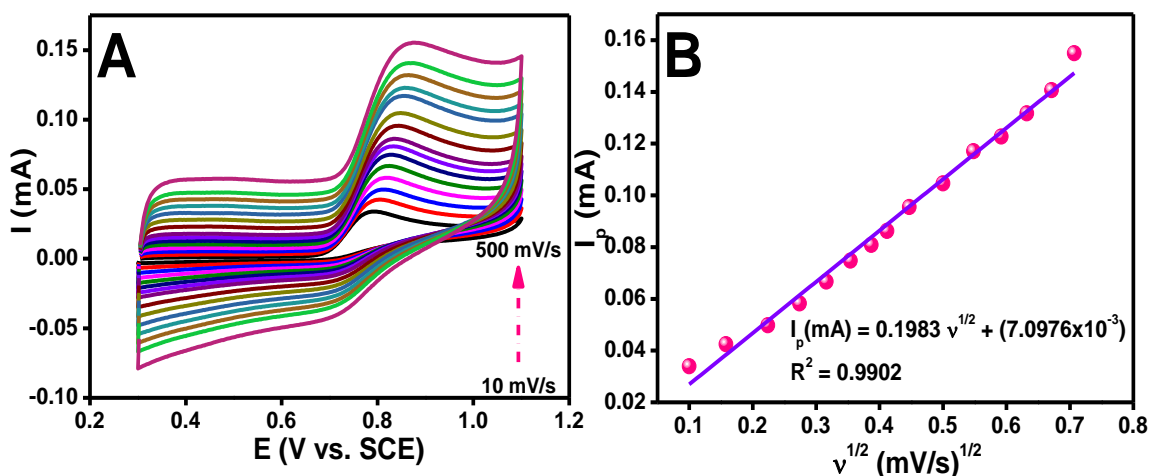


Figure 6.11: (A) CV curves of GC/rGO-Nf@Au8 modified electrode collected at different scan rates ranging from 10 to 500 mV/s in 0.1 M PBS (pH 2.5) containing 1 mM NO and (B) the corresponding plot of anodic peak current versus square root of scan rate.

Based on the calibration curve displayed in Figure 6.11(B), it shows a linear relationship between peak currents and square root of the scan rates with linearity coefficients of 0.9902. The respective linear equations obtained from the plot can be expressed as $I_p = 0.1983 v^{1/2} + 7.0976E - 3$. This result implies that the electrode reaction of NO on the GC/rGO-Nf@Au8 modified electrode was mainly controlled by

diffusion process. The diffusion coefficient value was calculated to be about $1.08 \times 10^{-4} \text{ cm}^2 \text{ s}^{-1}$.

(c) Effect of rGO-Nf@Au8 Loading

The influence of sample loading on the CV peak current of 1 mM NO was investigated in the volume range from 1 to 10 μL , as plotted in Figure 6.12. As shown in Figure 6.12(A), the current response was increased when we increase the rGO-Nf@Au8 loading content. The maximum value of current response appears at the sample volume of 6 μL , however the current started to decrease with the further increase of sample volume loaded on the surface of electrode (Figure 6.12(B)). This result demonstrates that the film thickness was affecting high current efficiency. Considering the obtained results, therefore, the rGO-Nf@Au8 loading content of 6 μL was selected as optimal condition for the detection throughout the study.

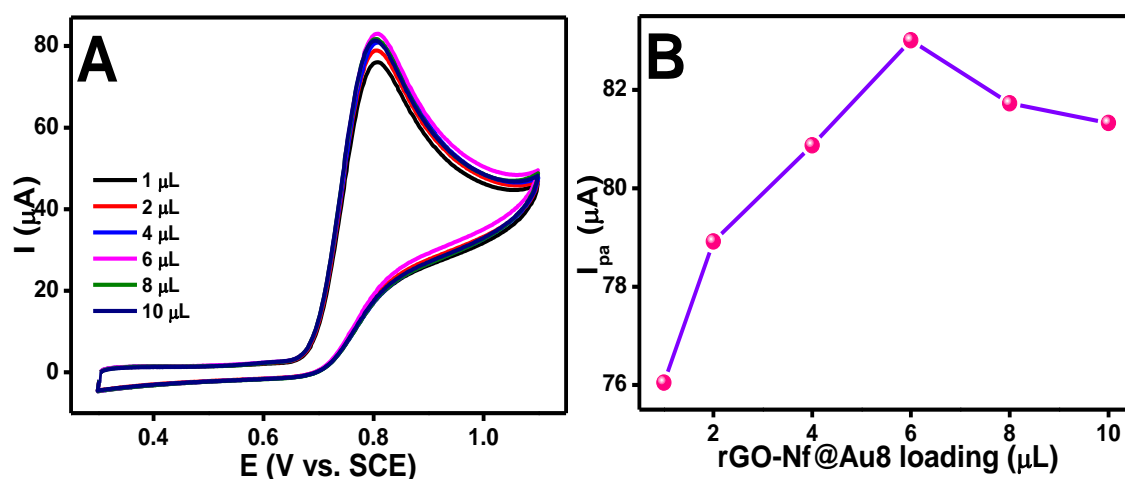


Figure 6.12: (A) CV curves obtained for GC/rGO-Nf@Au8 modified electrode with different amount of sample loading and (B) plot of rGO-Nf@Au8 loading versus anodic peak current response obtained for the 1 mM NO in 0.1 M PBS (pH 2.5) at a scan rate of 50 mV/s.

6.2.5.3 Amperometric Response of Nitric Oxide

The electrochemical NO sensors were fabricated and tested accordingly in order to examine the application of the rGO-Nf@Au nanohybrids. For an explicit comparison, the amperometric responses were recorded at different modified electrode in 0.1 M PBS (pH 2.5) with successive addition of 50 μM NO and plotted in Figure 6.13. After the addition of 50 μM NO, an increase in the current response with increasing NO concentration could be detected for all modified electrode as can be seen in Figure 6.13(A). This result reveals that the GC/rGO-Nf@Au8 modified electrode provides more amplified responses than bare GCE and other modified electrodes.

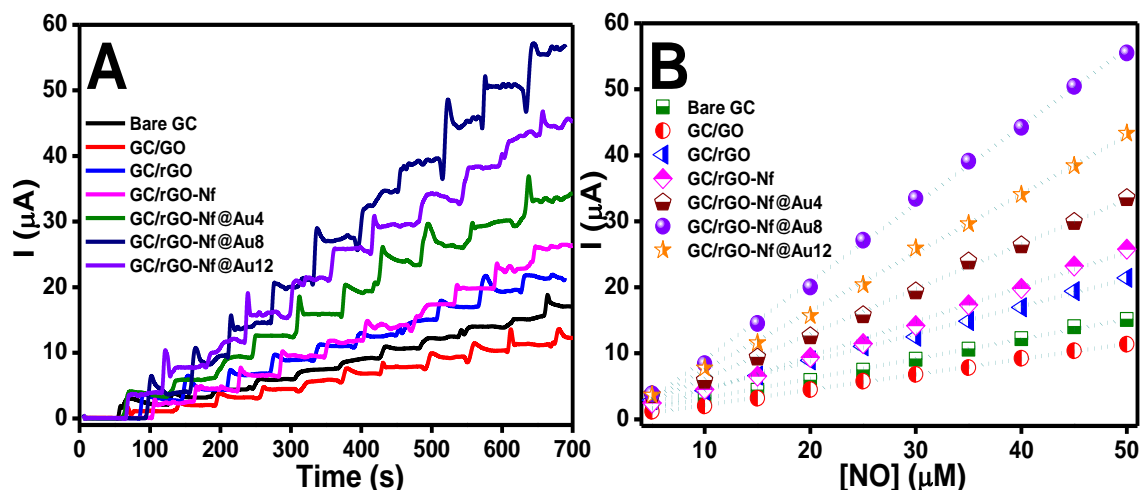


Figure 6.13: (A) Amperometric (I-t) response of different modified electrodes to subsequent additions of 50 μM NO in 0.1 M PBS (pH 2.5) at an applied potential of +0.8 V and (B) the corresponding calibration curve of current versus concentration of NO for different modified electrode.

The calibration plots obtained from the amperometric responses were presented in Figure 6.13(B). The enhancement of analyte interaction surface area and high electrical conductivity provided by rGO-Nf@Au8 nanohybrid contribute to the improvement in sensing performances of the GC/rGO-Nf@Au modified electrode over the other modified electrodes. However, when overloaded the AuNPs content in the nanohybrid,

the AuNPs may form agglomeration and increase the diffusion layer thickness, therefore reducing the electron transfer rate, thus lower the sensitivity of the sensor electrode. To put these results in perspective, the sensitivity of GC/rGO-Nf@Au8 modified electrode was the larger than that obtained with other modified electrode, hence this sensor electrode was chosen for further study in determine the low detection limit for NO in acidic solution.

The amperometric was recorded at an applied potential of +0.8 V for different NO concentrations in order to investigate the concentration detection limits for GC/rGO-Nf@Au8 modified electrode and was plotted in Figure 6.14. Figure 6.14(A) shows an excellent amperometric response with successive additions of different NO concentration for every 60 sec recorded at GC/rGO-Nf@Au8 modified electrode. Upon the injection of NO in the solution, a significant increase in the current response with increase in the concentration of NO could be observed.

The current response against the NO concentration in the response time ranging from 200 to 850 sec was shown in inset of Figure 6.14(A). Interestingly, the response time of the modified electrode was recorded to be within a second, indicating the rapid diffusion of NO on the GC/rGO-Nf@Au8 modified electrode surface; thereby this sensor electrode could be used for real time measurements. It can also be notices that the oxidation current increases linearly with the successive addition of NO into PBS (Figure 6.14(B)). The calibration curve between the peak currents and different NO concentrations in the range from 1 to 10 μ M was showed in the inset of Figure 6.14(B). The linear regression equation was expressed as $I = 0.062 [NO] + 1.037E - 8$ ($R^2 = 0.994$) with the limit of detection of 5×10^{-7} M (S/N= 3).

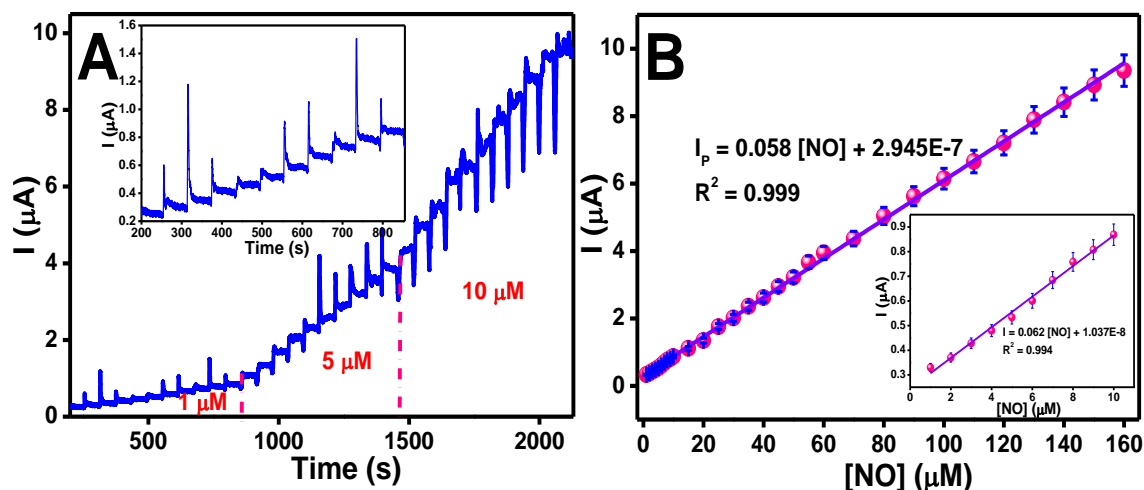


Figure 6.14: (A) Amperometric (I-t) response of GC/rGO-Nf@Au8 modified electrode in 0.1 M PBS (pH 2.5) at an applied potential of +0.8 V upon successive additions of different concentration of NO in a step of 1, 5, and 10 μM. Inset shows the I-t response from 200 to 850 sec and (B) the corresponding calibration curve of current versus concentration of NO. Inset shows the enlargement of the calibration curve from 1 to 10 μM of NO concentration.

Table 6.1 presents the performance of the GC/rGO-Nf@Au8 modified electrode in comparison with other amperometric sensors for the detection of NO. By comparison, the NO sensor presented in this work exhibits a comparable sensing performance with other sensor electrodes. It was believed that the good synergetic effect between rGO-Nf and AuNPs in forming the nanohybrids leads to the improvement in conductivity which will reduce the electron transfer resistance, hence increase the efficiency of the electron transfer between electrode and electrolyte. Moreover, the enhancement of the active surface area provided by rGO-Nf@Au8 nanohybrids allowed more analytes molecule to be adsorbed.

These factors give a positive effect in sensing performance of GC/rGO-Nf@Au8 modified electrode especially in increase its sensitivity toward detecting of NO. The low detection limit and high sensitivity with fast response time demonstrated by GC/rGO-Nf@Au8 modified electrode shows the potentiality of the GC/rGO-Nf@Au8 as the

alternative material for fabricating a sensor electrode for determining NO in biological analysis.

Table 6.1: Comparison in the sensing performance of GC/rGO-Nf@Au8 modified electrode with other reported sensor electrodes for the determination of NO.

| Electrode | Analytical method | Limit of detection | Linear range | Interferences | Reference |
|---|-------------------|--------------------|-------------------------------|--|------------------------------------|
| GC/Cyt _c -SDS-PAM | Amperometry | 0.1 μ M | 0.8-95 μ M | DA, AA, K ⁺ , Na ⁺ , NH ₄ ⁺ , Mg ²⁺ , Al ³⁺ , Ca ²⁺ , Cu ²⁺ , SO ₄ ²⁻ , CO ₃ ²⁻ , NO ₃ ⁻ , Cl ⁻ | (Chen <i>et al.</i> , 2009) |
| ITO/MPTS-FAuNPs | Amperometry | 0.31 nM | 12 nM-700 μ M | DA, AA, UA, cysteine, Na ⁺ , K ⁺ , Mg ²⁺ , Ni ²⁺ | (Kannan <i>et al.</i> , 2010) |
| Au/trans-[Ru(NH ₃) ₄ (Ist)(SO ₄)] ⁺ | SWV | 77.3 nM | 2.85-28.2 μ M | DA, serotonin, NO ₂ ⁻ | (Santos <i>et al.</i> , 2011) |
| GC/Hb-CPB-PAM | CV | 9.3 μ M | 9.8-100 μ M | - | (He <i>et al.</i> , 2006) |
| GC/Pt-Fe(III) | DPV | 18 nM | 84 nM-780 μ M | H ₂ O ₂ , DA, AA, UA, glucose, epinephrine, nor-epinephrine, L-glutamic acid, | (Wang <i>et al.</i> , 2005) |
| GC/rGO-CeO ₂ | Amperometry | 9.6 nM | 18.0 nM-5.6 μ M | Ca ²⁺ , K ⁺ , Na ⁺ , CO ₃ ²⁻ , NO ₃ ⁻ , Cl ⁻ , UA | (Hu <i>et al.</i> , 2015) |
| PG/Hb-sodium montmorillonite | CV | 20 pM | 4x10 ⁻⁵ -5 μ M | DA, ascorbate, UA, nitrite, epinephrine | (Fan <i>et al.</i> , 2004) |
| PG/Hb-MMT-PVA | CV | 0.5 μ M | 1-250 μ M | - | (Pang <i>et al.</i> , 2003) |
| GC/PADA-Au ₂₅ Ag ₇₅ NCs | Amperometry | 10 nM | 10-900 nM | glucose, urea, oxalate, NaCl, NO ₃ ⁻ | (Viswanathan <i>et al.</i> , 2015) |
| GC/rGO-Au-TPDT | Amperometry | 6.5 nM | 10-140 nM | glucose, urea, oxalate, NaCl | (Jayabal <i>et al.</i> , 2014) |
| Pt/GO-PB | LSV | 16.50 μ M | - | Cl ⁻ , NO ₃ ⁻ , SO ₃ ²⁻ , SO ₄ ²⁻ , NO ₂ ⁻ | (Adekunle <i>et al.</i> , 2015) |
| Pt/GO-Fe ₂ O ₃ | LSV | 13.04 μ M | - | Cl ⁻ , NO ₃ ⁻ , SO ₃ ²⁻ , SO ₄ ²⁻ , NO ₂ ⁻ | (Adekunle <i>et al.</i> , 2015) |
| GC/G-Nf | SWV | 11.61 μ M | 0.05-0.45 mM | DA, AA | (Yusoff <i>et al.</i> , 2015) |
| GC/rGO-Co ₃ O ₄ @Pt | Amperometry | 1.73 μ M | 10-650 μ M | DA, AA, UA, glucose, urea, NaCl | (Shahid <i>et al.</i> , 2015) |
| GC/rGO-Nf@Au8 | Amperometry | 0.5 μ M | 1-160 μ M | DA, AA, UA, glucose, urea, NaCl | This work |

Cyt c=cytochrome c; SDS=sodium dodecyl sulfate; ITO=indium tin oxide; MPTS=(3-mercaptopropyl)-trimethoxysilane; FAuNPs=fused spherical gold nanoparticles; CPB=cetylpyridinium bromide; PAM=polyacrylamide, Fe(III)=iron nanoparticles; rGO=reduced graphene oxide; CeO₂=ceria; MMT=montmorillonite; PVA=polyvinyl alcohol; Hb=hemoglobin; PG=pyrolytic graphite; TPDT= N1 - [3-(trimethoxysilyl)propyl];diethylene triamine; Pt=platinum;

6.2.5.4 Interference Study

Some possible coexisting components such as DA, AA, UA, glucose, NaCl, and urea were examined in order to evaluate the anti-interference of the constructed GC/rGO-Nf@Au8 modified electrode. Figure 6.15 shows the amperometric responses of GC/rGO-Nf@Au8 modified electrode for the successive addition of 1 μM NO and 10 μM DA, AA, UA, glucose, NaCl and urea at a regular interval of 60 sec in 0.1 M PBS (pH 2.5) at an applied potential value of +0.8 V. It can be seen that the aforementioned interference species did not influenced any amperometric responses despite higher concentrations had been used. However, the apparent current increase could be observed with the instantaneous addition of NO in the same solution, attest that this GC/rGO-Nf@Au8 modified electrode exhibits a favorable anti-interference capacity and selectivity characteristics toward the detection of NO. These results suggest that rGO-Nf@Au8 showed potential applications for the detection of NO in real sample analysis owing to its immunity against the common interfering species.

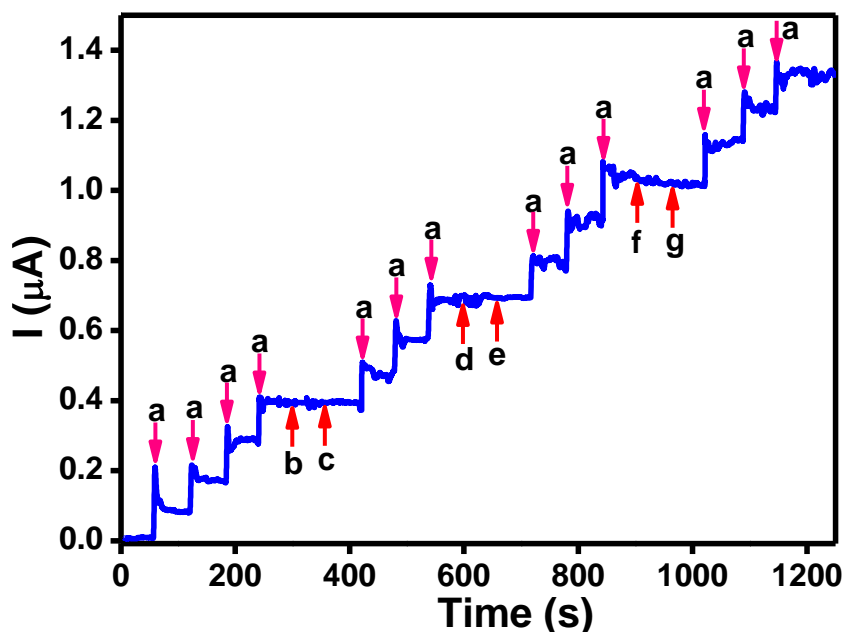


Figure 6.15: Amperometric (I-t) response of (a) 1 μM NO at GC/rGO-Nf@Au8 modified electrode in 0.1 M PBS (pH 2.5) with successive additions of different interfering species such as (b) DA, (c) AA, (d) UA, (e) NaCl, (f) glucose and (g) urea; each with 10 μM concentration.

6.2.5.5 Reproducibility, Repeatability, and Stability Studies

CV was used to determine the repeatability and reproducibility of the GC/rGO-Nf@Au8 modified electrode towards detection of NO. For the purpose of reproducibility study, ten GC/rGO-Nf@Au8 modified electrodes were prepared following the same fabrication method. The CV curves measured from ten sensor electrodes were demonstrated in Figure 6.16(A). It was shown that the sensor electrode exhibits a good reproducibility with a RSD of 2.99 % was obtained towards 1 mM NO, indicating the reliability of the method.

Moreover, the repeatability of GC/rGO-Nf@Au8 modified electrode was investigated by recording the CV curves for ten repetitive measurements of 1 mM NO on a single sensor electrode (Figure 6.16(B)). DI water was used to rinse the electrode surface after each measurement. It was found that the change in current response over the ten repetitive measurement was minimal with 93.13 % of its initial current response was retained. The RSD was calculated to be 2.13 %, indicating that the modified electrode was highly reproducible.

Furthermore, the stability of proposed sensor was investigated by comparing daily responses obtained after storing it at ambient temperature (Figure 6.16(C)). It was observed that the peak currents remained more than 95.12 % of their initial values after five days. The presence of Nf in the nanohybrid helped to improve the stability of the sensor electrode and in the same time prevent the nanohybrids from easily detached from surface of GCE. The above results suggest that the GC/rGO-Nf@Au8 modified electrode is suitable for practical use in detecting the NO due to its good stability, reproducibility and repeatability with high precision (low RDS).

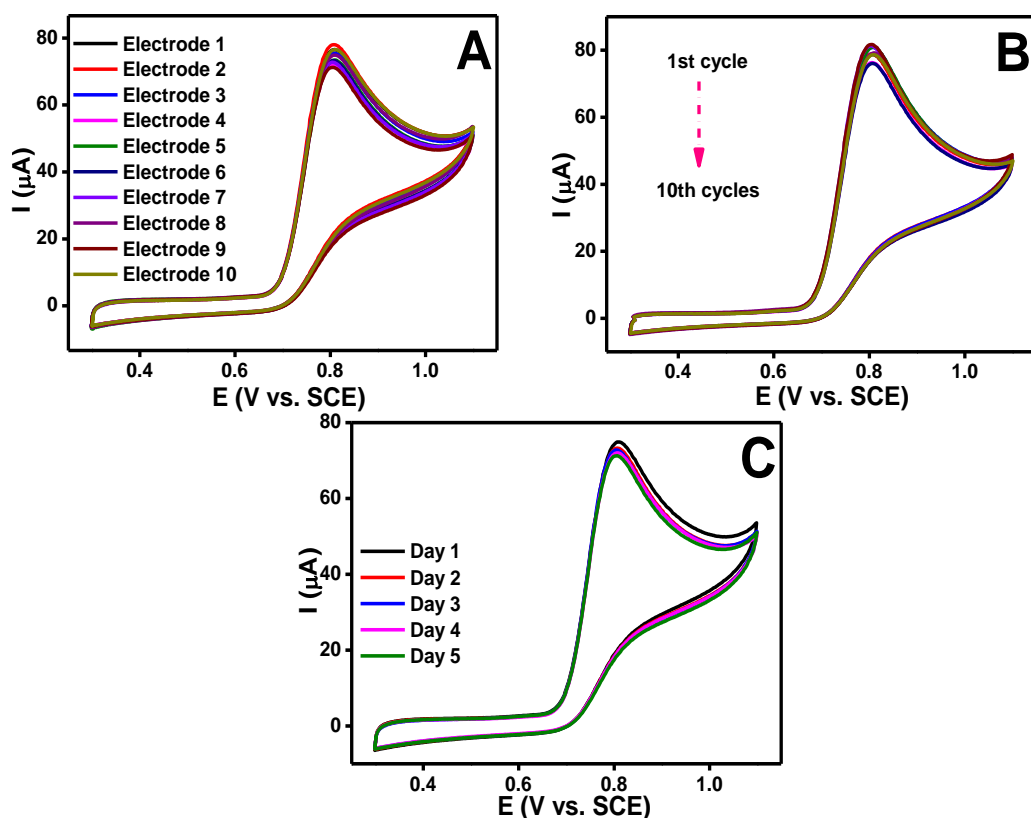


Figure 6.16: (A) CV curves of ten different GC/rGO-Nf@Au8 modified electrodes, (B) CV curves of ten successive measurements of GC/rGO-Nf@Au8 modified electrode with 1 mM NO in 0.1 M PBS (pH 2.5) at a scan rate of 50 mV/s and (C) CV curves of GC/rGO-Nf@Au8 modified electrode after placed in air for five days.

6.2.5.6 Real Sample Analysis

In order to certify the practicability of the GC/rGO-Nf@Au8 modified electrode in analytical applications, it was applied to detect NO in real water samples by the standard addition method. The recoveries of different concentrations (10, 50 and 100 μM) of NO were detected in the tap and lake waters which were sampled from University of Malaya. The recovery values for three parallel measurements were calculated to evaluate the accuracy of the sensor and the results were listed in Table 6.2. It is clear that the proposed sensor shows satisfactory results with the recovery in the range of 89 to 100.8 % and RSD values in the range of from 0.6 to 2.1 %, indicating that this method could be efficiently applied to determine NO with good accuracy.

Table 6.2: Detection and recovery of NO in real water samples by using the novel GC/rGO-Nf@Au8 modified electrode.

| Real samples | NO added (μM) | NO detected ^a (μM) | RSD (%) | Recovery (%) |
|--------------|----------------------------|--|---------|--------------|
| Tap water | 10 | 9.7 | 1.7 | 97 |
| | 50 | 50.4 | 0.7 | 100.8 |
| | 100 | 100.7 | 1.5 | 100.7 |
| Lake water | 10 | 8.9 | 2.1 | 89 |
| | 50 | 49.1 | 0.6 | 98.2 |
| | 100 | 97.9 | 0.6 | 97.9 |

^a Average of three determinations

6.3 Summary

The rGO-Nf@Au nanohybrids has been successfully synthesized by simple hydrothermal method and has been used to modify GCE before further applied to quantify NO in acidic solution. Three different rGO-Nf@Au nanohybrids has been synthesized where each of it has different Au content (4, 8 and 12 mM). All the GC/rGO-Nf@Au modified electrodes exhibit a good electrocatalytic activity towards the oxidation of NO and among these; the GC/rGO-Nf@Au8 modified electrode displayed the best sensing performance for determination of NO.

The GC/rGO-Nf@Au8 modified electrode has strong and sensitive current responses to NO with an amperometric detection limit of 5×10^{-7} M. It is noteworthy that this modified electrode is also highly resistant toward common interfering species such as DA, AA, UA, glucose, NaCl and urea, making it highly selective toward NO. Besides that, it also demonstrates an acceptable reproducibility, repeatability and excellent stability, which could be used as an amperometric biosensor for determination of NO. The excellent sensing performance shown by rGO-Nf@Au8 nanohybrids were attributed to the high conductivity and surface area provided by rGO-Nf sheets as well as the interface-dominated properties owned by AuNPs.

The strong synergistic effect between rGO-Nf and AuNPs was further enhancing the sensing performance as it leads to the effective electron transfer, hence improved the sensitivity of the sensor electrode. The satisfactory results obtained for NO analyses of tap and lake waters suggest that the proposed sensor is suitable for practical applications. In view of the above results, it has proven that the rGO-Nf@Au8 nanohybrid has a great potential for the development of new electrochemical sensing devices especially for the detection of NO.

CHAPTER 7

REDUCED GRAPHENE OXIDE/NAFION@PALLADIUM NANOHYBRID MODIFIED ELECTRODE FOR ELECTROCHEMICAL DETECTION OF L-CYSTEINE

7.1 Introduction

An organic compound which contain at least one amino group ($-\text{NH}_2$) and a carboxy ($-\text{COOH}$) group is known as amino acid. There are twenty types of amino acid in human genome which act as the precursor for proteins and incorporated into proteins during translation. This type of amino acid is called proteinogenic amino acid and one of it is the L-Cysteine (L-Cys). L-Cys is the simplest amino acid and fall in the non-essential amino acid category as it can be produced in the human liver from an essential amino acid called methionine. L-Cys is needed to protect the cells from free radicals and prevents it from harmful effects of tobacco and alcohol use as well as involved in the detoxification process.

Besides that, L-Cys play a critical role in antioxidant defenses due to the presence of sulfur-containing group in L-Cys and it also helps in boosting the immune system. The abnormal level of L-Cys may lead to several clinical situations that consisted of the slow growth, hair depigmentations, edema, liver damage, muscle and fat loss, skin lesions and weakness are the effect of L-Cys deficiency (Santhiago *et al.*, 2007; Wang *et al.*, 2005). Meanwhile, the excessive levels of L-Cys link to the Alzheimer's disease, Parkinson's disease and autoimmune deficiency syndrome (Zhang *et al.*, 2016). Therefore, the development of a simple and effective method for quantification of L-

Cys is of great significance in biological and clinical application especially in the disease diagnosis.

Up to now, various analytical methods have been reported in the literature with the attempt to determine L-Cys level such as colorimetric (Jongjinakool *et al.*, 2014; Wu *et al.*, 2016), high-performance liquid chromatography (Deáková *et al.*, 2015), fluorescence (Shankar *et al.*, 2015; Xu *et al.*, 2015) and mass spectrometry (Burford *et al.*, 2003). However, all these techniques has several limitation such as require complex instrument which is high cost, time consuming and suffer from low sensitivity and specificity. In order to overcome these problems, electrochemical method has been the best approach for developing a simple selective and sensitive sensor for L-Cys associated with their easy operation with low cost, rapid response, low detection limit and high sensitivity. In this regard, carbon-based materials including multi-walled carbon nanotubes (MWCNTs) (Azadbakht *et al.*, 2013), ordered mesoporous carbon (OMC) (Zhou *et al.*, 2007) and graphene (Falkowski *et al.*, 2017) were commonly employed as electrode materials for electrochemical sensor.

Considering the merits of graphene including large specific surface area, excellent conductivity, and good biocompatibility, it has been widely applied in electrochemical sensor especially for detecting various biomolecules. Up to date, the strategy of combining the metal nanoparticles with graphene to produce graphene-metal nanocomposites tend to showed great improvement in sensing performance (Zare *et al.*, 2016). Among the diverse metal nanomaterials, palladium nanoparticles (PdNPs) have attracted enormous attention owing to their outstanding physical and chemical properties including excellent electrical conductivity, good catalytic activity and excellent binding capability with graphene (Wu *et al.*, 2017). Nevertheless, the use of

graphene-metal nanocomposites as electrode modifier faces several problems like agglomeration, stability and cross-interference issues. In order to address those issues, several modified electrodes have been constructed with conducting polymer especially Nf. Nf is one of the most intensively investigated conducting polymer due to its excellent antifouling properties, high permeability to cations and chemical inertness. The hydrophobic backbone owned by Nf helps to improve the dispersity of graphene and imparted stability to the nanohybrid material (Liu *et al.*, 2009).

Herein, we synthesized a nanohybrid material based on reduced graphene oxide (rGO), Nf and PdNPs using simple hydrothermal technique. The prepared rGO-Nf@Pd nanohybrid was used to modify GCE to fabricate novel GC/rGO-Nf@Pd sensor for accurate detection of L-Cys. The rGO-Nf@Pd nanohybrids with three different Pd content were prepared to investigate the influence of Pd content on the electrocatalytic activity toward oxidation of L-Cys. The performance of the modified electrode at various experimental conditions (concentration of analyte, scan rates, sample loaded and pH) were tested with the intention of getting the optimum condition for the electrochemical determination of L-Cys. The proposed sensor exhibits a low detection limit with high sensitivity and selectivity under the optimized condition due to the synergetic effect between rGO-Nf films and PdNPs.

It is believed that the existence of large number of electrochemically favorable edge carbons per mass of graphene could greatly facilitate the electron transfer between the electroactive species and the electrode surface, thus promoting the electrocatalytic process (Bagheri *et al.*, 2017). Moreover, the presence of PdNPs in nanohybrid further induces the effective electrocatalytic oxidation of L-Cys. Nf was used to improve the dispersion of graphene in aqueous solution which at the same time enhance the stability

of the modified electrode. Other than that, it also play an important role as a binder to help other modifiers effectively adheres on electrode surface, thereby leading to faster diffusion of analyte into the electrode (Yang *et al.*, 2015). Additionally, this method was also successfully applied to determine L-Cys concentration in human urine and interestingly, it shows highly satisfactory results with excellent recoveries revealing its potential for practical application.

7.2 Results and Discussion

7.2.1 Crystalline and Structural Characterization of rGO-Nf@Pd Nanohybrids

The crystalline nature of the nanohybrids was examined by using X-ray diffraction (XRD) and the results were presented in Figure 7.1. The XRD patterns in inset of Figure 7.1 illustrate the diffraction obtained from GO and rGO. One sharp characteristic peak can be observed in the XRD pattern for GO that centered at $2\theta = 10.5^\circ$, which attributed to the introduction of various oxygen functional groups (hydroxyl, epoxy, carbonyl groups, etc.) on both sides of the graphene layers (Choi *et al.*, 2017). The appearance of a big bump at about $2\theta = 25^\circ$ in the XRD patterns of rGO demonstrates that the occurrence of GO reduction during the hydrothermal process to form rGO (Khandelwal *et al.*, 2015). A small peak at 2θ of 42.3° can be correlated with the (1 0 0) plane of the hexagonal structure of carbon (Zhang *et al.*, 2011).

Meanwhile, three obvious peaks can be seen at 40.2° , 46.7° and 68.2° which can be well indexed to the (1 1 1), (2 0 0) and (2 2 0) planes respectively, that derived from the standard Pd phase (JCPDS 01-089-4897) (Figure 7.1(i-iii)). The XRD features owing to the rGO almost disappear in the XRD patterns of rGO-Nf@Pd nanohybrids due to the strong diffraction pattern of Pd that become dominant. The sharp characteristic peaks observed in all XRD patterns of nanohybrids indicating the good crystallization of

the rGO-Nf@Pd nanohybrids. Moreover, it is important to note that the peak intensity increased with the increase in the concentration of Pd precursor from 3 to 9 mM, implying that more PdNPs has formed on the rGO-Nf sheets. The results of the XRD analysis reveal that the rGO-Nf@Pd nanohybrids have been successfully synthesized.

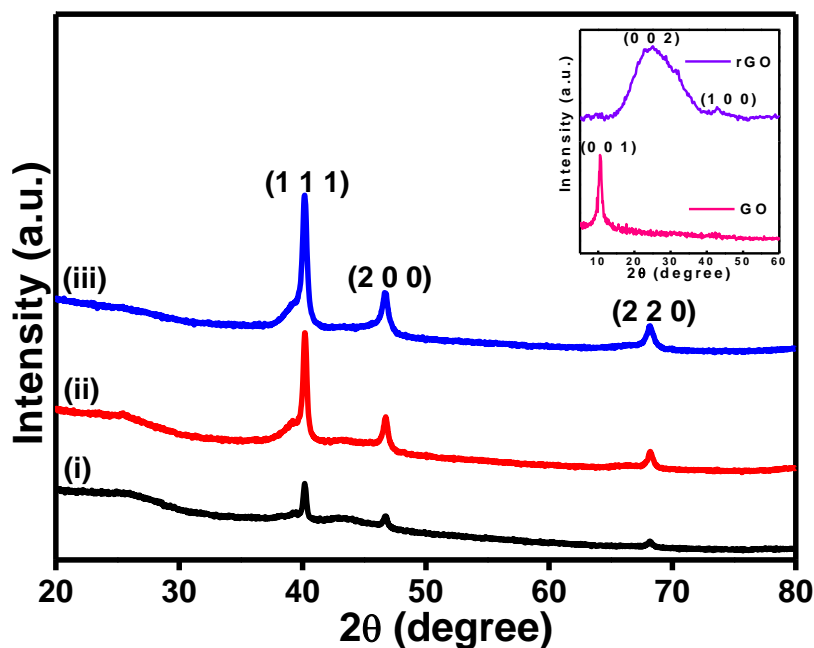


Figure 7.1: XRD patterns of (i) rGO-Nf@Pd3, (ii) rGO-Nf@Pd6, and (iii) rGO-Nf@Pd9 nanohybrids (Inset shows the XRD patterns for GO and rGO).

Raman spectroscopy is widely used to characterize the carbon based material as it provides information regarding the ordered and disordered crystalline structure. Figure 7.2 presents the Raman spectra of GO and three different rGO-Nf@Pd nanohybrids from 1200 to 1800 cm^{-1} , which reveal two prominent peaks appeared in Raman spectra for all samples. The first peak observed at 1355 cm^{-1} can be assigned to the D band which associated with structural defects and partially disordered structures of the sp^2 domains (Some *et al.*, 2016). The second peak observed at 1602 cm^{-1} was ascribed to the G band which originated from the vibrations of sp^2 carbon atom domains of graphite (Lv *et al.*, 2013). The intensity ratio of D to G bands (I_D/I_G) provides the information regarding the degree of graphitization. The I_D/I_G of nanohybrid samples

were higher than GO due to the defect after the removal of oxygen functional groups during the reduction process and introduction of large amounts of sp^2 carbon networks with small average sizes (Wong *et al.*, 2015).

These results further confirm the successful reduction of GO to form rGO after hydrothermal process. The blue shift in G band position of rGO-Nf@Pd nanohybrids compared with that of GO can be observed, which reveal the occurrence of chemical interaction between rGO-Nf and PdNPs. This shift in the G band could be attributed to the charge transfer from rGO-Nf to PdNPs as well as formation of a new bonding between them (Rao *et al.*, 1997). Among these nanohybrids, rGO-Nf@Pd6 nanohybrid showed highest blue shift in the G band ($+10\text{ cm}^{-1}$ from G band position for GO), thus indicate that it has the strongest interaction between rGO, Nf and PdNPs.

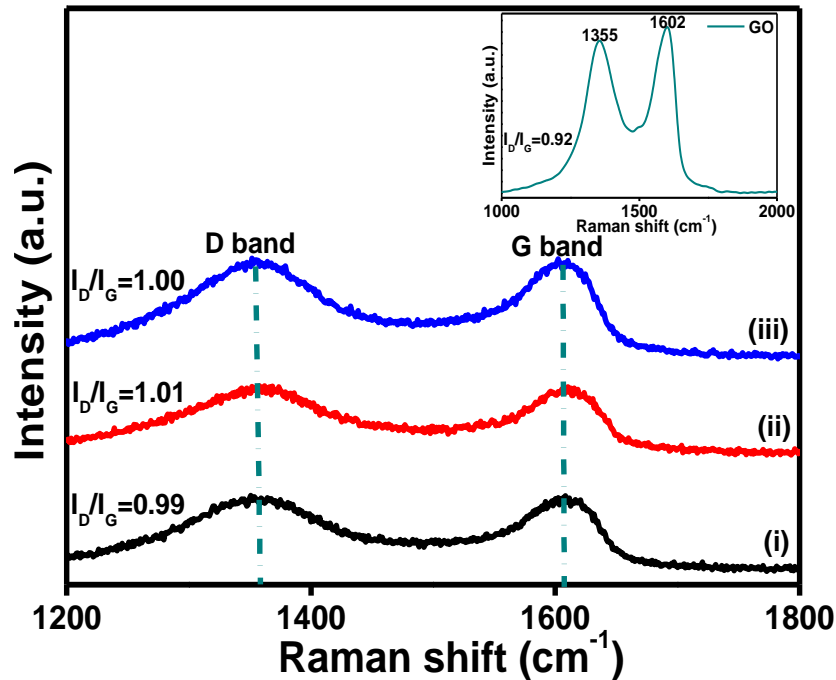


Figure 7.2: Raman spectra of (i) rGO-Nf@Pd3, (ii) rGO-Nf@Pd6 and (iii) rGO-Nf@Pd9 nanohybrids (Inset shows the Raman spectrum for GO).

7.2.2 Morphological Characterization of rGO-Nf@Pd Nanohybrids

The morphological characterization of rGO-Nf and rGO-Nf@Pd nanohybrids has been carried out by FESEM and the results were shown in Figure 7.3.

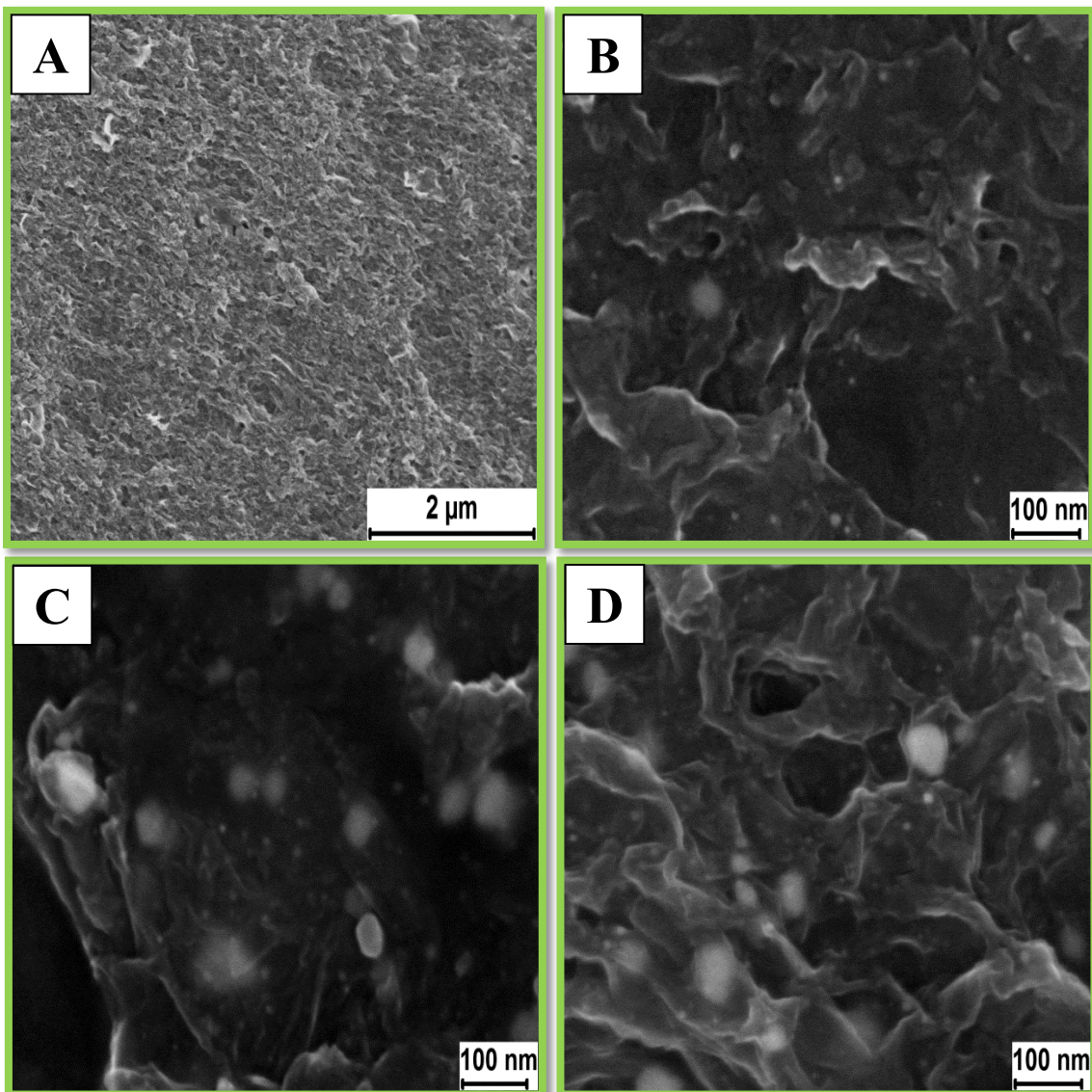


Figure 7.3: FESEM images of (A) rGO-Nf, (B) rGO-Nf@Pd3, (C) rGO-Nf@Pd6 and (D) rGO-Nf@Pd9 nanohybrids.

As illustrated in Figure 7.3(A), the rough surface structure suggesting that the Nf was adsorbed on the surfaces of rGO through π - π interaction, thus confirming the formation of rGO-Nf nanohybrid. Presence of PdNPs on the surface after hybridization with rGO-Nf was clearly evident in the FESEM image illustrated in Figure 7.3(B-D). It can be

observed that the rGO-Nf@Pd nanohybrids were composed of irregular Pd particles with spherical structure and a size less than 50 nm in diameter. The adherence of PdNPs between layers of rGO-Nf sheets illustrates the efficient nanohybrids formation by using the hydrothermal method.

The elemental mapping images obtained from FESEM of rGO-Nf@Pd6 nanohybrid revealed the distribution of Pd, carbon (C), oxygen (O) and fluorine (F) in the selected area of the rGO-Nf@Pd6 nanohybrid (Figure 7.4(A)). Notably, the presence of Pd element indicated that the PdNPs were uniformly distributed on the rGO-Nf surface.

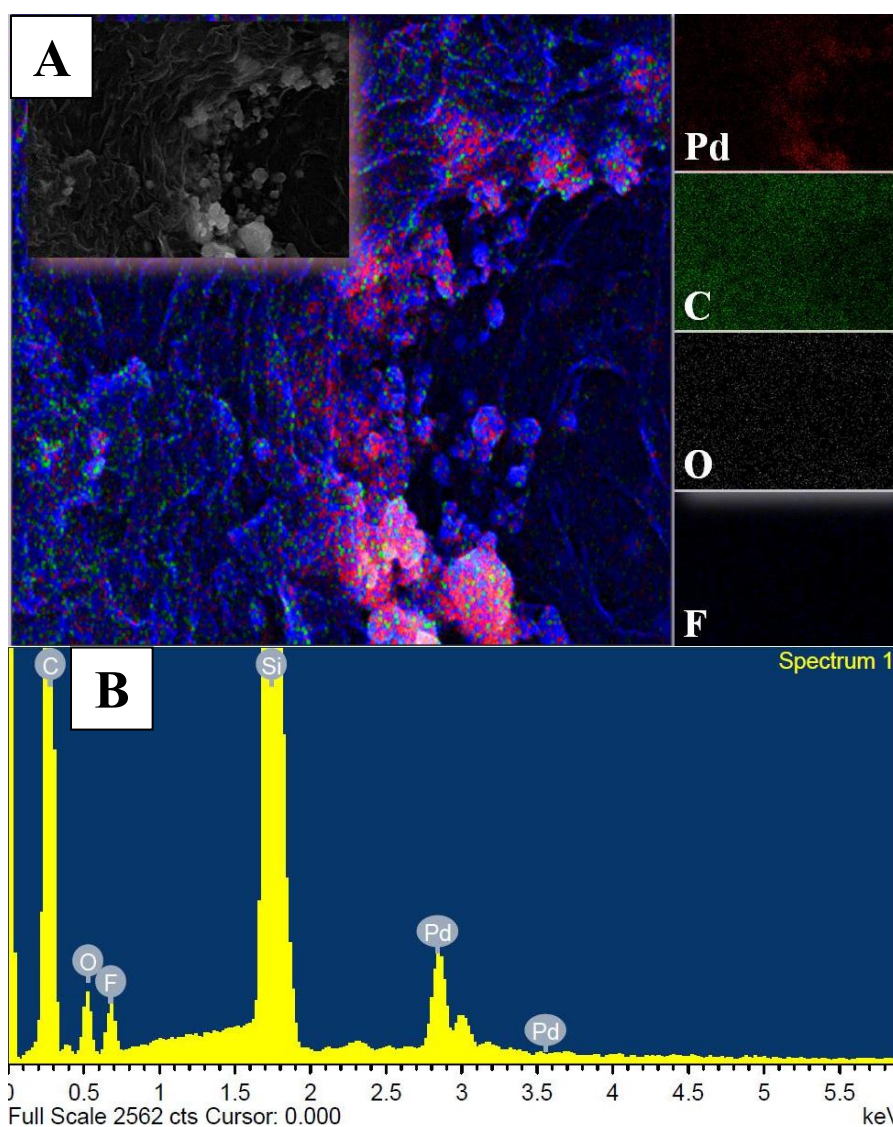


Figure 7.4: (A) Qualitative elemental mapping and (B) EDX analysis of rGO-Nf@Pd6 nanohybrid.

In order to further examine the chemical composition presence in the nanohybrid, the EDX was conducted and the result was shown in Figure 7.4(B). In the EDX spectra, strong signal was exhibited from C, F and Pd along with small signal from O atom. The C and O elements were arising from rGO while F element originates from Nf. This result was in accordance with the mapping results and it signified that the nanohybrid was composed of highly pure PdNPs decorating on the surface of rGO-Nf sheets. Note that the Si signal was arise from the Si substrate that used to deposite the sample.

In order to get clearer picture on the morphology of the rGO-Nf@Pd nanohybrids, the HRTEM analysis was conducted. It was clearly seen in Figure 7.5(A-C) that PdNPs has sphere structure with nanosize successfully loading on the surface of rGO-Nf sheets. This indicates that rGO-Nf is an effective supports for PdNPs. Notably, the PdNPs that attached to the rGO-Nf surface were scattered uniformly on the sheets with a large deposition density as the concentration of Pd precursor was increased, but the particles sizes do not change obviously. However, the PdNPs started to form agglomeration when increase the Pd precursor content to 9 mM due to the aggregative growth of the small particles during the reduction process. As shown in the inserted picture at the right bottom corner of Figure 7.5(C), the individual Pd particle on the rGO-Nf sheet shows a lattice spacing of 0.225 nm which corresponds to the (1 1 1) crystal plane for PdNPs. Figure 7.5(D-F) displays the particle size distribution histograms of PdNPs from HRTEM images of rGO-Nf@Pd nanohybrids. The particle sizes of Pd calculated from HRTEM image of rGO-Nf@Pd3 nanohybrid were found to be in the range of 4 to 16 nm. In the case of rGO-Nf@Pd6 nanohybrid, the PdNPs distributed on rGO-Nf sheet have a diameter size ranging from 4 to 12 nm. Meanwhile, the diameter size of PdNPs embedded on the surface was analyzed to be in the range of 6 to 10 nm. These observations prove that PdNPs were successfully embedded into the rGO-Nf sheet and

the concentration of Pd precursor does not obviously affect the particle size and morphology but it does influencing the distribution of PdNPs on the rGO-Nf surface.

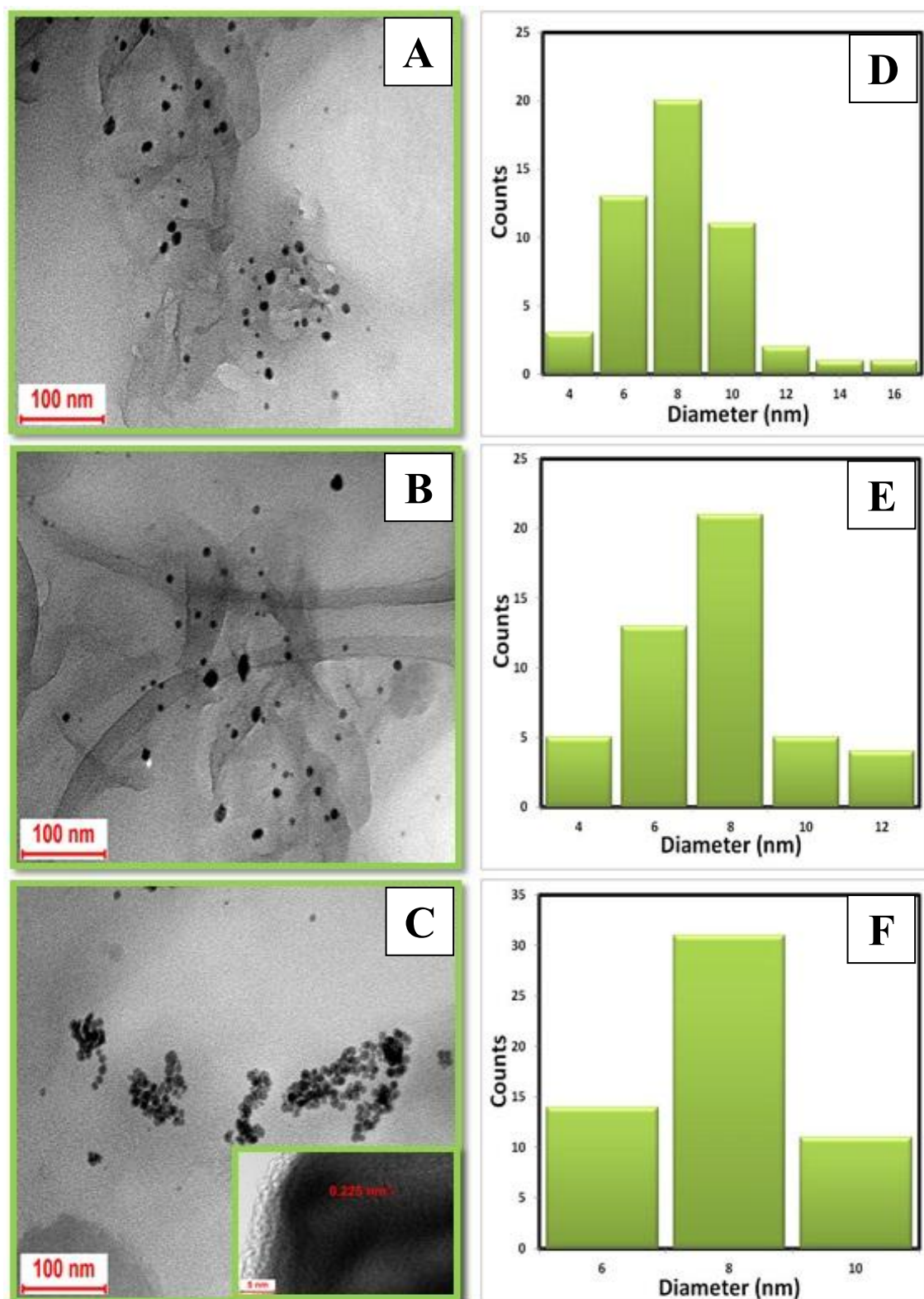


Figure 7.5: (A-C) HRTEM images of rGO-Nf@Pd3, rGO-Nf@Pd6 and rGO-Nf@Pd9 nanohybrids with their corresponding histogram of PdNPs sizes (D-F) (Inset shows the individual PdNPs on rGO-Nf sheet).

7.2.3 Electrochemical Characterization of GC/rGO-Nf@Pd Modified Electrode

A CV and electrochemical impedance spectroscopy (EIS) were used to investigate the electrochemical behavior of various modified electrodes. The CV test were performed at a scan rate of 50 mV/s in 0.1 M KCl with 5 mM $K_3[Fe(CN)_6]$ and the results were depicted in Figure 7.6. When GCE is modified with Nf, there was no obvious peak could be observed (Figure 7.6(A)). It was reported that the $[Fe(CN)_6]^{3-/4-}$ has been blocked from reaching the electrode surface resulted from the electrostatic interaction between negatively charged Nf and $[Fe(CN)_6]^{3-/4-}$ which tend to repel from each other. The GC/GO and GC/GO-Nf modified electrode exhibit a redox behavior with low current respond and peak to peak separation (ΔE_p) value higher than 150 mV. This result indicated that GO exhibits a slow electron transfer as a result of its structural effects such as oxygen-containing groups that might repel the negative redox couple as well as low edge plane content and low specific surface area (Jia *et al.*, 2015).

Meanwhile, it could be seen that a couple of well defined redox peaks appear on the bare GCE, GC/rGO, GC/rGO-Nf and three different GC/rGO-Nf@Pd modified electrodes as shown in Figure 7.6(B). These peaks were attributed to the quasireversible one-electron redox behaviour of $[Fe(CN)_6]^{3-/4-}$ ion. The ΔE_p was estimated for rGO-Nf@Pd3, rGO-Nf@Pd6 and rGO-Nf@Pd9 modified GCE to be 91, 82 and 89 mV, respectively. The lower ΔE_p obtained for rGO-Nf@Pd6 nanohybrid modified GCE indicates its improved electron transfer kinetics at the electrode surface when compared to other modified electrodes. These experimental results attributed to the fact that large surface area of the rGO-Nf films and the excellent conductivity owned by PdNPs, thus improved the electron transfer between $[Fe(CN)_6]^{3-/4-}$ ions and the electrode surface. An obvious increase of both cathodic and anodic peak currents could also been observed at

GC/rGO-Nf@Pd6 modified electrode which indicates the higher electrical conductivity due to the synergetic effect aroused between rGO-Nf and PdNPs.

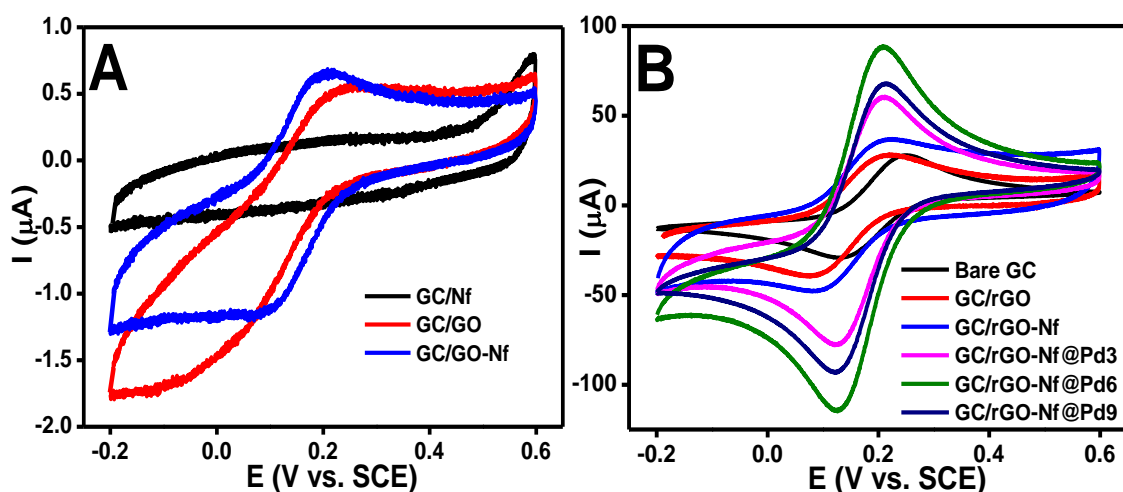


Figure 7.6: (A & B) CV curves obtained at various modified electrode in a 0.1 M KCl with 5 mM $K_3[Fe(CN)_6]$ (scan rate: 50 mV/s).

Figure 7.7(A) shows the Nyquist plot for bare GCE, GC/rGO-Nf@Pd3, GC/rGO-Nf@Pd6, and GC/rGO-Nf@Pd9 modified electrodes. As can be seen, the Nyquist plot obtained for bare GCE comprise of a semicircle portion at higher frequencies and a linear line in the lower frequency range which attribute to the electron transfer-limited process and limited mass transfer of the $[Fe(CN)_6]^{3-/4-}$ ion, respectively (Bagheri *et al.*, 2016). The diameter of this semicircle indicates the charge transfer resistance (R_{ct}) which controls the electron-transfer kinetics of the redox couple at the electrode interface (Kaur *et al.*, 2015). After the modification of GCE with rGO-Nf@Pd nanohybrids, the Nyquist plots displayed a nearly straight line indicating negligible R_{ct} . This result reflects the improvement in electrocatalytic activity and high interfacial electron transfer ability of the modified electrode. Based on the above characterizations, it were proven that the incorporation of PdNPs with rGO-Nf films enhance the conductivity of the electrode thus permitting rapid diffusion of $[Fe(CN)_6]^{3-/4-}$ ion toward the electrode surface. Figure 7.7(B) shows the equivalent circuit that fits the impedance

spectra of rGO-Nf@Pd6 that consists of resistance of the electrolyte (R_s), R_p (R_{ct}), CPE and Warburg impedance (Z_w). Z_w is used to model the linear semi-infinite diffusion, which occurs when the diffusion layer has an infinite thickness. It appears as a straight line with a 45° slope (phase angle) at low frequencies in the Nyquist plot.

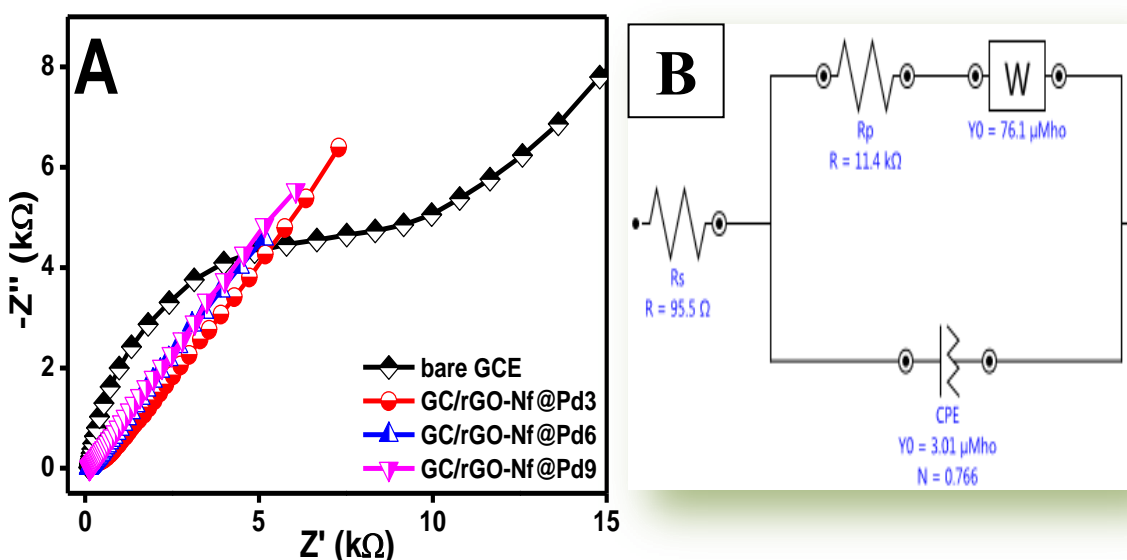


Figure 7.7: (A) Nyquist plots for bare GCE, GC/rGO-Nf@Pd3, GC/rGO-Nf@Pd6, and GC/rGO-Nf@Pd9 in a solution of 0.1 M KCl with 5 mM $K_3[Fe(CN)_6]$ (frequency range: 10 mHz to 10 kHz) and (B) the equivalent circuit for modelling of EIS experimental data of GC/rGO-Nf@Pd6.

7.2.4 Electrochemical Determination of L-Cysteine

7.2.4.1 Electrocatalytic Oxidation of L-Cysteine

Figure 7.8 exhibits the CV curves for bare GCE and other modified electrodes in the presence of 5 mM L-Cys. It can be seen in Figure 7.8(A) that there was no apparent redox peaks appeared under the applied potential range of 0 to +0.8 V in the presence of 5 mM L-Cys for bare GCE. However, there is negligible current response when the GC/Nf was used as working electrode. An apparent oxidation peak at +0.58 V could be observed in CV curves for GC/GO and GC/rGO where the current response for L-Cys at GC/rGO obviously higher than at GC/GO, as a result of high conductivity and large

specific surface area of rGO. It is notable that the peak current of L-Cys clearly increased after modifying the GC electrode with rGO-Nf@Pd nanohybrids as depicted in Figure 7.8(B).

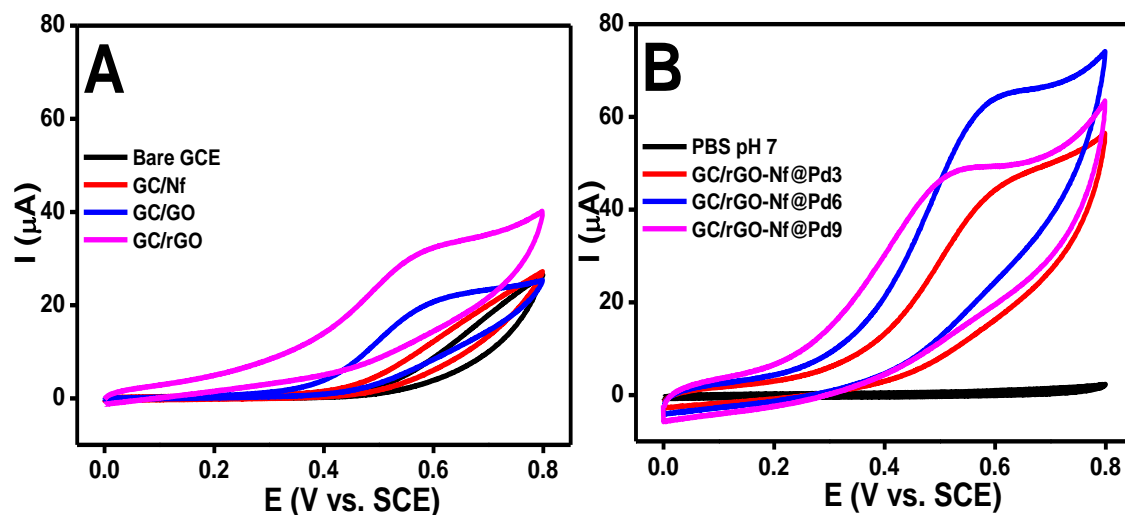
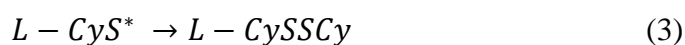
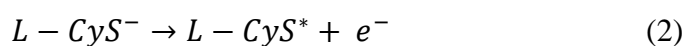
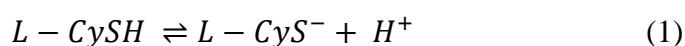


Figure 7.8: (A & B) CV curves of different modified electrodes in 0.1 M PBS (pH 7) containing 5 mM L-Cys at a scan rate of 50 mV/s.

This indicated that the rGO-Nf@Pd nanohybrids have excellent electrocatalytic ability towards the oxidation of L-Cys. The enhanced electrochemical performance of the GC/rGO-Nf@Pd modified electrode could be attributed to the following factors: (1) excellent electrical conductivity owned by rGO helps to promote and accelerate the electron transfer between modified electrode and target analytes, (2) synergistic effects of rGO-Nf films and PdNPs further facilitates the electron transfer processes between the electrolyte and the modified electrode, (3) the unique sheets-like structure of rGO-Nf films with large surface-to-volume ratio and high dispersity offers more active surface areas for the occurrence of the reaction, (4) the presence of nano size Pd particles provides higher effective surface area for analyte adsorption. The high density of PdNPs decorated rGO-Nf sheets (compare to rGO-Nf@Pd3 nanohybrid) with well distribution (compare to rGO-Nf@Pd9 nanohybrid) led to fast diffusion of target analyte into the nanohybrid film thus be the reason for the excellent electrocatalytic

performance of rGO-Nf@Pd6 nanohybrid compared to other nanohybrids. Based on this result, the GC/rGO-Nf@Pd6 modified electrode is suitable for detecting the L-Cys, therefore this sensor electrode will be used for the further studies.

As reported in previous literature, L-Cys will be electro-oxidized and forming Cystine upon the application of a potential to the GC/rGO-Nf@Pd modified electrode (Hosseini *et al.*, 2013). This electro-oxidation process of L-Cys involves the transfer of two electrons and two protons. The schematic diagram of the proposed sensing mechanism was presented in Figure 7.9. The electrochemical reaction was believed happen by following the equation expressed below (Geng *et al.*, 2016):



The overall reaction can be written as:

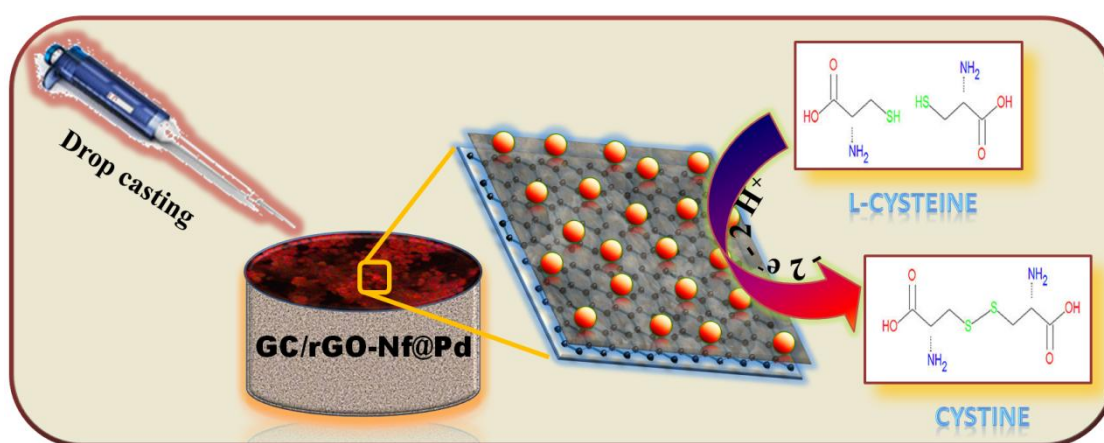
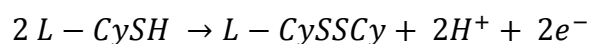


Figure 7.9: Schematic diagram of the electrocatalytic oxidation of L-Cys at the GCE/rGO-Nf@Pd modified electrode.

7.2.4.2 Optimization Studies

(a) Effect of Different Concentration of L-Cysteine

In order to evaluate the catalytic response of GC/rGO-Nf@Pd6 modified electrode toward the oxidation of L-Cys, a series of CV curves were recorded for different concentrations of L-Cys as shown in Figure 7.10(A). The enhancement in the current response could be observed as increased the concentration of L-Cys, indicating the dependence of current response with the concentration of L-Cys. Figure 7.10(B) shows that the sensor exhibits good linearity in the concentration ranging from 200 μ M to 5 mM. The corresponding linear regression equation for the variation of I_p versus concentration of L-Cys is given as $I_p = 0.010 [L - Cys] + 5.926\mu$ with a correlation coefficient (R^2) of 0.995. The oxidation peak current of L-Cys was linearly increased with increasing the L-Cys concentration reveals the electrocatalytic activity of GC/rGO-Nf@Pd6 modified electrode toward the oxidation of L-Cys.

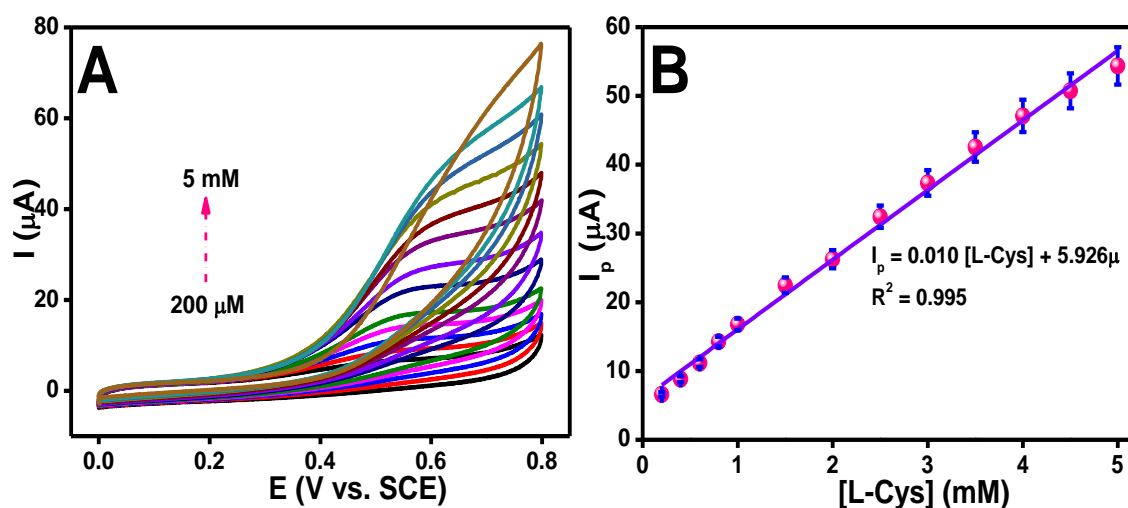


Figure 7.10: (A) CV curves of GC/rGO-Nf@Pd6 modified electrode in a 0.1 M PBS (pH 7) containing different concentrations of L-Cys scanning at a scan rate of 50 mV/s and (B) the corresponding plot of peak current versus concentration of L-Cys.

(b) Effect of Scan Rate

The influence of scan rates on the electrochemical oxidation of L-Cys at GC/rGO-Nf@Pd6 modified electrode was investigated by CV and the results are shown in Figure 7.11. According to the result in Figure 7.11(A), the scan rate of CV apparently affecting the peak potential and oxidation peak current of L-Cys. It was found that the oxidation peak potentials of L-Cys shift positively along with the increment of scan rates. Meanwhile, Figure 7.11(B) shows the relationship between anodic peak current with square root of scan rates. The oxidation peak current of L-Cys was increased when increasing the scan rate from 50 to 500 mV/s and are proportional to the square roots of the scan rates. The linear regression equation is expressed as $I_p = 4.714 \mu v^{1/2} - 9.061 \mu$ with $R^2 = 0.998$. This result demonstrate that the electrode process is diffusion-controlled process (Liu *et al.*, 2016).

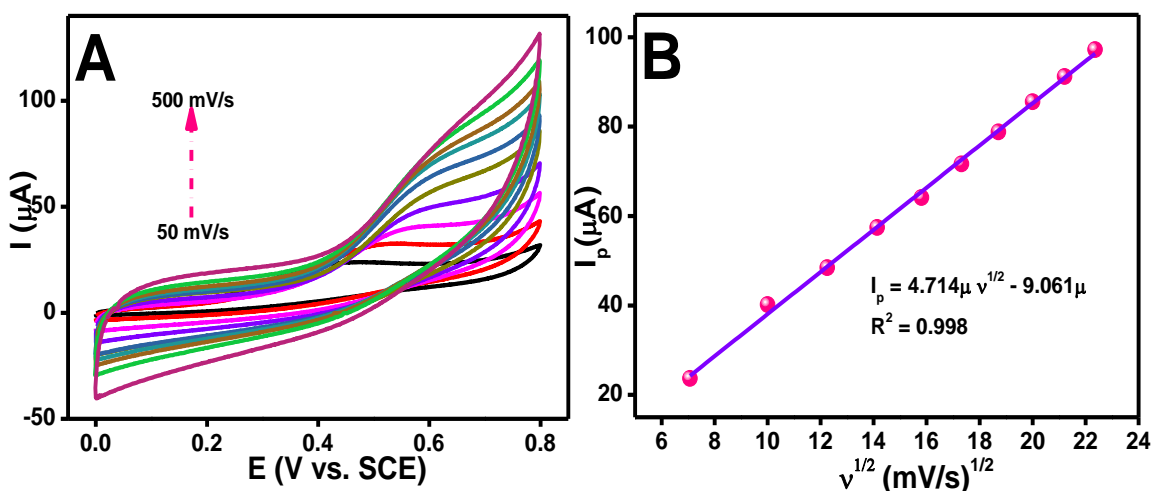


Figure 7.11: (A) CV curves of GC/rGO-Nf@Pd6 modified electrode in 0.1 M PBS (pH 7) containing 1 mM L-Cys scanning at different scan rates and (B) plotting of peak current as a function of scan rate ranging from 50 to 500 mV/s.

(c) Effect of rGO-Nf@Pd6 Loading

The effect of rGO-Nf@Pd6 nanohybrid loading amount on the electrocatalytic oxidation of L-Cys at the GC/rGO-Nf@Pd6 modified electrode was investigated by CV.

Figure 7.12(A) presents the CV curves of 1 mM L-Cys oxidized at the GC electrode that had been modified with different content of rGO-Nf@Pd6 nanohybrid. Obviously, the current response is mainly influenced by the loading amount of rGO-Nf@Pd6 nanohybrid. As can be seen in Figure 7.12(B), the anodic peak current increased with the increase amount of rGO-Nf@Pd6 loading in the range of 2 to 10 μL . However, further increase in the loading amount (more than 10 μL) leads to the decrease in the current response. The use of more sample content will lead to the formation of thick layer on the surface of electrode which then hinders the electron transfer, thus results in the low current response. Therefore, the loading amount of 10 μL was selected as optimal condition for the detection of L-Cys.

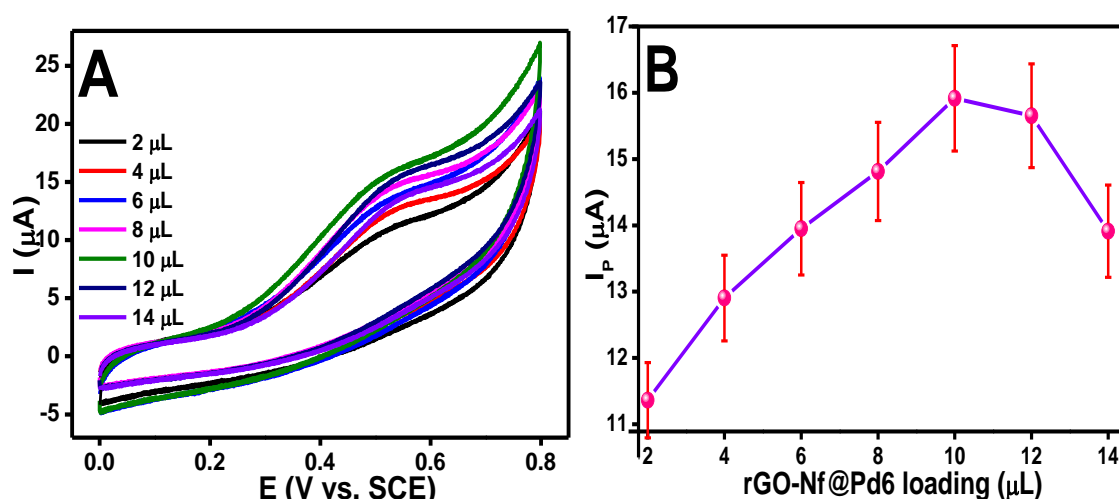


Figure 7.12: (A) CV curves of GCE modified by rGO-Nf@Pd6 nanohybrid with different loading amounts in 0.1 M PBS (pH 7) with the presence of 1 mM L-Cys at a scan rate of 50 mV/s and (B) the corresponding plot of anodic peak current as a function of different loading amount of rGO-Nf@Pd6 nanohybrid.

(d) Effect of pH

A series of CV curves were employed to investigate the influence of pH on the electrochemical behaviour of the GC/rGO-Nf@Pd6 modified electrode with 1 mM L-Cys in 0.1 M PBS. Different pH values were used ranging from 4 to 10 and the results were demonstrated in Figure 7.13. It can be observed that the anodic peak current of L-

Cys increased from pH 4 until it reached a maximum value at pH 7 (Figure 7.13(A)). Then, the anodic peak current started to decrease after pH 7, therefore pH 7 was used as an optimum pH for subsequent experiments. Furthermore, the anodic peak potentials shifted to more negative potentials with increased pH from 4 to 10. Evidently, the equal number of electron and proton involved in the electrode reaction, as the slope from the graph of anodic peak potential versus pH value shows a straight line ($E_p = -0.056(\text{pH}) + 0.978$; $R^2 = 0.982$) with a slope value of -0.056 V/pH (Figure 7.13(B)). This value is close to the Nernstian value of -0.059 V/pH which indicate that the proportion of the electron and proton involved in the reactions is 1:1 (Rajabi *et al.*, 2010).

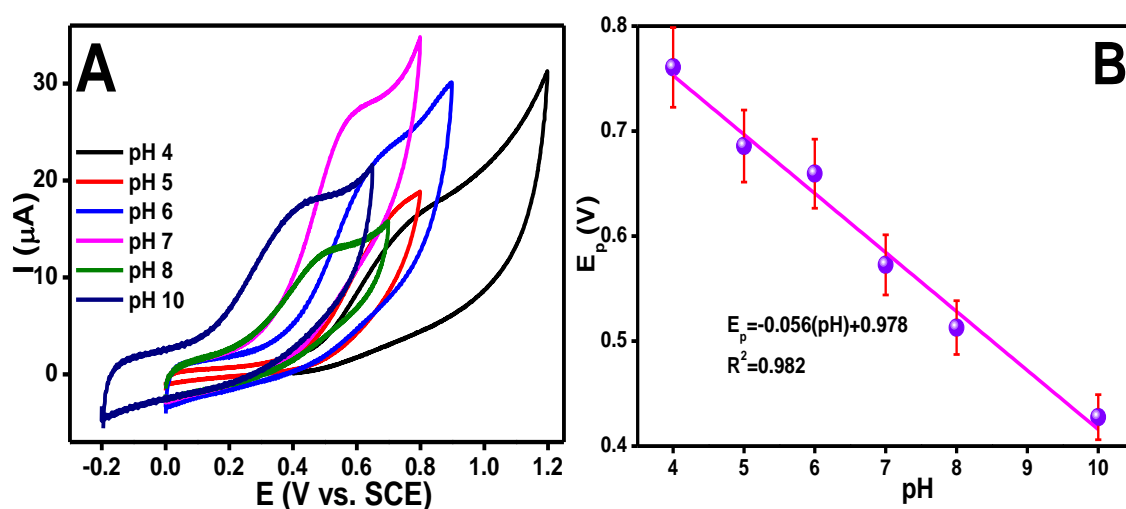


Figure 7.13: (A) CV curves of GC/rGO-Nf@Pd6 in 1 mM L-Cys at different pH (0.1 M PBS) at a scan rate of 50 mV/s and (B) plot of anodic peak potential versus pH values.

7.2.4.3 Amperometric Response of L-Cysteine

The amperometric method was employed under the optimum condition in order to determine L-Cys using GC/rGO-Nf@Pd6 modified electrode. Figure 7.14(A) shows the amperometric response of the GC/rGO-Nf@Pd6 modified electrode for successive addition of L-Cys into a stirred 0.1 M PBS (pH 7) under the ambient condition and with

a time interval of 60 sec. The amperometric detection was carried out at +0.6 V versus SCE reference electrode. The sensor does not show any current response in the 0.1 M PBS but the current started to increase upon the addition of 0.5 μM L-Cys. Interestingly, the proposed sensor electrode shows a fast respond as it took about 2 sec to achieve the steady-state current, hence suggesting the good catalytic activity toward L-Cys that owned by GC/rGO-Nf@Pd6 modified electrode.

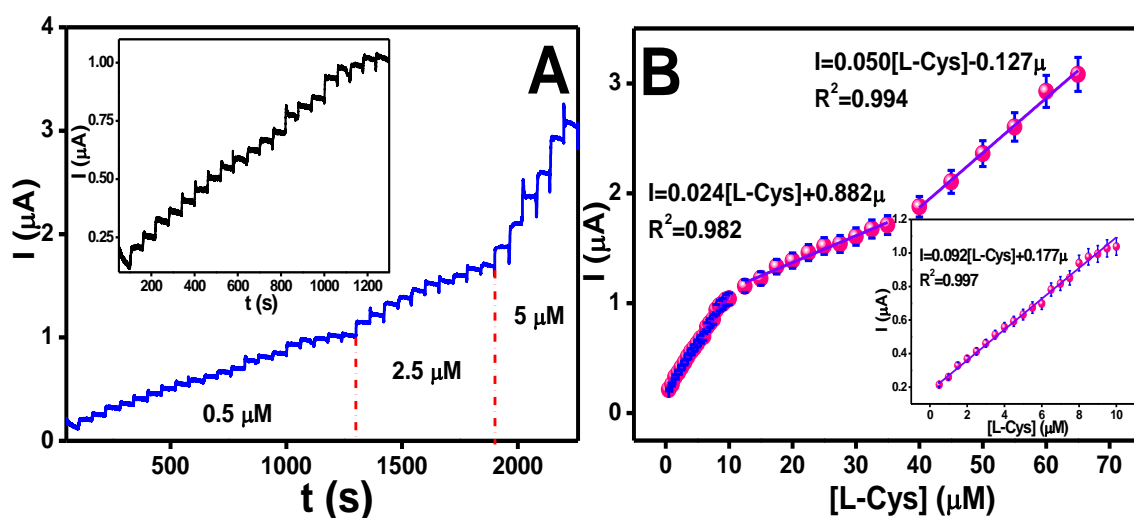


Figure 7.14: (A) Amperometric current response of GC/rGO-Nf@Pd6 for successive addition of L-Cys range from 0.5 μM to 65 μM in 0.1 M PBS (pH 7) at an applied potential of +0.6 V (Inset shows the enlarge image of the amperometric current response from 0 to 1240 sec) and (B) the corresponding calibration plot of current response versus L-Cys concentration (Inset shows the enlarge image of calibration plot for the low L-Cys concentration of 0.5 to 10 μM).

As presented in Figure 7.14(B), the calibration curve demonstrates three linear regimes in the regression line of current response dependence on the L-Cys concentration. The linear regression equation of the first regime was expressed as $I = 0.092 [\text{L} - \text{Cys}] + 0.177\mu$ with $R^2 = 0.997$ which responded to the concentration ranges of 0.5 to 10 μM . The second regime corresponds to the concentration ranging from 12.5 to 35 μM with a linear regression equation of $I = 0.024 [\text{L} - \text{Cys}] + 0.882\mu$ and $R^2 = 0.982$. The third linear sections in the regression line fit the equation of

$I = 0.050 [L - Cys] - 0.127\mu$ with $R^2 = 0.994$, for the concentration in the range from 40 to 65 μM . Based on the slope of first section in the linear regression line, the limit of detection (LoD) of this sensing system was calculated to be 145 nM, at a signal-to-noise (S/N) ratio of 3 and sensitivity of $0.092 \mu\text{A } \mu\text{M}^{-1}$.

Table 7.1 reviewed the comparison of analytical performance of the present study with earlier reports based on electrochemical sensors towards the detection of L-Cys. Particularly, this proposed GC/rGO-Nf@Pd6 modified electrode shows a comparable result with that reported previously. The excellent sensing performance with low detection limit at rapid response time as well as high sensitivity and selectivity toward L-Cys detection exhibited by GC/rGO-Nf@Pd6 modified electrode making it a promising platform for developing L-Cys sensors in biological applications.

Table 7.1: Comparison of the sensing performance of the proposed GC/rGO-Nf@Pd6 modified electrode with previously reported sensor electrodes for L-Cys detection.

| Electrode | Detection technique | Response time (sec) | Detection limit | Sensitivity | Interferences | Reference |
|---|---------------------|---------------------|--------------------|--|---|---------------------------------|
| GC/MoN/N-MWNTs | Amperometry | 1.5 | 3.64 μM | 198.59 $\text{nA } \mu\text{M}^{-1} \text{ cm}^{-2}$ | L-Glu, L-Val, L-Ile, L-Phe, L-Tyr and Glucose | (Geng <i>et al.</i> , 2016) |
| GC/GO/CNTs/Au NPs@MnO₂ | DPV | - | 3.4 nM | - | AA, Glutathione, Cystine, NH_4^+ , Na^+ , K^+ , Fe^{2+} , SO_4^{2-} , CO_3^{2-} | (Wang <i>et al.</i> , 2015) |
| GC/Au-SH-SiO₂@Cu-MOF | DPV | - | 8 nM | - | - | (Hosseini <i>et al.</i> , 2013) |
| GC/MnO₂-C/chit | Amperometry | 7 | 22 nM | - | Glutathione, Tryptophan, Tyrosine, L-lysine, Methionine | (Xiao <i>et al.</i> , 2011) |
| CPE/Y₂O₃ NPs/N-rGO | Amperometry | 5 | 0.8 μM | 12.33 $\mu\text{A } \mu\text{M}^{-1}$ | Tyrosine, Glucose, BSA, UA, AA | (Yang <i>et al.</i> , 2016) |
| GC/OMC | Amperometry | - | 2 nM | 23.6 $\mu\text{A } \text{mM}^{-1}$ | Tyrosine, tryptophan, UA | (Zhou <i>et al.</i> , 2007) |
| GC/NPG | Amperometry | - | 50 nM | 0.374 $\mu\text{A } \mu\text{M}^{-1}$ | Tryptophan, Tyrosine | (Liu <i>et al.</i> , 2012) |

Table 7.1, continued

| Electrode | Detection technique | Response time (sec) | Detection limit | Sensitivity | Interferences | Reference |
|--------------------------------------|---------------------|---------------------|--------------------|--------------------------------------|---|-----------------------------------|
| GC/Q–AgNPs–GNs | DPV | - | 0.28 μM | - | L-tryptophan, L-tyrosine, L-alanine, L-asparagine, Glycine, Methionine, Guanine, Glutathione, Glucose, Folic acid | (Zare <i>et al.</i> , 2016) |
| GC/Ag–Pd BNPs | CV | - | 2.8 μM | - | - | (Murugavelu <i>et al.</i> , 2014) |
| GC/AuNR/MWCNT | Amperometry | 1 | 8.25 nM | 120 nA μM^{-1} | Glutathione, homocystein, N-acetylcysteine mixture. AA, UA, NADH | (Silva <i>et al.</i> , 2013) |
| GC/MWCNTs–PVP/Cu²⁺ | Amperometry | 0.1 | 1.5 μM | 0.007 $\mu\text{A} \mu\text{M}^{-1}$ | L-glutathione, L-histidine, L-lysine, Glycine, L-tryptophan, | (e Silva <i>et al.</i> , 2012) |
| Ni(OH)₂ N P | CV | - | 1.2 μM | - | Homocysteine, Glutathione, AA, UA | (Jia <i>et al.</i> , 2011) |
| GC/rGO-Nf@Pd6 | Amperometry | 2 | 145 nM | 0.092 $\mu\text{A} \mu\text{M}^{-1}$ | DA, UA, AA, H ₂ O ₂ , glucose, urea. | This work |

MoN/N-MWNTs=Molybdenum nitride/nitrogen-doped multi-walled carbon nanotubes; L-Glu=L-glutamic; L-Val=L-valine; L-Ile=L-isoleucine; L-Phe=L-phenylalanine; L-Tyr=L-tyrosine; GO/CCNTs/AuNPs@MnO₂=graphene oxide/carboxylated multiwalled carbon nanotube/manganese dioxide/gold nanoparticles; Au-SH-SiO₂@Cu-MOF=gold-silicon dioxide-metal-organic framework; MnO₂-C/chit=manganese dioxide-carbon/chitosan; CPE/Y₂O₃-NPs/N-rGO=Carbon paste electrode/Yttrium oxide nanoparticles/nitrogen-doped reduced graphene oxide; BSA=Bovine serum albumin; OMC=ordered mesoporous carbon; Q–AgNPs–GNs= Quercetin silver nanoparticles graphene nanosheets; NPG=Nanoporous gold; Ag–Pd BNPs=Silver-palladium bimetallic nanoparticles; AuNR/MWCNT= multi-walled carbon nanotubes/gold nanorods; MWCNTs–PVP/Cu²⁺=multi-walled carbon nanotubes-poly(4-vinylpyridine)/copper ions.

7.2.4.4 Interference Study

The selectivity study is crucial for the practical application, therefore the interference study of the proposed sensor electrode in the presence of various common interfering species were tested. The amperometric response of GC/rGO-Nf@Pd6 modified electrode for the successive injections of L-Cys and several possible interfering substances into a continuously stirred 0.1 M PBS (pH 7) at a fixed potential of +0.6 V versus SCE was measured. As shown in Figure 7.15, a significant increase in the current

response was observed in the presence of 5 μM L-Cys, but no further obvious current change is observed with the subsequent addition of 100 μM of AA, UA, DA, H_2O_2 , urea and glucose. This result confirms that the stated substances do not interfere in the determination of L-Cys even though high concentrations of interfering substance (20 fold) were used. Therefore, the obtained results suggest that the proposed sensor electrode has excellent selectivity toward the detection of L-Cys.

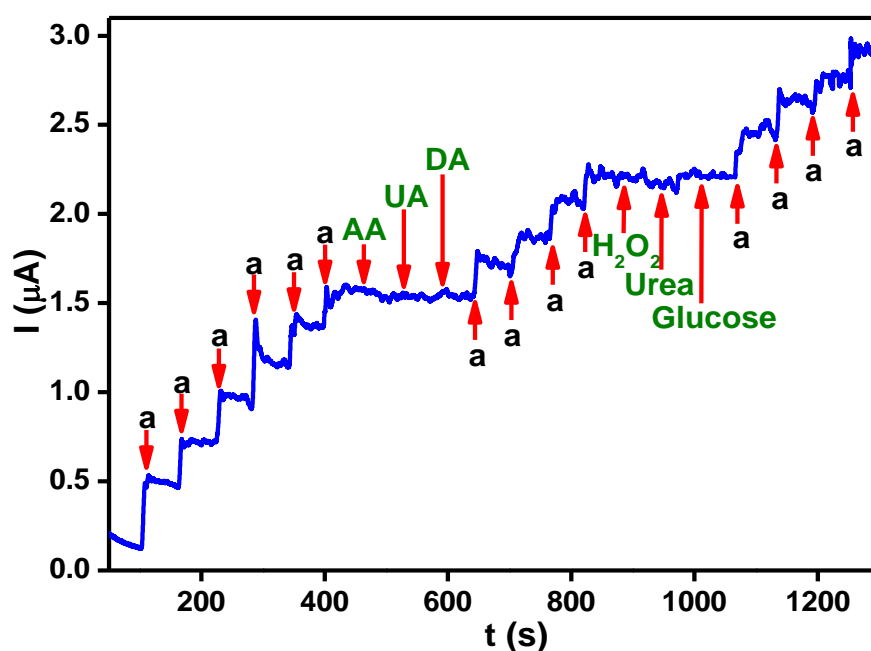


Figure 7.15: Amperometric (I-t) response of GC/rGO-Nf@Pd6 modified electrode at +0.6 V versus SCE in 0.1 M PBS (pH 7) with the successive addition of 5 μM L-Cys, and each 100 μM of AA, UA, DA, H_2O_2 , urea and glucose.

7.2.4.5 Reproducibility, Repeatability, and Stability Studies

Five electrodes modified by rGO-Nf@Pd6 nanohybrid were prepared under the same condition which used to study the reproducibility of the proposed sensor electrode. Their current responses to 1 mM concentration of L-Cys were recorded using CV and the result was presented in Figure 7.16(A). No obvious current changing can be observed and the RSD was calculated to be 1.48 %, thus verifying the high reproducibility of the proposed sensor electrode.

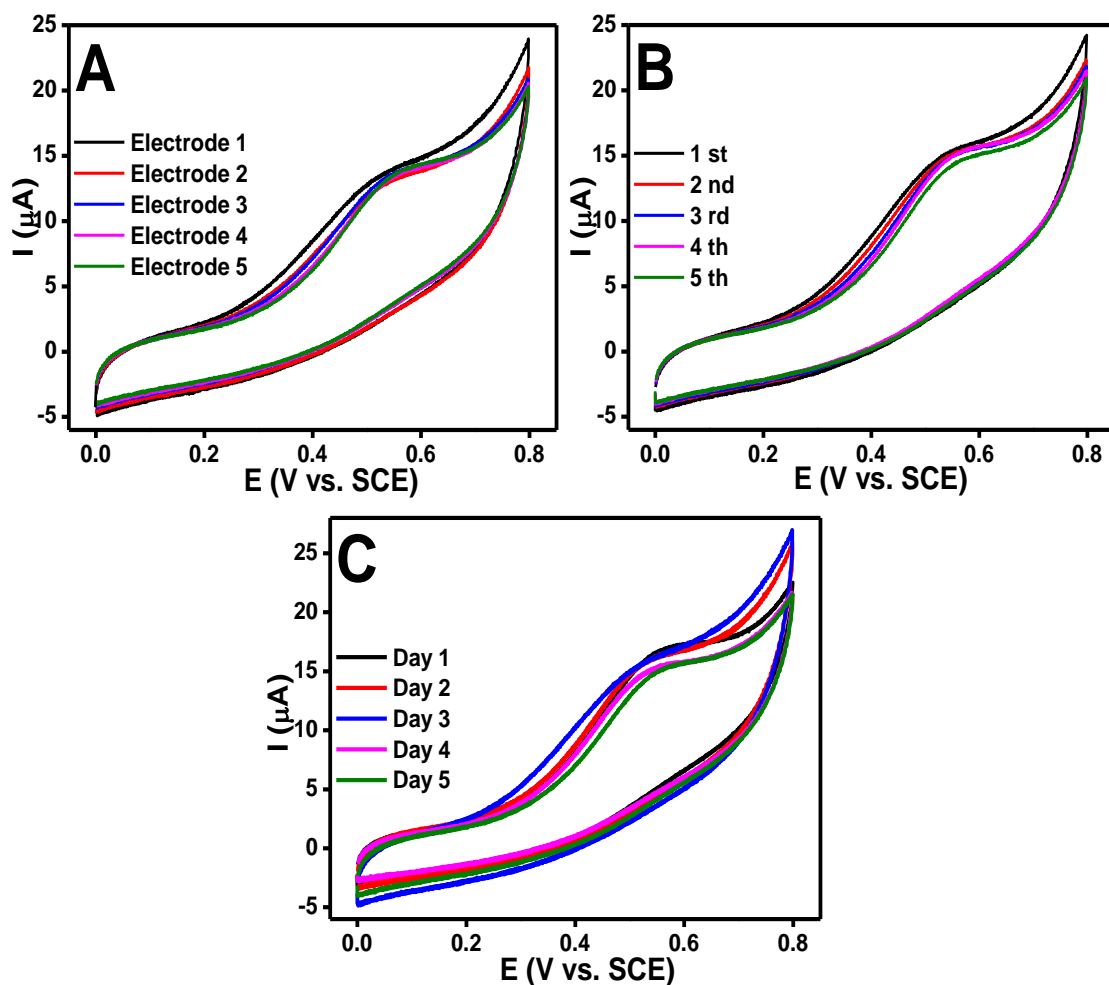


Figure 7.16: (A) CV curves of five different GC/rGO-Nf@Pd6 modified electrodes, (B) CV curves of five successive measurements of GC/rGO-Nf@Pd6 modified electrode with 1 mM L-Cys in 0.1 M PBS (pH 7) at a scan rate of 50 mV/s and (C) CV curves of GC/rGO-Nf@Pd6 modified electrode after placed in air at room temperature for five days.

Furthermore, to study the repeatability of the GC/rGO-Nf@Pd6 modified electrode for the determination of L-Cys, CV curves of 1 mM L-Cys were recorded over five repeating measurements on a single electrode (Figure 7.16(B)). The proposed sensor electrode was rinsed with DI water before taking each measurement. It was found that the GC/rGO-Nf@Pd6 modified electrode exhibit good repeatability with a RSD of about 1.88 % after being re-used for five successive measurements. In order to investigate the stability of the prepared GC/rGO-Nf@Pd6 modified electrode, CV was employed and the results were depicted in Figure 7.16(C). This modified electrode was

placed in air at room temperature for five days and CV curves in 1 mM of L-Cys were tested each day. The GC/rGO-Nf@Pd6 modified electrode retains 92.27 % of its initial current response of L-Cys after five days and have a RSD of 3.25 %, thereby revealing the good stability of the proposed sensor electrode for L-Cys determination.

7.2.4.6 Real Sample Analysis

An amperometric detection method was conducted to evaluate the practical applications of the sensor and the standard addition method was used to detect L-Cys in human urine samples. The urine samples were collected from two healthy individuals and it has been diluted 10 times with DI water before being used as the blank solution. Then, the diluted samples were spiked with appropriate concentration of L-Cys. A minimum of three determinations were recorded for each target concentration and the percentages of the recovery values were calculated by comparing the concentration that obtained from the samples with actually added concentration.

Table 7.2: Detection and recovery of L-Cys in human urine samples by using the novel GC/rGO-Nf@Pd6 modified electrode.

| Real samples | L-Cys added (μM) | L-Cys detected ^a (μM) | RSD (%) | Recovery (%) |
|--------------|-------------------------------|---|---------|--------------|
| Urine 1 | 5 | 4.87 | 2.01 | 97.40 |
| | 10 | 10.10 | 3.05 | 101.00 |
| | 20 | 19.45 | 1.08 | 97.25 |
| Urine 2 | 5 | 4.86 | 2.05 | 97.20 |
| | 10 | 10.04 | 1.36 | 100.4 |
| | 20 | 19.70 | 1.16 | 98.50 |

^a Average of three determinations.

The results of real sample analyses were summarized in Table 7.2. According to the obtained results, the calculated recovery percentage for three different concentration of L-Cys ranging from 97.2 to 101 % with RSD values ranging from 1.08 to 3.05 %. These

results verify the practical applicability of the proposed sensor for the determination of L-Cys in human urine samples with satisfactory results.

7.3 Summary

A well decorated spherical PdNPs on the rGO-Nf were synthesized using simple hydrothermal method. Three nanohybrids with different concentrations of Pd precursor were prepared in order to investigate its effect on the electrochemical sensing performance. The GC/rGO-Nf@Pd modified electrodes were fabricated using a simple drop-cast method and applied them for the electroanalytical determination of L-Cys. Under optimized experimental condition, the GC/rGO-Nf@Pd6 modified electrode shows the better sensing performance compared to other modified electrodes. This sensor electrode demonstrated a good sensing performance in terms of rapid response (less than 2 sec), lowest detection limit (145 nM), sensitivity ($0.092 \mu\text{A } \mu\text{M}^{-1}$), selectivity, reproducibility, repeatability and stability.

The excellent performance of the GC/rGO-Nf@Pd6 modified electrode towards L-Cys can be attributed to the high conductivity and large specific surface area possessed by rGO which facilitate the electron transfer. Moreover, the excellent catalytic activity toward the electrochemical oxidation of L-Cys owned by PdNPs further helps to enhance the sensitivity of this sensing system. The presence of Nf in this nanohybrid material was helped to increase the stability and selectivity of the proposed sensor as well as improve the dispersity of rGO and the adsorption of target analyte to electrode surface. The interference analysis result shows that the proposed sensor exhibits an excellent anti-interference performance toward coexisting compounds such as AA, UA, DA, H_2O_2 , urea, and glucose (up to 20-fold). Additionally, it was proven from the real sample analysis that the proposed method can be used for the detection of L-Cys in

practical samples such as human urine with satisfactory results. Overall, the rGO-Nf@Pd nanohybrid could be a promising sensing material for electrochemical sensing application.

CHAPTER 8

CONCLUSIONS

8.1 Conclusion

Over the past decade, carbon based nanomaterials have been extensively used in multi-functional applications especially in the fabrication of novel electrochemical sensors for the detection of biomolecules including DA, NO, H₂O₂ and L-Cys. Among all the carbon based materials, graphene have been widely used for the fabrication of electrochemical sensor because it offers the advantage features of high electrochemical active sites, favourable electron transfer and excellent electrocatalytic activity. However, several drawbacks associated with graphene such as poor solubility especially in water and high tendency to aggregate has become a serious drawback to the development of electrochemical sensor based on graphene material. Therefore, the study on the new material based on graphene that able to overcome these obstacles would give a great contribution to the field of electrochemical sensor application.

The main aim of this thesis is to provide fundamental knowledge on the newly synthesized materials based on graphene, Nf and metal nanoparticles. These nanohybrid materials were then being tested as an efficient electrocatalyst in electrochemical sensor for detecting various bioanalytes. The introduction about graphene, principle of electrochemical sensor and importance of biomolecules are discussed in Chapter 1. Detailed literature survey has been done and summarized in Chapter 2. The chemical reagents, methodology adopted for nanohybrid synthesis and characterization, fabrication of electrochemical sensor were provided in the Chapter 3. In order to achieve the above said goals, four main studies have been conducted and the results

were presented in Chapter 4 to 7. The findings in each study were summarized as below.

In Chapter 4, we present the preparation of the rGO-Nf nanohybrids by a facile two-steps process consisting of ultrasonication followed by hydrothermal treatment and used for the detection of DA in the presence of AA and UA. HRTEM study revealed that the rGO had a size of ~ 18 nm after 16 h of hydrothermal treatment. Furthermore, the rGO were well dispersed in the Nf matrix under the hydrothermal process at $180\text{ }^{\circ}\text{C}$. The influence of the hydrothermal treatment time on the formation of the rGO-Nf nanohybrids was studied. This showed that the rGO-Nf nanohybrid formed after 16 h of hydrothermal treatment had a more uniform distribution than the rGO-Nf nanohybrids obtained after 8 h and 24 h of hydrothermal treatment, which tended to agglomerate. These optimized hydrothermal conditions led to the excellent electrochemical detection of DA, with a lower detection limit of about 102 nM ($S/N=3$).

The results of this study demonstrated that this sample also exhibited an extraordinarily high sensitivity and selectivity to DA despite the interference of AA and UA. The as-modified electrode also shows a great potential as a sensor for DA detection in real sample analysis by using urine sample. Besides that, the novel GC/rGO-Nf (16 h) modified electrode also demonstrated an excellent performance toward the detection of NO, with a limit of detection of 11 μM ($S/N=3$) in a linear range of 0.05 to 0.45 mM. Moreover, this GC/rGO-Nf (16 h) modified electrode exhibited higher sensitivity of approximately $62\text{ }\mu\text{A mM}^{-1}$ and had a great selectivity toward NO in the presence of interference such as DA and AA. The combination of rGO and Nf generate a synergic effect, which facilitates excellent electron-transfer processes between the electrolyte and the GCE thus improved the sensing performance of the fabricated modified electrode.

In Chapter 5, a sensitive and novel electrochemical sensor was developed for the detection of H_2O_2 using GC/rGO-Nf@Ag. The GC/rGO-Nf@Ag electrode exhibited an excellent electrochemical sensing ability for determining H_2O_2 with high sensitivity and selectivity. The detection limit of the electrochemical sensor using the GC/rGO-Nf@Ag electrode for H_2O_2 determination was calculated to be 5.0×10^{-7} M with sensitivity of $0.4508 \mu\text{A } \mu\text{M}^{-1}$. The coupling between rGO-Nf with AgNPs significantly boosted the electroanalytical performance by providing more electroactive surface area for analyte interaction, thereby allowing more rapid interfacial electron transfer process. The interfering effect on the signal response of H_2O_2 was studied and the results revealed that the sensor electrode exhibited an excellent immunity from most common interferents. The proposed non-enzymatic electrochemical sensor was used for determining H_2O_2 in apple juice, and the sensor electrode provided satisfactory results with reliable recovery values. These studies revealed that the novel GC/rGO-Nf@Ag sensor electrode could be a potential candidate for the detection of H_2O_2 .

In Chapter 6, the formation of AuNPs with different concentration on the rGO-Nf film was studied for the purpose of enhancing the electrocatalytic performance toward the detection of NO. The nanohybrid consisting of AuNPs and rGO-Nf was synthesized *via* a simple hydrothermal method where ammonia acted as the reducing agent for the formation of AuNPs and rGO. The size distribution of the AuNPs was in the range of 50 to 200 nm with spherical in shape as proven by the FESEM analysis. As compared to other controlled modified electrodes, the rGO-Nf@Au nanohybrid modified GCE with 8 mM of Au precursor demonstrated an excellent electrocatalytic activity towards NO oxidation. The GC/rGO-Nf@Au modified electrode exhibited a high sensitivity for NO with an amperometric detection limit of 5.0×10^{-7} M (S/N=3) with a wide linear response ranging from 1 μM to 0.16 mM. The high surface area of the smaller AuNPs

with stronger synergistic effect between AuNPs and rGO-Nf film were believed to contribute the enhanced electrocatalytic activity of the rGO-Nf@Au nanohybrids and improved the sensitivity towards the detection of NO. The rGO-Nf@Au nanohybrid displayed a high selectivity over common interferent molecules such as DA, AA, UA, glucose, urea and NaCl despite of 5-fold concentration has been used. The result of the reproducibility study showed that this modified electrode was highly reproducible with high precision. The large surface area and unique conductivity of rGO, and the excellent electrocatalytic activity of AuNPs were the key factors for the sensitivity and selectivity of the rGO-Nf@Au nanohybrid. Therefore, the GC/rGO-Nf@Au modified electrode is a promising candidate for highly sensitive and selective electrochemical NO sensing application. Moreover, the effective recovery of NO in real water sample has further revealed the practicability of rGO-Nf@Au nanohybrid towards detection of NO in real sample.

Finally in Chapter 7, a novel electrochemical sensor based on rGO-Nf hybridized with PdNPs has been developed for the detection of L-Cys. The rGO-Nf films decorated by PdNPs was successfully synthesized using simple hydrothermal method where GO and Na_2PdCl_4 has been used as the precursor for rGO and PdNPs, respectively. Three different concentration of Pd precursor that are 3, 6 and 9 mM has been used in order to study how it is affecting the electrochemical sensing performance. Among three nanohybrids, rGO-Nf@Pd nanohybrid with 6 mM Pd precursor shows the excellent electro-oxidation behavior to L-Cys with highest current response under the optimum experimental conditions. Based on the amperometry result, the GC/rGO-Nf@Pd modified electrode exhibits a rapid response which is less than 2 sec and low detection limit of 145 nM ($S/N=3$) with the analytical sensitivity of $0.092 \mu\text{A } \mu\text{M}^{-1}$. Furthermore, the proposed electrochemical sensor shows an excellent selectivity toward interfering

elements, such as AA, UA, DA, H₂O₂, urea and glucose as well as good reproducibility, repeatability and stability. The applicability of the GC/rGO-Nf@Pd modified electrode has been verified as it achieved a good and reliable recovery and RSD value when applied for the determination of L-Cys in human urine samples. These results indicated that rGO-Nf@Pd nanohybrid is a good candidate of advanced electrode materials that could be used for more applications in the fields of bioelectroanalysis.

In this research, the candidate used ammonia solution as the reducing agent for all three metals in the presence of particular temperature. The AgNPs and PdNPs with the size less than 20 nm have successfully synthesized. Meanwhile, the size of AuNPs is in the range of 50 to 200 nm. The particle size might vary with respect to the oxidation states of precursor metal ions (Au³⁺ and Ag⁺) with the same reducing agent. So the nucleation and growth of nanoparticles were changed during the course of the reaction. The concentration of reducing agent also plays a vital role in controlling the nucleation of nanoparticles formation. Another factor that might influence the size of particles formed on the rGO-Nf sheets is the types of reducing agent that has been used. In order to reduce the size of AuNPs, other reducing agent can be use such as sodium borohydride (NaBH₄) because different reaction will occur if different reducing agent is used.

It has been demonstrated in this study that the introduction of metal nanoparticles to the nanohybrid materials had enhanced the electrocatalytic activity of the new material thereby improved the sensing performance toward the detection of bioanalytes. By taking the advantage of strong synergistic effect between rGO-Nf films and metal nanoparticles, these new nanohybrid materials proven to facilitate electron transfer thus enhanced the electrochemical reactivity. The high surface to volume ratio and excellent

catalytic activity owned by metal nanoparticles proved to be valuable in increasing the immobilization of target analytes concentration and provide a rapid response toward the target analytes. Moreover, the presence of Nf in these nanohybrids improved the solubility and dispersibility of graphene whereas the metal nanoparticles help to prevent the aggregation of graphene. As a conclusion, this study has open up new possibilities to use the rGO-Nf films hybridized with metal nanoparticles as electrocatalysts for advanced electrochemical sensor applications in the future.

8.2 Recommendations for Future Works

This thesis presents the preliminary work on developing an electrochemical sensor for detecting various biomolecules by using rGO-Nf films incorporated with metal nanoparticles as an electrocatalyst. By taking the results into consideration, some suggestions that are worth investigating in the future for electrochemical sensor developments were listed below:

1. It is believed that the structure of metal would affect the sensing performance in term of the sensitivity, selectivity, stability and reproducibility. This is due to different surface area, size and electronic properties owned by different structure of metal particles. Therefore, future efforts should focus on synthesizing rGO-Nf@metal nanohybrids with various metal nanostructures such as flower, cube, rod and other structures. The control synthesis of metal with different structure can be prepared by manipulating the pH, introduction of surfactant and capping agent in the reaction mixture before undergo hydrothermal process.
2. It will be advantageous to discover how anchoring other materials like metal oxide (titanium dioxide, copper oxide, nickel oxide, zinc oxide and etc.) and

conductive polymer (polypyrrole, polyaniline, polythiophene and etc.) on the rGO-Nf films would affect the electrocatalytic reaction toward target analytes. Recent years, both materials have been proven capable to act as a signal-enhancing element in electroanalytical applications due to their unique properties such as high electrical conductivity and excellent catalytic activity. By taking the advantage of both materials in term of green and simple preparation protocol, this will reduce the production cost, thus could be an alternative materials in fabricating the electrochemical sensor.

REFERENCES

- Abdolhosseinzadeh, S., Asgharzadeh, H., & Kim, H. S. (2015). Fast and fully-scalable synthesis of reduced graphene oxide. *Scientific Reports*, 5, 10160-10167.
- Adekunle, A. S., Lebogang, S., Gwala, P. L., Tsele, T. P., Olasunkanmi, L. O., Esther, F. O., & Ogunfowokan, A. O. (2015). Electrochemical response of nitrite and nitric oxide on graphene oxide nanoparticles doped with Prussian blue (PB) and Fe₂O₃ nanoparticles. *RSC Advances*, 5(35), 27759-27774.
- Aldana-González, J., Palomar-Pardavé, M., Corona-Avendaño, S., Montes de Oca, M. G., Ramírez-Silva, M. T., & Romero-Romo, M. (2013). Gold nanoparticles modified-ITO electrode for the selective electrochemical quantification of dopamine in the presence of uric and ascorbic acids. *Journal of Electroanalytical Chemistry*, 706, 69-75.
- Ansari, I., & Datta, A. (2003). An overview of sterilization methods for packaging materials used in aseptic packaging systems. *Food and Bioprocess Processing*, 81(1), 57-65.
- Aragaw, B. A., Su, W.-N., Rick, J., & Hwang, B.-J. (2013). Highly efficient synthesis of reduced graphene oxide–Nafion nanocomposites with strong coupling for enhanced proton and electron conduction. *RSC Advances*, 3(45), 23212-23221.
- Atta, N. F., Galal, A., & Ekram, H. (2015). Graphene—A Platform for Sensor and Biosensor Applications. In Rinken, T. (Ed), *Biosensors-Micro and Nanoscale Applications*. Retrived from <http://www.intechopen.com>.
- Augustine, A. K., Nampoori, V. P. N., & Kailasnath, M. (2014). Rapid synthesize of gold nanoparticles by microwave irradiation method and its application as an optical limiting material. *Optik - International Journal for Light and Electron Optics*, 125(22), 6696-6699.
- Avdagić, N., Zaćiragić, A., Babić, N., Hukić, M., Šeremet, M., Lepara, O., & Nakaš-Ićindić, E. (2013). Nitric oxide as a potential biomarker in inflammatory bowel disease. *Bosnian Journal of Basic Medical Sciences*, 13(1), 5-9.
- Avouris, P., Chen, Z., & Perebeinos, V. (2007). Carbon-based electronics. *Nature Nanotechnology*, 2(10), 605-615.
- Aydoğdu, G., Zeybek, D. K., Zeybek, B., & Pekyardımcı, Ş. (2013). Electrochemical sensing of NADH on NiO nanoparticles-modified carbon paste electrode and fabrication of ethanol dehydrogenase-based biosensor. *Journal of Applied Electrochemistry*, 43(5), 523-531.
- Azadbakht, A., & Abbasi, A. R. (2013). Fabrication of highly sensitive cysteine electrochemical sensor based on nanostructured compound and carbon nanotube modified electrode. *Russian Journal of Electrochemistry*, 49(12), 1127-1138.
- Bagheri, H., Pajoohehpour, N., Afkhami, A., & Khoshsafar, H. (2016). Fabrication of a novel electrochemical sensing platform based on a core–shell nano-

structured/molecularly imprinted polymer for sensitive and selective determination of ephedrine. *RSC Advances*, 6(56), 51135-51145.

Bagheri, H., Pajoohehpour, N., Jamali, B., Amidi, S., Hajian, A., & Khoshshafar, H. (2017). A novel electrochemical platform for sensitive and simultaneous determination of dopamine, uric acid and ascorbic acid based on Fe₃O₄SnO₂Gr ternary nanocomposite. *Microchemical Journal*, 131, 120-129.

Beckman, J. S., & Congert, K. A. (1995). Direct measurement of dilute nitric oxide in solution with an ozone chemiluminescent detector. *Methods*, 7(1), 35-39.

Bennett, M. D. (2005). *Electromechanical Transduction in Ionic Liquid-Swollen Nafion Membranes*. (Doctoral dissertation). Retrieved from <http://theses.lib.vt.edu>

Borsella, E., Cattaruzza, E., De Marchi, G., Gonella, F., Mattei, G., Mazzoldi, P., & Polloni, R. (1999). Synthesis of silver clusters in silica-based glasses for optoelectronics applications. *Journal of Non-Crystalline Solids*, 245(1), 122-128.

Bredt, D. S., & Snyder, S. H. (1992). Nitric oxide, a novel neuronal messenger. *Neuron*, 8(1), 3-11.

Bui, M.-P. N., Pham, X.-H., Han, K. N., Li, C. A., Kim, Y. S., & Seong, G. H. (2010). Electrocatalytic reduction of hydrogen peroxide by silver particles patterned on single-walled carbon nanotubes. *Sensors and Actuators B: Chemical*, 150(1), 436-441.

Burford, N., Eelman, M. D., Mahony, D. E., & Morash, M. (2003). Definitive identification of cysteine and glutathione complexes of bismuth by mass spectrometry: assessing the biochemical fate of bismuth pharmaceutical agents. *Chemical Communications* 1(1), 146-147.

Burnett, A. L. (1997). Nitric oxide in the penis: Physiology and pathology. *The Journal of Urology*, 157(1), 320-324.

Cech, T. R., Bennett, D., Jasny, B., Kelner, K. L., Miller, L. J., Szuromi, P. D., & Ray, L. B. (1992). The molecule of the year. *Science*, 258(5090), 1861.

Cederfjäll, E., Nilsson, N., Sahin, G., Chu, Y., Nikitidou, E., Björklund, T., & Kirik, D. (2013). Continuous DOPA synthesis from a single AAV: dosing and efficacy in models of Parkinson's disease. *Scientific Reports*, 3, 1-12.

Chabot, V., Higgins, D., Yu, A., Xiao, X., Chen, Z., & Zhang, J. (2014). A review of graphene and graphene oxide sponge: material synthesis and applications to energy and the environment. *Energy & Environmental Science*, 7(5), 1564-1596.

Chen, J.-C., Shih, J.-L., Liu, C.-H., Kuo, M.-Y., & Zen, J.-M. (2006). Disposable electrochemical sensor for determination of nitroaromatic compounds by a single-run approach. *Analytical Chemistry*, 78(11), 3752-3757.

- Chen, W., Cai, S., Ren, Q.-Q., Wen, W., & Zhao, Y.-D. (2012). Recent advances in electrochemical sensing for hydrogen peroxide: a review. *Analyst*, 137(1), 49-58.
- Chen, X.-m., Wu, G.-h., Jiang, Y.-q., Wang, Y.-r., & Chen, X. (2011). Graphene and graphene-based nanomaterials: the promising materials for bright future of electroanalytical chemistry. *Analyst*, 136(22), 4631-4640.
- Chen, X., Long, H.-Y., Wu, W.-L., & Yang, Z.-S. (2009). Direct electrochemical behavior of cytochrome c on sodium dodecyl sulfate modified electrode and its application to nitric oxide biosensor. *Thin Solid Films*, 517(8), 2787-2791.
- Choi, B. G., & Park, H. S. (2012). Superhydrophobic graphene/nafion nanohybrid films with hierarchical roughness. *The Journal of Physical Chemistry C*, 116(5), 3207-3211.
- Choi, J., Oh, H., Han, S.-W., Ahn, S., Noh, J., & Park, J. B. (2017). Preparation and characterization of graphene oxide supported Cu, Cu₂O, and CuO nanocomposites and their high photocatalytic activity for organic dye molecule. *Current Applied Physics*, 17(2), 137-145.
- Choi, W., Lahiri, I., Seelaboyina, R., & Kang, Y. S. (2010). Synthesis of graphene and its applications: a review. *Critical Reviews in Solid State and Materials Sciences*, 35(1), 52-71.
- Chou, J., Ilgen, T. J., Gordon, S., Ranasinghe, A. D., McFarland, E. W., Metiu, H., & Buratto, S. K. (2009). Investigation of the enhanced signals from cations and dopamine in electrochemical sensors coated with Nafion. *Journal of Electroanalytical Chemistry*, 632(1-2), 97-101.
- Chuang, C.-H., Wang, Y.-F., Shao, Y.-C., Yeh, Y.-C., Wang, D.-Y., Chen, C.-W., & Zhang, L. (2014). The effect of thermal reduction on the photoluminescence and electronic structures of graphene oxides. *Scientific Reports*, 4, 1-7.
- Clark, L. C., & Lyons, C. (1962). Electrode systems for continuous monitoring in cardiovascular surgery. *Annals of the New York Academy of Sciences*, 102(1), 29-45.
- Clark, L. C., Wolf, R., Granger, D., & Taylor, Z. (1953). Continuous recording of blood oxygen tensions by polarography. *Journal of Applied Physiology*, 6(3), 189-193.
- Claussen, J. C., Kim, S. S., Haque, A., Artiles, M. S., Porterfield, D. M., & Fisher, T. S. (2010). Electrochemical glucose biosensor of platinum nanospheres connected by carbon nanotubes. *Journal of Diabetes Science and Technology*, 4(2), 312-319.
- Clifford, D. P., & Repine, J. E. (1982). Hydrogen peroxide mediated killing of bacteria. *Molecular and Cellular Biochemistry*, 49(3), 143-149.
- Conoci, S., Petralia, S., Samorì, P., Raymo, F. M., Di Bella, S., & Sortino, S. (2006). Optically transparent, ultrathin Pt films as versatile metal substrates for molecular optoelectronics. *Advanced Functional Materials*, 16(11), 1425-1432.

- Cui, X., Wu, S., Li, Y., & Wan, G. (2014). Sensing hydrogen peroxide using a glassy carbon electrode modified with in-situ electrodeposited platinum-gold bimetallic nanoclusters on a graphene surface. *Microchimica Acta*, 182(1), 265-272.
- De Almeida, S. H., & Kawano, Y. (1997). Ultraviolet-visible spectra of Nafion membrane. *European Polymer Journal*, 33(8), 1307-1311.
- de Groot, H., & Littauer, A. (1989). Hypoxia, reactive oxygen, and cell injury. *Free Radical Biology and Medicine*, 6(5), 541-551.
- Deáková, Z., Ďuračková, Z., Armstrong, D. W., & Lehotay, J. (2015). Two-dimensional high performance liquid chromatography for determination of homocysteine, methionine and cysteine enantiomers in human serum. *Journal of Chromatography A*, 1408, 118-124.
- Dessie, Y., & Admassie, S. (2014). Electrochemical study of Conducting Polymer/Lignin Composites. *Oriental Journal of Chemistry*, 29(4), 1-11.
- Devadas, B., Rajkumar, M., Chen, S.-M., & Yeh, P.-C. (2014). A novel voltammetric p-nitrophenol sensor based on ZrO₂ nanoparticles incorporated into a multiwalled carbon nanotube modified glassy carbon electrode. *Analytical Methods*, 6(13), 4686-4691.
- Dong, Y., & Zheng, J. (2014). A nonenzymatic l-cysteine sensor based on SnO₂-MWCNTs nanocomposites. *Journal of Molecular Liquids*, 196, 280-284.
- Dröge, W. (1993). Cysteine and glutathione deficiency in AIDS patients: a rationale for the treatment with N-acetyl-cysteine. *Pharmacology*, 46(2), 61-65.
- E Edmondson, D. (2014). Hydrogen peroxide produced by mitochondrial monoamine oxidase catalysis: biological implications. *Current Pharmaceutical Design*, 20(2), 155-160.
- e Silva, C. d. C. C., Breitreitz, M. C., Santhiago, M., Corrêa, C. C., & Kubota, L. T. (2012). Construction of a new functional platform by grafting poly (4-vinylpyridine) in multi-walled carbon nanotubes for complexing copper ions aiming the amperometric detection of l-cysteine. *Electrochimica Acta*, 71, 150-158.
- Falkowski, M., Rebis, T., Kryjewski, M., Popenda, L., Lijewski, S., Jurga, S., & Goslinski, T. (2017). An enhanced electrochemical nanohybrid sensing platform consisting of reduced graphene oxide and sulfanyl metalloporphyrines for sensitive determination of hydrogen peroxide and l-cysteine. *Dyes and Pigments*, 138, 190-203.
- Fan, C., Li, G., Zhu, J., & Zhu, D. (2000). A reagentless nitric oxide biosensor based on hemoglobin-DNA films. *Analytica Chimica Acta*, 423(1), 95-100.
- Fan, C., Liu, X., Pang, J., Li, G., & Scheer, H. (2004). Highly sensitive voltammetric biosensor for nitric oxide based on its high affinity with hemoglobin. *Analytica Chimica Acta*, 523(2), 225-228.

- Fawcett, W. R., Fedurco, M., Kováčová, Z., & Borkowska, Z. (1994). Oxidation of cysteine, cysteinesulfinic acid and cysteic acid on a polycrystalline gold electrode. *Journal of Electroanalytical Chemistry*, 368(1-2), 265-274.
- Fazio, B., D'Andrea, C., Foti, A., Messina, E., Irrera, A., Donato, M. G., & Gucciardi, P. G. (2016). SERS detection of biomolecules at physiological pH via aggregation of gold nanorods mediated by optical forces and plasmonic heating. *Scientific Reports*, 6, 26952-26965.
- Ferrari, A., Meyer, J., Scardaci, V., Casiraghi, C., Lazzeri, M., Mauri, F., & Roth, S. (2006). Raman spectrum of graphene and graphene layers. *Physical Review Letters*, 97(18), 187401-187405.
- Gan, X., Liu, T., Zhu, X., & LI, G. (2004). An electrochemical biosensor for nitric oxide based on silver nanoparticles and hemoglobin. *Analytical Sciences*, 20(9), 1271-1275.
- Ganguly, A., Sharma, S., Papakonstantinou, P., & Hamilton, J. (2011). Probing the thermal deoxygenation of graphene oxide using high-resolution in situ X-ray-based spectroscopies. *The Journal of Physical Chemistry C*, 115(34), 17009-17019.
- Gao, F., Cai, X., Wang, X., Gao, C., Liu, S., Gao, F., & Wang, Q. (2013). Highly sensitive and selective detection of dopamine in the presence of ascorbic acid at graphene oxide modified electrode. *Sensors and Actuators B: Chemical*, 186, 380-387.
- Geetha Bai, R., Muthoosamy, K., Zhou, M., Ashokkumar, M., Huang, N. M., & Manickam, S. (2017). Sonochemical and sustainable synthesis of graphene-gold (G-Au) nanocomposites for enzymeless and selective electrochemical detection of nitric oxide. *Biosensors and Bioelectronics*, 87, 622-629.
- Geng, D., Li, M., Bo, X., & Guo, L. (2016). Molybdenum nitride/nitrogen-doped multi-walled carbon nanotubes hybrid nanocomposites as novel electrochemical sensor for detection l-cysteine. *Sensors and Actuators B: Chemical*, 237, 581-590.
- Ghorbani-Bidkorbeh, F., Shahrokhian, S., Mohammadi, A., & Dinarvand, R. (2010). Electrochemical determination of naltrexone on the surface of glassy carbon electrode modified with Nafion-doped carbon nanoparticles: Application to determinations in pharmaceutical and clinical preparations. *Journal of Electroanalytical Chemistry*, 638(2), 212-217.
- Goyal, R. N., Gupta, V. K., Oyama, M., & Bachheti, N. (2007). Gold nanoparticles modified indium tin oxide electrode for the simultaneous determination of dopamine and serotonin: Application in pharmaceutical formulations and biological fluids. *Talanta*, 72(3), 976-983.
- Grieshaber, D., MacKenzie, R., Voeroes, J., & Reimhult, E. (2008). Electrochemical biosensors-sensor principles and architectures. *Sensors*, 8(3), 1400-1458.
- Guedes da Silva, Q., Vieira Barbosa, N., de Pieri Troiani, E., & Censi Faria, R. (2011). Electrochemical determination of norepinephrine on cathodically pretreated poly

- (1, 5-diaminonaphthalene) modified electrode. *Electroanalysis*, 23(6), 1359-1364.
- Hai, H. T., Takamura, H., & Koike, J. (2013). Oxidation behavior of Cu–Ag core–shell particles for solar cell applications. *Journal of Alloys and Compounds*, 564, 71-77.
- Halliwell, B., Clement, M. V., & Long, L. H. (2000). Hydrogen peroxide in the human body. *FEBS Letters*, 486(1), 10-13.
- Han, D., Han, T., Shan, C., Ivaska, A., & Niu, L. (2010). Simultaneous determination of ascorbic acid, dopamine and uric acid with chitosan-graphene modified electrode. *Electroanalysis*, 22(17-18), 2001-2008.
- He, X., & Zhu, L. (2006). Direct electrochemistry of hemoglobin in cetylpyridinium bromide film: redox thermodynamics and electrocatalysis to nitric oxide. *Electrochemistry Communications*, 8(4), 615-620.
- Hosseini, H., Ahmar, H., Dehghani, A., Bagheri, A., Tadjarodi, A., & Fakhari, A. R. (2013). A novel electrochemical sensor based on metal-organic framework for electro-catalytic oxidation of L-cysteine. *Biosensors and Bioelectronics*, 42, 426-429.
- How, G. T. S., Pandikumar, A., Ming, H. N., & Ngee, L. H. (2014). Highly exposed {001} facets of titanium dioxide modified with reduced graphene oxide for dopamine sensing. *Scientific Reports*, 4, 5044-5052.
- Hu, F. X., Le Xie, J., Bao, S. J., Yu, L., & Li, C. M. (2015). Shape-controlled ceria-reduced graphene oxide nanocomposites toward high-sensitive in situ detection of nitric oxide. *Biosensors and Bioelectronics*, 70, 310-317.
- Hu, S., Wang, A., Li, X., Wang, Y., & Löwe, H. (2010). Hydrothermal synthesis of ionic liquid [Bmim] OH-Modified TiO₂ nanoparticles with enhanced photocatalytic activity under visible light. *Chemistry, an Asian Journal*, 5(5), 1171-1177.
- Huang, D., Chen, C., Wu, Y., Zhang, H., Sheng, L., Xu, H.-J., & Liu, Z.-D. (2012). The determination of dopamine using glassy carbon electrode pretreated by a simple electrochemical method. *International Journal of Electrochemical Science*, 7, 5510-5520.
- Huang, J., Liu, Y., Hou, H., & You, T. (2008). Simultaneous electrochemical determination of dopamine, uric acid and ascorbic acid using palladium nanoparticle-loaded carbon nanofibers modified electrode. *Biosensors and Bioelectronics*, 24(4), 632-637.
- Ignarro, L. (2002). Nitric oxide as a unique signaling molecule in the. *Journal of Physiology and Pharmacology*, 53(4), 503-514.
- Ignarro, L. J., Buga, G. M., Wood, K. S., Byrns, R. E., & Chaudhuri, G. (1987). Endothelium-derived relaxing factor produced and released from artery and vein

is nitric oxide. *Proceedings of the National Academy of Sciences*, 84(24), 9265-9269.

- Ignat, T., Munoz, R., Irina, K., Obieta, I., Mihaela, M., Simion, M., & Iovu, M. (2009). Nanostructured Au/Si substrate for organic molecule SERS detection. *Superlattices and Microstructures*, 46(3), 451-460.
- Ito, E., Watabe, S., Morikawa, M., Kodama, H., Okada, R., & Miura, T. (2013). Detection of H₂O₂ by fluorescence correlation spectroscopy. *Methods Enzymol*, 526, 135-143.
- Jain, P. K., Lee, K. S., El-Sayed, I. H., & El-Sayed, M. A. (2006). Calculated absorption and scattering properties of gold nanoparticles of different size, shape, and composition: Applications in biological imaging and biomedicine. *The Journal of Physical Chemistry B*, 110(14), 7238-7248.
- Jain, R., & Sharma, S. (2012). Glassy carbon electrode modified with multi-walled carbon nanotubes sensor for the quantification of antihistamine drug pheniramine in solubilized systems. *Journal of Pharmaceutical Analysis*, 2(1), 56-61.
- Janata, J., & Josowicz, M. (2003). Conducting polymers in electronic chemical sensors. *Nature Materials*, 2(1), 19-24.
- Jayabal, S., Viswanathan, P., & Ramaraj, R. (2014). Reduced graphene oxide–gold nanorod composite material stabilized in silicate sol–gel matrix for nitric oxide sensor. *RSC Advances*, 4(63), 33541-33548.
- Jia, D., Li, F., Sheng, L., Ren, Q., Dong, S., Xu, S., & Miao, Y. (2011). Synthesis and assembly of ultrathin film of Ni(OH)₂ nanoparticles at gas/liquid interface, its high electrocatalytical oxidation toward bio-thiols and selective determination of cysteine. *Electrochemistry Communications*, 13(10), 1119-1122.
- Jia, X., & Ji, X. (2015). Electrochemical probing of carbon quantum dots: not suitable for a single electrode material. *RSC Advances*, 5(130), 107270-107275.
- Jiang, B.-B., Wei, X.-W., Wu, F.-H., Wu, K.-L., Chen, L., Yuan, G.-Z., & Ye, Y. (2014). A non-enzymatic hydrogen peroxide sensor based on a glassy carbon electrode modified with cuprous oxide and nitrogen-doped graphene in a nafion matrix. *Microchimica Acta*, 181(11-12), 1463-1470.
- Jiang, D., Zhang, Y., Huang, M., Liu, J., Wan, J., Chu, H., & Chen, M. (2014). Carbon nanodots as reductant and stabilizer for one-pot sonochemical synthesis of amorphous carbon-supported silver nanoparticles for electrochemical nonenzymatic H₂O₂ sensing. *Journal of Electroanalytical Chemistry*, 728, 26-33.
- Jiang, Y., Zheng, B., Du, J., Liu, G., Guo, Y., & Xiao, D. (2013). Electrophoresis deposition of Ag nanoparticles on TiO₂ nanotube arrays electrode for hydrogen peroxide sensing. *Talanta*, 112, 129-135.

- Jiang, Z., Jiang, Z.-j., Tian, X., & Chen, W. (2014). Amine-functionalized holey graphene as a highly active metal-free catalyst for the oxygen reduction reaction. *Journal of Materials Chemistry A*, 2(2), 441-450.
- Johra, F. T., Lee, J.-W., & Jung, W.-G. (2014). Facile and safe graphene preparation on solution based platform. *Journal of Industrial and Engineering Chemistry*, 20(5), 2883-2887.
- Jongjinakool, S., Palasak, K., Bousod, N., & Teepoo, S. (2014). Gold nanoparticles-based colorimetric sensor for cysteine detection. *Energy Procedia*, 56, 10-18.
- Kalimuthu, P., & John, S. A. (2009). Electropolymerized film of functionalized thiadiazole on glassy carbon electrode for the simultaneous determination of ascorbic acid, dopamine and uric acid. *Bioelectrochemistry*, 77(1), 13-18.
- Kan, K., Xia, T., Li, L., Bi, H., Fu, H., & Shi, K. (2009). Amidation of single-walled carbon nanotubes by a hydrothermal process for the electrooxidation of nitric oxide. *Nanotechnology*, 20(18), 185502-185509.
- Kang, M.-G., Joon Park, H., Hyun Ahn, S., & Jay Guo, L. (2010). Transparent Cu nanowire mesh electrode on flexible substrates fabricated by transfer printing and its application in organic solar cells. *Solar Energy Materials and Solar Cells*, 94(6), 1179-1184.
- Kannan, P., & John, S. A. (2010). Highly sensitive electrochemical determination of nitric oxide using fused spherical gold nanoparticles modified ITO electrode. *Electrochimica Acta*, 55(10), 3497-3503.
- Kaur, B., Srivastava, R., & Satpati, B. (2015). A novel gold nanoparticle decorated nanocrystalline zeolite based electrochemical sensor for the nanomolar simultaneous detection of cysteine and glutathione. *RSC Advances*, 5(115), 95028-95037.
- Khan, M. E., Khan, M. M., & Cho, M. H. (2015). Biogenic synthesis of a Ag-graphene nanocomposite with efficient photocatalytic degradation, electrical conductivity and photoelectrochemical performance. *New Journal of Chemistry*, 39(10), 8121-8129.
- Khandelwal, M., & Kumar, A. (2015). One-step chemically controlled wet synthesis of graphene nanoribbons from graphene oxide for high performance supercapacitor applications. *Journal of Materials Chemistry A*, 3(45), 22975-22988.
- Khlebtsov, N., & Dykman, L. (2011). Biodistribution and toxicity of engineered gold nanoparticles: a review of in vitro and in vivo studies. *Chemical Society Reviews*, 40(3), 1647-1671.
- Khudaish, E. A., Al-Ajmi, K. Y., Al-Harthi, S. H., & Al-Hinai, A. T. (2012). A solid state sensor based polytyramine film modified electrode for the determination of dopamine and ascorbic acid in a moderately acidic solution. *Journal of Electroanalytical Chemistry*, 676, 27-34.

- Kim, C. H., Kim, B.-H., & Yang, K. S. (2012). TiO₂ nanoparticles loaded on graphene/carbon composite nanofibers by electrospinning for increased photocatalysis. *Carbon*, 50(7), 2472-2481.
- Kipping, P. J., & Jeffery, P. (1963). Detection of nitric oxide by gas-chromatography. *Nature*, 200, 1314.
- Kosminsky, L., Mori, V., & Bertotti, M. (2001). Electrochemical studies on the oxidation of nitric oxide (NO) at glassy carbon electrodes modified by molybdenum oxides. *Journal of Electroanalytical Chemistry*, 499(1), 176-181.
- Kuang, X., Ye, S., Li, X., Ma, Y., Zhang, C., & Tang, B. (2016). A new type of surface-enhanced Raman scattering sensor for the enantioselective recognition of D/L-cysteine and D/L-asparagine based on a helically arranged Ag NPs@homochiral MOF. *Chemical Communications*, 52(31), 5432-5435.
- Kuppusamy, P., Wang, P., Samouilov, A., & Zweier, J. L. (1996). Spatial mapping of nitric oxide generation in the ischemic heart using electron paramagnetic resonance imaging. *Magnetic Resonance in Medicine*, 36(2), 212-218.
- Lacy, F., O'Connor, D. T., & Schmid-Schönbein, G. W. (1998). Plasma hydrogen peroxide production in hypertensives and normotensive subjects at genetic risk of hypertension. *Journal of Hypertension*, 16(3), 291-303.
- Langer, J. J., Filipiak, M., Jasnowska, J., Włodarczak, J., & Buładowski, B. (2004). Polyaniline biosensor for choline determination. *Surface Science*, 573(1), 140-145.
- Lee, J., Novoselov, K. S., & Shin, H. S. (2010). Interaction between metal and graphene: dependence on the layer number of graphene. *ACS Nano*, 5(1), 608-612.
- Lee, S. U., Choi, B. G., & Hong, W. H. (2013). *Simple Fabrication of Exfoliated Graphene/Nafion Hybrid as Glucose Bio-sensor Electrodes*. Paper presented at the 4th International Conference on Biomedical Engineering in Vietnam.
- Lei, J., Ju, H., & Ikeda, O. (2004). Catalytic oxidation of nitric oxide and nitrite mediated by water-soluble high-valent iron porphyrins at an ITO electrode. *Journal of Electroanalytical Chemistry*, 567(2), 331-338.
- Lesiak, M., Binczarski, M., Karski, S., Maniukiewicz, W., Rogowski, J., Szubiakiewicz, E., & Witońska, I. (2014). Hydrogenation of furfural over Pd-Cu/Al₂O₃ catalysts. The role of interaction between palladium and copper on determining catalytic properties. *Journal of Molecular Catalysis A: Chemical*, 395, 337-348.
- Lévesque, D., & Rouillard, C. (2007). Nur77 and retinoid X receptors: crucial factors in dopamine-related neuroadaptation. *Trends in Neurosciences*, 30(1), 22-30.
- Li, C. M., Zang, J., Zhan, D., Chen, W., Sun, C. Q., Teo, A. L., & Mookhala, S. (2006). Electrochemical detection of nitric oxide on a SWCNT/RTIL composite gel microelectrode. *Electroanalysis*, 18(7), 713-718.

- Li, Q., Qin, X., Luo, Y., Lu, W., Chang, G., Asiri, A. M., & Sun, X. (2012). One-pot synthesis of Ag nanoparticles/reduced graphene oxide nanocomposites and their application for nonenzymatic H₂O₂ detection. *Electrochimica Acta*, 83, 283-287.
- Li, S.-J., Du, J.-M., Zhang, J.-P., Zhang, M.-J., & Chen, J. (2014). A glassy carbon electrode modified with a film composed of cobalt oxide nanoparticles and graphene for electrochemical sensing of H₂O₂. *Microchimica Acta*, 181(5), 631-638.
- Li, X., Wang, L., Wu, Q., Chen, Z., & Lin, X. (2014). A nonenzymatic hydrogen peroxide sensor based on Au–Ag nanotubes and chitosan film. *Journal of Electroanalytical Chemistry*, 735, 19-23.
- Li, X., Zhu, Y., Cai, W., Borysiak, M., Han, B., Chen, D., & Ruoff, R. S. (2009). Transfer of large-area graphene films for high-performance transparent conductive electrodes. *Nano Letters*, 9(12), 4359-4363.
- Li, Y., Gu, Y., Zheng, B., Luo, L., Li, C., Yan, X., & Zhang, Z. (2017). A novel electrochemical biomimetic sensor based on poly(Cu-AMT) with reduced graphene oxide for ultrasensitive detection of dopamine. *Talanta*, 162, 80-89.
- Li, Y., Song, H., Zhang, L., Zuo, P., Ye, B.-c., Yao, J., & Chen, W. (2016). Supportless electrochemical sensor based on molecularly imprinted polymer modified nanoporous microrod for determination of dopamine at trace level. *Biosensors and Bioelectronics*, 78, 308-314.
- Li, Y., Xu, Y., Chen, X.-y., Ge, F., & Zhu, R.-l. (2014). High catalytic activity of Mo–Zn–Al–O catalyst for dye degradation: Effect of pH in the impregnation process. *Applied Catalysis B: Environmental*, 160–161, 115-121.
- Lim, S. P., Pandikumar, A., Lim, H. N., Ramaraj, R., & Huang, N. M. (2015). Boosting photovoltaic performance of dye-sensitized solar cells using silver nanoparticle-decorated N,S-Co-doped-TiO₂ photoanode. *Scientific Reports*, 5, 11922-11936.
- Lin, C.-Y., & Chang, C.-T. (2015). Iron oxide nanorods array in electrochemical detection of H₂O₂. *Sensors and Actuators B: Chemical*, 220, 695-704.
- Liu, F., Tang, T., Feng, Q., Li, M., Liu, Y., Tang, N., & Du, Y. (2014). Tuning photoluminescence of reduced graphene oxide quantum dots from blue to purple. *Journal of Applied Physics*, 115(16), 164307-164311.
- Liu, J., Zhang, M., Liu, J., & Zheng, J. (2016). Synthesis of Ag@Pt core-shell nanoparticles loaded onto reduced graphene oxide and investigation of its electrochemical sensing properties. *Analytical Methods*, 8(5), 1084-1090.
- Liu, S., Yu, B., & Zhang, T. (2013). Preparation of crumpled reduced graphene oxide–poly (p-phenylenediamine) hybrids for the detection of dopamine. *Journal of Materials Chemistry A*, 1(42), 13314-13320.
- Liu, X., Shanguan, E., Li, J., Ning, S., Guo, L., & Li, Q. (2017). A novel electrochemical sensor based on FeS anchored reduced graphene oxide

nanosheets for simultaneous determination of dopamine and acetaminophen. *Materials Science and Engineering: C*, 70, Part 1, 628-636.

- Liu, X., Xu, X., Zhu, H., & Yang, X. (2013). Synthesis of graphene nanosheets with incorporated silver nanoparticles for enzymeless hydrogen peroxide detection. *Analytical Methods*, 5(9), 2298-2304.
- Liu, X., Zhu, H., & Yang, X. (2014). An electrochemical sensor for dopamine based on poly (o-phenylenediamine) functionalized with electrochemically reduced graphene oxide. *RSC Advances*, 4(8), 3706-3712.
- Liu, Y., Chen, S.-S., Wang, A.-J., Feng, J.-J., Wu, X., & Weng, X. (2016). An ultra-sensitive electrochemical sensor for hydrazine based on AuPd nanorod alloy nanochains. *Electrochimica Acta*, 195, 68-76.
- Liu, Y., Gao, L., Sun, J., Wang, Y., & Zhang, J. (2009). Stable Nafion-functionalized graphene dispersions for transparent conducting films. *Nanotechnology*, 20(46), 465605.
- Liu, Y. M., Punckt, C., Pope, M. A., Gelperin, A., & Aksay, I. A. (2013). Electrochemical sensing of nitric oxide with functionalized graphene electrodes. *ACS Applied Materials & Interfaces*, 5(23), 12624-12630.
- Liu, Z., Forsyth, H., Khaper, N., & Chen, A. (2016). Sensitive electrochemical detection of nitric oxide based on AuPt and reduced graphene oxide nanocomposites. *Analyst*, 141(13), 4074-4083.
- Liu, Z., Zhang, H., Hou, S., & Ma, H. (2012). Highly sensitive and selective electrochemical detection of L-cysteine using nanoporous gold. *Microchimica Acta*, 177(3), 427-433.
- LoRESTANI, F., SHAHNAVAZ, Z., MN, P., ALIAS, Y., & MANAN, N. S. A. (2015). One-step hydrothermal green synthesis of silver nanoparticle-carbon nanotube reduced-graphene oxide composite and its application as hydrogen peroxide sensor. *Sensors and Actuators B: Chemical*, 208, 389-398.
- Lu, Q., Zhang, J., Liu, X., Wu, Y., Yuan, R., & Chen, S. (2014). Enhanced electrochemiluminescence sensor for detecting dopamine based on gold nanoflower/graphitic carbon nitride polymer nanosheet-polyaniline hybrids. *Analyst*, 139(24), 6556-6562.
- Lv, X., & Weng, J. (2013). Ternary composite of hemin, gold nanoparticles and graphene for highly efficient decomposition of hydrogen peroxide. *Scientific Reports*, 3, 3285-3295.
- Lv, Y., Wang, F., Zhu, H., Zou, X., Tao, C.-a., & Wang, J. (2016). Electrochemically reduced graphene oxide-nafion/Au nanoparticle modified electrode for hydrogen peroxide sensing. *Nanomaterials and Nanotechnology*, 6(30), 1-7.
- Malinski, T. (2000). The vital role of nitric oxide. *Oakland Journal*, 1, 47-56.

- Mazloun-Ardakani, M., Rajabi, H., Beitollahi, H., Mirjalili, B. B. F., Akbari, A., & Taghavinia, N. (2010). Voltammetric determination of dopamine at the surface of TiO₂ nanoparticles modified carbon paste electrode. *International Journal of Electrochemical Science*, 5, 147-157.
- Mazloun-Ardakani, M., Taleat, Z., Beitollahi, H., & Naeimi, H. (2010). Electrocatalytic oxidation of dopamine on 2,2[prime or minute]-[3,6-dioxa-1,8-octanediy]bis(nitriloethylidyne)]-bis-hydroquinone modified carbon paste electrode. *Analytical Methods*, 2(2), 149-153.
- Mehrali, M., Moghaddam, E., Shirazi, S. F. S., Baradaran, S., Mehrali, M., Latibari, S. T., & Osman, N. A. A. (2014). Synthesis, Mechanical Properties, and in Vitro Biocompatibility with Osteoblasts of Calcium Silicate–Reduced Graphene Oxide Composites. *ACS Applied Materials & Interfaces*, 6(6), 3947-3962.
- Mei, H., Wu, W., Yu, B., Wu, H., Wang, S., & Xia, Q. (2016). Nonenzymatic electrochemical sensor based on Fe@Pt core–shell nanoparticles for hydrogen peroxide, glucose and formaldehyde. *Sensors and Actuators B: Chemical*, 223, 68-75.
- Mhamane, D., Ramadan, W., Fawzy, M., Rana, A., Dubey, M., Rode, C., & Ogale, S. (2011). From graphite oxide to highly water dispersible functionalized graphene by single step plant extract-induced deoxygenation. *Green Chemistry*, 13(8), 1990-1996.
- Moradi Golsheikh, A., Huang, N. M., Lim, H. N., Zakaria, R., & Yin, C.-Y. (2013). One-step electrodeposition synthesis of silver-nanoparticle-decorated graphene on indium-tin-oxide for enzymeless hydrogen peroxide detection. *Carbon*, 62, 405-412.
- Mulchandani, A., Wang, C.-L., & Weetall, H. H. (1995). Amperometric detection of peroxides with poly (anilinomethylferrocene)-modified enzyme electrodes. *Analytical Chemistry*, 67(1), 94-100.
- Mulchandani, A., & Wang, C. L. (1996). Bionzyme sensors based on poly (anilinomethylferrocene)-modified electrodes. *Electroanalysis*, 8(5), 414-419.
- Murugavelu, M., & Karthikeyan, B. (2014). Study of Ag–Pd bimetallic nanoparticles modified glassy carbon electrode for detection of L-cysteine. *Superlattices and Microstructures*, 75, 916-926.
- Musameh, M., Wang, J., Merkoci, A., & Lin, Y. (2002). Low-potential stable NADH detection at carbon-nanotube-modified glassy carbon electrodes. *Electrochemistry Communications*, 4(10), 743-746.
- Mutyala, S., & Mathiyarasu, J. (2016). A reagentless non-enzymatic hydrogen peroxide sensor presented using electrochemically reduced graphene oxide modified glassy carbon electrode. *Materials Science and Engineering: C*, 69, 398-406.
- Napoli, C., & Ignarro, L. J. (2001). Nitric oxide and atherosclerosis. *Nitric Oxide*, 5(2), 88-97.

- Narayana, P., Reddy, T. M., Gopal, P., Raghu, P., Reddaiah, K., & Srinivasulu, M. (2014). Development of trypan blue polymer film based electrochemical sensor for the determination of dopamine and its simultaneous detection in presence of ascorbic acid and uric acid: a voltammetric method. *Analytical and Bioanalytical Electrochemistry*, 6(4), 485-500.
- Nguyen, V. H., Tran, T. H., & Shim, J.-J. (2014). Glassy carbon electrode modified with a graphene oxide/poly(o-phenylenediamine) composite for the chemical detection of hydrogen peroxide. *Materials Science and Engineering: C*, 44, 144-150.
- Nien, P. C., Tung, T. S., & Ho, K. C. (2006). Amperometric glucose biosensor based on entrapment of glucose oxidase in a poly (3, 4-ethylenedioxythiophene) film. *Electroanalysis*, 18(13-14), 1408-1415.
- Nigović, B., Sadiković, M., & Sertić, M. (2014a). Multi-walled carbon nanotubes/Nafion composite film modified electrode as a sensor for simultaneous determination of ondansetron and morphine. *Talanta*, 122, 187-194.
- Noor, A. a. M., Shahid, M. M., Rameshkumar, P., & Huang, N. M. (2015). A glassy carbon electrode modified with graphene oxide and silver nanoparticles for amperometric determination of hydrogen peroxide. *Microchimica Acta*, 183(2), 911-916.
- Nyoni, S., & Nyokong, T. (2014). Electrocatalytic behaviour of cobalt tetraminophthalocyanine in the presence of a composite of reduced graphene nanosheets and of multi-walled carbon nanotubes. *Electrochimica Acta*, 136, 2240-2249.
- Oikawa, S. (2005). Sequence-specific DNA damage by reactive oxygen species: Implications for carcinogenesis and aging. *Environmental Health and Preventive Medicine*, 10(2), 65-71.
- Olowu, R. A., Arotiba, O., Mailu, S. N., Waryo, T. T., Baker, P., & Iwuoha, E. (2010). Electrochemical aptasensor for endocrine disrupting 17 β -estradiol based on a poly (3, 4-ethylenedioxythiophene)-gold nanocomposite platform. *Sensors*, 10(11), 9872-9890.
- Özden, S., Tathpinar, S., Bigçer, N., Yaylali, V., Yildirim, C., Özbay, D., & Güner, G. (2003). Basal serum nitric oxide levels in patients with type 2 diabetes mellitus and different stages of retinopathy. *Canadian Journal of Ophthalmology/Journal Canadien d'Ophthalmologie*, 38(5), 393-396.
- Özkan, Y., Yardim-Akaydin, S., Firat, H., Çaliskan-can, E., Ardic, S., & Şimsek, B. (2007). Usefulness of homocysteine as a cancer marker: total thiol compounds and folate levels in untreated lung cancer patients. *Anticancer Research*, 27(2), 1185-1189.
- Palanisamy, S., Chen, S.-M., & Saraswathi, R. (2012). A novel nonenzymatic hydrogen peroxide sensor based on reduced graphene oxide/ZnO composite modified electrode. *Sensors and Actuators B: Chemical*, 166, 372-377.

- Palanisamy, S., Lee, H. F., Chen, S.-M., & Thirumalraj, B. (2015). An electrochemical facile fabrication of platinum nanoparticle decorated reduced graphene oxide; application for enhanced electrochemical sensing of H₂O₂. *RSC Advances*, 5(128), 105567-105573.
- Palmieri, M. C., Sell, S., Huang, X., Scherf, M., Werner, T., Durner, J., & Lindermayr, C. (2008). Nitric oxide-responsive genes and promoters in *Arabidopsis thaliana*: a bioinformatics approach. *Journal of Experimental Botany*, 59(2), 177-186.
- Pandikumar, A., How, G. T. S., See, T. P., Omar, F. S., Jayabal, S., Kamali, K. Z., & John, S. A. (2014). Graphene and its nanocomposite material based electrochemical sensor platform for dopamine. *RSC Advances*, 4(108), 63296-63323.
- Pandikumar, A., & Ramaraj, R. (2011). Aminosilicate sol-gel embedded core-shell (T102-Au) nps nanomaterials modified electrode for the electrochemical detection of nitric oxide. *Indian Journal of Chemistry-Part A InorganicPhysical Theoretical and Analytical*, 50(9), 1388-1393.
- Pang, J., Fan, C., Liu, X., Chen, T., & Li, G. (2003). A nitric oxide biosensor based on the multi-assembly of hemoglobin/montmorillonite/polyvinyl alcohol at a pyrolytic graphite electrode. *Biosensors and Bioelectronics*, 19(5), 441-445.
- Petros, A., Bennett, D., & Vallance, P. (1991). Effect of nitric oxide synthase inhibitors on hypotension in patients with septic shock. *The Lancet*, 338(8782), 1557-1558.
- Petros, A., Lamb, G., Leone, A., Moncada, S., Bennett, D., & Vallance, P. (1994). Effects of a nitric oxide synthase inhibitor in humans with septic shock. *Cardiovascular Research*, 28(1), 34-39.
- Phan, N. T. N., Hanrieder, J., Berglund, E. C., & Ewing, A. G. (2013). Capillary Electrophoresis Mass Spectrometry based Detection of Drugs and Neurotransmitters in *Drosophila* Brain. *Analytical Chemistry*, 85(17), 8448-8454.
- Pocklanova, R., Rathi, A. K., Gawande, M. B., Datta, K. K. R., Ranc, V., Cepe, K., & Zboril, R. (2016). Gold nanoparticle-decorated graphene oxide: Synthesis and application in oxidation reactions under benign conditions. *Journal of Molecular Catalysis A: Chemical*, 424, 121-127.
- Ponnusamy, V. K., Mani, V., Chen, S.-M., Huang, W.-T., & Jen, J. (2014). Rapid microwave assisted synthesis of graphene nanosheets/polyethyleneimine/gold nanoparticle composite and its application to the selective electrochemical determination of dopamine. *Talanta*, 120, 148-157.
- Prasad, B. B., & Singh, R. (2015). A new micro-contact imprinted l-cysteine sensor based on sol-gel decorated graphite/multiwalled carbon nanotubes/gold nanoparticles composite modified sandpaper electrode. *Sensors and Actuators B: Chemical*, 212, 155-164.

- Pryor, W. A., & Church, D. F. (1991). Aldehydes, hydrogen peroxide, and organic radicals as mediators of ozone toxicity. *Free Radical Biology and Medicine*, 11(1), 41-46.
- Qi, S., Zhao, B., Tang, H., & Jiang, X. (2015). Determination of ascorbic acid, dopamine, and uric acid by a novel electrochemical sensor based on pristine graphene. *Electrochimica Acta*, 161, 395-402.
- Qin, X., Lu, W., Luo, Y., Chang, G., Asiri, A. M., Al-Youbi, A. O., & Sun, X. (2012). Green photocatalytic synthesis of Ag nanoparticle-decorated TiO₂ nanowires for nonenzymatic amperometric H₂O₂ detection. *Electrochimica Acta*, 74, 275-279.
- Rahman, M. A., Kumar, P., Park, D.-S., & Shim, Y.-B. (2008). Electrochemical sensors based on organic conjugated polymers. *Sensors*, 8(1), 118-141.
- Raj, M. A., & John, S. A. (2013). Fabrication of electrochemically reduced graphene oxide films on glassy carbon electrode by self-assembly method and their electrocatalytic application. *The Journal of Physical Chemistry C*, 117(8), 4326-4335.
- Rajaram, R., Anandhakumar, S., & Mathiyarasu, J. (2015). Electrocatalytic oxidation of NADH at low overpotential using nanoporous poly (3, 4)-ethylenedioxythiophene modified glassy carbon electrode. *Journal of Electroanalytical Chemistry*, 746, 75-81.
- Rao, A. M., Eklund, P., Bandow, S., Thess, A., & Smalley, R. E. (1997). Evidence for charge transfer in doped carbon nanotube bundles from Raman scattering. *Nature*, 388(6639), 257-259.
- Raoof, J. B., Teymoori, N., Khalilzadeh, M. A., & Ojani, R. (2016). Synergistic signal amplification based on ionic liquid-ZnO nanoparticle carbon paste electrode for sensitive voltammetric determination of acetaminophen in the presence of NADH. *Journal of Molecular Liquids*, 219, 15-20.
- Rastogi, P. K., Ganesan, V., & Krishnamoorthi, S. (2014). A promising electrochemical sensing platform based on a silver nanoparticles decorated copolymer for sensitive nitrite determination. *Journal of Materials Chemistry A*, 2(4), 933-943.
- Reina, A., Jia, X., Ho, J., Nezich, D., Son, H., Bulovic, V., & Kong, J. (2008). Large area, few-layer graphene films on arbitrary substrates by chemical vapor deposition. *Nano Letters*, 9(1), 30-35.
- Revin, S. B., & John, S. A. (2012). Highly sensitive determination of uric acid in the presence of major interferents using a conducting polymer film modified electrode. *Bioelectrochemistry*, 88, 22-29.
- Rotariu, L., Istrate, O.-M., & Bala, C. (2014). Poly (allylamine hydrochloride) modified screen-printed carbon electrode for sensitive and selective detection of NADH. *Sensors and Actuators B: Chemical*, 191, 491-497.

- Roy, K., Sarkar, C. K., & Ghosh, C. K. (2014). Photocatalytic activity of biogenic silver nanoparticles synthesized using yeast (*Saccharomyces cerevisiae*) extract. *Applied Nanoscience*, 5(8), 953-959.
- Santhiago, M., & Vieira, I. C. (2007). L-Cysteine determination in pharmaceutical formulations using a biosensor based on laccase from *Aspergillus oryzae*. *Sensors and Actuators B: Chemical*, 128(1), 279-285.
- Santos, V. N., Cabral, M. F., Ferreira, J. S., Holanda, A. K., Machado, S. A., Sousa, J. R., & de Lima Neto, P. (2011). Study of a gold electrode modified by trans-[Ru(NH₃)₄(1st SO₄)⁺ to produce an electrochemical sensor for nitric oxide. *Electrochimica Acta*, 56(16), 5686-5692.
- Schurman, J. J. (2001). *Antibacterial activity of hydrogen peroxide against Escherichia coli O157: H7 and Salmonella spp. in fruit juices, both alone and in combination with organic acids*. (Master's thesis). Retrieved from <http://theses.lib.vt.edu>
- Sekar, N., & Ramasamy, R. P. (2013). Electrochemical impedance spectroscopy for microbial fuel cell characterization. *Journal of Microbial & Biochemical Technology*, 6(2), 1-13.
- Selvaraju, T., & Ramaraj, R. (2003a). Simultaneous determination of ascorbic acid, dopamine and serotonin at poly(phenosafranine) modified electrode. *Electrochemistry Communications*, 5(8), 667-672.
- Selvaraju, T., & Ramaraj, R. (2003b). Simultaneous determination of dopamine and serotonin in the presence of ascorbic acid and uric acid at poly(o-phenylenediamine) modified electrode. *Journal of Applied Electrochemistry*, 33(8), 759-762.
- Selvaraju, T., & Ramaraj, R. (2005). Electrochemically deposited nanostructured platinum on Nafion coated electrode for sensor applications. *Journal of Electroanalytical Chemistry*, 585(2), 290-300.
- Selvaraju, T., & Ramaraj, R. (2014). Signal amplification of dopamine using lanthanum hexacyanoferrate-modified electrode. *Journal of Chemical Sciences*, 126(1), 11-16.
- Shaban, M., & Galaly, A. R. (2016). Highly sensitive and selective in-situ SERS detection of Pb²⁺, Hg²⁺, and Cd²⁺ using nanoporous membrane functionalized with CNTs. *Scientific Reports*, 6, 25307-25316.
- Shah, B., Lafleur, T., & Chen, A. (2013). Carbon nanotube based electrochemical sensor for the sensitive detection of valacyclovir. *Faraday Discussions*, 164, 135-146.
- Shahid, M. M., Rameshkumar, P., Pandikumar, A., Lim, H. N., Ng, Y. H., & Huang, N. M. (2015). An electrochemical sensing platform based on a reduced graphene oxide-cobalt oxide nanocube@ platinum nanocomposite for nitric oxide detection. *Journal of Materials Chemistry A*, 3(27), 14458-14468.

- Shankar, S., & John, S. A. (2015). 4-Amino-6-hydroxy-2-mercaptopyrimidine capped gold nanoparticles as fluorophore for the ultrasensitive and selective determination of l-cysteine. *Sensors and Actuators B: Chemical*, 221, 1202-1208.
- Shen, H.-X., Yao, J.-L., & Gu, R.-A. (2009). Fabrication and characteristics of spindle Fe₂O₃@Au core/shell particles. *Transactions of Nonferrous Metals Society of China*, 19(3), 652-656.
- Shi, Y., Liu, Z., Zhao, B., Sun, Y., Xu, F., Zhang, Y., & Li, Z. (2011). Carbon nanotube decorated with silver nanoparticles via noncovalent interaction for a novel nonenzymatic sensor towards hydrogen peroxide reduction. *Journal of Electroanalytical Chemistry*, 656(1–2), 29-33.
- Shiekh, G. A., Ayub, T., Khan, S. N., Dar, R., & Andrabi, K. I. (2011). Reduced nitrate level in individuals with hypertension and diabetes. *Journal of Cardiovascular Disease Research*, 2(3), 172-176.
- Shrivastava, A., & Gupta, V. B. (2011). Methods for the determination of limit of detection and limit of quantitation of the analytical methods. *Chronicles of Young Scientists*, 2(1), 21-26.
- Silva, F. d. A. d. S., da Silva, M. G. A., Lima, P. R., Meneghetti, M. R., Kubota, L. T., & Goulart, M. O. F. (2013). A very low potential electrochemical detection of l-cysteine based on a glassy carbon electrode modified with multi-walled carbon nanotubes/gold nanorods. *Biosensors and Bioelectronics*, 50, 202-209.
- Sivanesan, A., & John, S. A. (2010). Highly sensitive electrochemical sensor for nitric oxide using the self-assembled monolayer of 1, 8, 15, 22-Tetraaminophthalocyanatocobalt (II) on glassy carbon electrode. *Electroanalysis*, 22(6), 639-644.
- Skúlason, E., Karlberg, G. S., Rossmeisl, J., Bligaard, T., Greeley, J., Jónsson, H., & Nørskov, J. K. (2007). Density functional theory calculations for the hydrogen evolution reaction in an electrochemical double layer on the Pt (111) electrode. *Physical Chemistry Chemical Physics*, 9(25), 3241-3250.
- Smith, A. D., & Taylor, D. R. (2005). Is exhaled nitric oxide measurement a useful clinical test in asthma? *Current Opinion in Allergy and Clinical Immunology*, 5(1), 49-56.
- Some, S., Sohn, J. S., Kim, J., Lee, S.-H., Lee, S. C., Lee, J., & Jun, S. C. (2016). Graphene-iodine nanocomposites: Highly potent bacterial inhibitors that are bio-compatible with human cells. *Scientific Reports*, 6, 20015-20027.
- Srinivas, A. R. G., Peng, H., Barker, D., & Travas-Sejdic, J. (2012). Switch on or switch off: an optical DNA sensor based on poly (p-phenylenevinylene) grafted magnetic beads. *Biosensors and Bioelectronics*, 35(1), 498-502.
- Sroysee, W., Chairam, S., Amatatongchai, M., Jarujamrus, P., Tamuang, S., Pimmongkol, S., & Somsook, E. (2016). Poly(m-ferrocenylaniline) modified carbon nanotubes-paste electrode encapsulated in nafion film for selective and

sensitive determination of dopamine and uric acid in the presence of ascorbic acid. *Journal of Saudi Chemical Society*.

- Stone, J. R., & Yang, S. (2006). Hydrogen peroxide: a signaling messenger. *Antioxidants & Redox Signaling*, 8(3-4), 243-270.
- Sun, C.-L., Lee, H.-H., Yang, J.-M., & Wu, C.-C. (2011). The simultaneous electrochemical detection of ascorbic acid, dopamine, and uric acid using graphene/size-selected Pt nanocomposites. *Biosensors and Bioelectronics*, 26(8), 3450-3455.
- Tobiška, P., Hugon, O., Trouillet, A., & Gagnaire, H. (2001). An integrated optic hydrogen sensor based on SPR on palladium. *Sensors and Actuators B: Chemical*, 74(1), 168-172.
- Tripatara, P., Patel, N. S., Webb, A., Rathod, K., Lecomte, F. M., Mazzon, E., & Thiemermann, C. (2007). Nitrite-derived nitric oxide protects the rat kidney against ischemia/reperfusion injury in vivo: role for xanthine oxidoreductase. *Journal of the American Society of Nephrology*, 18(2), 570-580.
- Turner, A. P. (2013). Biosensors: sense and sensibility. *Chemical Society Reviews*, 42(8), 3184-3196.
- Uang, Y.-M., & Chou, T.-C. (2003). Fabrication of glucose oxidase/polypyrrole biosensor by galvanostatic method in various pH aqueous solutions. *Biosensors and Bioelectronics*, 19(3), 141-147.
- Védrine, C., Fabiano, S., & Tran-Minh, C. (2003). Amperometric tyrosinase based biosensor using an electrogenerated polythiophene film as an entrapment support. *Talanta*, 59(3), 535-544.
- Vidya, H., Kumara Swamy, B. E., & Schell, M. (2016). One step facile synthesis of silver nanoparticles for the simultaneous electrochemical determination of dopamine and ascorbic acid. *Journal of Molecular Liquids*, 214, 298-305.
- Vijayalakshmi, K., & Jereil, S. D. (2016). High performance electrochemical H₂O₂ sensor based on MWCNT thin films fabricated by novel electron beam evaporation. *Ceramics International*, 42(14), 15493-15501.
- Viswanathan, P., Manivannan, S., & Ramaraj, R. (2015). Polyelectrolyte stabilized bi-metallic Au/Ag nanoclusters modified electrode for nitric oxide detection. *RSC Advances*, 5(67), 54735-54741.
- Wada, M., & Takagi, H. (2006). Metabolic pathways and biotechnological production of l-cysteine. *Applied Microbiology and Biotechnology*, 73(1), 48-54.
- Wallace, J. L., & Woodman, R. C. (1995). Detection of nitric oxide by bioassay. *Methods*, 7(1), 55-58.
- Wang, H., Robinson, J. T., Li, X., & Dai, H. (2009). Solvothermal reduction of chemically exfoliated graphene sheets. *Journal of the American Chemical Society*, 131(29), 9910-9911.

- Wang, S., & Lin, X. (2005). Electrodeposition of Pt-Fe (III) nanoparticle on glassy carbon electrode for electrochemical nitric oxide sensor. *Electrochimica Acta*, 50(14), 2887-2891.
- Wang, W., Rusin, O., Xu, X., Kim, K. K., Escobedo, J. O., Fakayode, S. O., & Strongin, R. M. (2005). Detection of homocysteine and cysteine. *Journal of the American Chemical Society*, 127(45), 15949-15958.
- Wang, X., Luo, C., Li, L., & Duan, H. (2015). Highly selective and sensitive electrochemical sensor for l-cysteine detection based on graphene oxide/multiwalled carbon nanotube/manganese dioxide/gold nanoparticles composite. *Journal of Electroanalytical Chemistry*, 757, 100-106.
- Wang, Y.-L., & Zhao, G.-C. (2011). Electrochemical sensing of nitric oxide on electrochemically reduced graphene-modified electrode. *International Journal of Electrochemistry*, 2011(0), 1-6.
- Wang, Y., Li, C., & Hu, S. (2006). Electrocatalytic oxidation of nitric oxide at nano-TiO₂/Nafion composite film modified glassy carbon electrode. *Journal of Solid State Electrochemistry*, 10(6), 383-388.
- Wang, Y., Polavarapu, L., & Liz-Marzán, L. M. (2014). Reduced graphene oxide-supported gold nanostars for improved SERS sensing and drug delivery. *ACS Applied Materials & Interfaces*, 6(24), 21798-21805.
- Wang, Y., Wan, Y., & Zhang, D. (2010). Reduced graphene sheets modified glassy carbon electrode for electrocatalytic oxidation of hydrazine in alkaline media. *Electrochemistry Communications*, 12(2), 187-190.
- Weber, J. E., Pillai, S., Ram, M. K., Kumar, A., & Singh, S. R. (2011). Electrochemical impedance-based DNA sensor using a modified single walled carbon nanotube electrode. *Materials Science and Engineering: C*, 31(5), 821-825.
- Wennmalm, Å., Lanne, B., & Petersson, A.-S. (1990). Detection of endothelial-derived relaxing factor in human plasma in the basal state and following ischemia using electron paramagnetic resonance spectrometry. *Analytical Biochemistry*, 187(2), 359-363.
- Wong, C. P. P., Lai, C. W., Lee, K. M., & Hamid, S. B. A. (2015). Advanced chemical reduction of reduced graphene oxide and its photocatalytic activity in degrading Reactive Black 5. *Materials*, 8(10), 7118-7128.
- Wu, C., Fan, D., Zhou, C., Liu, Y., & Wang, E. (2016). Colorimetric strategy for highly sensitive and selective simultaneous detection of histidine and cysteine based on G-Quadruplex-Cu(II) metalloenzyme. *Analytical Chemistry*, 88(5), 2899-2903.
- Wu, L.-L., Wang, L.-Y., Xie, Z.-J., Pan, N., & Peng, C.-F. (2016). Colorimetric assay of l-cysteine based on peroxidase-mimicking DNA-Ag/Pt nanoclusters. *Sensors and Actuators B: Chemical*, 235, 110-116.

- Wu, T., Li, T., Liu, Z., Guo, Y., & Dong, C. (2017). Electrochemical sensor for sensitive detection of triclosan based on graphene/palladium nanoparticles hybrids. *Talanta*, 164, 556-562.
- Wynne, A. M., Reid, C. H., & Finnerty, N. J. (2014). In vitro characterisation of ortho phenylenediamine and Nafion®-modified Pt electrodes for measuring brain nitric oxide. *Journal of Electroanalytical Chemistry*, 732, 110-116.
- Xi, X., & Ming, L. (2012). A voltammetric sensor based on electrochemically reduced graphene modified electrode for sensitive determination of midecamycin. *Analytical Methods*, 4(9), 3013-3018.
- Xiao, C., Chen, J., Liu, B., Chu, X., Wu, L., & Yao, S. (2011). Sensitive and selective electrochemical sensing of l-cysteine based on a caterpillar-like manganese dioxide-carbon nanocomposite. *Physical Chemistry Chemical Physics*, 13(4), 1568-1574.
- Xu, X., Qiao, J., Li, N., Qi, L., & Zhang, S. (2015). Fluorescent probe for turn-on sensing of l-cysteine by ensemble of AuNCs and polymer protected AuNPs. *Analytica Chimica Acta*, 879, 97-103.
- Xu, X., Yang, L., Jiang, S., Hu, Z., & Liu, S. (2011). High reaction activity of nitrogen-doped carbon nanotubes toward the electrooxidation of nitric oxide. *Chemical Communications*, 47(25), 7137-7139.
- Xu, Z., Huang, Y., Min, C., Chen, L., & Chen, L. (2010). Effect of γ -ray radiation on the polyacrylonitrile based carbon fibers. *Radiation Physics and Chemistry*, 79(8), 839-843.
- Yan, Y., Li, K., Dai, Y., Chen, X., Zhao, J., Yang, Y., & Lee, J.-M. (2016). Synthesis of 3D mesoporous samarium oxide hydrangea microspheres for enzyme-free sensor of hydrogen peroxide. *Electrochimica Acta*, 208, 231-237.
- Yang, B., Zhu, J., Deng, C., & Duan, G. (2006). Development of a sensitive and rapid liquid chromatography/tandem mass spectrometry method for the determination of apomorphine in canine plasma. *Rapid Communications in Mass Spectrometry*, 20(12), 1883-1888.
- Yang, L., Liu, D., Huang, J., & You, T. (2014). Simultaneous determination of dopamine, ascorbic acid and uric acid at electrochemically reduced graphene oxide modified electrode. *Sensors and Actuators B: Chemical*, 193, 166-172.
- Yang, L., Wang, B., Qi, H., Gao, Q., Li, C.-z., & Zhang, C. (2015). Highly sensitive electrochemical sensor for the determination of 8-Hydroxy-2-deoxyguanosine incorporating SWCNTs-Nafion composite film. *Journal of Sensors*, 2015, 1-11.
- Yang, L., Xu, C., Ye, W., & Liu, W. (2015). An electrochemical sensor for H₂O₂ based on a new Co-metal-organic framework modified electrode. *Sensors and Actuators B: Chemical*, 215, 489-496.

- Yang, N., Song, H., Wan, X., Fan, X., Su, Y., & Lv, Y. (2015). A metal (Co)–organic framework-based chemiluminescence system for selective detection of L-cysteine. *Analyst*, 140(8), 2656-2663.
- Yang, S., Li, G., Wang, Y., Wang, G., & Qu, L. (2016). Amperometric L-cysteine sensor based on a carbon paste electrode modified with Y₂O₃ nanoparticles supported on nitrogen-doped reduced graphene oxide. *Microchimica Acta*, 183(4), 1351-1357.
- Ye, Z., Wang, L., & Wen, J. (2015). A simple and sensitive method for determination of Norfloxacin in pharmaceutical preparations. *Brazilian Journal of Pharmaceutical Sciences*, 51(2), 429-437.
- Yeh, M.-H., Sun, C.-L., Su, J.-S., Lin, L.-Y., Lee, C.-P., Chen, C.-Y., & Ho, K.-C. (2012). A low-cost counter electrode of ITO glass coated with a graphene/Nafion® composite film for use in dye-sensitized solar cells. *Carbon*, 50(11), 4192-4202.
- Yeh, Y.-C., Creran, B., & Rotello, V. M. (2012). Gold nanoparticles: preparation, properties, and applications in bionanotechnology. *Nanoscale*, 4(6), 1871-1880.
- Yin, H., Zhou, Y., Ma, Q., Ai, S., Ju, P., Zhu, L., & Lu, L. (2010). Electrochemical oxidation behavior of guanine and adenine on graphene–Nafion composite film modified glassy carbon electrode and the simultaneous determination. *Process Biochemistry*, 45(10), 1707-1712.
- Yin, J., Qi, X., Yang, L., Hao, G., Li, J., & Zhong, J. (2011). A hydrogen peroxide electrochemical sensor based on silver nanoparticles decorated silicon nanowire arrays. *Electrochimica Acta*, 56(11), 3884-3889.
- Yu, A., Liang, Z., Cho, J., & Caruso, F. (2003). Nanostructured electrochemical sensor based on dense gold nanoparticle films. *Nano Letters*, 3(9), 1203-1207.
- Yu, C.-M., Fung, P. C.-W., Chan, G., Lai, K. W.-H., Wang, Q., & Lau, C.-P. (2001). Plasma nitric oxide level in heart failure secondary to left ventricular diastolic dysfunction. *The American Journal of Cardiology*, 88(8), 867-870.
- Yusoff, N., Kumar, S. V., Pandikumar, A., Huang, N., Marlinda, A., & An'amt, M. (2014). Core-shell Fe₃O₄-ZnO nanoparticles decorated on reduced graphene oxide for enhanced photoelectrochemical water splitting. *Ceramics International*, 41(2), 5117-5128.
- Yusoff, N., Kumar, S. V., Rameshkumar, P., Pandikumar, A., Shahid, M. M., Ab Rahman, M., & Huang, N. M. (2016). A facile preparation of titanium dioxide-iron oxide@ silicon dioxide incorporated reduced graphene oxide nanohybrid for electrooxidation of methanol in alkaline medium. *Electrochimica Acta*, 192, 167-176.
- Yusoff, N., Pandikumar, A., Marlinda, A., Huang, N., & Lim, H. (2015). Nanosized graphene/Nafion hybrid modified electrode for electrochemical detection of dopamine. *Science of Advanced Materials*, 7(12), 2692-2703.

- Yusoff, N., Pandikumar, A., Marlinda, A. R., Huang, N. M., & Lim, H. N. (2015). Facile synthesis of nanosized graphene/Nafion hybrid materials and their application in electrochemical sensing of nitric oxide. *Analytical Methods*, 7(8), 3537-3544.
- Zainy, M., Huang, N. M., Vijay Kumar, S., Lim, H. N., Chia, C. H., & Harrison, I. (2012). Simple and scalable preparation of reduced graphene oxide–silver nanocomposites via rapid thermal treatment. *Materials Letters*, 89, 180-183.
- Zamfir, L.-G., Rotariu, L., Marinescu, V. E., Simelane, X. T., Baker, P. G. L., Iwuoha, E. I., & Bala, C. (2016). Non-enzymatic polyamic acid sensors for hydrogen peroxide detection. *Sensors and Actuators B: Chemical*, 226, 525-533.
- Zare, H. R., Jahangiri-Dehaghani, F., Shekari, Z., & Benvidi, A. (2016). Electrocatalytic simultaneous determination of ascorbic acid, uric acid and l-Cysteine in real samples using quercetin silver nanoparticles–graphene nanosheets modified glassy carbon electrode. *Applied Surface Science*, 375, 169-178.
- Zarei, K., & Helli, H. (2015). Electrochemical determination of aminopyrene on glassy carbon electrode modified with multi-walled carbon nanotube–sodium dodecyl sulfate/Nafion composite film. *Journal of Electroanalytical Chemistry*, 749, 10-15.
- Zeng, Q., Jim, C. K., Lam, J. W., Dong, Y., Li, Z., Qin, J., & Tang, B. Z. (2009). A new disubstituted polyacetylene for the detection of α -amino acids. *Macromolecular Rapid Communications*, 30(3), 170-175.
- Zhang, F., Li, Y., Gu, Y.-e., Wang, Z., & Wang, C. (2011). One-pot solvothermal synthesis of a Cu₂O/Graphene nanocomposite and its application in an electrochemical sensor for dopamine. *Microchimica Acta*, 173(1-2), 103-109.
- Zhang, J., Gao, L., Sun, J., Liu, Y., Wang, Y., Wang, J., & Noda, K. (2008). Dispersion of single-walled carbon nanotubes by nafion in water/ethanol for preparing transparent conducting films. *The Journal of Physical Chemistry C*, 112(42), 16370-16376.
- Zhang, Y., Jiang, J., Li, M., Gao, P., Zhou, Y., Zhang, G., & Dong, C. (2016). Colorimetric sensor for cysteine in human urine based on novel gold nanoparticles. *Talanta*, 161, 520-527.
- Zhang, Y., Zhang, M., Wei, Q., Gao, Y., Guo, L., Al-Ghanim, K. A., & Zhang, X. (2016). An easily fabricated electrochemical sensor based on a graphene-modified glassy carbon electrode for determination of octopamine and tyramine. *Sensors*, 16(4), 535-549.
- Zhong, L., Gan, S., Fu, X., Li, F., Han, D., Guo, L., & Niu, L. (2013). Electrochemically controlled growth of silver nanocrystals on graphene thin film and applications for efficient nonenzymatic H₂O₂ biosensor. *Electrochimica Acta*, 89, 222-228.

- Zhou, M., Ding, J., Guo, L.-p., & Shang, Q.-k. (2007). Electrochemical behavior of l-Cysteine and its detection at ordered mesoporous carbon-modified glassy carbon electrode. *Analytical Chemistry*, 79(14), 5328-5335.
- Zhou, M., Zhai, Y., & Dong, S. (2009). Electrochemical sensing and biosensing platform based on chemically reduced graphene oxide. *Analytical Chemistry*, 81(14), 5603-5613.
- Zhu, L., Zhang, Y., Xu, P., Wen, W., Li, X., & Xu, J. (2016). PtW/MoS₂ hybrid nanocomposite for electrochemical sensing of H₂O₂ released from living cells. *Biosensors and Bioelectronics*, 80, 601-606.

LIST OF PUBLICATIONS AND PAPERS PRESENTED

Full-research paper (ISI-cited):

- 1) **Yusoff, N.**, Rameshkumar, P., Mehmood, M. S., Huang, S. T., & Huang, N. M. (2017). Amperometric detection of nitric oxide using a glassy carbon electrode modified with gold nanoparticles incorporated into a nanohybrid composed of reduced graphene oxide and Nafion. *Microchimica Acta*, 1, 1-9.
- 2) **Yusoff, N.**, Rameshkumar, P., Mehmood, M. S., Pandikumar, A., Lee, H. W., & Huang, N. M. (2017). Ternary nanohybrid of reduced graphene oxide-nafion@silver nanoparticles for boosting the sensor performance in non-enzymatic amperometric detection of hydrogen peroxide. *Biosensors and Bioelectronics*, 87, 1020-1028.
- 3) **Yusoff, N.**, Pandikumar, A., Marlinda, A. R., Huang, N. M., & Lim, H. N. (2015). Nanosized graphene/nafion hybrid modified electrode for electrochemical detection of dopamine. *Science of Advanced Materials*, 12, 2692-2703.
- 4) **Yusoff, N.**, Pandikumar, A., Marlinda, A. R., Huang, N. M., & Lim, H. N. (2015). Facile synthesis of nanosized graphene/Nafion hybrid materials and its application in electrochemical sensing of nitric oxide. *Analytical Methods*, 7, 3537-3544.
- 5) Marlinda, A. R., Pandikumar, A., **Yusoff, N.**, Huang, N. M., & Lim, H. N. (2014). Electrochemical sensing of nitrite using a glassy carbon electrode modified with reduced functionalized graphene oxide decorated with flower-like zinc oxide. *Microchimica Acta*, 5, 1113-1122.
- 6) Marlinda, A. R., Pandikumar, A., Jayabal, S., **Yusoff, N.**, Suriani, A. B., & Huang, N. M. (2016). Voltammetric determination of nitric oxide using a

glassy carbon electrode modified with a nanohybrid consisting of myoglobin, gold nanorods, and reduced graphene oxide. *Microchimica Acta*, 183, 3077-3085.

- 7) An'amt, M. N., Rameshkumar, P., **Yusoff, N.**, Huang, N. M., & Sajab, M. S. (2016). Microwave synthesis of reduced graphene oxide decorated with silver nanoparticles for electrochemical determination of 4-nitrophenol. *Ceramics International*, 16, 18813-18820.
- 8) Nurzulaikha, R., Lim, H. N., Harrison, I., Lim, S. S., Pandikumar, A., Huang, N. M., Lim, S. P., Thien, G. S. H., **Yusoff, N.**, & Ibrahim, I. (2015). Graphene/SnO₂ nanocomposite modified electrode for the electrochemical detection of dopamine. *Sensing Bio-Sensing Research*, 5, 42-49.

Review article (ISI-cited):

- 1) **Yusoff, N.**, Pandikumar, A., Ramaraj, R., Lim, H. N., & Huang, N. M. (2015). Gold nanoparticle based optical and electrochemical sensing of dopamine. *Microchimica Acta*, 13, 2091-2114.
- 2) Pandikumar, A., How, G. T. S., Teo, P. S., Fatin, S. O., Jayabal, S., Kamali, K. Z., **Yusoff, N.**, Ashilah, J., Ramaraj, R., Abraham John, S., Lim, H. N., & Huang, N. M. (2014). Graphene and its nanocomposites material based electrochemical sensor platform for dopamine. *RSC Advances*, 4, 63296-63323.

Book chapter:

- 1) **Yusoff, N.**, Pandikumar, A., Huang, N. M., Lim, H. N. (2015). Graphene based electrochemical platform for biosensor applications. In Ashutosh, T., Hirak, K. P., & Anthony P. F. T. (Eds.), *Advanced Bioelectronic Materials* (pp. 187-214). Hoboken, NJ, USA.

Paper presented in international conference:

- 1) **Yusoff, N.** & Huang, N. M. (2015, Dec). *Nanosized graphene/Nafion hybrid modified electrode for electrochemical detection of dopamine*. Paper presented at the International Conference on Recent Advances in Materials and Chemical Sciences (ICRAMCS), Gandhigram Rural Institute-Deemed University, Tamil Nadu, India.